On the Cosmological Propagation of High Energy Particles in Magnetic Fields

Dissertation with the aim of achieving a doctoral degree
at the Faculty of Mathematics, Informatics and Natural Sciences
Department of Physics
Universität Hamburg

submitted by

Rafael Alves Batista

from Uberaba, Brazil

Hamburg
2015

Day of oral defense: April 8th, 2015
Examiners of the oral doctoral defense:
Prof. Dr. Dieter Horns
Prof. Dr. Johannes Haller
Prof. Dr. Andreas Ringwald
The following evaluators recommend the admission of the dissertation:
Prof. Dr. Günter Sigl
Prof. Dr. Robi Banerjee

Acknowledgements

During this journey many people have contributed to my personal and academic growth. These pages are dedicated to express my gratitude to all those individuals who, in some way, have directly or indirectly contributed to this work. I apologize for forgetting and omitting some names.

First of all, I would like to express my gratitude to my supervisor Günter Sigl for his guidance during these three years. Without him this work definitely would not have been possible.

I would like to specially thank my mom, Helena Maria Alves, who has always supported me in all possible ways, alongside with my dad, Francisco Batista. They provided me with all the necessary conditions to trail this path. I thank Luciana Oliveira Fernandes who was always there to support and cheer me up during difficult times and the long nights when I was working and asking myself *"will I ever get this done?"*. I also thank all my close friends for their support.

I thank Dmitri Semikoz (APC, Paris) and Julien Devriendt and Min-Su Shin (University of Oxford) for their hospitality during multiple visits to their institutes. I am indebted to Dmitri Semikoz for his help and guidance in many parts of this work. I also gratefully acknowledge the cosmological simulations performed by Julien Devriendt and Min-Su Shin, which were the core of chapter 6, and thank them for productive discussions.

I acknowledge the crucial contribution of the CRPropa developers team (Martin Erdmann, Carmelo Evoli, Karl-Heinz Kampert, Daniel Kuempel, Gero Mueller, Guenter Sigl, Arjen van Vliet, David Walz, Tobias Winchen) to this work. My special thanks to David Walz for many discussions and for promptly helping me solving some problems with the code.

I thank Carmelo Evoli, Andrey Saveliev, Peter Schiffer and Arjen van Vliet for discussions, and Andrey for his contribution to the development of the gamma ray propagation code. I also thank my fellow colleagues from the Pierre Auger Collaboration for useful discussions.

My life in Hamburg would not have been the same without the companionship of former and current members of the astroparticle theory group. Thank you all! I am also glad for having had such great friends office mates (Andrey Saveliev and Martin Vollmann).

I cannot fail to mention two people who mentored me in the early stages of my career: my former advisor Ernesto Kemp, who supervised me for 5 years, and my former co-supervisor Rogerio de Almeida, who patiently guided my first steps in the field of cosmic rays.

This work was possible thanks to the support of the Forschungs- und Wissenschaftsstiftung Hamburg through the program "Astroparticle Physics with Multiple Messengers". I also acknowledge the complementary funding from the Helmholtz Alliance for Astroparticle Physics (HAP).

Abstract

In the present work the connection between high energy particles and cosmic magnetic fields is explored. Particularly, the focus lies on the propagation of ultra-high energy cosmic rays (UHECRs) and very-high energy gamma rays (VHEGRs) over cosmological distances, under the influence of cosmic magnetic fields.

The first part of this work concerns the propagation of UHECRs in the magnetized cosmic web, which was studied both analytically and numerically. A parametrization for the suppression of the UHECR flux at energies $\sim 10^{18}$ eV due to diffusion in extragalactic magnetic fields was found, making it possible to set an upper limit on the energy at which this magnetic horizon effect sets in, which is $\lesssim 10^{17}$ eV.

To confront theoretical models with experimental data collected by large cosmic ray experiments such as the Pierre Auger Observatory, and at the same time to address the open questions regarding the origin and nature of UHECRs, the CRPropa code was developed. It allows the propagation of UHECRs and secondary gamma rays and neutrinos in the universe including all relevant energy loss and interaction processes as well as effects of galactic and extragalactic magnetic fields. The newest version, CRPropa 3, is discussed in details, including the novel feature of cosmological effects in three-dimensional simulations, which enables time dependent studies considering simultaneously magnetic field effects and the cosmological evolution of the universe.

An interesting possibility is to use UHECRs to constrain properties of cosmic magnetic fields, and vice-versa. Numerical simulations of the propagation of UHECRs in the magnetized cosmic web, obtained through magnetohydrodynamical simulations of structure formation, were performed. It was studied the effects of different magnetic field seeds on the distribution of cosmic magnetic fields today, and their impact on the propagation of cosmic rays. Furthermore, the influence of uncertainties of the strength of intergalactic magnetic fields on the propagation of UHECRs was analyzed. It is shown that magnetic fields are crucial for the propagation of cosmic rays, and the lack of knowledge about their properties can spoil the possibilities of identifying individual sources of UHECRs. The prospects for UHECR astronomy are discussed in light of these results.

The second part of this work concerns the propagation of VHEGRs in the universe. Gamma rays interact with pervasive photon fields creating electron-positron pairs which scatter background photons, in a process known as electromagnetic cascade. The electron-positron pairs can provide valuable information about the intervening magnetic fields, including the possibility of constraining the strength of these fields. A new Monte Carlo code for propagating VHEGRs in the universe was developed, based on the code structure of CRPropa. This code was applied to the study of pair halos from blazars under the assumption of different magnetic field configurations. The results suggest that the observation of pair halos can provide important clues on the strength of intergalactic magnetic fields, as well as the maximal energy attainable by VHEGR sources.

Zusammenfassung

In der vorliegenden Dissertation wird die Beziehung zwischen hochenergetischen Teilchen und kosmischen Magnetfeldern erforscht. Insbesondere geht es dabei um die Ausbreitung der ultrahochenergetischen kosmischen Strahlung (UHECRs) und der sehr hochenergetischen Gammastrahlung (VHEGRs) in kosmichen Magnetfeldern.

Der erste Teil dieser Arbeit betrifft die Ausbreitung der UHECRs im kosmischen Netz, die analytisch und numerisch untersucht wurde. Es wurde eine Parametrisierung der Unterdrückung des UHECR-Flusses bei Energien $\sim 10^{18}$ eV aufgrund der Diffusion in extragalaktischen Magnetfeldern gefunden, die es ermöglicht, eine Obergrenze für die Energie, bei der dieser Effekt des magnetischen Horizonts einsetzt, zu bestimmen, nämlich $\lesssim 10^{17}$ eV.

Um theoretische Modelle mit Daten von Großexperimenten zur kosmischen Strahlung wie dem Pierre Auger Observatorium zu vergleichen und um gleichzeitig die offenen Fragen in Bezug auf den Ursprung und die Natur der UHECRs zu beantworten, wurde die Software CRPropa entwickelt. Mit dieser ist es möglich, die Ausbreitung von UHECRs sowie der sekundären Gammastrahlung und Neutrinos im Universum zu simulieren, einschließlich aller relevanter Energieverlust- und Wechselwirkungsprozesse sowie der Auswirkungen der galaktischen und extragalaktischen Magnetfelder. Die neueste Version, CRPropa 3, wird detailliert diskutiert, darunter die neue Möglichkeit der Einbeziehung der kosmologischen Effekte bei dreidimensionalen Simulationen, welche zeitabhängige Studien unter gleichzeitiger Beachtung von Magnetfeldern und der kosmologischen Entwicklung des Universums ermöglicht.

Es ist eine interessante Möglichkeit, UHECRs zu benutzen, um Eigenschaften der kosmischen Magnetfelder einzuschränken und umgekehrt. Numerische Simulationen der Ausbreitung von UHECRs im magnetisierten kosmischen Netz, welches durch magnetohydrodynamische Simulationen der Strukturbildung erhalten wurde, wurden durchgeführt. Die Effekte unterschiedlicher Saatmagnetfelder auf die heutige kosmische Magnetfeldverteilung sowie ihre Auswirkung auf die Ausbreitung der kosmischen Strahlung wurden untersucht. Weiterhin wurde eine Analyse gemacht, um den Einfluss der Unsicherheiten der Stärke intergalaktischer Magnetfelder auf die Ausbreitung der UHECRs zu verstehen. Es wird gezeigt, dass Magnetfelder entscheidend für die Ausbreitung der kosmischen Strahlung sind und dass die mangelnde Kenntnis ihrer Eigenschaften die Identifizierung der Quellen der UHECRs teilweise verhindern können. Die Perspektiven für die UHECR-Astronomie werden angesichts diese Ergebnisse diskutiert.

Der zweite Teil dieser Arbeit behandelt die Ausbreitung der VHEGRs im Universum. Die Wechselwirkung der Gammastrahlen mit den durchdringenden Photonenfeldern kann Elektron-Positron-Paare erzeugen, die wiederum die Hintergrundphotonen streuen. Dieser Prozess ist die sogenannte elektromagnetische Kaskade. Die Elektron-Positron-Paare können wertvolle Informationen über die den von ihnen durchquerten Raum durchziehenden Magnetfelder liefern, einschließlich der Möglichkeit der Einschränkung der Stärke dieser Felder. Basierend auf der Struktur von CRPropa wurde ein neuer Monte-Carlo-Code für die Ausbreitung von VHEGRs im Universum entwickelt. Dieser Code wurde für die Untersuchung von Paarhalos von Blazaren verwendet, um verschiedene Magnetfeldmodelle zu vergleichen. Die Ergebnisse weisen darauf hin, dass die Beobachtung von Paarhalos wichtige Hinweise sowohl auf die Stärke der intergalaktischen Magnetfelder als auch auf die maximal erreichbare Energie der Gammastrahlen, die von einer Quelle emittierten werden, geben können.

Contents

Prologue **1**

1 The Universe: Exordium **5**
1.1 Cosmology: essential concepts and mathematical machinery . . . 5
1.1.1 The Friedmann-Lemaître-Robertson-Walker Universe . . . 5
1.1.2 Distance and time measures in cosmology . . . 6
1.2 The Big Bang and its aftermath . . . 8
1.3 The cosmic web . . . 8
1.4 Cosmic photon backgrounds . . . 9
1.4.1 Cosmic Microwave Background . . . 9
1.4.2 Cosmic Infrared Background . . . 10
1.4.3 Cosmic Radio Background . . . 10
1.5 Cosmic magnetic fields . . . 11
1.5.1 Constraint methods . . . 11
1.5.1.1 Polarization of star light . . . 11
1.5.1.2 Synchrotron emission . . . 12
1.5.1.3 Zeeman effect . . . 12
1.5.1.4 Faraday rotation . . . 13
1.5.1.5 Big Bang Nucleosynthesis . . . 14
1.5.1.6 CMB anisotropies . . . 14
1.5.1.7 Magnetic diffusion bounds on the coherence length . . . 15
1.5.1.8 Ultra-high energy cosmic rays . . . 15
1.5.1.9 Gamma-ray induced electromagnetic cascades . . . 15
1.5.2 On the cosmological magnetogenesis . . . 17
1.5.2.1 Astrophysical origin . . . 17
1.5.2.2 Primordial origin . . . 18
1.5.3 Extragalactic magnetic fields . . . 20
1.5.3.1 Magnetic fields in clusters of galaxies . . . 20
1.5.3.2 Magnetic fields in the Local Supercluster . . . 21
1.5.3.3 Magnetic fields in filaments . . . 21
1.5.3.4 Cosmological magnetic fields? . . . 21
1.5.4 Galactic magnetic field . . . 21
1.5.4.1 Logarithmic spiral models and symmetries . . . 22
1.5.4.2 An example of logarithmic spiral . . . 23
1.5.4.3 A toroidal model . . . 24
1.5.4.4 The Jansson-Farrar model . . . 24

2 Cosmic Rays **27**
2.1 A short history of cosmic ray physics . . . 27
2.1.1 Early history (1900s – 1930s) . . . 27
2.1.2 First measurements outside Earth (1930s – 1950s) . . . 28
2.1.3 The first high energy cosmic ray experiments (1960s – 1980s) . . . 29
2.1.4 The 1980s, 1990s and early 2000s . . . 29
2.2 Extensive air showers . . . 30

2.3 The cosmic ray spectrum . . . 31
2.4 Nature of cosmic rays: composition . . . 34
2.5 Origin and acceleration mechanisms of UHECRs . . . 34
2.5.1 Fermi acceleration . . . 34
2.5.1.1 2nd order Fermi acceleration . . . 34
2.5.1.2 1st order Fermi acceleration . . . 36
2.5.2 Acceleration by unipolar inductors . . . 36
2.5.3 Other acceleration mechanisms . . . 37
2.5.4 Possible acceleration sites . . . 37
2.5.4.1 Neutron stars . . . 37
2.5.4.2 Magnetars . . . 38
2.5.4.3 Gamma Ray Bursts . . . 38
2.5.4.4 Active Galactic Nuclei . . . 39
2.6 Interactions and energy losses . . . 39

3 High Energy Gamma Rays 43
3.1 A brief history of gamma rays . . . 43
3.2 Interactions and energy losses . . . 44
3.2.1 Electron bremsstrahlung . . . 44
3.2.2 Annihilation of electron pairs . . . 44
3.2.3 Nuclear emission . . . 44
3.2.4 Pion decay . . . 45
3.2.5 Pair production . . . 45
3.2.6 Inverse Compton scattering . . . 46
3.3 Sources . . . 46
3.3.1 Supernova remnants . . . 47
3.3.2 Pulsars . . . 48
3.3.3 Pulsar wind nebulae . . . 48
3.3.4 Binary systems . . . 48
3.3.5 Galactic center and Fermi bubbles . . . 49
3.3.6 Starburst galaxies . . . 49
3.3.7 Blazars . . . 49
3.3.8 Unconfirmed candidates and unidentified sources . . . 50
3.4 Experimental methods . . . 50
3.4.1 Ground-based air shower detectors . . . 50
3.4.2 Imaging air Cherenkov technique . . . 50

4 Diffusion of cosmic rays in extragalactic magnetic fields 53
4.1 The diffusive cosmic ray spectrum . . . 53
4.2 Extragalactic magnetic fields . . . 56
4.3 Parametrization of the flux suppression . . . 58
4.4 Upper limits on the magnetic suppression . . . 60
4.5 Discussion . . . 61
4.6 Remarks on the validity of the approximations . . . 63

5 CRPropa 3.0 65
5.1 About the code . . . 65
5.2 Technical aspects . . . 65
5.3 Code structure and propagation algorithm . . . 66
5.4 Interaction and energy losses . . . 68
5.4.1 Pair production . . . 68
5.4.2 Photopion production . . . 69
5.4.3 Photodisintegration . . . 70
5.4.4 Nuclear decay . . . 73
5.5 Adiabatic energy losses . . . 76
5.6 Sources and Observers . . . 77

5.7 The 4D mode . . . 78
5.8 Magnetic Fields . . . 78
5.8.1 Extragalactic magnetic fields . . . 78
5.8.2 Galactic magnetic fields . . . 79
5.8.3 Galactic lensing . . . 79
5.9 CIB: models and redshift dependence . . . 80
5.10 Applications . . . 81
5.10.1 1D propagation with secondaries . . . 81
5.10.2 3D propagation . . . 81

6 Propagation of UHECRs in the cosmic web **85**
6.1 The simulated cosmic web . . . 85
6.1.1 Checking the impact of the magnetic field normalization . . . 86
6.1.2 Checking the convergence of the MHD simulations . . . 87
6.2 Handling AMR grids in CRPropa . . . 88
6.3 UHECR "tomography" of the cosmic web . . . 88
6.4 Effects of primordial magnetic field seeds . . . 89
6.5 Impact of the normalization choice . . . 90
6.5.1 Choice of the magnetic field normalization . . . 90
6.5.2 Setup of the simulation . . . 92
6.5.3 Results and discussion . . . 93
6.6 Further remarks . . . 94

7 Propagation of UHECRs over cosmological distances **99**
7.1 Introduction . . . 99
7.2 Cosmological effects in three-dimensional simulations of propagation of UHECRs . . . 99
7.2.1 First attempt: redshift correction . . . 99
7.2.2 A novel approach: correction table . . . 101
7.2.2.1 The method . . . 101
7.2.2.2 Applications . . . 102
7.2.2.3 General remarks . . . 103
7.2.3 A "hybrid" approach . . . 104
7.2.3.1 The method . . . 104
7.2.3.2 Application . . . 104
7.2.3.3 General remarks and setbacks of the method . . . 106
7.3 4D propagation of UHECRs . . . 109
7.3.1 Simulation setup . . . 109
7.3.2 Results and discussion . . . 110

8 GRPropa 1.0 **113**
8.1 Introduction . . . 113
8.2 An overview of the code . . . 113
8.3 Interactions and energy losses . . . 114
8.3.1 Pair production . . . 114
8.3.2 Inverse Compton scattering . . . 115
8.3.3 Synchrotron emission . . . 116
8.3.4 Adiabatic losses . . . 116
8.4 Detection methods . . . 116
8.5 Comparisons with Elmag . . . 117
8.6 Applications . . . 118
8.6.1 Spectrum of the blazar 1ES 0229+200 . . . 118
8.6.2 Extended emission at $E \gtrsim 10$ TeV . . . 118

9 Blazar pair halos and EGMFs **121**
9.1 Overture . . . 121
9.2 An analytical description of the formation of pair halos . . . 121
9.2.1 Extended emission around point sources . . . 123
9.2.2 Time delay . . . 124
9.3 Setup of simulations . . . 125
9.4 Result of analysis . . . 126
9.5 Discussion . . . 126

10 Conclusions **131**

Epilogue **133**

A Diffusive cosmic ray spectrum in an expanding universe **137**
A.1 Diffusion equation in an expanding universe . . . 137
A.2 The diffusive cosmic ray spectrum . . . 138

B Magnetic suppression: best fit parameters **141**

Prologue

Cosmic magnetic fields are ubiquitous, and their existence has been confirmed in scales ranging from planets to clusters of galaxies [1]. The intensity of these fields can vary from $\sim 10^{-10}$ G in filaments, which are possibly the largest magnetized structures in the universe up to 10^{15} G in magnetars, the astrophysical objects with the largest magnetic fields known. Even lower magnetic fields ($\sim 10^{-20}$ G) can exist in the vast regions devoided of matter called cosmic voids. The mechanisms which originated cosmic magnetic fields in the universe are an unsolved problem in cosmology. Understanding the magnetogenic process is extremely important for understanding the early universe, how the structures observed today were formed, and how they evolved.

Intergalactic magnetic fields (IGMFs) are the ones possibly present in the voids whose existence is not yet confirmed. Upper bounds for the strength of these fields do exist and are of the order of 1 aG, and some studies claim to have found a lower limit of the order of 10^{-16} G [2] based on the observation of gamma ray-induced electromagnetic cascades from TeV blazars, although this lower bound has been questioned in some recent works [3, 4]. These fields may carry imprints of the process of generation of magnetic fields in the early universe, since they are virtually unaffected by magnethohydrodynamical processes. Imprints of IGMFs may be present in the voids. Because the density of these regions is extremely low, magnetohydrodynamical amplification of seed fields might not have occurred, hence keeping the properties of these fields approximately unaltered.

Matter in the universe is not randomly distributed, but hierarchically clustered into larger objects. Galaxies are grouped in clusters, which are dense nodes connected to each other through filaments, composing a gigantic network called the cosmic web. The cosmic web contains regions with low matter density, the voids, which fill most of the volume of the universe.

The universe is also pervaded by omnipresent photon fields, namely the cosmic microwave background (CMB), a relic of the matter-radiation decoupling after the Big Bang, and the extragalactic background light (EBL), which comprises electromagnetic radiation in a wide range of frequencies. Together with cosmic magnetic fields, photon fields provide a background for the propagation of particles in the universe. On one hand these particles can bring valuable information about the environments which they traverse or where they are immerse, thus serving as astrophysical and/or cosmological probes (particle physics $\rightarrow$ astrophysics/cosmology). On the other hand, the knowledge about astrophysics and cosmology allow the study the properties of these particles (astrophysics/cosmology $\rightarrow$ particle physics). The present work focus essentially on two types of particles: ultra-high energy cosmic rays (UHECRs) and very-high energy gamma rays (VHEGRs).

Cosmic rays[1] are energetic particles from outer space that reach Earth. It is remarkable that the cosmic ray spectrum spans almost 13 orders of magnitude, from 100 MeV to $\sim$100-1000 EeV[2]. Today,

[1] There is no consensus on the definition of cosmic rays. In the present work cosmic rays are defined as any nucleon or atomic nuclei with energy larger than 100 MeV that reach Earth.

[2] One exaelectronvolt (EeV) is defined as 10^{18} eV.

more than one century after the first experimental detection of cosmic rays, the origin and nature of the most energetic[3] particles in the universe, the UHECRs, still remain a mystery.

The flux of cosmic rays at ultra-high energies is very low (~ 1 particle per square kilometer per century), thus requiring detectors covering a large area. Today, the largest UHECR experiment is the Pierre Auger Observatory, in Argentina, which has been operational since 2004. The interpretation of experimental data entails comparisons with theoretical models. Due to the large uncertainties in the models a large parameter space has to be covered. This can be done using advanced simulation engines which include all relevant interactions as well as the current knowledge about cosmic magnetic fields, such as CRPropa [5–9], SimProp [10] and HERMES [11].

At energies above $\sim 10^{19}$ eV the distance that UHECRs can travel is strongly limited by the pervasive photon fields, which imply the existence of an interaction horizon, beyond which cosmic rays cannot reach Earth without suffering severe energy losses. Therefore, at the highest energies UHECRs have a local origin. Nevertheless, for energies $\sim 10^{18}$ eV most of the cosmic ray flux can be dominated by the contribution of sources at cosmological distances. In addition, a key factor that should be considered is the existence of cosmic magnetic fields. Depending on the distance of the source, the propagation time of particles in magnetic fields can be comparable to the age of the universe, and consequently they would not reach Earth. This provides another constraint on the distance of sources of UHECRs: a magnetic horizon.

An interesting feature of the cosmic ray spectrum is the suppression of the flux at approximately 6×10^{19} eV, whose interpretation can be two-fold: at this energy the Greisen-Zatsepin-Kuz'min (GZK) cutoff due to the interaction of UHE protons with the CMB sets in; or this suppression is related to the maximal acceleration energy at the source; or a combination thereof. Whilst the former hypothesis requires a (mostly) protonic composition, the latter is compatible with a heavier composition. Furthermore, experimental results from the two largest UHECR experiments, the Pierre Auger Observatory and the Telescope Array (TA), are apparently contradictory. Auger measures an increasingly heavier composition toward higher energies [12], whereas TA's results are compatible with a pure proton composition [13, 14]. These results are strongly dependent upon the hadronic interaction model assumed, and there are solid evidences that hadronic interaction models are not correct at such high energies [15]. Furthermore, the discrepancies in the composition measurements may be hinting towards new physics at energies that are beyond the capacity of current particle accelerators such as the Large Hadron Collider. While this problem is not solved, it is not possible to confirm nor refute the GZK or maximal acceleration hypotheses.

The second type of particle herein studied are gamma rays, particularly the very high energetic ones. They are one of the most important messengers of the non thermal universe, being generated by means of leptonic and hadronic processes. They are also unique probes of fundamental physics, being useful for indirect dark matter searches and tests of quantum gravity. Moreover, they can be used to probe IGMFs.

With the advent of imaging atmospheric Cherenkov telescopes (IACTs) the study of very energetic astrophysical processes in the universe became possible. A potentially rich source of astrophysical information are blazar jets of VHEGRs. By analyzing the spectrum and arrival directions of VHEGRs it is possible to study the signatures of cosmic photon fields and intervening magnetic fields. The propagation of VHEGRs from blazars to Earth has been explored in many works (see e. g. refs. [2, 16–19]), in order to constrain the strength of magnetic fields along the line of sight.

The propagation of gamma rays in the universe is connected to a more fundamental question: the opacity of the universe. Already in the turn of the eighteenth century the issue of the darkness of the sky had been raised by Heinrich Olbers. Although his argument stood upon premises of an infinite and eternal universe, this question is valid. Today it is known that the universe is not infinite and is about 13 billion

[3] This statement is, to the current knowledge, valid, albeit unknown particles with higher energies may exist.

years old, which partially provides an answer to Olbers' paradox. However, another factor plays an important role in the question of the opacity of the universe: the existence of pervasive photon fields. At energies above ~ 10 GeV electromagnetic radiation (gamma rays) are attenuated by background photons, initiating electromagnetic cascades.

The development of electromagnetic cascades in the intergalactic medium can give rise to the appearance of halos around sources of VHE gamma radiation, creating an extended signal. These halos can be large enough to be detected by the current generation of IACTs, and their extension is intrinsically connected to the maximal acceleration energy of the sources and the magnetic field along the line of sight.

As discussed, the propagation of UHECRs and VHEGRs in the universe are intimately connected to properties of cosmic magnetic fields and pervasive photon fields. By simulating the propagation of these particles in the magnetized cosmic web and comparing with experimental data, it is possible to constrain the strength and power spectrum of IGMFs, possibly shedding light on magnetogenic processes in the primeval universe.

This thesis[4] is divided as follows:

- in chapter 1 it is presented some mathematical machinery for cosmology as well relevant concepts and information concerning the cosmic web and photon fields, accompanied by an extensive review on cosmic magnetism;
- in chapter 2 the state-of-the art of astrophysics of cosmic rays is presented;
- in chapter 3 some aspects VHEGR astrophysics are concisely described;
- in chapter 4 an analytical treatment for the suppression of the UHECR flux due to magnetic horizon effects spawned by diffusion of cosmic rays in inhomogeneous extragalactic magnetic fields is presented, including upper limits for the energy at which the aforementioned suppression can occur;
- chapter 5 contains a detailed description of the CRPropa 3 code, which is currently in its final stages of development;
- in chapter 6 the propagation of UHECRs in the magnetized cosmic web is studied, focusing on the effects of different primordial magnetic field seeds and the uncertainties on the strength of intergalactic magnetic fields on the propagation;
- chapter 7 is a compendium of results related to the propagation of UHECRs over cosmological distances, and the effects of magnetic fields on their trajectories;
- in chapter 8 a new Monte Carlo code for three-dimensional propagation of VHEGRs including the cosmological evolution of the universe is introduced;
- chapter 9 contains an application of the aforementioned gamma ray propagation code to the study of pair halos from blazars;
- and finally, in chapter 10 the conclusions are presented.

[4] The material which composes this thesis was partially published in journals and conference proceedings (refs. [7–9, 20, 21]). Chapters 6, 8 and 9 are still unpublished.

chapter 1

The Universe: Exordium

In this chapter a concise overview of several astrophysical and cosmological aspects relevant for this work is presented. First, the standard cosmological model is briefly described, focusing on the expansion of the universe and the cosmic microwave background radiation. Afterwards, brief insights on important matters regarding cosmological structure formation and distribution of matter in the universe are provided, establishing the connections with the subsequent section about cosmic magnetic fields. At the end of the chapter the galactic magnetic field is discussed.

1.1 Cosmology: essential concepts and mathematical machinery

1.1.1 The Friedmann-Lemaître-Robertson-Walker Universe

Before introducing the current cosmological model, it is important to describe the underlying theoretical framework upon which the model was built. It is based on the theory of General Relativity, which establishes a connection between the metric of spacetime and the density of matter/energy in the universe.

One of the pillars of modern cosmology is the cosmological principle, which essentially states that at large enough scales the universe is homogeneous and isotropic. A universe with these properties is described by the Friedmann-Lemaître-Robertson-Walker (FLRW) metric:

$$ds^2 = c^2 d\tau^2 = c^2 dt^2 - a^2(t)\left[\frac{dr^2}{1-kr^2} + r^2\left(d\theta^2 + \sin^2\theta d\varphi^2\right)\right], \tag{1.1}$$

where (r, θ, φ) are comoving coordinates at time t, c is the speed of light in the vacuum, $a(t)$ is the scale factor, and k is a parameter which depends on the geometry of the universe: $k < 1$ for an open universe, $k > 0$ for closed, and $k = 0$ for flat. Particularly, if $k = -1$ the universe has hyperboloidal shape (actually a 3-hyperboloid), and spherical (actually a 3-sphere) if $k = +1$.

Einstein's field equation for general relativity is given by

$$R_{\mu\nu} - \frac{1}{2}R g_{\mu\nu} = 8\pi G T_{\mu\nu}, \tag{1.2}$$

where $T_{\mu\nu} = diag(-\rho, P, P, P)$ is the energy-momentum tensor, $R_{\mu\nu}$ is the Ricci tensor, G is Newton's gravitational constant, and $g_{\mu\nu}$ is defined as

$$g_{\mu\nu} = \begin{pmatrix} -1 & 0 & 0 & 0 \\ 0 & 1 & 0 & 0 \\ 0 & 0 & 1 & 0 \\ 0 & 0 & 0 & 1 \end{pmatrix}. \tag{1.3}$$

The solution to Einstein's field equation for a universe with a FLRW metric can be expressed through a set of equations obtained by Friedmann [22, 23], which reads:

$$\left(\frac{1}{a}\frac{\partial a}{\partial t}\right)^2 = \frac{8\pi G}{3}\rho - \frac{kc^2}{a^2} + \frac{\Lambda c^2}{3} \tag{1.4}$$

$$\frac{1}{a}\frac{\partial^2 a}{\partial t^2} = \frac{4\pi G}{3}\left(\rho + \frac{3P}{c^2}\right) + \frac{\Lambda c^2}{3}, \tag{1.5}$$

with ρ being the energy and mass density of the universe, P the pressure of diverse cosmic components, and Λ the cosmological constant.

The time dependent Hubble constant (or Hubble parameter) is defined as

$$H(t) = \frac{1}{a}\frac{\partial a}{\partial t}. \tag{1.6}$$

The Hubble constant is defined as the value of the Hubble parameter at present time, i. e., $H(0) \equiv H_0$. It is also convenient to introduce the dimensionless normalized Hubble constant[1] (h), defined as $h \equiv H_0\,\mathrm{km^{-1}\,s\,Mpc}/100$.

For a stationary flat universe the critical density ρ_c is

$$\rho_c(t) = \frac{3H^2(t)}{8\pi G}. \tag{1.7}$$

For a universe with multiple components, including matter and vacuum energy, it can be shown from Friedmann's equations that the matter ($\Omega_m(t)$) and vacuum energy ($\Omega_\Lambda(t)$) densities are

$$\Omega_m(t) = \frac{\rho_m(t)}{\rho_c(t)}, \tag{1.8}$$

and

$$\Omega_\Lambda(t) = \frac{\Lambda(t)}{3H^2(t)}, \tag{1.9}$$

where $\rho_m(t)$ is the density of matter. For non flat universes ($k \neq 0$), there is also a contribution from the spatial curvature density, given by

$$\Omega_k(t) = \frac{-kc^2}{H^2(t)}. \tag{1.10}$$

The total density (Ω_t) of the universe is written as the sum of each component. It reads

$$\Omega_t(t) = \Omega_m(t) + \Omega_\Lambda(t) + \Omega_k(t). \tag{1.11}$$

1.1.2 Distance and time measures in cosmology

While in a static (time independent) euclidean universe the space and time measures can be unambiguously defined, this is not true in an arbitrarily curved expanding spacetime. Therefore, some distance and time measures have to be defined. In this section some relevant measures are introduced, following refs. [24, 25]

At this point it is important to explain the concept of redshift (z), which is defined as

$$z = \frac{a(t_0)}{a(t)} - 1. \tag{1.12}$$

[1] Throughout this work the term "Hubble constant" may be used indistinctly to refer both to the Hubble constant and to the normalized Hubble constant.

If the observation takes place at present time, then $a(t_0) = 1$.

It is convenient to introduce the function $E(z)$:

$$E(z) \equiv \sqrt{\Omega_m(1+z)^3 + \Omega_k(1+z)^2 + \Omega_\Lambda}. \tag{1.13}$$

From this expression it is possible to derive the expression for the comoving distance (r_c) between a source and an observer at $z = 0$:

$$r_c(z) = \frac{c}{H_0} \int_0^z \frac{1}{E(z')} dz'. \tag{1.14}$$

The comoving distance r_c is defined as the spatial distance between two world lines which follow the cosmic flow. In other words, it is the distance measure which remains constant over time for a source and an observer accompanying the Hubble flow.

The light travel time (or lookback time, t_l) is the time the light takes to travel from the source to the observer. It is given by

$$t_l = \frac{1}{H_0} \int_0^z \frac{1}{E(z')} \frac{1}{1+z'} dz'. \tag{1.15}$$

The light travel distance (or physical distance) is defined as the time light takes to travel from the source to the observer times the speed of light. The comoving distance and the light-travel distance (x) are related through the following expression

$$x = \frac{r_c}{1+z}. \tag{1.16}$$

The transverse comoving distance (r_m) of two events at same redshift (z) with angular separation $\delta\theta$ is $r_m \delta\theta$, with r_m given by

$$r_m = \begin{cases} r_c & \text{if } \ k = 0 \\ \dfrac{c}{H_0} \dfrac{1}{\sqrt{\Omega_k}} \sinh\left(\dfrac{r_c}{R_H}\sqrt{\Omega_k}\right) & \text{if } \ k > 0 \\ \dfrac{c}{H_0} \dfrac{1}{\sqrt{|\Omega_k|}} \sin\left(\dfrac{r_c}{R_H}\sqrt{|\Omega_k|}\right) & \text{if } \ k < 0 \end{cases}. \tag{1.17}$$

When dealing with quantities such as number densities, it is convenient to use the comoving volume ($\mathcal{V}$). The comoving volume element per solid angle per redshift interval is

$$\frac{d\mathcal{V}}{dz d\Omega} = \frac{c}{H_0} \frac{(1+z)^2}{E(z)} \left(\frac{r_m}{1+z}\right)^2, \tag{1.18}$$

which can be integrated yielding

$$\mathcal{V} = \begin{cases} \dfrac{4\pi c^3}{2H_0^3\Omega_k} \left[\dfrac{r_m}{R_H}\sqrt{1+\Omega_k\dfrac{r_m^2}{R_H^2}} - \dfrac{1}{\sqrt{\Omega_k}} \sinh\left(\sqrt{\Omega_k}\dfrac{r_m}{R_H}\right)\right] & \text{if } \ k > 0 \\ \dfrac{4\pi c^3}{2H_0^3\Omega_k} \left[\dfrac{r_m}{R_H}\sqrt{1+\Omega_k\dfrac{r_m^2}{R_H^2}} - \dfrac{1}{\sqrt{|\Omega_k|}} \sin\left(\sqrt{|\Omega_k|}\dfrac{r_m}{R_H}\right)\right] & \text{if } \ k < 0 \end{cases}. \tag{1.19}$$

An important relation between redshift and time can be derived from Friedmann's equations. The redshift evolution can be written as

$$\frac{dz}{dt} = \frac{H_0 E(z)}{a(z)}. \tag{1.20}$$

In a flat universe dominated by matter and vacuum energy, this expression reduces to

$$\frac{dt}{dz} = \frac{1}{H_0(1+z)} \frac{1}{\sqrt{\Omega_m(1+z)^3 + \Omega_\Lambda}}. \tag{1.21}$$

1.2 The Big Bang and its aftermath

According to the prevalent cosmological paradigm the universe is about 13.8 billions years old [26]. In the very first instants[2], the so-called inflationary era, the whole universe underwent an extremely fast expansion, increasing its size by a factor between 10^{30} and 10^{50} in 10^{-30} s. Baryogenesis occured when the universe was about one second old. As the expansion continued, the plasma cooled, and thermonuclear reactions in this plasma allowed the formation of the first atomic nuclei, in a process known as Big Bang nucleosynthesis (BBN), which took place in the first few minutes after the Big Bang.

After the BBN the universe was crammed with baryons and photons in a plasma state, which decreased the effective mean free path for photons, confining them within the primordial plasma. As the universe expanded and cooled down to a temperature of the order of 3000 K, electrons could bind to nuclei, forming the first atoms, in a process known as recombination. As recombination occurred the density of electrons in the plasma decreased, allowing matter to decouple from radiation. Consequently, the mean free path for photons increased, and they could start to move freely, generating the cosmic microwave background radiation.

1.3 The cosmic web

The assumption that at large scales the universe is homogeneous and isotropic is reasonable. At small scales, however, it is clearly inhomogeneous. Structures grew from small perturbations in an almost smooth universe. These perturbations, usually described as random gaussian fields, frozen-in during inflation, serving as seeds for the formation of the structures observed today. The density fluctuations led to a hierarchial process of clusterization of smaller collapsed objects into larger structures.

The largest gravitationally bound objects are clusters of galaxies[3], a gigantic gathering of galaxies with a total mass $\sim 10^{15} M_\odot$, out of which about 90% is in the form of dark matter. Typical cluster dimensions are of the order of a few Mpc.

Other structures generated during structure formation include filaments, sheets and the large empty regions known as voids. These structures are linked together through a network know as cosmic web [31].

Many surveys such as the 2dF (2 degree Field survey), SDSS (Sloan Digital Sky Survey) and BOSS (Baryon Oscillation Spectroscopic Survey) have constructed three-dimensional maps of the universe. These data combined can bring relevant information of the cosmic web, such as the spatial distribution of matter. They have revealed large structures with dimensions as large as a few hundred Mpc, as shown in figure 1.1. In this figure it is possible to notice filamentary structures lined up over large scales.

A recent study [32] found out that the Local Group of galaxies, formerly considered to be in Virgo supercluster, is actually a part of a larger structure composed by many cluster named Laniakea (or Local Supercluster). This finding may have important consequences for the distribution of magnetic fields in the local universe (see also section 1.5.3).

[2] The goal of this chapter is to present an introduction to relevant concepts that will be used later. For comprehensive introductions to the topic the reader can refer, e. g., to [27–29]. The interesting albeit complex debate concerning the origin of the universe itself, as well as the ontological consequences therefrom will not be discussed.

[3] For a review on formation of galaxy clusters see ref. [30].

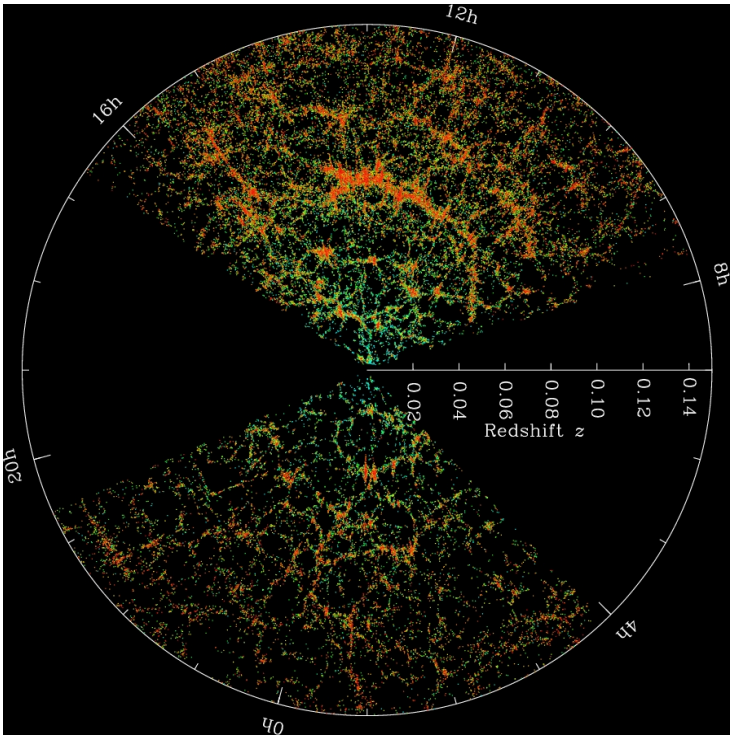

Figure 1.1: Three-dimensional map of the distribution of galaxies (colored points) in the universe, centered at Earth, up to a distance $\sim$ 600 Mpc. The color scale indicates the age of the galaxies, from colder (younger) to warmer colors (older). *[Image courtesy: Sloan Digital Sky Survey].*

1.4 Cosmic photon backgrounds

1.4.1 Cosmic Microwave Background

The history of CMB studies dates back to the early 1940s when a bolometric temperature of approximately 2.3 K was registered during attempts to measure the temperature of the interstellar medium [33]. The first theoretical models for the CMB were proposed by Dicke *et al.* [34] in 1946, and by Gamow, Alpher[4] and collaborators [36–39], between 1948 and 1953. In the next ten years there were some observations and improved estimates for the temperature of the background radiation.

In the 1964 Penzias and Wilson observed a "noise" in the their equipment, concluding that this was an actual measurement, rather than a hardware problem. In 1965 they measured the background radiation [40], result which was accompanied by a theoretical interpretation by Dicke *et al.* [41].

Today the CMB is well-understood and measured. It has a blackbody spectrum with temperature of approximately 2.7 K. It is the last scattering surface for photons at the end of recombination, indicating the decoupling of matter and radiation. The CMB is essentially a black body, and therefore can be approximated by a Planck distribution with temperature T_{CMB}. Its number density (n_{CMB}) as a function of the photon energy ε, is given by

$$n(\varepsilon) = \frac{\varepsilon^2}{\pi^2 c^3 \hbar^3} \frac{1}{e^{\frac{\varepsilon}{k_B T}} - 1}, \tag{1.22}$$

with $T = T_{CMB} \approx 2.7\,\mathrm{K}$ being the CMB blackbody temperature. This is shown in figure 1.2. The redshift

[4] For historical accounts regarding the often overlooked contribution of Alpher to the Big Bang theory and nucleosynthesis, usually completely attributed to Gamow, see ref. [35].

dependence of the CMB is a simple scaling of its present value, as follows:

$$n(\varepsilon, z) = (1+z)^2\, n(\varepsilon, z=0). \tag{1.23}$$

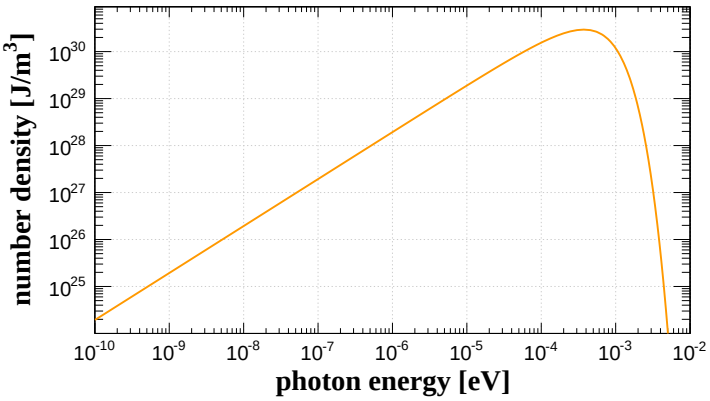

Figure 1.2: Number density of the cosmic microwave background at $z = 0$, as a function of the photon energy.

1.4.2 Cosmic Infrared Background

The Extragalactic Background Light (EBL) is a diffuse extragalactic field pervading the universe. It encompasses electromagnetic radiation ranging from infrared to ultraviolet. Measurements of the EBL, are difficult to the lack of unique spectral signatures, its strong dependence on source properties, the distribution of dust, among others. Unlike the CMB, which remains the same since the decoupling of matter and radiation, the EBL can be viewed as a calorimeter for the energy released during structure formation.

The Cosmic Infrared Background[5] (CIB) is the the most expressive component of the EBL, and the one which mostly impacts the propagation of high energy particles in the specific energy range of interest of this work. It is believed that gravitational and nuclear processes released energy into this background, which might have originated at earlier times. As the universe expanded short wavelengths were absorbed by dust and re-emitted at longer wavelengths, which can possibly explain the spectral profile of this background [42].

The spectral density of infrared photons is not as trivial as the CMB, and depends on the knowledge of source luminosities and dust emission. Several groups have attempted to model the CIB. In figure 5.9 a comparison of predictions is shown for the following models: Kneiske *et al.*(2004) [45], Stecker *et al.* (2006) [46], Dole *et al.* (2006) [47], Franceschini *et al.* (2008) [48], Kneiske *et al.*(2010) [49], Finke *et al.* (2010) [50], Gilmore *et al.* (2012) [51].

The redshift dependence of the CIB is also not trivial, due to the fact that various populations of sources emitted radiation with different wavelengths at different redshifts. Therefore, complete models of the CIB should describe not only the spectrum of the infrared background today, but also at larger redshifts.

1.4.3 Cosmic Radio Background

The Cosmic Radio Background (CRB) consists on the radio signal resulting from diffuse and discrete emissions in the frequency range of ∼1 kHz - 100 GHz by the Milky Way, external galaxies, intergalactic

[5] For reviews on the CIB, see refs. [42–44].

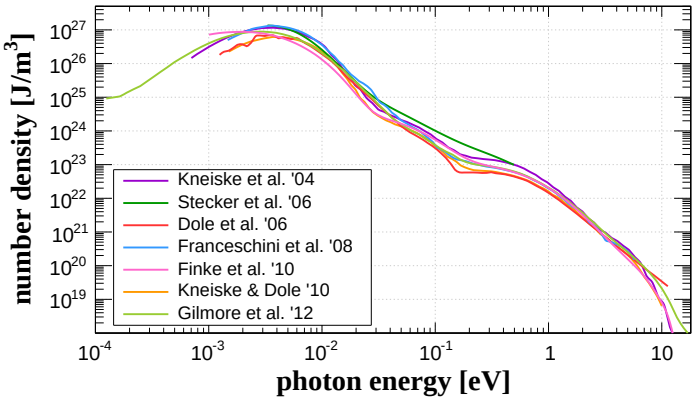

Figure 1.3: Number density of the CIB at $z = 0$, as a function of the photon energy, for various models

medium and possible cosmological backgrounds. The main contributions to the CRB come from normal and radio galaxies.

Recently data from the ARCADE-2 experiment has been analyzed and an isotropic excess of radio emission which cannot be explained by any known sources has been found [52, 53][6]. This is consistent with a brighter than expected CRB that can be modeled by a power law with spectral index ≈ -2.6 and a temperature of 1.17 K at 1 GHz.

The comoving number density of the CRB for the models of Protheroe & Biermann [55] and the parametrization for the ARCADE-2 data [52,53], as a function of the photon energy, are shown in figure 1.4.

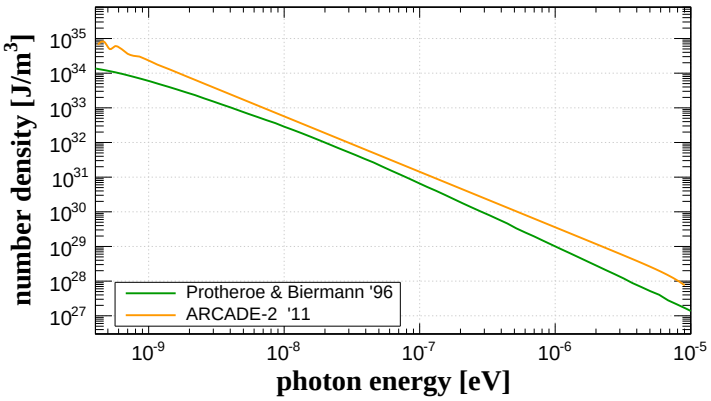

Figure 1.4: Number density of the CRB at $z = 0$, as a function of the photon energy.

1.5 Cosmic magnetic fields

1.5.1 Constraint methods

1.5.1.1 Polarization of star light

The large scale structure of the Milky Way and nearby galaxies can be studied through analyses of the polarization of the light emitted by stars. The first observational evidence of this polarization was provided by

[6] See ref. [54] for alternative explanations to this excess.

Hiltner [56,57], and Hall and Mikesell [58]. The first theoretical model to attempt to explain this polarization was developed by Davis and Greenstein [59], who suggested that external magnetic fields could induce a torque in non orbicular dust grains, causing a direction dependent absorption of incident star light. In this model the angular momentum of rotating dust grains is aligned with the magnetic field lines and absorbs preferentially the component of the incident light with electric field parallel to the major axis of the grain, in such a way that the light is polarized in the same direction as the magnetic field. In the aforementioned work the authors concluded that there is an interstellar magnetic field in the Milky Way, oriented along the galactic plane. Observations of other spiral galaxies reveal the same magnetic field structure, from estimates based on the polarization of star light.

Despite the fact that this method is powerful to infer the direction of the magnetic field, particularly of galaxies, it is not possible to estimate the strength of the magnetic field through this kind of measurement. Furthermore, this method can not be easily applied to extragalactic objects, except for nearby ones. Moreover, the exact mechanism which induces the alignment of the dust grains is not well understood [60].

1.5.1.2 Synchrotron emission

Relativistic electrons moving through magnetic fields emit synchrotron radiation. The proper estimation of the magnetic field strength in the medium depends upon the electron density ($n_e(E)$) distribution. This distribution can be modeled by a power law of the form [60]

$$n_e(E)dE = n_e(E_0)\left(\frac{E}{E_0}\right)^{-\gamma} dE, \tag{1.24}$$

where E_0 is a characteristic energy and γ is the spectral index of this power law, assuming a value of $\gamma \approx 2.6 - 3.0$ in spiral galaxies [60].

The synchrotron emissivity (j) is [61]

$$j_\nu \propto n_e B_\perp^{\frac{1+\gamma}{2}} \nu^{\frac{1-\gamma}{2}}, \tag{1.25}$$

with $B_\perp$ designating the component of the magnetic field perpendicular to the line of sight, and ν the frequency. This expression reduces to

$$j_\nu \propto B^{\frac{5+\gamma}{2}} \tag{1.26}$$

if one assumes equipartition of the energy between cosmic ray electrons and the magnetic field. This assumption, however, has to be taken cautiously, and its validity is topic of constant debate (see e.g. refs. [62, 63]).

1.5.1.3 Zeeman effect

The Zeeman effect consists on the splitting of the energy levels of molecules or atoms in the presence of an external magnetic field. A direct way to estimate the magnetic field of an astrophysical object or a region of it is through the Zeeman splitting of electronic transitions lines in the gas which composes the interstellar medium, which is given by [64]:

$$\omega = \omega_{mn} \pm \frac{eB}{4\pi m_e c}, \tag{1.27}$$

where m_e is the electron mass, ω_{mn} is a transition between the energy levels m and n, $\omega = 2\pi\nu$ is the observed frequency, and B is the magnetic field strength.

The advantage of this method is that it provides an *in situ* value for the magnetic field, i. e., directly in the region of interest, unlike other methods such as Faraday rotation, which provides the magnetic field integrated along the line of sight, and synchrotron emission, which provides only the perpendicular component.

The mensuration of the magnetic field strength through the Zeeman effect is extremely difficult, since the change in frequency induced by the presence of the field is often small in comparison to the thermal width of the lines, thus requiring regions with low temperature and high magnetization for the successful estimation of the field. In light of these difficulties, extragalactic magnetic fields were never measured through this method.

Whilst the potential of the Zeeman effect for estimating the strength of cosmic magnetic fields was known since 1957 [65], due to the challenging nature of this measurement the first successful results were obtained only in 1968, by Davies *et al.* [66], and Verschuur [67].

1.5.1.4 Faraday rotation

Faraday rotation is an optomagnetic effect caused by the interaction of electromagnetic waves with free electrons in the presence of an external parallel magnetic field.

A linearly polarized wave can be described as a combination of waves with circular polarization in opposite directions. During the propagation in a medium, these two components acquire different phase velocities, which spawns a rotation of the polarization plane, as shown in figure 1.5. In the interstellar medium this effect can be understood as a change in the refraction index of the medium due to the two polarization modes.

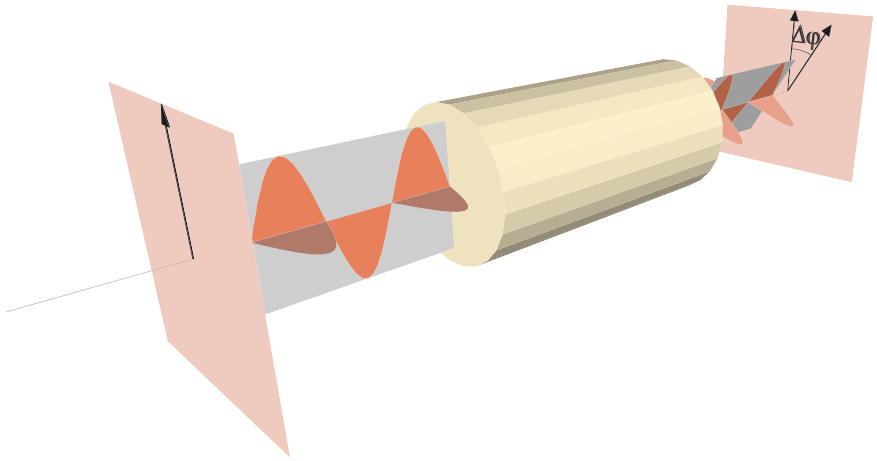

Figure 1.5: Pictorial representation of the rotation of the polarization plane of an electromagnetic wave, when trasversing a medium.

The rotation of the polarization plane from an initial phase φ_0 to φ, as depicted in figure 1.5, can be described by the equation [61]

$$\Delta\varphi = \varphi - \varphi_0 = \frac{e^3\lambda^2}{2\pi m_e^2 c^4} \int_0^D n_e(\ell) B_{\parallel}(\ell) d\ell, \tag{1.28}$$

where λ is the wavelength of the radiation emitted by a source at distance D trasversing a medium with electron density n_e along the line of sight, and $B_{\parallel}$ is the component of the magnetic field parallel to the line of sight.

The rotation measure is usually abbreviated as RM, and explicitly reads

$$RM = \frac{\Delta\varphi}{\lambda^2} = \frac{e^3}{2\pi m_e^2 c^4} \int_0^D n_e(\ell) B_\parallel(\ell) d\ell = \frac{0.46^\circ}{10^{-10}} \frac{1}{m^2} \int_0^D \left(\frac{n_e}{\mathrm{cm}^{-3}}\right) \left(\frac{B_\parallel}{\mu\mathrm{G}}\right) \left(\frac{dl}{\mathrm{kpc}}\right). \tag{1.29}$$

Typical objects which allow the estimate of the magnetic field via Faraday rotation are pulsars and/or extragalactic radio sources. For measurements over large distances the rotation measures from individual components such as the intergalactic medium, the galaxy, and the source, can be added [68].

1.5.1.5 Big Bang Nucleosynthesis

The impact of primordial magnetic fields on the BBN has been studied in several contexts[7]. Pioneer works [70–74] studied the effects of these fields on several observables, such as the decay rate for neutrons and the ^{4}He abundance.

If primordial intergalactic magnetic fields are larger than a given critical value (B_c), then the wave function of electrons and positrons will become periodic in the plane orthogonal to the field [69], discretizing the total energy of the electron. Consequently, it can be shown that the rate of conversion of neutrons into protons ($\Gamma_{n\to p}$) is [69]

$$\Gamma_{n\to p}(B) \propto \frac{B}{B_c}. \tag{1.30}$$

Hence one concludes that for $B > B_c$ the rate of conversion $\Gamma_{n\to p}$ increases with the magnetic field strength. This effect typically occurs for extremely high critical fields ($B_c \gtrsim 10^{13}\,\mathrm{G}$), and was studied by [75, 76]. Another approach can be found in ref. [77].

A higher decay rate of neutrons into protons imply that many neutrons would not live long enough to form composite nuclei, then a suppression in the flux of ^{4}He and other elements would be expected. Nevertheless, as shown in ref. [78], this effect is subdominant.

1.5.1.6 CMB anisotropies

The CMB is highly sensitive to the presence of magnetic fields. The main effects of these fields are: non gaussianities, Faraday rotation of the CMB polarization, spectral distortions of the monopole spherical harmonic, perturbations in the metric affecting polarization and temperature, among others.

The possibility of constraining primordial magnetic fields using the CMB has been suggested almost half a century ago [70], and most of the models are based on assumptions of anisotropies, such as a preferential magnetic axis, which implies an anisotropic energy-momentum tensor due to the change in the metric. The anisotropic expansion of the universe would be a direct consequence of the existence of a magnetic field at decoupling time ($z_d \approx 1100$).

A uniform primordial magnetic field oriented along a preferential axis was considered in several works [79–81]. Since the metric of the universe is affected by the presence of the field, the expansion in the direction of the field causes the field lines to stretch, working against magnetic tension. The magnetic pressure in the directions orthogonal to the direction of the field aids the expansion. The global consequence of this is a slower expansion parallel to the magnetic field vector, compared to the case in the absence of a magnetic field[8].

Anisotropic universes such as this are one case of the general class of Bianchi spacetimes. For a flat universe with a primordial uniform magnetic field, the CMB anisotropies can be related to the magnetic field

[7] A detailed review on the topic is presented in ref. [69].
[8] See [60, 69] and references therein for details.

as follows [60]:

$$B^2 \lesssim \frac{3H^2\Omega_t}{4G(1+z_d)}\frac{\Delta T}{T}, \tag{1.31}$$

where T is the CMB temperature, and $\Delta T/T$ is obtained from anisotropies, either from models, as done in ref. [79], or data, as in ref. [81].

In ref. [82] it was shown that primordial magnetic fields can also be constrained through Faraday rotation. In this case the polarization signal of the CMB would be affected by the presence of a magnetic field prior to or at decoupling time, being rotated through the Faraday effect.

Magnetohydrodynamical (MHD) effects neglected in the simplified approach previously described can distort the CMB spectrum, as shown in ref. [83]. If MHD modes are damped, the photon-baryon fluid will be heated through the dissipation of magnetic energy at small scales, changing the shape of the CMB spectrum.

1.5.1.7 Magnetic diffusion bounds on the coherence length

A method to constrain the coherence length of magnetic fields, rather than the field strength itself, is the diffusion time (t_d) for decay of magnetic field, given by

$$t_d = 4\pi\sigma\ell^2, \tag{1.32}$$

where ℓ is the scale over which the magnetic field varies, and σ is the conductivity. A given configuration of primeval magnetic field will survive over one Hubble time if $t_d \geq t_H$, where $t_H \equiv R_H/c$ is the age of the universe. Therefore, the coherence length (ℓ_c) of magnetic fields should be larger than than ℓ. This condition thus imply

$$\ell_c \gtrsim \sqrt{\frac{t_H}{4\pi\sigma}}. \tag{1.33}$$

Adopting $\sigma \approx 10^{11}\,\mathrm{s}^{-1}$ as the conductivity of the universe after recombination [84], the coherence length of the magnetic fields today should be $\ell_c \gtrsim 10^{11}\,\mathrm{m}$ ($\ell_c \gtrsim 10^{-12}\,\mathrm{Mpc}$).

1.5.1.8 Ultra-high energy cosmic rays

A possibility particularly interesting to break the degeneracy of models of the galactic magnetic fields are UHECR multiplets, which are filamentary structures originating from magnetic deflections of cosmic rays with different energies from the same source. This method has been first presented in ref. [85] and further explored in refs. [86, 87]. Different symmetries of the galactic magnetic field clearly lead to different orientation of multiplets, as shown in figure 1.6. Although this method is powerful to constrain models of the galactic magnetic field, it is very limited, since it requires nearby sources and/or low extragalactic magnetic fields. Moreover, no UHECR multiplets have been observed so far [89].

1.5.1.9 Gamma-ray induced electromagnetic cascades

A method to constrain intergalactic magnetic fields based on gamma-ray induced electromagnetic cascades was proposed by Plaga [90]. Very high energy gamma rays ($E \gtrsim 100\,\mathrm{GeV}$) can produce electron-positron pairs, which will be split due to magnetic fields[9].

[9] This statement is actually not totally precise. If the Larmor radius of the pairs is much larger than the typical cooling distance for inverse Compton scattering, then the referred scattering process may occur faster than the split of the electrons and positrons.

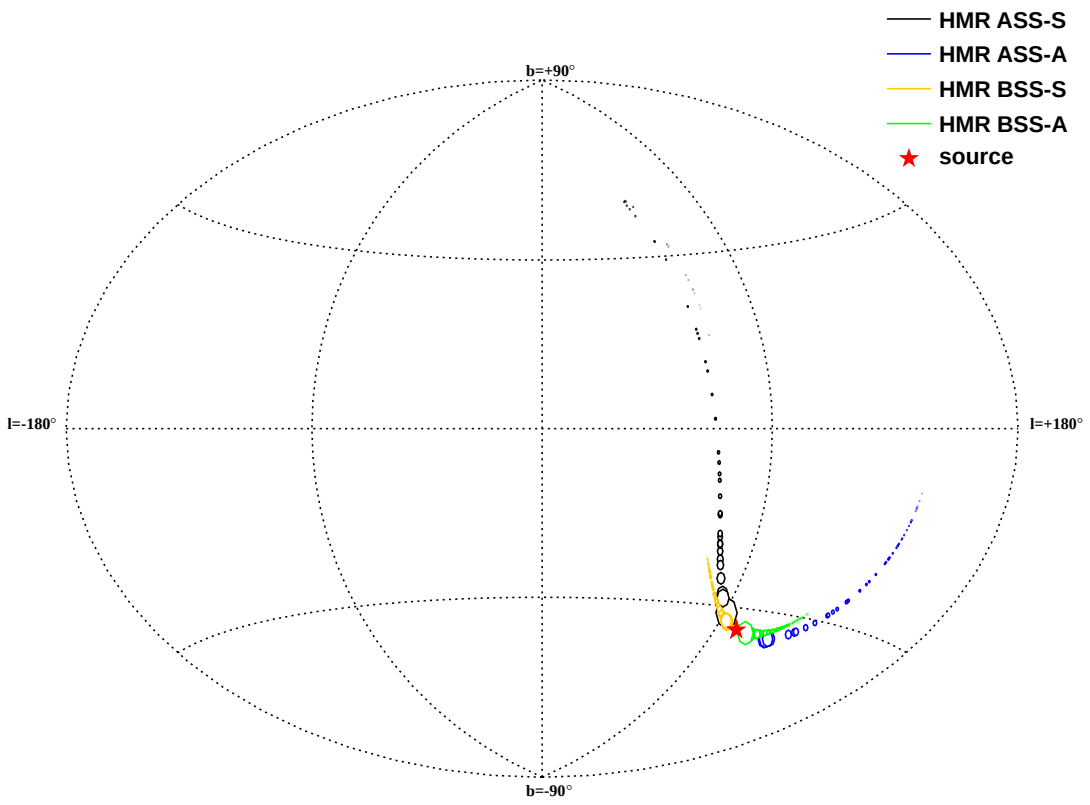

Figure 1.6: Energy-ordered multiplets from a hypothetical source indicated by the red star. The multiplets are formed by the deflection of ultra-high energy cosmic rays in the galactic magnetic field according to the models proposed by Harari, Mollerach and Roulet (HMR) [88]. The different symmetries (ASS-A, ASS-S, BSS-A and BSS-S) are explained in section 1.5.4. Circles are arrival directions of cosmic rays on Earth, and their radii are proportional to the energy of the particle (assumed to be protons).

The development here presented follows ref. [90]. Let E_γ denote the energy of the primary gamma ray. Electrons and positrons will roughly have half of the energy of the initial gamma ray, i.e

$$E_e \approx \frac{E_\gamma}{2}, \tag{1.34}$$

where E_e designates both the energy of electrons and positrons, treated indistinctly in this first approach. Electrons and positrons will interact with background photons via inverse Compton scattering, producing new gamma rays with energy

$$E'_\gamma \approx 0.8 \left(\frac{E_\gamma^2}{\text{TeV}}\right)^2 \text{ GeV}. \tag{1.35}$$

Assuming that the energy loss of electrons/positrons per unit distance due to scattering with CMB photons is proportional to the square of the energy of these particles, one can show that the maximum mean free path is

$$\lambda_{max} \sim 0.04 \sqrt{\frac{\text{TeV}}{E_\gamma}}. \tag{1.36}$$

Consequently, the maximum deflection angle of electrons/positrons is

$$\delta \lesssim \frac{\lambda_{max}}{R_L}, \tag{1.37}$$

where R_L is the Larmor radius of the electrons/positrons, given by

$$R_L = 10\sqrt{\frac{E_\gamma}{\text{TeV}}}\left(\frac{pG}{B}\right)\ \text{Mpc}, \tag{1.38}$$

with B designating the strength of the intergalactic magnetic field. The associated timed delay (Δt) can be easily calculated, yielding

$$\Delta t \lesssim \frac{D\delta}{8c}, \tag{1.39}$$

where D is the distance to the source, assumed to be relatively nearby in order to allow the neglection of cosmological effects.

1.5.2 On the cosmological magnetogenesis

There are essentially two classes of models to explain the origin of magnetic fields in the universe: astrophysical and cosmological scenarios. The former is characterized by the relatively late generation of the seed fields through astrophysical mechanisms, whereas in the latter models magnetic field seeds would have been formed during processes taking place in the early universe, such as inflation, phase transition, among others[10].

The quest for an adequate theory of cosmological magnetogenesis faces many difficulties, particularly related to the generation of fields in small and large scales. On one hand cosmological magnetic fields may have been created in the early universe, but on the other hand they may have decayed quickly, whilst seeds from astrophysical scenarios could have lived for a longer period of time, feeding dynamos which amplified these fields. Moreover, it is also possible that the magnetic fields observed today resulted from a combination of different astrophysical and cosmological processes.

Here only a succint overview of magnetogenesis mechanisms will be presented. For further details the reader is asked to refer to [1, 60, 69, 91–93].

1.5.2.1 Astrophysical origin

Astrophysical mechanisms for the origin of cosmic magnetic fields predict that they were produced during structure formation. In these models a seed field is amplified by the action of astrophysical dynamos. The main question astrophysical magnetogenic mechanisms attempt to address is the creation of magnetic fields from zero via "local" processes.

A notorious example of astrophysical mechanism is the Biermann battery [94, 95]. In this scenario plasma fluctuations causes a pressure gradient ($\vec{\nabla}P_e$), which induces an electric field ($\vec{E}$):

$$\vec{E} = -\frac{\vec{\nabla}P_e}{en_e}, \tag{1.40}$$

with n_e designating the electron density. Applying Faraday's law, one has

$$\frac{\partial\vec{B}}{\partial t} = -\vec{\nabla}\times\vec{E} = \frac{1}{e}\vec{\nabla}\times\left(\frac{\vec{\nabla}P_e}{n_e}\right) = \frac{-1}{en_e^2}\vec{\nabla}n_e\times\vec{\nabla}P_e. \tag{1.41}$$

It can be seen in this equation that as long as the density and pressure gradients are not parallel, a magnetic field may be generated.

[10] The definition of astrophysical and cosmological mechanisms is not clear. In this work the astrophysical mechanisms are defined as local processes, whilst the cosmological ones occurr globally in the whole universe.

Already in the 1970s [96–98] it has been shown that electrons and protons bathed in radiation drift with different velocities due to their opposite charges and different masses, generating magnetic fields. More recently Davies and Widrow [99] have studied the generation of vorticity and magnetic fields in protogalaxies. Assuming that the vorticity of the proton fluid is given by $\vec{\nabla} \times \vec{v}_p$, then the magnetic field at a time t is given by

$$\vec{B}(t) = -\frac{m_p}{e}\left[1 - \frac{a(t_0)}{a(t)}\right]\vec{\nabla} \times \vec{v_p}, \tag{1.42}$$

where m_p is the mass of the proton, $a(t)$ is the scale factor of the universe, and t_0 is the time of generation of this magnetic field. The seed magnetic field obtained in this case is $B \sim 10^{-19}$ G.

Quasars, dwarf galaxies or population III stars are candidates to be formed during the reionization period could are capable of generating magnetic fields through Biermann battery, as shown in refs. [100,101]. Kulsrud *et al.* [102] performed numerical simulations and obtained a seed magnetic field of the order of 10^{-21} G.

As pointed out in ref. [60], it is worth stressing that the Biermann battery is not only a hypothesis, but rather a genuine effect reproduced in laboratory [103]. The main issue is to understand whether this process can generate the μG fields observed today, whether it dominates over other magnetogenic mechanisms, and if the conditions present in the universe propitiate its occurance .

In a recent study [104] it was suggested that a flux of cosmic ray protons ($\vec{j_{cr}}$) propagating away from a galaxy generates a current, which propagates through an inhomogeneous intergalactic medium, inducing a return current. This magnetic field is given by

$$\frac{\partial \vec{B}}{\partial t} = \left|\vec{\nabla} \times \left(\eta_{Sp}\vec{j_{cr}}\right)\right|, \tag{1.43}$$

where η_{Sp} is the so-called Spitzer resistivity.

Another relevant issue is the formation of smaller scale magnetic fields, discussed in details in ref. [92]. Many models predict that seed fields were provided by astrophysical objects, such as active galactic nuclei (AGNs). AGNs may be capable of magnetizing the intergalactic medium, although it is unclear to which extent. For instance, Hoyle [105] predicted a magnetization up to $\sim$ μG level for this scenario. Daly and Loeb [106] studied in detail the interactions of AGN jets and concluded that magnetized ejecta from these objects can provide seed magnetic fields for galaxies prior to their formation, and possibly magnetize the intergalactic medium.

Astrophysical mechanisms are capable of describing the observed magnetic fields in astrophysical objects, in spite of the fact that it is rather difficult to explain the existence of non zero magnetic fields in the intergalactic medium with these models, particularly in the voids. For instance, the sole action of astrophysical objects such as AGNs may not be capable of expelling enough material to magnetize the intergalactic medium. Furthermore, these models require the action of dynamos at galactic scale to amplify the seed fields, which has several limitations, including the boundary conditions in the presence of weak seed fields. Further discussion on these limitations can be found in refs. [92, 107].

1.5.2.2 Primordial origin

There exist a number of primordial magnetogenic mechanisms. Archetypical classes of models include inflationary generation and phase transitions. An interesting consequence of primordial mechanisms is the existence of a non zero intergalactic magnetic field pervading the universe, making observational constraints possible. For reviews on this class of models see refs. [60, 69, 93, 108].

Inflationary magnetogenesis was subject of many studies [84, 109–114], for inflation provides an

adequate set of initial condition to generate magnetic fields. For instance, as discussed in [84], inflation provides kinematical means for producing coherent field over large scales, and allows the dilution of the density of charged particles decreasing the conductivity of the universe. Many estimates for the inflation-generated magnetic field have been made, and they range from $B \sim 10^{-18}$ G down to $B \sim 10^{-50}$ G. In the model proposed by Turner and Widrow [84] the time dependence of the magnetic field in Fourier space ($\vec{\mathcal{B}}_k$) in terms of the conformal time η is

$$\frac{\partial^2 \vec{\mathcal{B}}_k}{\partial \eta^2} + k^2 \vec{\mathcal{B}}_k + \left[\frac{6\alpha_1 + \alpha_2}{a} \frac{\partial^2 a}{\partial \eta^2} + \alpha_2 \left(\frac{1}{a} \frac{\partial a}{\partial \eta} \right)^2 \right] \vec{\mathcal{B}}_k = 0, \tag{1.44}$$

where k is the wave number corresponding to this Fourier mode, a is the scale factor of the universe, and α_1 and α_2 are dimensionless parameters.

Hogan [115] was the first to address the issue of cosmological magnetogenesis through first order phase transitions. In his model magnetic fields are created in bubbles through a battery mechanism, and amplified by a dynamo. These magnetized bubbles collide inducing magnetic reconnection from fields of different bubbles. This way, the characteristic length of the field increases with the number of bubble collisions. The magnetic field strength (B_ℓ) over a length scale of ℓ is

$$B_\ell \approx B_b \left(\frac{\ell_b}{\ell} \right)^{\frac{3}{2}}, \tag{1.45}$$

where ℓ_b is the typical size of the bubbles, and B_b their magnetic field. In many models the initial magnetization of the bubbles is a direct consequence of the baryon asymmetry in the universe, as noted in ref. [116].

Quantum chromodynamics (QCD) predicts that at very high temperatures the coupling between quarks and gluons is weak, and they both coexist freely in a plasma. As the primeval universe expanded it cooled down, reaching temperatures $T < T_{QCD}$, where $T_{QCD} \approx 150\,\mathrm{MeV}/k_B$ [69] is the threshold temperature for quark-gluon (de)coupling. Typically a first order phase transition occurs through bubble nucleation, whereby latent heat from bubbles containing the hadronic phase is released into the quark-gluon plasma as supersonic shock waves, reheating the plasma back to T_{QCD}. As thermal equilibrium is reached and the universe keeps expanding, both phases coexist and hadronization occurs. Eventually the quark-gluon plasma is completely hadronized and the phase transition ceases.

The magnetic fields generated through QCD phase transition[11] are rather low ($B \sim 1$ G at comoving scales of ~ 1 m at the time of the transition), and correspond to a small fraction of the total energy density of the universe. In refs. [118, 119] it is suggested that stronger fields could exist during the coexistence phase, leading to $B \sim 10^6 - 10^8$ G at the time of the QCD phase transition, and $B \sim 10^{-26} - 10^{-24}$ G over comoving scales of 100 kpc, at recombination time.

First order electroweak phase transitions are also capable of generating primordial magnetic fields, through the break of the electroweak symmetry group $\mathrm{SU}(2)_L \times \mathrm{U}(1)_Y$ into the electromagnetic group $\mathrm{U}(1)_{em}$. This process is similar to the QCD phase transition in spite of the different phase components. In ref. [120] ring-like magnetic fields from bubble collisions were analyzed, including MHD effects, resulting in $B_{rms} \sim 10^{-21}$ G, with coherence lengths of the order of 10 Mpc at present time.

Vachaspati [121] has shown that second order electroweak phase transitions can lead to magnetic fields of the order of $q_{EW}^{-1} T_{EW}^{-2}$ (in "natural units"), where q_{EW} is the Higgs field coupling constant and T_{EW} the temperature at transition time. This mechanism was revisited in ref. [122] and numerically confirmed

[11] It has been shown [117] that the QCD phase transition is not a proper phase transition, but rather a cross over, jeopardizing many models.

by Díaz-Gil *et al.* [123] in the context of hybrid inflation. Although plausible, this scenario has yet to be confirmed. According to this model fluctuations of the Higgs field are amplified via instabilities. Nucleation of bubbles with random gaussian Higgs fields spawns electroweak symmetry breaking, generating Z-strings which decay shortly thereafter. The long wavelength modes of the magnetic field have non zero helicity and may also decay.

Another important ingredient for understanding primeval magnetic fields is helicity. As the universe expands, larger scales gain magnetic energy from smaller scales, conserving magnetic helicity. This energy transfer is known as inverse cascade and leads to the following relation [60]

$$B_{rms}(t) = \left(\frac{a(t_0)}{a(t)}\right)^2 \left(\frac{t_0}{t_{eq}}\right)^{\frac{1}{6}} B_{rms}(t_0), \tag{1.46}$$

and

$$\ell(t) = \frac{a(t_0)}{a(t)} \left(\frac{t_0}{t_{eq}}\right)^{\frac{1}{3}} \ell(t_0), \tag{1.47}$$

with t_{eq} designating the time the system reaches equilibrium, t_0 the time of creation of the magnetic field, and ℓ the typical characteristic length of the magnetic field with root mean square magnetic field B_{rms}.

This process was investigated in numerous works [124, 125]. In the recent work of Saveliev *et al.* [126] it was shown that primordial helicity may increase the magnetic field today by a factor $\sim 10^4$ compared to the non helical case, assuming magnetic fields generated during the electroweak phase transition.

1.5.3 Extragalactic magnetic fields

1.5.3.1 Magnetic fields in clusters of galaxies

As remarked in refs. [127, 128], the existence of magnetic fields in clusters of galaxies can be inferred by the existence of large scale synchrotron sources in the intracluster medium, unrelated to any specific galaxy of the cluster, and Faraday rotation measures of this medium . These sources are classified in three groups depending on their location inside the cluster and morphology: radio relics, halos and mini-halos. Relics are located in the outskirts of the galaxy and have elongated or often irregular shape. Radio halos are megaparsec-scale structures found near the center of clusters. Mini-halos have sizes typically $\sim 100\,\mathrm{kpc}$ and are present far from the center of clusters. These three structures are tracers of magnetic fields in clusters.

The first observational evidence of magnetic fields in clusters of galaxies was the detection of a radio halo in the Coma cluster [129]. Recent measurements of the field in this cluster suggest field strengths of $\sim 5\,\mu\mathrm{G}$ [130]. Since then many other estimates of the magnetic field in clusters were made. These results, however, depend on the knowledge of the electron density in the medium. For detailed reviews of magnetic fields in individual clusters see refs. [1, 131].

The radial profile of the magnetic field in clusters is not well-known. Dolag *et al.* [132] have found indications that their strength decrease radially with the distance to the center. In this work central regions can have $B \sim 40\,\mu\mathrm{G}$, with coherence length $\ell_c \sim 50\,\mathrm{kpc}$. In the cluster Abell 665 a central field of 1.3 μG radially decreasing with r^{-1} was found [133]. This finding is in accordance with previous studies for Abell 2255 [134]. In a study by Murgia *et al.* [135] $2\,\mu\mathrm{G}$ fields were found in the center of mini halos, decreasing exponentially to $0.1\,\mu\mathrm{G}$ 1 Mpc away from the center.

Many studies suggest magnetic fields of the order of $10\,\mu\mathrm{G}$ in the core of clusters [136]. Rotation measures in other regions suggest $\sim$ μG fields [137, 138]. In irregular clusters the field in central regions is $\sim 5\,\mu\mathrm{G}$, compared to $B \sim 10 - 30\,\mu\mathrm{G}$ in regular ones [134].

Today it is known that clusters have magnetic fields with strength $B_{rms} \sim 10^{-7} - 10^{-5}\,\mathrm{G}$ and

coherence length $\ell_c \sim 1 - 100\,\mathrm{kpc}$ [131, 139, 140]. The exact radial profile of the field in clusters is not known, but there are evidences that it is $\propto r^{-1}$.

1.5.3.2 Magnetic fields in the Local Supercluster

The Milky Way is part of the Local Group of galaxies, which is part of the so-called Local SuperCluster (LSC), or Lanikea. The LSC is centered on the Virgo cluster, approximately 17 Mpc away from Earth. There is observational evidence for the existence of magnetic fields with strength $B \approx 2\,\mu\mathrm{G}$, coherent over scales of $\ell_c \sim 100\,\mathrm{kpc}$, based on Faraday rotation measures [141, 142].

Polarization studies of quasars in the LSC suggest an alignement of the polarization vector [143]. This effect can be due to the magnetization of the Virgo cluster, and can imply coherence lengths as large as 20 Mpc [1].

1.5.3.3 Magnetic fields in filaments

The existence of magnetic fields in filaments has never been confirmed, although there are many numerical studies and observational data supporting their existence.

Bagchi *et al.* [144] have found a diffuse radio emission from filaments. This can be interpreted in terms of a $\sim 3\,\mu\mathrm{G}$ magnetic field, contingent upon the validity of the hypothesis that the detected emission is synchrotron radiation from relativistic electrons.

Numerical simulations of structure formation predicts a magnetic field of $\sim 10\,\mathrm{nG}$, aligned with the filament [145]. Recent study by Vazza *et al.* [146] suggests $B \sim \mathrm{nG}$. An interesting result derived in this work is the absence of a significant dynamo amplification in these regions, which may be related to magnetogenic mechanisms.

1.5.3.4 Cosmological magnetic fields?

Kim *et al.* [147] have found indications for the existence of magnetic fields in a scale larger than clusters. A radio emission in a region between the clusters of Coma and Abell 1367, distance approximately 40 Mpc from each other, was detected. The strength of this field is $\sim 0.3 - 0.6\,\mu\mathrm{G}$. In ref. [148] similar results were also obtained.

Observations by Enßlin *et al.* [149] of the radiogalaxy NGC 315 support the existence of magnetic fields beyond cluster scales. The peculiar motion of this galaxy indicates the presence of a cosmological shock wave with dimensions $\sim 100\,\mathrm{Mpc}$.

Even though some observations support the existence of magnetic fields beyond superclusters, in the Bootes Void, which has dimension of the order of 120 Mpc, magnetic fields were not observed implying $B \lesssim 0.1\,\mu\mathrm{G}$ for the regular component of the field [150].

Ignoring the possible role of plasma instabilities, lower limits on intergalactic magnetic fields have been obtained by numerous authors [2, 17, 18, 151–153] through observations of electromagnetic cascades in the intergalactic medium (see section 1.5.1.9).

A combined plot for the strength and coherence length of cosmological magnetic fields using different methods of constrain (see section 1.5.1) is shown in figure 1.7.

1.5.4 Galactic magnetic field

The Milky Way is a barred spiral galaxy situated in the Local Group of galaxies, with a radius of $\approx$15–18 kpc. It contains $\sim$300 billion stars and has a mass of the order of $10^{12} M_\odot$ [154], with four spiral

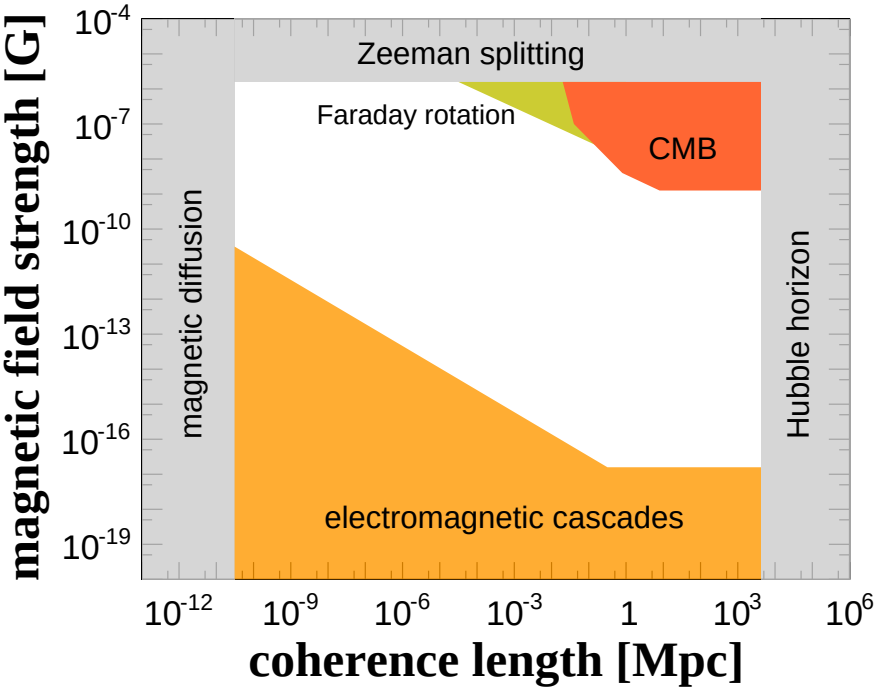

Figure 1.7: Bounds on the magnetic field strength and coherence length. Plot adapted from [2].

arms [155]. The solar system is located at a galactocentric distance of approximately 8.5 kpc.

The galactic magnetic field[12] can be decomposed into three components: regular, turbulent, striated. The regular component is a field coherent over large scales. The turbulent random component is totally random with small coherence length. The striated component has a zero average strength, and is aligned with the regular component.

Important features to characterize the large scale configuration of magnetic fields in spiral galaxies are field reversals inside or between arms. In the Milky Way at least one field reversal near or in the Sagittarius spiral arm has been identified [157]. It is not clear, however, if there are others reversals. Between the solar system and Perseus arm, for instance, some authors claim to have found one or more additional reversals [158–160], whereas others have found none [161, 162].

1.5.4.1 Logarithmic spiral models and symmetries

Among the many classes of models attempting to describe the galactic magnetic field (GMF) a recurrent one in the literature are logarithmic spirals. These models can be divided into two groups, depending on the parity[13] of the magnetic field with respect to the following transformation of the azimuthal angle θ: $\theta \to \theta + \pi$. Axisymmetric spiral (ASS) models are even under this transformation, whereas bisymmetric spiral (BSS) models are odd. These models can be further divided according to their parity under the transformation $z \to -z$, usually modeled as exponentials with maximum value exactly on the disk. Symmetric models, henceforth designated by "-S" are even under this transformation, whereas antisymmetric ("-A") are odd. Consequently, four big classes of models can be defined: ASS-S, ASS-A, BSS-A and BSS-S.

[12] For reviews on galactic magnetism see, for example, ref. [60, 156].
[13] Different authors adopt different conventions. Throughout this work the definitions here presented will be adopted in a self consistent way, regardless of the nomenclature adopted by other authors in their work.

In general spiral models can be described by a logarithmic spiral of the form

$$r = r_0 \exp(\theta \tan p), \tag{1.48}$$

where r_0 is a scale-related parameter which assumes different values in different spiral galaxies, and p is the pitch angle[14].

Some works in the literature which propose new GMF models or improve the existing ones are based on logarithmic spiral and can be found in refs. [163–172].

A method to relate Faraday rotation measures with the azimuthal symmetry of the field was devised by Tosa & Fujimoto [173], and has been widely used for model building. Since then many models have been built to fit measurements not only obtained through Faraday rotation measures, but also through other methods.

The class of models above described are rather general, and many adaptations were made to suit various purposes. Nevertheless, the underlying concept of a logarithmic spiral remains unaltered. The ASS class of models [150, 174] provides one of the simplest descriptions of the GMF. As pointed out in ref. [175], it is compatible with scenarios of non-primordial origin through dynamo mechanisms [174], and capable of describing up to three field reversals between the spiral arms [150]. The BSS class of models [163, 166, 176], on the other hand, is compatible with a primordial origin for cosmic magnetism, as discussed in ref. [175], and is capable of explaining the observed magnetic field reversals between the spiral arms of the Milky Way. There are currently no conclusive results favoring or refuting these models, although there are clear indications that the actual configuration of the magnetic field in the Milky Way is more complex than these rustic models [177–179].

Other notorious simplified models include additional regular components, beside the logarithmic spiral one. For instance, toroidal magnetic fields describing the the disk and halo altogether were used in refs. [168, 169, 180, 181]. Ref. [168] also proposes a poloidal component to describe the halo. A model for the disk was presented by Sun *et al.* [171], and consists on a logarithmic axisymmetric spiral with rings to account for field reversals.

A comparison of different GMF models bases on data from the Wilkinson Microwave Anisotropic Probe (WMAP5) was presented in ref. [182]. None of the models considered in this work were capable of reproducing the data. Moreover, antisymmetry with respect to the transformation $z \to -z$ is disfavored for the disk component and preferred for the case of halo fields in the innermost part of the galaxy.

1.5.4.2 An example of logarithmic spiral

Antisymmetric (ASS) and bisymmetric (BSS) logarithmic spiral models were described by Tinyakov and Tkachev [167]. In this model the magnetic field is given by

$$B(r,\theta) = B_0(r)\cos\left(\theta - \frac{1}{\tan p}\ln\frac{r}{r_0} + \varphi\right), \tag{1.49}$$

r, θ, r_0 and p follow the notation from section 1.5.4, with r being the radial distance to the center of the galaxy, θ the azimuthal angle, p the pitch angle of the logarithmic spiral, r_0 a parameter which has different values in different spiral galaxies, and φ a phase. In this model the radial dependence of the field is

$$B(r) = B_0 R\left\{r\cos\left[\frac{1}{\tan p}\ln\left(1+\frac{d}{R}\right) - \frac{\pi}{2}\right]\right\}, \tag{1.50}$$

[14] The pitch angle at a distance r from a logarithmic spiral is defined as the angle formed by the intersection of the line tangent to the circle at radius r and the line tangent to the spiral at the same point.

where d is the distance to the nearest field reversal. The magnetic field in the galactic halo is, in the BSS case

$$B_z(z) = \exp\left(-\frac{|z|}{z_0}\right), \tag{1.51}$$

and

$$B_z(z) = \text{sign}(z)\exp\left(-\frac{|z|}{z_0}\right) \tag{1.52}$$

for the ASS model.

1.5.4.3 A toroidal model

Toroidal fields were used in many works, including refs. [168, 171]. They can be described by the equation

$$\vec{B}_{tor} = -B_T \sin\theta\hat{x} + B_T \cos\theta\hat{y}, \tag{1.53}$$

where $\hat{x}$ and $\hat{y}$ are unitary vectors in cartasian coordinates, centered in the galactic center, and B_T consists on two circular lorentzian profiles in the $\hat{z}$ direction, above and below the disk. It is given by

$$B_T = B_{max}\left[1 + \left(\frac{|z|-z_0}{z_1}\right)^2\right]^{-1} \frac{r}{r_0}\exp\left(1 - \frac{r}{r_0}\right), \tag{1.54}$$

with r_0 being the scale radius of the galaxy, z_0 is the extension of the torus above the galactic plane, z_1 the half-width of the lorentzian profile, and B_{max} the maximum intensity of the magnetic field.

1.5.4.4 The Jansson-Farrar model

One of the most up-to-date GMF models is the one by Jansson and Farrar [183, 184], henceforth abbreviated as JF12 model. It was built using WMAP7 data and unlike many of the models mentioned so far, it explicitly ensures a divergence-free magnetic field ($\vec{\nabla}\cdot\vec{B} = 0$). It is composed by three components: regular, turbulent and striated. The large scale regular disk component is described by a toroidal field from 3–5 kpc, and a logarithmic spiral with eight arms beyond that. The magnetic field assumes different values in each arm. A purely toroidal component is used to describe the field in the galactic halo. The so-called "X-field", an out-of-plane poloidal component, is also present.

The field in the disk is modeled for galactocentric radii $3\,\text{kpc} < r < 20\,\text{kpc}$ in cylindrical coordinates (r, θ, z). In the molecular ring ($3\,\text{kpc} < r < 5\,\text{kpc}$) the field is azimuthal with strength B_{ring}. The outer region is composed by eight logarithmic spirals with pitch angle $p = 11.5°$ at galactocentric radii r =5.1, 6.3, 7.1, 8.3, 9.8, 11.4, 12.7, 15.5 kpc (where the spiral crosses the x-axis). The halo has a purely toroidal component given by

$$B_{tor} = \begin{cases} B_N \exp\left(-\frac{|z|}{z_0}\right) L(z, h_{disk}, w_{disk})\,(1 - L(r, r_N, w_h)) & \text{if } z < 0 \\ B_S \exp\left(-\frac{|z|}{z_0}\right) L(z, h_{disk}, w_{disk})\,(1 - L(r, r_S, w_h)) & \text{if } z < 0 \end{cases}, \tag{1.55}$$

where w_{disk} is the width of the transition region, h_{disk} is the distance where the transition disk halo occurs, z_0 is a characteristic height parameter, B_N and B_S are, respectively the normalization of the magnetic field in the northern (subscript N) and sourthern (subscript S) hemispheres, r_N and r_S are the radial extent of

the halo field in both hemispheres, and the function $L = L(z, h, w)$ is given by

$$L(z, h, w) = \frac{1}{1 + \exp\left(-\frac{2(|z|-h)}{w}\right)}. \tag{1.56}$$

The out-of-plane component referred to as "X-field" can be written as

$$B_x(r_p) = B_x \exp\left(-\frac{r_p}{r_x}\right), \tag{1.57}$$

with

$$r_p = \begin{cases} \dfrac{r r_{x,c}}{r_{x,c} + \frac{|z|}{\tan\Theta_{x,0}}} & \text{if } r < r_{c,0} \\ r - \dfrac{|z|}{\tan\Theta_{x,0}} & \text{otherwise} \end{cases} \tag{1.58}$$

where the elevation angle Θ_x is

$$\Theta_x = \begin{cases} \tan^{-1}\left(\dfrac{|z|}{r - r_p}\right) & \text{if } r < r_{x,c} \\ \Theta_{x,0} & \text{otherwise} \end{cases} \tag{1.59}$$

is the elevation angle. Here B_x is the normalization of the field, $\Theta_{x,0}$ the constant elevation angle (with respect to the mid-plane) for $r > r_{c,x}$, and r_x a characteristic distance.

The striated random field follows the regular field, and is written as

$$B_{str}^2 = \beta B_{reg}^2. \tag{1.60}$$

The random field has RMS strength $B_{rnd} = \sqrt{B_{disk}^2 + B_{halo}^2}$. The random halo field is

$$B_{rnd,halo} = B_0 \exp\left(-\frac{r}{r_0}\right) \exp\left(-\frac{z^2}{z_0^2}\right). \tag{1.61}$$

The RMS strength of the striated component in the JF12 model is locally proportional to the strength of the regular component. The turbulent component is a superposition of the disk component with a smooth halo component, but with field strength independently obtained from fits. A graphical representation of the regular, striated, turbulent and total components can be seen in figure 1.8.

Improvements to the description of the random and striated components of the JF12 model were recently proposed by Beck *et al.* [185]. These enhancements were motivated by the improvement of electron density models, which are essential to fit synchrotron emission and Faraday rotation measure distributions, thus affecting the galactic magnetic field model.

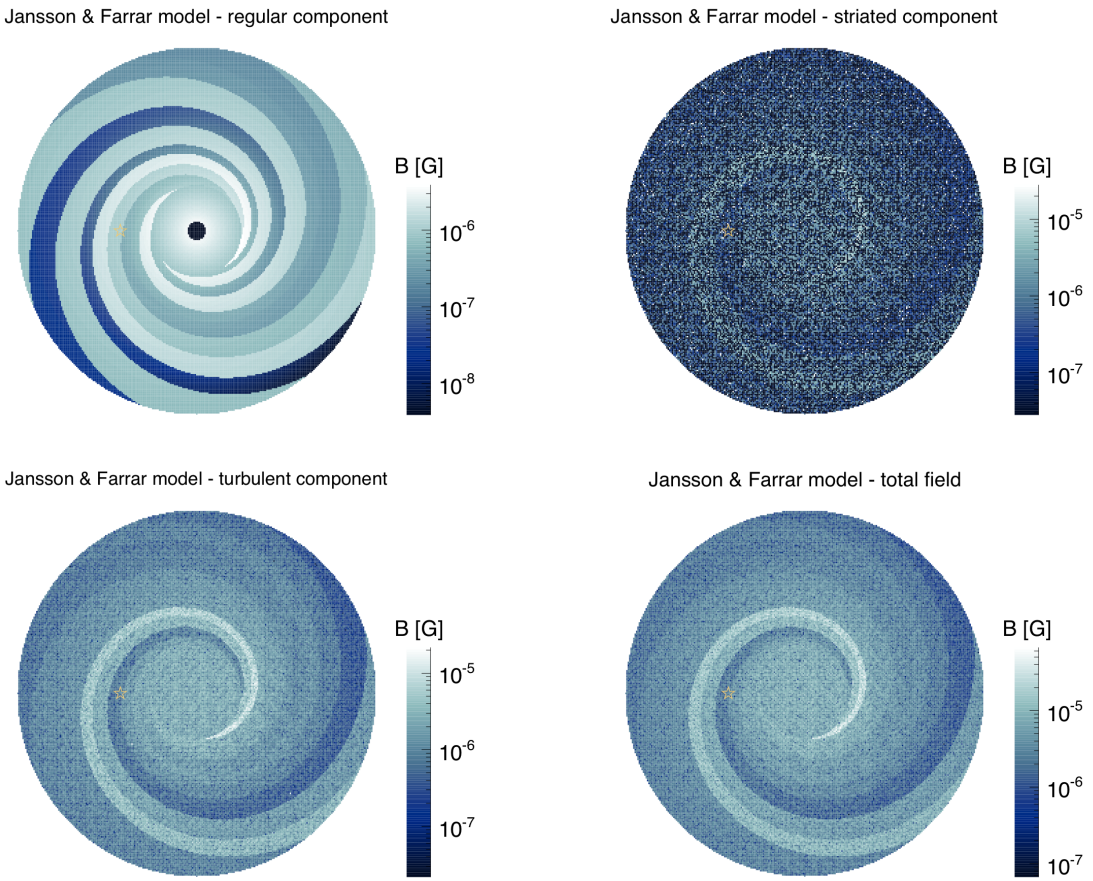

Figure 1.8: Regular (top left), striated (top right), turbulent (bottom left) and total (bottom right) components of the JF12 GMF model.

chapter 2

Cosmic Rays

2.1 A short history of cosmic ray physics

In this section an immanent overview of the main accomplishments on cosmic ray research in the twentieth century is presented. This subjective compendium of main achievements in the field should not be deemed as the complete and accurate description of historical events, but as a terse summary of significant accomplishments. For a detailed account of the history of cosmic ray research the reader could refer to refs. [186–190]. For the early history of the cosmic ray research in France and Italy more information can be found in ref. [191] and [192], respectively, and ref. [193] for cosmic ray works published in german language.

2.1.1 Early history (1900s – 1930s)

In the nineteenth century many progresses were made in the study of discharges in gases. These experiments were usually conducted using vacuum tubes, but atmospheric analogues were also being sought. After the discovery of radioactivity many physicists were studying related phenomena in the geosphere, upper atmosphere and other environments. Both fields of research swayed the interests of the respective communities towards the study of ionizing radiation in the atmosphere. In the early 1900s. Charles Wilson, Julius Elster and Hans Geitel [194–196] pointed out that even without a source of ionizing radiation electroscopes would be discharged when in contact with the air, suggesting the existence of free ions in this medium. This triggered subsequent investigations, and in 1909 the possible extraterrestrial origin of these ions grew into a heated debate. It was proposed that the origin of these ions could be the extraterrestrial [194, 197] or the Earth's mantle [198]. The geophysical origin of the ionizing particles was mainstream at the time. To test these hypotheses subaquatic and balloon experiments were conducted.

The first noteworthy investigation of the phenomenon was done by the german pioneer Theodore Wulf [199]. In 1910 he performed an experiment at the top of the Eiffel tower using his recently developed electrometer [200]. The results were inconclusive and the hypothesis of the terrestrial origin of the ionizing radiation in the air could not be confirmed. Albert Gockel conducted similar experiments at higher altitudes, but the results were also inconclusive [201].

A series of notorious experiments were performed by the austrian physicist Victor Hess, between 1910 and 1913. He took electroscopes aboard balloons up to high altitudes, expecting to measure a decrease in the ionizing power due to the increasing distance between him and the natural sources of radiation (Earth). In the first flight he did not observe this effect, and in subsequent flights the observed effect was actually the opposite: at very high altitudes the amount of ionizing radiation was increasing [202]. This led him to the conclusion that this radiation had extraterrestrial origin, which was later confirmed by Werner Kolhörster, in 1913 and 1914 [203].

Despite the confirmation of the extraterrestrial origin of the cosmic rays, verified through many experiments, the issue was not settled, and doubts still existed [186]. Millikan conducted more experiments, verifying that the number of ions in water decreased, and that the number of pairs of ions at high altitudes increased. In 1926 in a paper by himself and G. H. Cameron, he explicitly said that there are *"quite unambiguous evidence for the existence of very hard ethereal rays of cosmic origin entering the Earth uniformly from all directions"* [204]. It was also Millikan who coined the term "cosmic rays" to designate these particles.

In 1927 Skobeltzyn accidentally obtained the first photographic record of the trajectory of a cosmic ray during an experiment [205]. However, the nature of cosmic rays was still a mystery. Millikan proposed that they might be photons, and that a secondary electron signature was expected due to Compton scattering in the atmosphere. In 1929 Bothe and Kolhörster discovered charged cosmic rays with high penetration power.

In 1933 Arthur Compton has shown that cosmic rays were influenced by the magnetic latitude of Earth[1], and therefore they were charged particles [207–209]. In 1934 Bruno Rossi noticed that separate detectors would coincidentally accuse the detection of particles [210]. However, Rossi did not carry this study forth. This effect was rediscovered by Pierre Auger and his group in 1938 [211, 212], landmarking the discovery of extensive air showers (EASs).

2.1.2 First measurements outside Earth (1930s – 1950s)

In the first decades after the discovery of cosmic rays many studies were performed aboard balloons, as had been done in earlier years by Hess, Kolhörster and others. As pointed out in ref. [186], there were diverging ideas regarding the nature of the cosmic rays, so many experimental setups were used, including electroscopes, cloud chambers, photographic emulsions, among others.

A recurrent problem in unmanned balloon flights was the inability of the experimental setup to withstand extreme conditions from the atmosphere. This motivated the german pioneer Regener to develop a container capable of harboring many experiments and resisting these conditions. Unfortunately, his invention was lost during World War II [213]. After the war a similar invention was made and used to launch rockoons[2], which led to the discovery of a radiation belt around Earth, today known as Van Allen belt [214], and the first studies of auroras [215]. Furthermore, Van Allen himself noticed that the geomagnetic field shields the planet from the majority of cosmic rays [216].

The use of cloud chambers was very important for particle physics studies, and at that time both fields were indissociable. A notorious discovery in particle physics was, in reality, made during cosmic ray studies. In 1932 Anderson observed in a cloud chamber tracks of particles which behaved like electrons, but with a positive charge, which led to the discovery of the positron [217].

The study of cosmic rays were also conducted in mountains. In the 1940s the photographic emulsion technique was significantly enhanced. By using plates at different altitudes the trajectory of air shower could be studied in details. Another illustrious example of the interplay between particle and cosmic ray physics was the discovery of the pion in 1947, by Lattes *et al.* [218].

In the 1950s bubble, spark and drift chambers were invented. Nevertheless they were mostly used in accelerators. At this time particle and cosmic ray physics began to dissociate, and much of the interest in cosmic rays swayed toward particle accelerator experiments.

In the late 1940s and early 1950s two groups developed techniques for the reconstruction of air

[1] There is a proceedings of a conference [206] which shows that J. Clay had measured the latitude dependence of the cosmic ray flux due to the geomagnetic field, indicating that the primary particle is electrically charged. This discovery, however, was consigned to oblivion.

[2] Rockoons are a type of balloon-borne rockets used for extraterrestrial studies.

showers using arrays of detectors, which would be later used by the first ground array experiments such as Agassiz, which operated from 1954 to 1957 [219], and measured the spectrum and arrival directions of cosmic rays in the energy range from 10^{15} eV to 10^{18} eV. This pioneer experiment detected one event with energy above 10^{18} eV, which motivated the construction of a larger array, the Volcano Ranch experiment.

2.1.3 The first high energy cosmic ray experiments (1960s – 1980s)

The study of more energetic cosmic rays through indirect detection techniques started with Agassiz and the first large scale experiment devoted for this purpose, the Volcano Ranch experiment, whose planning and construction was led by John Linsley and Livio Scarsi. Volcano Ranch was the first experiment dedicated to the study of very high energy cosmic rays. It was located in New Mexico, USA, and operated from 1959 to 1978. The first detection of a cosmic ray with energy above 10^{20} eV was made by this experiment [220].

In 1968 two ground array experiments started collecting data, the Sydney University Giant Air shower Recorder (SUGAR), in Sidney, Australia, and the Haverah Park experiment, in North Yorkshire, UK, the former covering an area of approximately 60 km^2 and the latter 12 km^2.

In 1960 Kenneth Greisen proposed that the radiation originating from the interactions between the air shower particles with the atmosphere could be observed, suggesting the possibility of using fluorescence light or even radio to study cosmic rays. Some developments were made in this direction in the 1960s [221–225], culminating in the construction of the first fluorescence cosmic ray detector, the Fly's Eye experiment.

2.1.4 The 1980s, 1990s and early 2000s

The Haverah Park experiment operated until 1987. Its data were re-analyzed ten years after, and some important results can be found in refs. [226–228]. SUGAR stopped its activities in 1979. Some of its main results can be found in refs. [229, 230].

In 1981 the Fly's Eye experiment, the first purely optical system for studying high energy cosmic rays, began to operate. It recorded the most energetic cosmic ray ever detected, with an energy of about 3.2×10^{20} eV [231], ceasing its activities in 1993. Further enhancements transformed the Fly's Eye into the High Resolution Fly's Eye (HiRes), which began operations in 1997. Some important results obtained by Fly's Eye can be found in refs. [231–233].

In 1990 the Akeno Giant Air Shower Array (AGASA) started operating. It consisted on an array of surface detectors covering an area of approximately 100 km^2. Although AGASA's accomplished many important achievements, some results were contradictory. A notorious one was the non observation of the suppression of the flux at the highest energies [234], which sparked many alluring unconventional explanations. In 2004 this experiment terminated its activities.

An important experiment to study cosmic rays in the energy is the KASCADE (KArlsruhe Shower Core and Array DEtector), in Karlsruhe, Germany. Its goal is to study the cosmic rays in the energy between 10^{13} and 10^{17} eV. The KASCADE-Grande consists on enhancements on KASCADE to extend its energy range by one order of magnitude and study cosmic rays with energies between 10^{16} and 10^{18} eV.

The main results of the next generation of experiments, including HiRes, KASCADE-Grande, Telescope Array and the Pierre Auger Observatory are described in the forthcoming sections, together with the state of the art of the field.

2.2 Extensive air showers

Extensive air showers are a direct consequence of the interaction of cosmic rays with the atmosphere. For energies above 100 TeV the primary cosmic ray generates secondary particles from their interaction with the air. The main components of an air shower are the hadronic, muonic (including the neutrino counterparts) and electromagnetic (comprised of photons, electrons and positrons), the last of which carries approximately 90% of the energy of the shower. A first toy model for EASs was proposed by W. Heitler [235] and since then has been referred to as "Heitler model".

The detailed analysis of EASs in the atmosphere are not the subject of this work, and only two simple toy models are described[3].

First the electromagnetic showers will be described. They are initiated by photons or electrons[4]. The development of this shower is mainly driven by the interplay between electron *bremsstrahlung* ($e^{\pm} + {}^{A}_{Z}X \rightarrow e^{\pm} + {}^{A}_{Z}X + \gamma$) and pair production by photons ($\gamma + {}^{A}_{Z}X \rightarrow e^{+} + e^{-} + {}^{A}_{Z}X$). In Heitler's toy model each particle generates two others, and after n interactions this number doubles. Each interaction is assumed to occur after the particle propagated one mean free path (λ) in the atmosphere. The total number of particles after n interactions is therefore $N = 2^n$. By hypothesis, the energy is equally divided between the particles generated at each interaction, and after n interactions each individual particle will have energy $E_n = E/2^n$ and will have traveled a distance $x = n\lambda$. At a given point in the atmosphere the number of particles in the shower stops increasing and starts to decrease, for their energies drop below the interaction threshold required for production of more particles, squelching the development of the cascade. At this point the number of particles reaches its maximum (N_{max}), and the corresponding distance traveled is called the shower maximum (x_{max}). Since the development of an air shower depends on the atmospheric density (ρ), one can work with the density-averaged quantities X and X_{max}, instead of x and x_{max}. X_{max} is also called the depth of the shower maximum, and is usually written in units of mass per area. Based on this argument, one concludes that

$$N_{max} = \frac{E}{E_{thr}}, \tag{2.1}$$

where E_{thr} is the critical energy at which the cascade is quenched. Furthermore, one can easily see that

$$x_{max} = \frac{\lambda}{\ln 2} \ln\left(\frac{E}{E_{thr}}\right). \tag{2.2}$$

For showers initiated by hadrons a slightly more complex reasoning has to be applied. The interaction of a hadron with the atmosphere will generate mostly charged and neutral pions. Neutral pions will decay into two photons ($\pi^0 \rightarrow \gamma + \gamma$) and charged pions into (anti)muons plus (anti)neutrinos ($\pi^+ \rightarrow \mu^+ + \nu_\mu$ and $\pi^- \rightarrow \mu^- + \bar{\nu}_\mu$). The cascade initiated by neutral pions will then develop as the electromagnetic shower already discussed. Charged pions will have a branching ratio of approximately 2/3 and therefore this fraction of the energy will then remain in the cascade[5]. The lifetime of the π^0 is of the order of 10^{-17} s, whereas the charged ones live much longer ($\sim 10^{-8}$ s).

Assuming that one (anti)muon is produced per decay of charged pion, then after n interactions the threshold and the initial (E_0) energies are related through the following expression:

$$E_0 = E_{thr} N_{tot}^n, \tag{2.3}$$

[3] For details the reader can refer to ref. [236–240].

[4] In this section the term "electrons" is used to designate both electrons and positrons.

[5] The charged pions together with the neutral one constitute an isospin triplet of the strong interaction, and hence the branching ratio for the neutral one is 1/3.

where $N_{tot} = N_{\pi^\pm} + N_{\pi^0}$ is the total number of pions created. Hence one can write the total number of muons produced:

$$N_\mu = (N_{\pi^\pm})^n = \left(\frac{E}{E_{thr}}\right)^k, \tag{2.4}$$

with

$$k = \frac{\ln(N_{\pi^\pm})}{\ln(N_{tot})}. \tag{2.5}$$

As mentioned before, the combined branching ratio of charged pions is 2/3. So after the n-th interaction the energy of hadronic component is

$$E = \left(\frac{2}{3}\right)^n E_0. \tag{2.6}$$

Finally, combing the hadronic and electromagnetic descriptions in this toy model one can write the depth of shower maximum for a hadron-induced shower. To first order this can be written as

$$x_{max,had} \approx \lambda_{had} + x_{max,em} + \left(\frac{E}{N_{tot}}\right), \tag{2.7}$$

where the subscripts 'had' and 'em' refer, respectively, to the hadronic and electromagnetic components of this shower, and $x_{max,em}$ is given by equation 2.2. Notice that this result approximately holds for X_{max}.

For nuclei one can treat the nucleus of mass number A as a superposition of A protons initiating independent showers [241]. In this case, simple calculations allow one to conclude that at the shower maximum the number of particles is

$$N_{max,A} = A\frac{E_0/A}{E_{thr,em}} = N_{max}, \tag{2.8}$$

indicating that at this point the number of particles is approximately the same, regardless of the mass of the primary hadron. Furthermore, one can show that

$$x_{max,A} = x_{max}\left(\frac{E_0}{A}\right). \tag{2.9}$$

Another important observable of air showers is the number of muons, which in this case is

$$N_{\mu,A} = A\left(\frac{E_0/A}{E_{thr,had}}\right)^k = A^{1-k}N_\mu, \tag{2.10}$$

with k given by equation 2.5.

Despite their relatively low cross sections, neutrinos are also capable of inducing air showers in some particular circumstances.

2.3 The cosmic ray spectrum

The cosmic ray spectrum spans several orders of magnitude, with energies ranging roughly from 10^{18} to 10^{21} eV and fluxes between 10^{-21} and 10^{13} $m^{-2}eV^{-1}s^{-1}sr^{-1}$. It follows approximately a power law, with different spectral indexes at different energies. In figure 2.1 it is displayed a compilation of measurements of the cosmic ray spectrum, namely: Proton satellite [242], Akeno [243], Haverah Park [226], LEAP satellite [244], AGASA [245], Fly's Eye [233], CASA-BLANCA [246], DICE [247], Yakutsk [248], Yoshida *et al.* (balloon experiment) [249], HiRes [250], KASCADE [251] and Auger [252]. A similar figure weighted by $E^{2.5}$ for the very high energies ($E < 10^{16}$ eV) is shown in figure 2.2. .

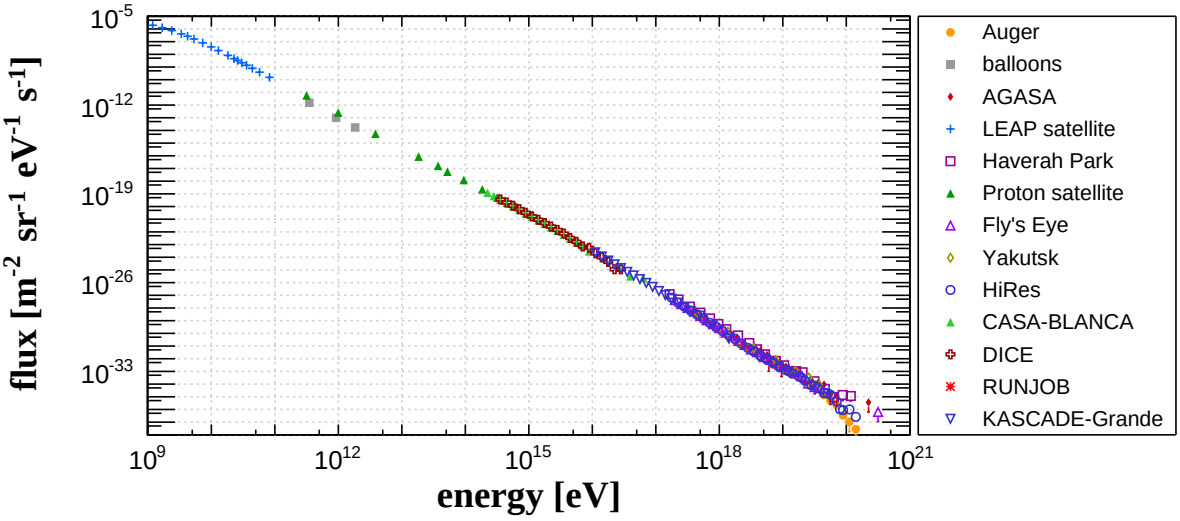

Figure 2.1: Compilation of the spectrum measured by several experiments.

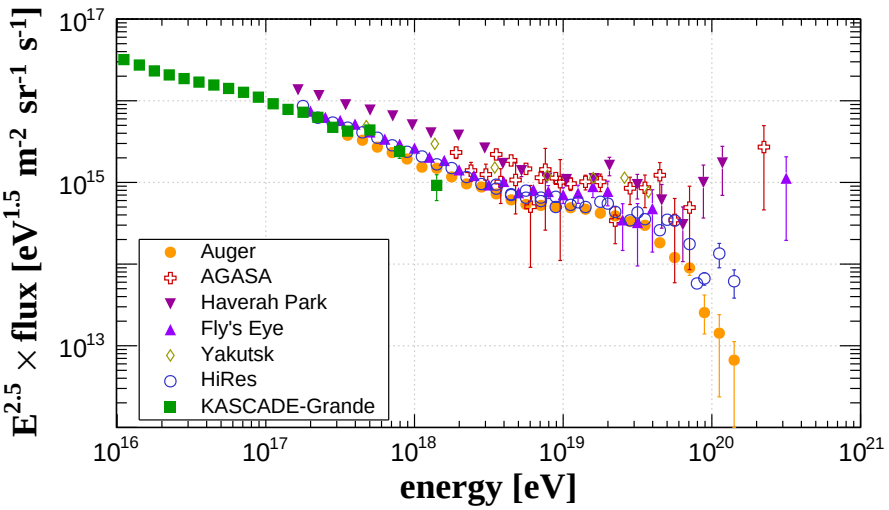

Figure 2.2: Compilation of the spectrum measured by several experiments for the energy range above 10^{16} eV, weighted by E^3.

Some remarkable features are noticeable in the cosmic ray spectrum. One is a break at $E \approx 3 \times 10^{15}$ eV, the so-called "first knee"[6], an abrupt change in the spectral index from approximately -2.7 to -3.1. The first observation of the knee feature dates back to 1958 [253]. Since its "discovery", several other experiments have observed this feature [245, 246, 254–262]. Another feature is the "second knee", at $E \approx 8 \times 10^{16}$ eV, observed by various experiments [251, 257, 259, 263–265], in which the spectral index changes to approximately -3.3.

The first and second knee can be conjointly interpreted as signatures of a light (proton-dominated) component accelerated up to the first knee, and a heavy component accelerated up to the second, as a result of the Peters' cycle [266], in which the maximum acceleration energy of an element is proportional to its charge Z. In that case, the second knee would indicate the end of the galactic spectrum and the emergence of another component, be it galactic or extragalactic. This rigidity dependence is supported by

[6] The reason for this name is that when the cosmic ray is plotted multiplied by E^2 (or other powers of E), the spectrum resembles a human leg and the change in spectral index at this energies causes a feature similar to a bent knee.

many experimental results [251, 257, 259, 263–265].

There are several models aiming to interpreting the rigidity dependent of the knee. The trivial interpretation is that the knee features are due to the maximum acceleration of sources. This idea was extensively discussed in refs. [267–270] and more recently in refs. [271, 272]. There are more sophisticated models such as the ones put forward by Ginzburg and Syrovatskii [273], which interprets the knee as a signature of the small angle scattering of cosmic rays in magnetic fields. In refs. [274–276] rigidity dependent scenarios based on the drift of cosmic rays in the regular component of the galactic magnetic field are proposed. A more recent model by Gianciti *et al.* [277] explains the knee in terms of the escape of cosmic rays from the galaxy.

An interesting interpretation for the second knee was put forward in refs. [278, 279]. In this case, the second knee would be where the transition between galactic and extragalactic cosmic rays takes place. In this model the extragalactic cosmic ray spectrum would be suppressed due to magnetic horizon effects[7], and for energies below the second knee it would fade away, with the galactic component dominating.

At $E \approx 7 \times 10^{18}$ eV the cosmic ray spectrum presents another feature called the "ankle"[8], observed by various experiments [233, 281–289]. It has been first observed by Linsley [281] in 1963, and its interpretation is still a matter of debate. In the original paper Linsley mentioned the possibility of the ankle being a signature of the transition between galactic and extragalactic cosmic rays. Another interpretation was given in ref. [290] in the context of the so-called dip model. In this model the ankle is a signature of pair production of UHE protons interacting with background photon fields, which is in tension with data from the largest cosmic ray experiment, the Pierre Auger Observatory [291].

At the highest energies, around 5×10^{19} eV, there is an abrupt suppression of the flux. This flux suppression was observed by the HiRes[9] experiment [250] and the Pierre Auger Observatory [284], but not by the AGASA [234]. Both HiRes and Auger have much larger exposure than AGASA, and today it is believed that AGASA's results were incorrect, possibly due to systematical errors in the energy estimates. The standard interpretation until few years ago was that this feature was the well-known Greisen-Zatsepin-Kuz'min [292, 293] (GZK) cutoff, due to the interaction of UHE protons with CMB photons. Since the occurrence of this effects requires a significant fraction of protons above the GZK threshold, it is in tension with data from the Pierre Auger Observatory [291], although HiRes explicitly mention that the suppression they observed was the GZK cutoff.

The existence of the GZK cutoff ($E_{GZK} \approx 5 \times 10^{19}$ eV) implies the existence of a horizon, which henceforth will be called GZK horizon. UHECRs, particularly protons, with energy above the GZK threshold from sources distant more than 70 Mpc are expected to lose their energy on their way to Earth due to photopion production in the CMB, having its flux strongly suppressed for $E > E_{GZK}$. Conversely, one can say that if cosmic rays with $E > E_{GZK}$ are detected they are within the GZK horizon.

Another interpretation for the observed flux suppression was proposed by Aloisio *et al.* in the context of the "disappointing model" [294]. In this model there is a proton-dominated component around 1–3 EeV, and an increasingly heavy component above. It is also argued that the maximum acceleration energy for protons is $E_p \sim 4 - 10$ EeV, implying a maximum energy ($E_{max} = Z \times E_p$) between 100 and 200 EeV for the heaviest composition possible, if one assumes a rigidity dependent acceleration.

[7] Magnetic horizon effects will be discussed in details in chapter 4.
[8] For a review on recent developments on the research of the ankle in light of the latest measurements, see ref. [280].
[9] HiRes stands for High Resolution Fly's Eye. It operated from 1997 to 2006, being superseded by the Telescope Array.

2.4 Nature of cosmic rays: composition

At low energies ($E \lesssim 10^{14}$ eV) the composition of cosmic rays can be directly measured. They are mostly atomic nuclei, but there is also a fraction of charged leptons such as electrons and positrons. At high energies ($E \gtrsim 10^{14}$ eV) it is impossible to directly detect the primary particle at Earth, and only secondaries created from their interaction with the atmosphere are detectable. For this reason, the experiments have to cover a large area to detect the secondaries, reconstruct the air shower and estimate its composition.

The inference of the mass composition of the primary cosmic rays requires a detailed understanding of the hadronic interactions taking place in the atmosphere. For these purposes several hadronic interaction models were developed. Some well-known models used to describe interactions at ultra-high energies are SIBYLL2.1 [295], QGSJETII-03 [296, 297], updated to QGSJETII-04 [298] and EPOS1.99 [299, 300], recently superseded by EPOS-LHC [301]. Although the general approach in these models are similar[10], there are some differences which might affect the final results[11].

Important observables in the study of the composition are the $\langle X_{max} \rangle$, defined as the depth in the atmosphere where the number of particles in the extensive air shower reaches its maximum, and its variance $\sigma(X_{max})$. All experimental composition results hereafter will be discussed in terms of these observables, for the energy range above ∼PeV.

As discussed in section 2.3, there are indications that the composition between the first and the second knee becomes increasingly heavier [251, 257, 259, 263–265]. KASCADE-Grande results for the composition between the second knee and the ankle suggest roughly equal fluxes for the light and heavy components, which seems to contradict results from Auger, HiRes and TA at these energies. Nevertheless, one should keep in mind that uncertainties of the KASCADE-Grande measurements are large, and there is a significant dependence on the hadronic interaction model adopted.

Experimental results obtained in the last decade suggest that the composition measured by Auger [12] is different to that of HiRes [13] and TA [14]. Auger observes an increasingly heavier composition towards higher energies, whereas HiRes and TA observe a predominantly light composition up to the highest energies. These results depend on the hadronic interaction model adopted, which are known to be incapable of completely describing the interactions between cosmic rays and the atmosphere. For instance, these models are not capable of correctly describing the number of muons at ground level, as shown by the Pierre Auger Collaboration [15]. Among the possible explanations for the observed discrepancies is the simple fact that the extrapolations of hadronic interaction models to higher energies, based on accelerator data, are incorrect. Other possibilities are "new physics" scenarios, in which some unknown process alters the development of the air showers in the atmosphere, leading to these results.

2.5 Origin and acceleration mechanisms of UHECRs

2.5.1 Fermi acceleration

2.5.1.1 2nd order Fermi acceleration

The Fermi mechanism was proposed by Enrico Fermi in 1949 [309]. This stochastic process is capable of accelerating particles up to high energies, through collisions with a magnetized shock wave. In the original model proposed by Fermi irregularities in the structure of the magnetic field scatter off charged particles.

[10] These models are constructed based on Gribov's Reggeon approach [302, 303] and, at high energies, extrapolation from accelerator data.

[11] For discussions on the differences between these models see, for example, refs. [304–308].

Below a development of the energy gain through second order Fermi acceleration is presented, following refs. [310, 311].

Scattering centers move randomly and "reflect" the incident particle. Let E_i and $\vec{p}_i$ be the energy and momentum of the particle before the collision, in the reference frame of the cloud, and E_f and $\vec{p}_f$ its energy and momentum after the collision, in the same reference frame. Let θ_i denote the incident angle of the particle, and θ_f the angle after scattering. Boosting into the reference frame of the cloud one has

$$E_i' = \gamma E_i(1 - \beta\cos\theta_i), \tag{2.11}$$

where $\beta = V/c$ and $\gamma = (1-\beta^2)^{-1}$ is the Lorentz factor. After the particle leaves the cloud its energy is

$$E_f = \gamma E_f'(1 + \beta\cos\theta_f'). \tag{2.12}$$

In the cloud reference frame the energy remains constant, so $E_i' = E_f'$. Every time the cosmic ray is scattered by a magnetized center, the energy gain is

$$\frac{\Delta E}{E} = \frac{E_f - E_i}{E_i} = \frac{\gamma E_f'(1+\beta\cos\theta_f') - \dfrac{E_i'}{\gamma(1-\beta\cos\theta_i)}}{\dfrac{E_i'}{\gamma(1-\beta\cos\theta_i)}}. \tag{2.13}$$

Rewriting this expression in a more convenient way, one has

$$\frac{\Delta E}{E} = \gamma\frac{E_f'}{E_i'}\left(1 - \beta\cos\theta_i + \beta\cos\theta_f' - \beta^2\cos\theta_i\cos\theta_f'\right) - 1. \tag{2.14}$$

The scattering of the cosmic rays by the irregularities in the magnetic field is approximately random. Therefore, the average energy gain can be obtained by averaging over the angles θ_i and θ_f'. In the reference frame of the cloud the particles are randomly scattered in all directions, and hence $\langle\cos\theta_f'\rangle = 0$. The average value of θ_i depends on the geometry of the scattering. The probability of collision depends on the solid angle. Assuming azimuthal symmetry, the angular dependence is only θ_i. Considering that the particles are ultrarelativistic ($v \to c$) and averaging over all angles in the range from 0 to π one obtains

$$\langle\cos\theta_i\rangle = \frac{\int_{-1}^{1} x(1+\beta x)dx}{\int_{-1}^{1}(1+\beta x)dx} = -\frac{\beta}{3}, \tag{2.15}$$

where $x \equiv \cos\theta_i$. In the limit of $\beta \equiv V/c \ll 1$, where V is the speed of propagation of the cloud, the average energy gain reduces to

$$\left\langle\frac{\Delta E}{E}\right\rangle \approx \frac{4}{3}\beta^2. \tag{2.16}$$

This is the second order Fermi mechanism, because the energy gain goes with the second power of β. Notice that although $\langle\Delta E/E\rangle > 0$, the energy gain is small.

It is possible to show that the obtained spectrum is a power law[12] of the form

$$N(E) = E^{-\alpha}, \tag{2.17}$$

where $N(E)$ the number of particles and $\alpha \equiv \kappa t_{esc}$, with t_{esc} being the time the cosmic ray remains in the

[12] Details can be found in ref. [311].

cloud before escaping, and $\kappa \equiv -(1/E)(dE/dt)$.

2.5.1.2 1st order Fermi acceleration

The second order Fermi mechanism cannot reach very high energies. For this reason, more efficient mechanisms were devised, such as the first order Fermi mechanism [312–316].

The idea of this mechanism is similar to the second order one, and is based on equations 2.11 and 2.12. In this case, particles moving with velocity $\vec{V}_p$ interact with the front of the shock which moves with velocity $\vec{V}_s$. Cosmic rays will gain energy by interacting with irregularities of the magnetic field, as in the case of the second order mechanism. One can see that[13]

$$\left\langle \frac{\Delta E}{E} \right\rangle \approx \frac{4}{3}\beta. \tag{2.18}$$

It is possible to show (see e.g. ref. [311]) that the differential spectrum is

$$\frac{dN(E)}{dE} \propto E^{\alpha}, \tag{2.19}$$

where $\alpha \approx$ is the spectral index.

Further developments in the theory of diffusive shock acceleration were made by several authors [317–319]. The model presented in ref. [320] predicts a spectrum slightly steeper ($\alpha = 2.2 - 2.3$), for highly relativistic shocks.

In many studies [321–324] it is argued that this is a rather complex process and the simplified assumptions commonly used may induce an overestimation in the efficiency of the process. For instance, in ref. [325] it is suggested that Fermi acceleration at relativistic shock waves cannot happen if the Larmor radius of the cosmic ray is much smaller than the typical coherence length of the magnetic field in the cloud. Moreover, in realistic scenarios the cosmic ray can gain energy as in the first order order Fermi mechanism only the first time it crosses the stream, and subsequently it behaves as a second order process, because the time available to isotropize the distribution of cosmic rays after it crosses the shock for the first time is not enough [326].

Although the most common versions of Fermi acceleration face many problems, some alternative models for diffusive shock acceleration inspired by first order Fermi mechanism predict that similar mechanisms can accelerate particles up to $E \sim 10^{18}$ eV, such as the ones presented in refs. [327–329].

2.5.2 Acceleration by unipolar inductors

Rapidly rotating and highly magnetized astrophysical objects such as neutrons stars can induce large electric fields capable of accelerating particles to ultra-high energies. This kind of model has been originally proposed in refs. [330, 331].

The general idea is that electrons are extracted from the object's surface due to the electric field. Since the magnetic field of the object is assumed to be dipolar, as in the case of neutron stars, the electrons will move along these field lines emitting radiation due to the curvilinear motion. The photons emitted interact with the surroundings of the object and the magnetic field generating electron-positron pairs, providing feedback for the repetition of the process. The growing number of pairs produces a large amount of electrons and positrons which fill the magnetosphere. Acceleration happens due to the difference of potential, given

[13] This development is analagous to the one for the second order Fermi acceleration mechanism, presented in section 2.5.1.1. More details can be found in refs. [310, 311].

by [332]

$$V = \frac{\omega R_s^3 B}{c R_L} \approx 80 \left(\frac{\omega}{\mathrm{Hz}}\right)^2 \left(\frac{B}{\mathrm{G}}\right) \ \mathrm{V}, \tag{2.20}$$

where ω is the angular frequency of rotation, B is the magnetic field, and R_s the radius of the star.

Blasi *et al.* [330] pointed out that this kind of mechanism could accelerate cosmic rays to energies as high as

$$E_{max} \sim Z \times 10^{19} \eta \left(\frac{B}{\mathrm{PG}}\right) \left(\frac{R_s}{10\,\mathrm{km}}\right)^3 \left(\frac{\omega}{\mathrm{kHz}}\right)^2 \ \mathrm{eV}. \tag{2.21}$$

This class of models predicts hard spectral indexes for the sources ($\alpha \sim 1.0 - 1.5$).

2.5.3 Other acceleration mechanisms

Other astrophysical acceleration mechanisms exist, such as magnetic reconnection [333], wake-field acceleration and reacceleration in sheared jets. More details about these mechanisms can be found in ref. [332].

2.5.4 Possible acceleration sites

There are two classes of models to describe the acceleration of cosmic rays to ultra-high energies: bottom-up and top-down models.

Top-down models predict that UHECRs are not accelerated by astrophysical objects, but are the result of the decay of massive particles. For instance, many top-down models involve some sort of topological deffect (for example, cosmic strings, magnetic monopoles, among others) produced during phase transitions in the early universe or decay of very massive partcles. A characteristic signature of most of these models is the large number of photons produced. Results from the Pierre Auger Observatory constrain most of these models by imposing upper limits to the photon fraction [334, 335].

In bottom-up models no exotic physics is invoked[14]. They predict that UHECRs are accelerated by electromagnetic fields in astrophysical objects. Hillas has shown [337] that it is possible to constrain the magnetic field strength and the size of the site capable of accelerating cosmic rays. The maximum energy (E_{max}) above which cosmic rays escape a magnetized environment of dimension R and magnetic field B is

$$E_{max} = 2\beta c Z e B R_L, \tag{2.22}$$

where $\beta \equiv v/c$ is the ratio between the speed of the particle and the speed of light, Ze is the charge of a nucleus, and R_L is the Larmor radius. This relation can be seen in figure 2.3.

2.5.4.1 Neutron stars

Acceleration of cosmic rays to ultra-high energies by pulsars can be done through the unipolar induction process previously described. Typically neutron stars/pulsars have magnetic fields $B \sim 10^{13}$ G and angular frequency of rotation $\omega \sim 3000$ s. Therefore, using equation 2.21 one can see that cosmic rays can reach energies $\sim 10^{21}$ eV via unipolar induction.

Recently the hypothesis of pulsars being the sources of UHECRs was revisited by Fang *et al.* [338–340]. In this work the authors claim that young extragalactic pulsars can accelerate UHECRs. Furthermore, they argue that if this hypothesis is true, a neutrino counterpart with energies as high as 1 EeV can be detected in the future by the IceCube experiment.

[14] A detailed review on astrophysical sources of UHECRs can be found in ref. [336].

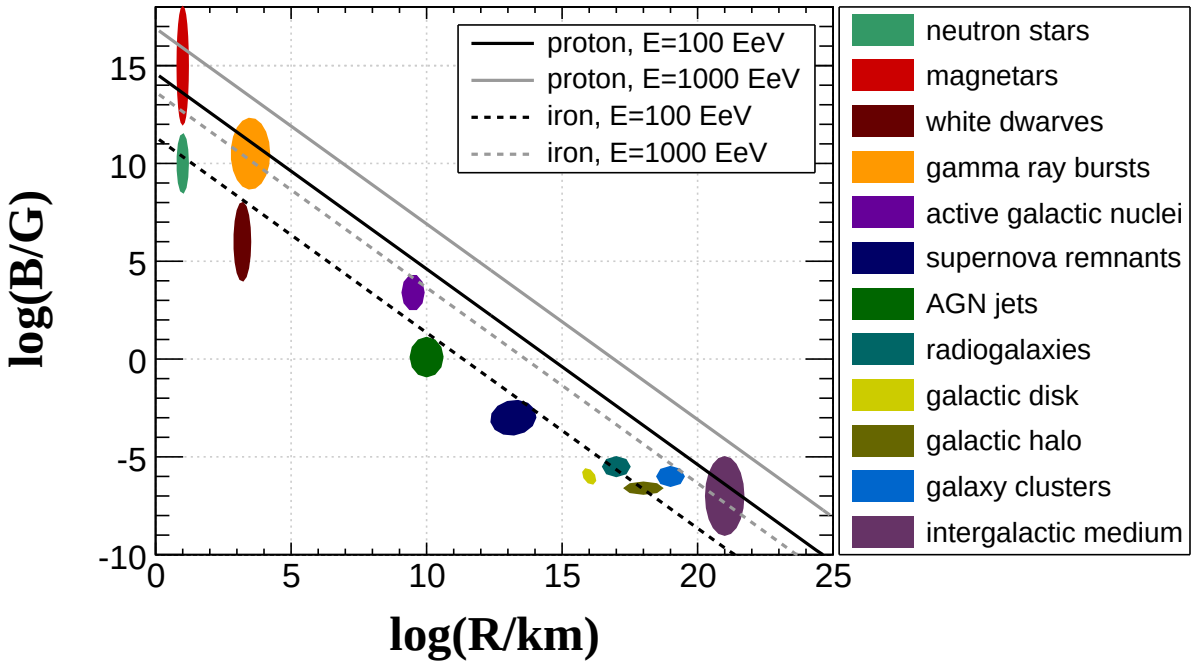

Figure 2.3: Hillas diagram, which indicates possible astrophysical objects capable of accelerating cosmic rays to ultra-high energies. The lines delimit the regions of the parameter space in which cosmic rays are not confined.

2.5.4.2 Magnetars

The mechanism of acceleration of UHECRs by magnetars was originally proposed by Arons [331]. The acceleration occurs essentially as explained in the case of unipolar inductors. The maximum energy to which a cosmic ray of atomic number Z can be accelerated is

$$E_{max} = 10^{21} Z \left(\frac{B}{\mathrm{PG}}\right) \left(\frac{\omega}{10\,\mathrm{kHz}}\right)^2 \; eV. \tag{2.23}$$

Recent results of the Pierre Auger Collaboration did not find an excess of UHECRs in the direction of magnetars [341].

2.5.4.3 Gamma Ray Bursts

Gamma ray bursts (GRBs) are emissions of high energy radiation in a short time interval. The most common phenomenological model for acceleration of UHECRs by GRBs is the "fireball" model [342] (see also refs. [343, 344] for comprehensive reviews). In this model the acceleration occurs via Fermi mechanism. Baryonic pollution traps radiation until most of its energy is converted into bulk motion with Lorentz factors $\sim 10^2 - 10^3$. The dissipative ultrarelativistic wind satisfy the constraints for Fermi acceleration, as can be seen in figure 2.3.

Most models of acceleration of UHECR by GRBs require protons for the acceleration. However, it has been argued that heavier nuclei can also be accelerated in internal, (external) reverse, and forward shock models [345].

2.5.4.4 Active Galactic Nuclei

Active galactic nuclei (AGNs) are candidates to accelerate cosmic rays to ultra-high energies. Some kinds of AGNs such as blazars have a jet of radiation pointing approximately toward Earth, hence being excellent candidates. In most models acceleration takes place in shocks, as long as energy losses by synchrotron emission and photon-proton collisions are subdominant. The maximal energy attainable assuming a Kolmogorov turbulent field is [336]

$$E_{max} \approx 10^{21} \left(\frac{\mu G}{B}\right)^{\frac{5}{4}} \left(\frac{kpc}{R}\right) \frac{u^{3/4}\beta_{jet}^{3/2}}{(1+Aa)^{3/4}} \ eV, \tag{2.24}$$

where u is the ratio between turbulent to ambient magnetic energy density around the shock, $\beta_{jet} \equiv v_{jet}/c$ is the speed of the jet over the speed of light, a is the ratio of photon to magnetic energy densities and A is related to the relative strength of proton-photon interactions versus synchrotron emission.

Many studies claim to have found correlations between AGNs and arrival directions of UHECRs. The authors of ref. [346] found a correlation with radio-loud quasars, which was refuted in posterior analyses by other groups [347]. In ref. [348] a correlation between UHECRs detected by AGASA and Yakutsk with BL Lacs was claimed and soon thereafter refuted based on data from Volcano Ranch and Haverah Park experiments [349]. Perhaps the most interesting result on this subject was obtained by the Pierre Auger Collaboration, in 2007 [350], who claimed to have found correlation between AGNs and arrival directions of UHECRs with energies above 60 EeV, with a confidence level of 99%. Nevertheless, this signal faded away in a more recent analysis including more data [351].

Many studies [352–357] have investigated the possibility of the nearest AGN, Centaurus A (Cen A), being the source of UHECRs. So far there many theoretical works and a (so far) not significant excess observed by Auger [291], and no conclusive results have been achieved.

2.6 Interactions and energy losses

The main interaction and energy loss processes taking place at ultra-high energies are:

- photopion production;
- pair production;
- expansion of the universe;
- photodisintegration.

The energy loss length for a nucleus of atomic number Z and mass A through production of electron/positron pairs can be written as [6]

$$\frac{dE}{dt} = 3\alpha\sigma_T Z^2 h^{-3} (m_e c^2 k_B T)^2 f(\gamma), \tag{2.25}$$

where $\alpha \approx 1/137$ is the fine structure constant, σ_T is the Thomson cross section, h the Planck constant, k_B the Boltzmann constant, γ the Lorentz factor and $f(\gamma)$ a function taken from ref. [358]. The threshold energy for this interaction is $E_{thr} \approx 5(\text{meV}/\epsilon)$ EeV.

Photopion production occurs when an EBL photon is scattered by a nucleon. In the case of protons, the two main interaction channels are

$$p + \gamma \rightarrow \Delta^+ \rightarrow \begin{cases} p + \pi^0 \\ n + \pi^+ \end{cases} .$$

The energy threshold for this process is $E_{thr} \approx 70(\text{meV}/\epsilon)$ EeV. For a CMB photon with $\epsilon \approx 0.6$ meV, $E_{thr} \approx 4 \times 10^{19}$ eV, which is the expected energy for the well-known Greisen-Zatsepin-Kuzmin (GZK) cutoff. The pions produced through the interaction between nucleons and photons decay as follows:

$$\begin{cases} \pi^+ \rightarrow \mu^+ + \nu_\mu \\ \pi^0 \rightarrow \gamma + \gamma \end{cases} .$$

This process is extremely important for multimessenger studies due to the production of secondary gamma rays and neutrinos.

The interaction of atomic nuclei with EBL photons causes these nuclei to split into parts, through a photodisintegration process. The mean free path for this process can be written in terms of the cross section σ as follows:

$$\lambda^{-1}(\gamma) = \frac{1}{2\gamma^2} \int_{\epsilon_{min}}^{\epsilon_{max}} \int_0^{2\gamma\epsilon} n(\epsilon, z) \frac{1}{\epsilon^2} \epsilon' \sigma(\epsilon') d\epsilon' d\epsilon, \tag{2.26}$$

where γ is the Lorentz factor, ϵ the photon energy, $\sigma(\epsilon')$ the cross section of the nucleus-photon interaction, and ϵ_{max} the maximum energy of the background photon, which is $\sim$10 meV for the CMB and $\sim$100 eV for the CIB.

Unstable nuclei produced during photopion production or photodisintegration can have short lifetimes compared to the propagation length, and suffer decays during their trajectory. Therefore, this process also has to be taken into account when simulating the propagation of UHECRs in the universe.

The expansion of the universe itself is another source of energy loss. This adiabatic energy loss is given by

$$E = \frac{E_0}{1 + z}, \tag{2.27}$$

where E_0 is the initial energy.

The energy loss length for photopion production, photodisintegration, pair production and adiabatic expansion of the universe are summarized in figure 2.4, for the case of iron and proton primaries. Further details about these interactions will be provided in section 5.4, in the context of the CRPropa code.

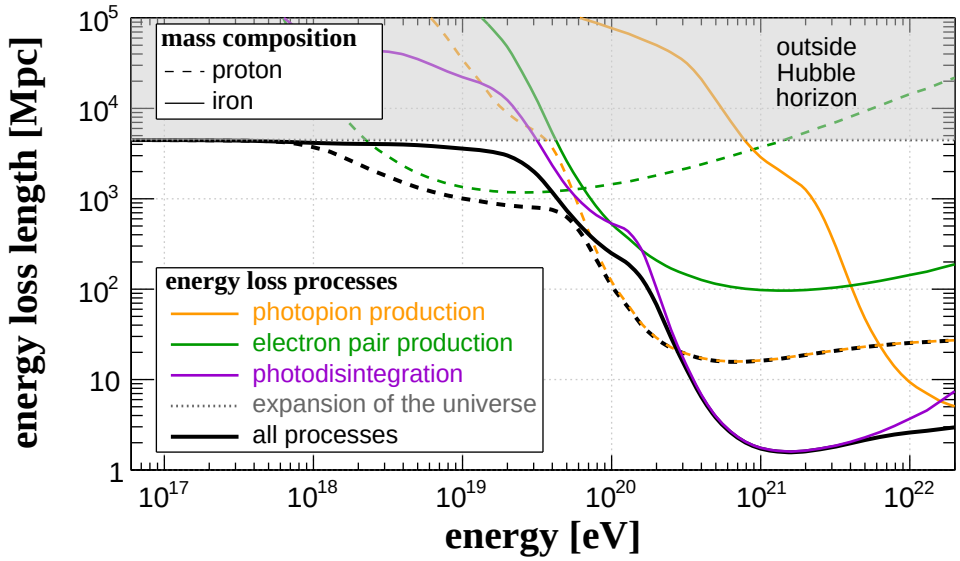

Figure 2.4: Energy loss lengths for different processes: photopion production (orange), electron pair production (green), photodisintegration (purple), adiabatic expansion of the universe (gray) and total (black). Solid lines are for iron nuclei, and dashed lines for protons. The photon backgrounds used here are the cosmic microwave background and infrared background from ref. [45].

chapter 3

High Energy Gamma Rays

Astrophysical objects such as stars emit radiation in a wide range of the electromagnetic spectrum by means of thermal processes. However, the typical temperatures of these objects are not sufficient for emission of a significant amount of gamma rays at high energies. In this case, non thermal processes such as shock acceleration of relativistic charged particles, which scatter ambient photons to high energies. Gamma rays are valuable cosmic messengers. Because they are neutral, they are not deflected by cosmic magnetic fields, as are cosmic rays. Unlike neutrinos, which are produced only through hadronic processes, gamma rays can also be produced through leptonic processes. Therefore, they are useful probes of relativistic processes taking place in different environments. In this chapter an introduction to gamma rays will be presented, focusing on very-high energy gamma rays (VHEGRs)[1].

3.1 A brief history of gamma rays

In the end of the nineteenth century after the serendipitous discovery of radioactivity[2] many people were actively working on the topic. The discovery of gamma radiation dates back to 1900, when Paul Villard was studying radioactivity properties of the radium. He noticed that the penetration power of this radiation was far beyond the ones of alpha and beta radiation. Ernest Rutherford in 1903, who extended the nomenclature previously used [362].

In the early twentieth century, together with the discovery of cosmic rays, the possibility of cosmic rays being gamma rays was enthusiastically considered [363]. In 1913 it was shown that gamma rays suffered reflection in crystals, indicating that they behaved as electromagnetic waves.

In the 1940s the first theoretical studies of gamma ray production via hadronic and leptonic processes were done [364], although the actual detection of extraterrestrial gamma rays took place only in the 1960s with military satellites [186]. At the time this emission was not properly interpreted in terms of emission by astrophysical objects. In the 1970s and 1980s balloon-borne experiments were launched with the goal of studying extraterrestrial gamma rays, and they detected gamma ray signatures in the whole sky.

Around 1980 it was possible to study the electromagnetic spectrum in all energy ranges. In 1989 a new window to the universe was opened, with the detection of TeV gamma rays from the Crab nebula[3], using an air Cherenkov telescope [365]. Since then the Crab nebula became a standard candle for measurements of VHEGRs and hundreds of sources were discovered.

[1] Very-high energy gamma rays are here defined as the ones with energies $\sim$ 10 GeV-100 TeV.

[2] This discovery is usually attributed to Henri Becquerel. However, the exact contribution of Becquerel has been questioned (see refs. [359–361]).

[3] The Crab nebula is the remnant of the supernova observed in 1054 A.D., although it was observed in TeV energies only in 1989.

3.2 Interactions and energy losses

There are many important interactions involving gamma rays, either through production, absorption and scattering. In this section only a few astrophysically relevant process will be described. More detailed treatments on production and absorption of gamma rays and radiative processes in astrophysics can be found in refs. [61, 366]

3.2.1 Electron bremsstrahlung

Electron bremsstrahlung essentially consists on the emission of radiation by electrons when interaction with matter occurs. Electrons losing energy through this process have a lifetime [366]

$$\tau = E_e \left| \frac{dt}{dE_e} \right|, \tag{3.1}$$

with the average energy loss rate for an electron with energy E_e given by

$$\frac{dE_e}{dt} = -\frac{m_p c n(\varepsilon)}{X_0} E_e, \tag{3.2}$$

where $n(\varepsilon)$ is the number density of the ambient gas and m_p is the mass of the proton. The value of X_0 depends on the composition of the gas. For instance, for a hydrogen gas its average value is $\langle X_0 \rangle \approx 60\,\mathrm{g/cm^2}$. This process is one of the responsibles for producing high energy gamma rays.

3.2.2 Annihilation of electron pairs

The annihilation of electron-positron pairs ($e^+ + e^- \rightarrow 2\gamma$) is important for astrophysical studies, specially at lower energies, due to the production of a line at 0.511 MeV. It depends mainly on the number density of electrons in the medium, and the amount of relativistic positrons injected. The differential spectrum of gamma rays produced through this process is given by [366]

$$\frac{dN_\gamma}{dE} = \frac{3\sigma_T c n_e}{8\gamma_+ \sqrt{\gamma_+^2 - 1}} \left[a\chi - \chi^2 \right], \tag{3.3}$$

with

$$a = \frac{E_\gamma^2 + (E_+ - E_\gamma + m_e c^2)^2}{E_+ + m_e c^2} + 2 m_e c^2, \tag{3.4}$$

and

$$\chi = \frac{m_e c^2}{E_\gamma} + \frac{m_e c^2}{E_+ - E_\gamma + m_e c^2}. \tag{3.5}$$

Here E_+ is the energy of the positron with Lorentz factor γ_+ injected in a medium with electron density n_e, and σ_T is the Thomson cross section.

3.2.3 Nuclear emission

Two astrophysical processes can generate gamma rays: decay of radioactive nuclei created in processes of nucleosynthesis, and de-excitation of nuclei by cosmic rays. A comprehensive account of these processes in light of experimental data can be found in ref. [367, 368].

Radioactive nuclide ejected by astrophysical objects during processes such as explosive nucleosynthesis can emit gamma rays if they are not absorbed in the stellar interior. The typical energy of the emitted gamma

rays is of the order of a 10–100 MeV per nucleon.

3.2.4 Pion decay

Pion decay is an important hadronic process whose role in the production of gamma rays was recognized long ago [273]. Inelastic photohadronic collisions of protons with ambient photons produce secondary pions. For instance, photopion production can produce neutral pions (π^0), which has the following decay channel:

$$\pi^0 \rightarrow 2\gamma.$$

The gamma ray emissivity for a pion with energy E_{π^0} is [366]

$$q_\gamma(E_\gamma) = 2 \int_{E_{min}}^{\infty} \frac{q_{\pi^0}(E_{\pi^0})}{\sqrt{E_{\pi^0}^2 - m_e^2 c^4}} dE_{\pi^0}, \tag{3.6}$$

with $E_{min} = E_\gamma + m_{\pi^0}^2 c^4 / 4E_\gamma$. Here q_{π^0} is the emissivity of pions[4]. The emissivity of secondary pions is

$$q_{\pi^0}(E_{\pi^0}) = c n_H \int \delta \left[E_{\pi^0} - \kappa_{\pi^0}(E_p - m_p c^2)\right] \sigma_{pp}(E_p) n_p(E_p) dE_p, \tag{3.7}$$

with κ_{π^0} designating the mean fraction of kinetic energy, m_p the mass of the proton, and the $n_p(E_p)$ the energy distribution of protons. The proton-proton cross section (σ_{pp}) was experimentally measured by several groups at various energies [370, 371].

3.2.5 Pair production

Pair production is the creation of electron-positron pairs due to the collision of two photons:

$$\gamma + \gamma \rightarrow e^+ + e^-.$$

Already in the 1960s it had been realized that the flux of high energy gamma rays traversing large distances could be attenuated [372]. This attenuation is described by an exponential of the form[5]

$$j(E) = j_0(E) \exp\left(-\tau(E)\right), \tag{3.8}$$

where $j_0(E)$ is the initial flux at the source and $j(E)$ is the observed energy. The parameter $\tau(E)$ is the so-called optical depth, which depends on the mean free path for pair production. For VHEGRs from astrophysical sources the mean free path for this process depends on the density of background photons, dominated by the EBL, which is model dependent.

The spectrum of electrons produced via pair production can be written as [373]

$$\frac{dN}{dE_e} = \frac{3\sigma_T}{32\varepsilon^2 E_e^3} \left[\frac{4E_\gamma^2}{\chi} \ln\left(\frac{4\varepsilon\chi}{E_\gamma}\right) - 8\varepsilon E_\gamma + \frac{2(2\varepsilon E_\gamma - 1)E_\gamma^2}{\chi} - \left(1 - \frac{1}{\varepsilon E_\gamma}\right)\frac{E_\gamma^4}{\chi}\right], \tag{3.9}$$

with

$$\chi \equiv E_e(E_\gamma - E_e), \tag{3.10}$$

[4] A detailed treatment of this process can be found in ref. [369].

[5] In this description cosmological effects are neglected for the sake of simplicity. The complete treatment is presented in chapter 9.

where E_γ is the energy of the photon, E_e the energy of the electron, and $\varepsilon = s/E_e$. For a power law spectrum with spectral index α this reduces to [374]

$$\frac{dN}{dE} \approx \left(1.1 - 1.60\alpha + 1.17\alpha^2\right) \frac{\exp\left(-\frac{1}{1-x}\right)}{E_{min} x (1 + \frac{0.07x^\alpha}{\ln x})}, \tag{3.11}$$

where $x \equiv E_e/E_\gamma$, and E_{min} is the minimum energy kinematically allowed. Since two particles (electron and positron) are produced per interaction, the integral of this equation should yield 2.

This results is important for analytical calculations, specially when one is interested in spectrum of secondary photons generated by the interaction of electrons with background photons via inverse Compton scattering.

This interaction will be revisited and extensively discussed in chapter 8.

3.2.6 Inverse Compton scattering

Inverse Compton scattering (ICS) consists on the scattering of a low energy photon of energy ε by an electron of energy E_e. The cross section for this process can be written as [375]

$$\sigma_{ICS} = \frac{3\sigma_T}{8\varepsilon E_e}\left[\left(1 - \frac{2m_e^2c^4}{\varepsilon E_e} - \frac{2m_e^4c^8}{\varepsilon^2 E_e^2}\right)\ln\left(1 + \frac{2m_e^2c^4}{\varepsilon E_e}\right) + \frac{4m_e^2c^4}{\varepsilon E_e} - \frac{1}{2\left(1 + \frac{\varepsilon E_e}{2m_e^2c^4}\right)^2} + \frac{1}{2}\right]. \tag{3.12}$$

Two regimes can be identified here. If $4\varepsilon E_e \ll 1$ the cross section reduces to the Thomson cross section. For $4\varepsilon E_e \gg 1$ one is in the Klein-Nishina regime.

The spectrum of gamma rays produced via ICS is given by [376]

$$\frac{dN(\theta, E_\gamma)}{dE_\gamma d\Omega} = \frac{3\sigma_T m_e^2 c^4}{16\pi\varepsilon E_e^2}\left[1 + \frac{\frac{E_\gamma^2}{E_e^2}}{2\left(1 - \frac{E_\gamma}{E_e}\right)} - 2\frac{\frac{E_\gamma}{E_e}}{2(1-\cos\theta)\varepsilon E_e\left(1 - \frac{E_\gamma}{E_e}\right)} + 2\frac{\frac{E_\gamma^2}{E_e^2}}{((1-\cos\theta)\varepsilon E_e)^2\left(1 - \frac{E_\gamma}{E_e}\right)^2}\right]. \tag{3.13}$$

This equation holds for photons of energy ε traversing a homogeneous and isotropic medium filled with relativistic electrons of energy E_e [366]. For some astrophysical applications high energy electrons scatter low energy ambient photons, and the process can be treated in a similar fashion by boosting into another frame of reference. In this case, equation 3.13 can also be applied, with the appropriate considerations.

This interaction will also be revisited in chapter 8 in the context of the GRPropa code.

3.3 Sources

Many processes can accelerate gamma rays. Of particular interest for this work are the sources of VHEGRs with energies $\sim$ TeV. There are two classes of models for production of gamma rays in this energy range. In the top-down models the acceleration of gamma rays to very-high energies is attributed to the decay of heavy (and often exotic) particles. Bottom-up scenarios predict that VHEGRs are the by-product of the interaction of charged particles with ambient photons. These charged particles can be nuclei or

electrons. Scenarios in which cosmic ray nuclei accelerate gamma rays are usually referred to as hadronic, whilst electron-induced acceleration is a leptonic process. Naturally, a combination of both processes is also possible.

The main leptonic channel for acceleration of gamma rays to very-high energies by electrons is inverse Compton scattering of ambient photons, ranging from microwave to X rays. In hadronic scenarios gamma rays are accelerated to very high energies through the up-scattering of ambient photons by cosmic rays. Consequently, in these models gamma rays trace cosmic ray acceleration sites and propagation environment.

Today there are about 150 known sources of VHEGRs. Many of them are galactic sources, although a number of extragalactic sources has been detected in recent years. A summary of the known sources of TeV gamma rays has been compiled in the TeVCat[6] and is shown in figure 3.1. Reviews on these topics can be found in refs. [377–379].

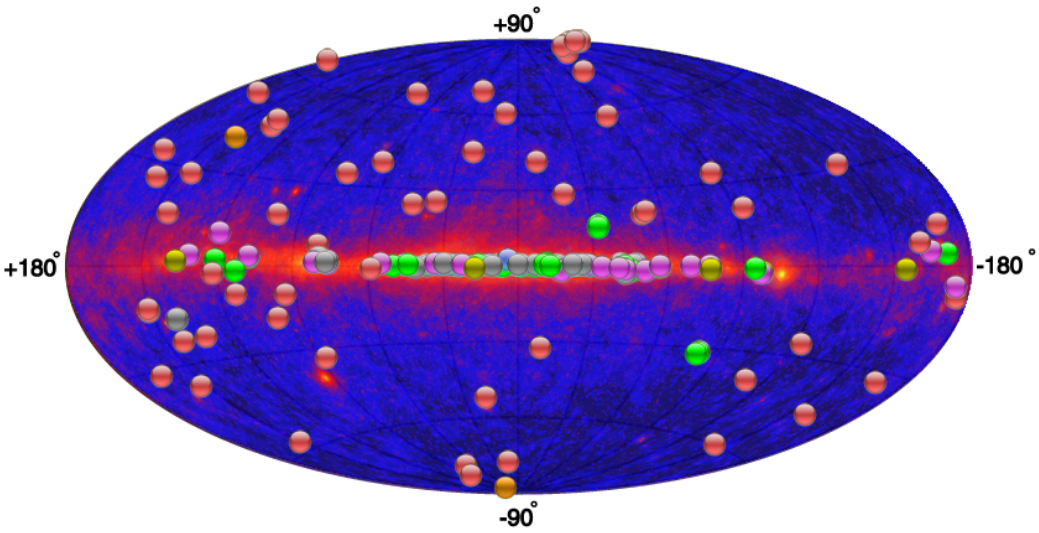

Figure 3.1: Skymap containing the position (in galactic coordinates) of sources of TeV gamma rays, overlaid with the Fermi skymap. The colored circles are different types of sources: pulsar wind nebulae (magenta), starburst galaxies (orange), X ray binaries/pulsars (yellow), supernova remnants/molecular clouds/superbubbles (green), AGNs (red), µquasar/star forming regions/Wolf-Rayet stars (blue), and unidentified sources (gray). This image was taken from http://tevcat.uchicago.edu/.

3.3.1 Supernova remnants

Supernova remnants (SNRs) are efficient sites for acceleration of cosmic rays to high energies ($E \sim 10^{15} - 10^{17}$ eV). Already in 1939 Zwicky [380] had argued that SNRs are likely sources of galactic cosmic rays. A simple phenomenological argument to understand this is that the energy output required to maintain the density of cosmic rays in the galaxy is of the order of a few percent of the energy released by supernovae explosions. Although other source populations could also contribute, the acceleration of gamma rays up to high energies comes naturally by considering diffusive shock acceleration of charged particles in SNRs, which scatter ambient photons to very-high energies. Recently the Fermi-LAT collaboration has finally proved this hypothesis [381] by studying characteristic pion decay signatures in the gamma ray spectra of two SNRs.

[6] The catalog is available online in http://tevcat.uchicago.edu/.

3.3.2 Pulsars

Pulsars are rotating highly magnetized objected ($B \sim 10^{12}\,\mathrm{G}$) neutron stars. It is believed that they can accelerate charged particles to very high energies ($\sim 1\,\mathrm{PeV}$), which then produce gamma radiation. A dipole moment due to the misalignment between the axis of rotation and the magnetosphere exists. The rotation of this dipole moment induces the emission of electromagnetic radiation at a rate [377]

$$\frac{dE}{dt} \sim 10^{26} \left(\frac{B}{10^{12}\,\mathrm{G}}\right)^2 \left(\frac{\mathrm{ms}}{P}\right)^4 \ \mathrm{J/s}, \tag{3.14}$$

where B is the superficial magnetic field, and P the rotation period, usually of the order of milliseconds. The rate of energy loss via spin-down is [377]

$$\frac{dE(t)}{dt} = \frac{dE(0)}{dt} \left(\frac{\tau}{\tau + t}\right)^p, \tag{3.15}$$

where τ is the characteristic spin-down time, and $p \equiv (n+1)/(n-1)$ is a geometrical factor. For instance, the dipolar case is $n = 2$.

The difference of potential due to the rotating magnetic field is

$$\Delta V \sim 10^{17} \left(\frac{B}{10^{12}\,\mathrm{G}}\right)^2 \left(\frac{\mathrm{ms}}{P}\right)^2 \ \mathrm{V}. \tag{3.16}$$

Typically these processes produce gamma rays with energies $\sim 10 - 100\,\mathrm{GeV}$.

3.3.3 Pulsar wind nebulae

Pulsar wind nebulae (PWNe) are efficient accelerators of gamma rays to high energies. In fact, the first TeV gamma ray source ever detected, the Crab nebula, is a PWN. Part of the rotational energy of pulsars can be transfered to the surrounding environment by relativistic winds. This process is an efficient accelerator of charged particles up to high energies, via expansion or collisions of the winds with the surroundings. High energy leptons such as electrons and positrons can interact with radiation fields via inverse Compton or with magnetic fields emitting synchrotron radiation, resulting in the production of non thermal radiation with energies as high as 100 TeV.

3.3.4 Binary systems

Binary systems can also produce VHEGRs via accretion-powered jets [382, 383] (microquasar scenarios) or via shocks between pulsars and star winds [384, 385] (wind-wind scenarios). In microquasar scenarios a jet originating from the accretion disk is responsible for the acceleration, similar to what happens in active galactic nuclei. In wind-wind scenarios the interaction takes place by means of the interaction of the pulsar wind with radiation field of the star. High energy particles are produced via synchrotron and inverse Compton scattering.

Typically, binaries whose majority of the gamma ray flux is produced via leptonic channels will appear as points. Moreover, the relatively small timescale involved imply a large variability for these sources. On the other hand, hadronic processes produce steady and extended gamma ray emissions if the energy losses suffered by accelerated cosmic rays escaping the production site are negligible.

3.3.5 Galactic center and Fermi bubbles

TeV emission close to the galactic center has been detected by various observatories [386–388]. The exact source associated to the emission cannot be identified, due to the complexity of the region. The observed spectrum in the GeV-TeV energy range is rather complex and combined Fermi-Lat and HESS analyses [389, 390] suggest that this could be explained by the interaction of protons and the dense gas near the galactic center. More detailed discussion on this topic can be found in refs. [379, 391].

Two remarkable structures with emission of VHE gamma rays were discovered recently [392], the so-called Fermi bubbles. These structures are located around the galactic center, approximately symmetric with respect to the galactic plane, with an extension of about 10 kpc above and below this plane. The associated gamma ray emission has a spectrum slightly harder than the one produced by inverse Compton scattering by electrons in the galactic disk.

Particle acceleration in the Fermi bubbles is probably highly efficient. The two main scenarios for explaining theemission of high energy gamma rays by these structures are inverse Compton emission due to relativistic electrons interacting with radiation fields, or proton-proton interactions, process which generates neutral pions which decay into gamma rays.

3.3.6 Starburst galaxies

Starburst galaxies are characterized by their high star formation rate in some regions. As a results, there is a high number of SNRs which can accelerate charged particles to very high energies, hence increasing the gamma ray output by these galaxies. Typically the energy of protons required to produce TeV gamma rays is [379]

$$W \approx L_\gamma t_{pp}, \tag{3.17}$$

where L_γ is the required luminosity ($\sim 10^{39}$ erg/s) and t_{pp} is the time scale for proton-proton collisions.

3.3.7 Blazars

Blazars are quasi-stellar objects believed to be type of active galactic nucleus (AGN) whose emission is beamed toward Earth [393]. It comprises mainly two classes of objects, namely BL Lacertae (BL Lacs) and flat spectrum radio quasars (FSRQ), the former having weak or non existent emission lines, and the latter typically having broader lines. The vast majority of blazars detected so far are BL Lacs. It is believed that they can accelerate gamma rays to very-high energy inside jets. Blazars were the first extragalactic sources of VHEGRs identified, specifically the BL Lac object Mrk 421 discovered in 1992 [394].

The standard picture for acceleration of VHEGRs by blazars predicts that flares are created when high energy electrons are injected into a spherical blob containing a stream of particles along the axis of the jet [395]. Particles in the blob are moving relativistically, therefore reducing the power required for acceleration due to the boost of the emission. This reduction is proportional to the fourth power of the Doppler factor $\mathcal{D} \equiv \gamma(1-\beta\cos\theta)^{-1}$, where θ denotes the angle between the axis of the jet and the observer, and γ is the Lorentz factor of the bulk motion of the jet. The blob has a typical size $R \sim c t_{var}\mathcal{D}$, where t_{var} is the typical variability time.

A leptonic scenario for acceleration of VHEGRs by blazars was presented in ref. [395]. In this model synchrotron radiation emitted by particles in the blob is up-scattered by electrons in a process known as synchrotron self Compton (SSC). Purely hadronic models can hardly explain the acceleration of VHEGRs, due to the long cooling time scale of relevant processes, which makes it difficult to explain rapid variability. A detailed description of other acceleration scenarios including lepto-hadronic models can be found in ref. [396].

3.3.8 Unconfirmed candidates and unidentified sources

Surprisingly, VHEGRs from Gamma Ray Bursts (GRBs) have never been detected so far, and only upper limits exist [397–399]. Nevertheless they are suitable source candidates. In the context of leptonic models, synchrotron radiation and photons accelerated via inverse Compton scattering can generate extended TeV emissions. In hadronic models the scattering of ambient photon by cosmic ray nuclei (mostly protons) or proton-proton interactions can produce VHEGRs.

Another candidate are passive black holes (PBHs). These supermassive objects have typical mass $\sim 10^9 M_\odot$ and low luminosity. They are candidates for producing UHECRs, which might generate very energetic gamma rays through photohadronic mechanisms and other processes taking place in the magnetosphere [400].

There are also many TeV sources unassociated to any known astrophysical object. It is not known if these regions are actually sources in the astrophysical sense, nor which kind of mechanism is responsible for the emission. One possibility for these are top-down explanations, which include self annihilation of dark matter particles, assumed here to be WIMPs[7] (see e.g. [401, 402]).

3.4 Experimental methods

3.4.1 Ground-based air shower detectors

At VHE it is rather hard to detect gamma rays using satellite-borne detectors, due to the large areas required. In this case, ground-based detection is a good alternative.

As is the case for cosmic rays (see chapter 2), the atmosphere is not transparent to the propagation of high energy gamma rays, and gamma rays can induce air showers of secondary particles in the atmosphere, which can be detected using ground arrays. The main advantage of this technique is the high duty cycle (detector operates day and night), and the large field of view (FoV) covering essentially the whole sky observable from that latitude. Due to the background of cosmic rays, it is rather hard to achieve high sensitivity.

A notorious example of ground-based air shower detector is the Milagro experiment [403, 404], which ceased operation in 2008 and has detected many TeV sources. Other detectors of the kind are ARGO-YBJ [405, 406] and Tibet-$AS\gamma$ [407] and the upcoming HAWC [408].

3.4.2 Imaging air Cherenkov technique

Imaging air Cherekov telescopes (IACTs) are perhaps the most promising detectors. The detection technique consists on the observation of the Cherekov light emitted by gamma ray when interacting in the atmosphere. Stereoscopic observations with IACTs allow the separation of hadronic and electromagnetic showers, and provide a good angular resolution ($\sim 0.1^\circ$). The drawback of this method is the low duty cycle (detector operates only at night), and the small field of view of ($\sim$a few degrees).

IACTs can be used to study extended sources as long as their angular size is of the order of the FoV and larger than the point spreading function (PSF) of the detector. Successful IACTs have been operating for more than a decade, and have largely contributed to the understanding of the non thermal universe. Some notorious ones are the High Energy Stereoscopic System (HESS) [409, 410], the Major Atmospheric Gamma Imaging Cherekov (MAGIC) [410, 411], the Collaboration of Australia and Nippon for a Gamma

[7] The acronym WIMP stands for weakly interacting massive particle, and is a promising dark matter candidate.

Ray Observatory in the Outback (CANGOROO) [412, 413] and the High Energy Gamma Ray Astronomy (HEGRA) [414]. A comparative chart summarizing the main IACT facilities is shown in table 3.1.

The next generation of IACTs will increase by at least one order of magnitude the flux sensitivity, expanding the energy range down to $\sim 10\,\mathrm{GeV}$ and possibly beyond $\sim 100\,\mathrm{TeV}$. The first IACT of this new generation is the Cherenkov Telescope Array (CTA) [415], which is expected to start taking data in the next few years.

Table 3.1: Summary of the the major IACT facilities, including details on location, number and area of the telescopes, field of view (FoV) and current operational status. Table adapted from [416].

observatory	altitude (m)	telescopes	FoV	location	operation
HESS	1800	$4 \times 107\,\mathrm{m}^2$	5.0°	Namibia	until 2012
HESS II	1800	$1 \times 615\,\mathrm{m}^2$	3.6°	Namibia	active
MAGIC-II	2230	$2 \times 226\,\mathrm{m}^2$	3.5°	Canary Islands	active
VERITAS	1268	$4 \times 106\,\mathrm{m}^2$	3.5°	Arizona, USA	active
HEGRA	2200	$5 \times 8.5\,\mathrm{m}^2$	4.8°	Canary Islands	until 2002
CANGOROO-III	165	$4 \times 57\,\mathrm{m}^2$	4.0°	Australia	until 2011

chapter 4

Diffusion of cosmic rays in extragalactic magnetic fields

The propagation of cosmic rays through extragalactic magnetic fields can be diffusive, if their scattering length is much smaller than their distance to the observer, or ballistic, if this distance is much smaller than the scattering length. The exact region of the parameter space where the transition between these two regimes occurs is not clear. This effect may be responsible for the vanishing extragalactic cosmic ray component at energies below $\lesssim 1$ EeV.

When the propagation time of cosmic rays is comparable to the age of the universe, a suppression in the flux relative to the case in the absence of magnetic fields will occur. This implies the existence of a magnetic horizon, a distance beyond which most of the flux from a given source is suppressed due to the diffusive trajectories described by the particles. This effect was previously studied in refs. [20, 278, 279, 417]

In this chapter the diffusive propagation of cosmic rays with energies $\sim 10^{18}$ eV in extragalactic magnetic fields is discussed, following ref. [20]. Approximate parametrizations for the suppression at energies $\lesssim Z \times 10^{18}$ eV using several magnetic field distributions are found. Furtheremore, model dependent upper limits for the energy at which the flux is significantly suppressed are also derived, as a function of the coherence length of these fields.

4.1 The diffusive cosmic ray spectrum

Berezinsky & Gazizov [418] have derived and solved the diffusion equation in the expanding universe for the case of a position independent diffusion coefficient. The mathematical formalism underlying these calculations is described in details in appendix A.

For cosmic rays located at position $\vec{r}$, with energy E, at a time t, in an expanding comoving volume of the universe, the flux (j) for a single source is given by [418]:

$$j(E, B, r_g) = \frac{c}{4\pi} \int_0^{z_{max}} dz \left|\frac{dt}{dz}\right| Q(E_g(E,z),z) \frac{\exp\left(-\frac{r_g^2}{4\lambda^2}\right)}{(4\pi\lambda^2)^{\frac{3}{2}}} \frac{dE_g}{dE}, \tag{4.1}$$

where $\vec{r}_g = \vec{r} - \vec{r}_s$ are the comoving coordinates of the source at a distance $\vec{r}_s$ from the observer. Here the standard ΛCDM cosmology is used, with the redshift evolution given by eq. 1.21, which is transcribed here for completeness:

$$\left|\frac{dt}{dz}\right| = \frac{1}{H_0(1+z)} \frac{1}{\sqrt{\Omega_m(1+z)^3 + \Omega_\Lambda}}. \tag{4.2}$$

The source term $Q(E_g(E,z),z)$ depends on redshift evolution function of the source emissivity ($f(z)$), the injected spectrum, which is a power law with spectral index γ, and the shape of the source cutoff function, associated to the maximum acceleration energy that the source can reach, assumed to be a hyperbolic cosine, as in ref. [419]. Therefore, the source term reads:

$$Q(E,z) = \frac{\xi_Z f(z) E^{-\gamma}}{\cosh\left(\frac{E}{E_{max}}\right)}, \tag{4.3}$$

with ξ_Z being the contribution of the nucleus of atomic number Z, E its observed energy and E_{max} the cutoff energy. E_g and E are related in the following way [420]:

$$\frac{dE_g}{dE} = (1+z)\exp\left(\int_0^z dz' \left|\frac{dt'}{dz'}\right| \frac{\partial}{\partial E_g} b(E_g, z')\right), \tag{4.4}$$

with E_g denoting the initial energy of the particle at redshift z' ($0 < z' < z$), if the observed energy at present time is E. From this point onward only the adiabatic energy losses due to the expansion of the universe will be considered, since the focus of the work is in the energy range $E \lesssim$ EeV.

$\lambda = \lambda(E,z,B)$ is known as the Syrovatskii variable[1], first introduced by Syrovatskii [421] to address the problem of the distribution of relativistic electrons in the galaxy. The generalization of the Syrovatskii solution for an expanding universe was given by Berezinsky and Gazizov [418], and can be written as

$$\lambda(E,z,B) = \sqrt{\int_0^z dz' \left|\frac{dt}{dz'}\right| \frac{D(E_g,z',B)}{a^2(z')}}. \tag{4.5}$$

The diffusion coefficient is written as a combination of the diffusion coefficients for the quasi-linear regime ($D \propto E^{1/3}$), dominant at lower energies, and the non resonant regime ($D \propto E^2$), dominant at higher energies, following refs. [419, 422, 423]:

$$D(E,z,B) = \frac{c l_c(z)}{3}\left[a_L\left(\frac{E}{E_c(z,B)}\right)^{\frac{1}{3}} + a_H\left(\frac{E}{E_c(z,B)}\right)^2\right], \tag{4.6}$$

where the parameters a_L and a_H are, respectively, 0.3 and 4 [419]. This expression approximately holds for the resonant and non-resonant regimes, for the case of a Kolmogorov turbulence. The dependence of the diffusion coefficient as a function of $x \equiv E/\langle E_c\rangle$ is shown in figure 4.1.

The coherence length ($l_c(z) = l_{c,0}/(1+z)$) and magnetic field strength ($B(z) = B_0(1+z)^{2-m}$) depend on the redshift. Here the subscript '0' is used to indicate the value of a given quantity at present time, and m is a parameter due to the MHD amplification of the field. The critical energy $E_c = E_c(z,B)$ is defined as the energy for which the Larmor radius of the particle is equal to the coherence length of the magnetic field, i.e., $R_L(E_c) = l_c$. Its redshift dependence is: $E_c(z) = E_{c,0}(1+z)^{1-m}$. The Larmor radius is given by

$$R_L(E,B) = \frac{E}{cZeB} \approx \left(\frac{E}{\text{EeV}}\right)\left(\frac{\text{nG}}{B}\right) \text{ Mpc}, \tag{4.7}$$

with B being the magnetic field strength, and E the energy. The explicit form of E_c can be obtained from

[1] This definition of λ differs by a square from the original definition given by him [421] and ref. [418], and follows ref. [419]. This way, λ has dimension of length and can be translated into the magnetic horizon.

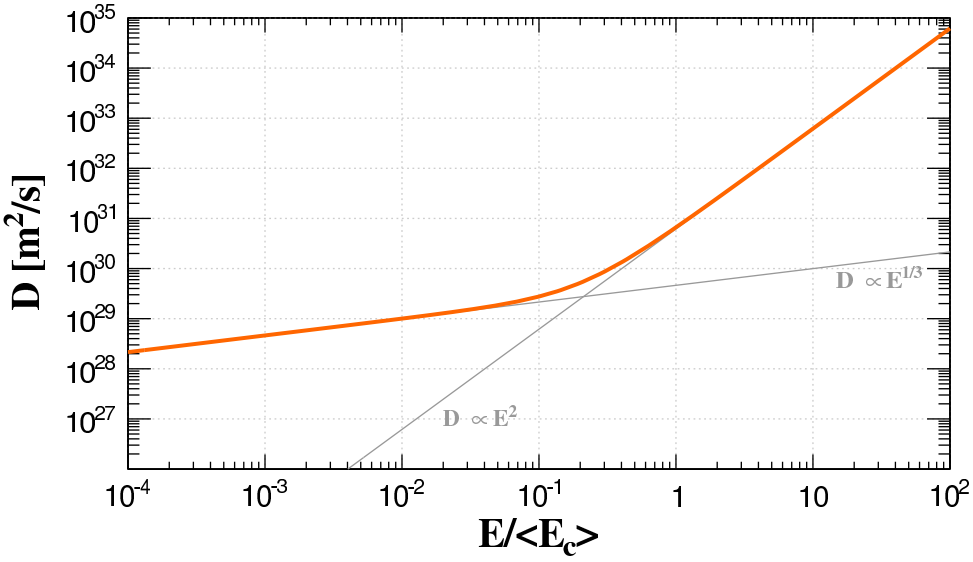

Figure 4.1: Diffusion coefficient as a function of $x \equiv E/\langle E_c \rangle$. Thin gray lines are the two energy dependent diffusion coefficients used to obtain the one adopted in this work, represented by the orange thick line. This case is for $z = 0$.

equation 4.7 and reads

$$E_c(z, B, l_c) = cZeB(z)l_c(z) \approx 0.9Z \left(\frac{B}{\text{nG}}\right)\left(\frac{l_c}{\text{Mpc}}\right) \text{ EeV}, \tag{4.8}$$

with $B = B(z)$ and $l_c = l_c(z)$.

The spectrum for a single source is given by equation 4.1. For N_s sources, each one located at a distance r_i from Earth, the total spectrum can be written as the superposition of the spectra of individual sources, this is,

$$j_t(E, B) = \sum_{i=1}^{N_s} j_s(E, B, r_i) = \frac{c}{4\pi} \int_0^{z_{max}} dz \left|\frac{dt}{dz}\right| Q(E_g(E, z), z) \frac{dE_g}{dE} \sum_{i=1}^{N_s} \frac{\exp\left(-\frac{r_i^2}{4\lambda^2}\right)}{(4\pi\lambda^2)^{\frac{3}{2}}}. \tag{4.9}$$

In the limit of a continuous source distribution, i.e., if the N_s is large, then the discrete sum can be replace by an integral, which can be calculated assuming spherical symmetry, yielding unity if the average separation between sources is small enough. In this case it can be shown that the dependence on the Syrovatskii variable will no longer be present, implying that the spectrum will not depend on the modes of propagation and hence the magnetic field. This result is known as the propagation theorem [422]. The spectrum obtained under these assumptions will be henceforth called universal spectrum.

For simplicity of notation it is convenient to introduce a factor F, related to modes of propagation of cosmic rays from different sources. This factor can be written as

$$F = \frac{1}{N_s} \sum_{i=1}^{N_s} \frac{\exp\left(-\frac{r_i^2}{4\lambda^2}\right)}{(4\pi\lambda^2)^{\frac{3}{2}}}, \tag{4.10}$$

where a possible realization for a uniform distribution of sources can be defined according to ref. [419]:

$$r_i = d_s \left(\frac{3}{4\pi}\right)^{\frac{1}{3}} \frac{\Gamma(i + 1/3)}{(i-1)!}. \tag{4.11}$$

Here d_s is the average separation between the sources, obtained from the source density.

The total spectrum shown in equation 4.9 can be written in terms of F, as follows:

$$j_t(E,B) = \frac{c}{4\pi}\int_0^{z_{max}} dz \left|\frac{dt}{dz}\right| Q(E_g(E,z),z)\frac{dE_g}{dE}F(E,z,B), \tag{4.12}$$

where z_{max} is the maximum redshift of the sources which contribute to the flux. The volume average of the spectrum can be calculated by weighting it by the magnetic field distribution:

$$\begin{aligned} j(E) &= \int_0^{\infty} j_t(E,B)p(B)dB \\ &= \frac{c}{4\pi}\int_0^{z_{max}} dz \left|\frac{dt}{dz}\right| Q(E_g(E,z),z)\frac{dE_g}{dE}\left(\int_0^{\infty} dB F(E,z,B)p(B)\right), \end{aligned} \tag{4.13}$$

where $p(B)$ is the probability distribution function corresponding to the magnetic field distribution.

4.2 Extragalactic magnetic fields

Four extragalactic magnetic field models obtained from MHD simulations of the cosmic web were considered: Miniati [424], Dolag *et al.* [425], Das *et al.* [426] and Donnert *et al.* [427]. Each one of these authors adopted different numerical methods to perform the simulations, and used different assumption. For instance, Miniati assumed that magnetic fields were generated through a Biermann battery and later the field was rescaled in such a way as to reproduce the measured magnetic fields in clusters of galaxies, whereas Das *et al.* used properties of the gas such as vorticity and energy density to estimate the magnetic field. Dolag *et al.* started with a seed field at high redshift with a strength such that, at the present epoch, the field in clusters would be of the order of a few μG, in a similar fashion to Donnert *et al.*, who also included other effects at low redshift, namely magnetic pollution.

There are many other models to describe the extragalactic magnetic field in the cosmic web. The method here presented can be applied to any model, provided that one has the magnetic field distribution, or conversely the filling factors, such as the ones shown in figure 6.1. The cumulative filling factors are defined as the fraction of the volume that has a magnetic field strength higher than a given value.

From these magnetic field models distributions of field strengths are available. The magnetic field used in the calculations presented in the previous sections is a turbulent Kolmogorov field, with strengths following these distributions, and coherence length arbitrarily chosen. Although there is a redshift dependence for B in the calculations outlined in the previous section, the proper redshift evolution of the magnetic field according to these models is not taken into account. Instead, the magnetic field strength at present time is extrapolated to higher redshifts assuming that $B(z) = B_0(1+z)^{2-m}$.

The integration of equation 4.5 over the distribution of magnetic field strengths eliminates the B dependence, making it possible to obtain the value of λ taking into account the inhomogeneity of the field. In this work this integration is done between 10^{-15} G and 10^{-5} G, and the field is considered zero elsewhere. The mean and RMS values for each one of these extragalactic magnetic field models are shown in table 4.1.

The redshift dependence of the Syrovatskii variable is shown in figure 4.3, between z=0 and z=4, for the different extragalactic magnetic fields considered. In this same figure the mean values of the corresponding magnetic field distributions are also shown, as well as two extreme cases ($B = 1.0 \times 10^{-14}$ G and

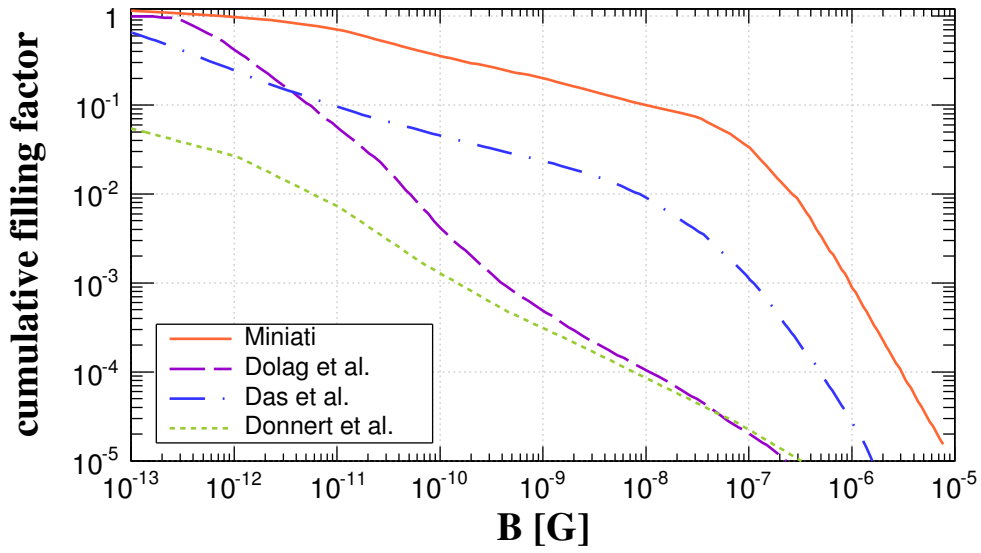

Figure 4.2: Cumulative filling factors for the cosmological simulations considered in this work.

Table 4.1: Mean and RMS values for the considered magnetic field distributions, in the range between 10^{-15} G and 10^{-5} G.

	Miniati	Dolag *et al.*	Das *et al.*	Donnert *et al.*
$\langle B \rangle$ [G]	1.8×10^{-8}	5.5×10^{-11}	1.2×10^{-9}	6.3×10^{-11}
B_{rms} [G]	1.7×10^{-7}	1.5×10^{-8}	5.7×10^{-8}	1.7×10^{-8}

$B = 1.0 \times 10^{-6}$ G), for the sake of comparison. It can be seen in figure 4.3 that the inhomogeneity of the

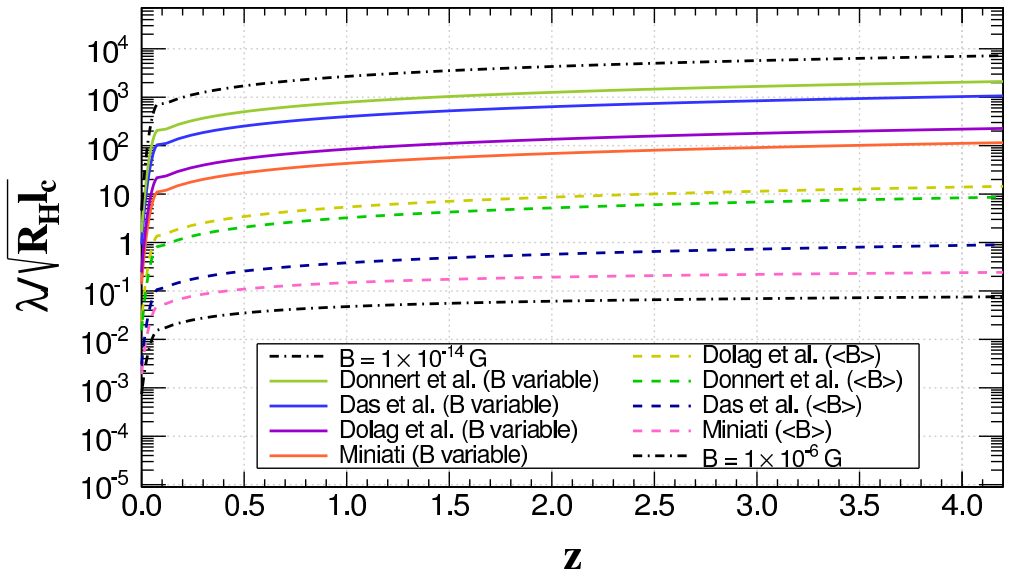

Figure 4.3: Volume averaged Syrovatskii variable for the magnetic fields from the large scale structure simulations (solid lines), in the case of constant magnetic fields equal to their average value (dashed lines), and two extreme cases (dotted dashed lines). The legend follows the same order as the curves, from top to bottom. This particular case is for $E/Z = 10^{16}$ eV, $l_{c,0} = 0.6$ Mpc, $m = 1$, $\gamma = 2.0$ and $z_{max} = 4.0$.

field implies a larger Syrovatskii variable, due to the larger contribution of regions with low magnetic fields,

such as voids. Moreover, the Syrovatskii variable when defined in units of length translates into the magnetic horizon. For instance, if $l_{c,0} = 1$ Mpc and the two black (dotted dashed) lines from figure 4.3 are chosen, the estimated magnetic horizon is approximately 47 Gpc for B=10^{-14} G and 60 Mpc for B=10^{-6} G, taking into account the contribution of all sources up to $z_{max} = 4$. Furthermore, this plot also shows that the approximation of a turbulent magnetic field with a given RMS, as assumed in ref. [419], may not be good enough, since most of the volume is filled by magnetic fields with low intensity in a more realistic scenario.

The magnetic horizon as a function of the energy can be calculated from equation 4.5. It is shown in figure 4.4. One should carefully interpret this figure, since for energies $\gtrsim Z$ EeV the interactions, neglected in this work, start to become relevant, decreasing the effective horizon of the cosmic ray.

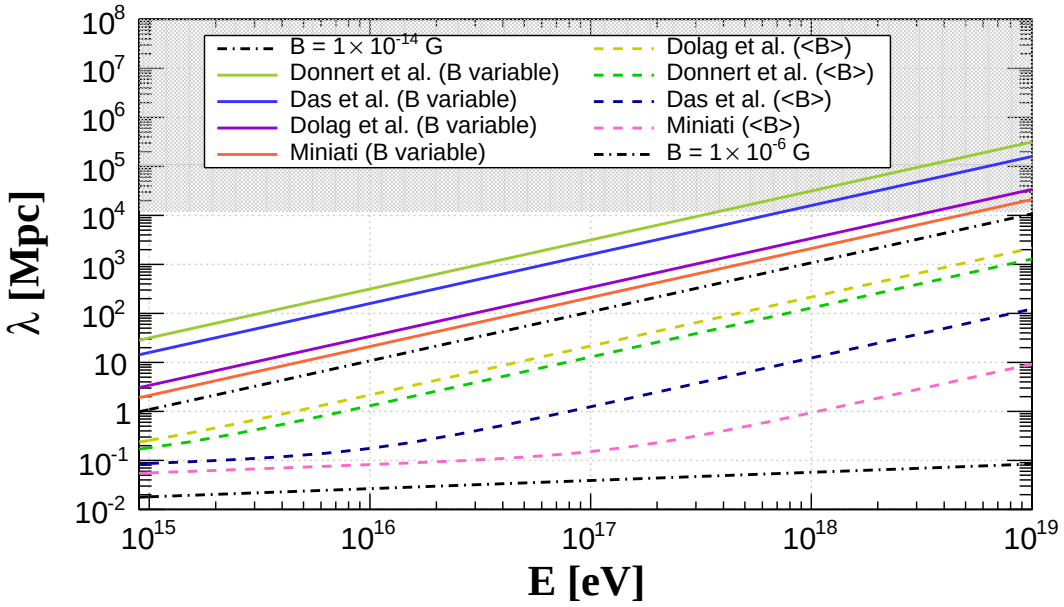

Figure 4.4: Volume averaged Syrovatskii variable for the magnetic fields from the large scale structure simulations (solid lines), in the case of constant magnetic fields equal to their average value (dashed lines), and two extreme cases (dotted dashed lines), as a function of the energy. The legend follows the same order as the curves, from top to bottom. This particular case is for $l_{c,0} = 0.6$ Mpc, $m = 1$, $\gamma = 2.0$ and $z_{max} = 4.0$. Notice that interactions are not considered, and therefore these results above $\gtrsim 10^{18}$ eV cannot be interpreted in a straightforward.

4.3 Parametrization of the flux suppression

If the factor F, defined in equation 4.10, is equal to 1, the spectrum will be universal. Let $j_0(E)$ be the universal spectrum, and $j(E)$ a generic one. The suppression factor can be defined as the ratio between these two spectra[2], i.e.:

$$G = \frac{j(E)}{j_0(E)}. \tag{4.14}$$

Using equation 4.12 the spectra for the cosmological simulations whose filling factors are shown in figure 6.1 is obtained. A parametrization for the suppression factor is introduced[3], following ref. [419], and is given

[2] In this work, as well as in refs. [20, 419], this is called the suppression factor, even though the most appropriate name should be 'transmission factor'. Strictly speaking, the suppression factor is one minus the transmission factor. To be consistent with these references, here the suppression factor should be understood as the fraction of the flux not suppressed by magnetic horizon effects.

[3] The choice of this function is somehow arbitrary. Other functions could fit the suprression as well as, or even better than this. This choice was motivated by ref. [419], and proved itself to be adequate for the purposes of this work.

by:

$$G(x) = \exp\left[-\frac{(aX_s)^\alpha}{x^\alpha + bx^\beta}\right], \tag{4.15}$$

where α, β, a and b are free parameters, x is the ratio between the energy of the particle (E) and the average critical energy ($\langle E_{c,0}\rangle$), and X_s is given by

$$X_s = \frac{d_s}{\sqrt{R_H l_c}}. \tag{4.16}$$

The average separation between the sources for a source density of n_s is

$$d_s = \left(\frac{3}{4\pi n_s}\right)^{\frac{1}{3}}. \tag{4.17}$$

Notice that the source density is assumed to be constant over the evolution of the universe.

Unlike in ref. [419], here the best fit parameters obtained by fitting the suppression factors obtained from eq. 4.14 with the function from eq. 4.15 are not constant. It depends on the value of X_s and m, whereas in the aforementioned reference the best fit values are $\alpha = 1.43$, $\beta = 0.19$, $a = 0.20$, $b = 0.09$. A summary of the best fit values as a function of X_s can be seen in figure 4.5, for $m = 0$ [4]. It is important stress that the best fit values do not have a significant dependence on the spectral index of the source (γ) nor the cutoff energy (E_{max}), so they can be used generically. Also, since the suppression factor is written in terms of $E/\langle E_{c,0}\rangle$, it will be the same for all nuclei with energy E and rigidity E/Z. The parameter m, however, can affect the suppression factor, changing the values of the fit parameters, especially for the case of strong evolution ($m \gtrsim 2$). A proper estimation of all the parameters for each values of m would be required to obtain a more accurate description. Nevertheless, there are so many uncertainties involved (e.g. coherence length, power spectrum of the magnetic field, source density, source evolution), that the improvement of the fit parameters would not necessarily lead to better results.

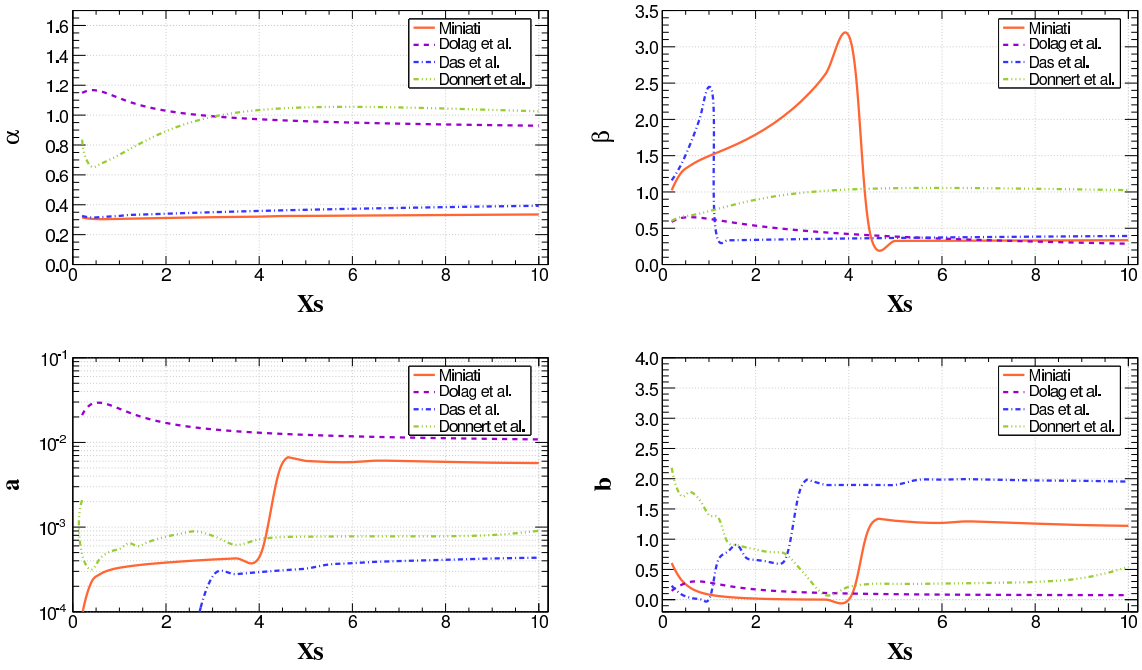

Figure 4.5: Values of the best fit parameters α, β, a and b as a function of X_s, for $m = 0$.

[4] Tables containing the values of each parameter for $m = 0, 1, 2$ are available in appendix B.

Examples of the fit of the function shown in equation 4.15 to the values obtained from equation 4.14 are shown in figure 4.6

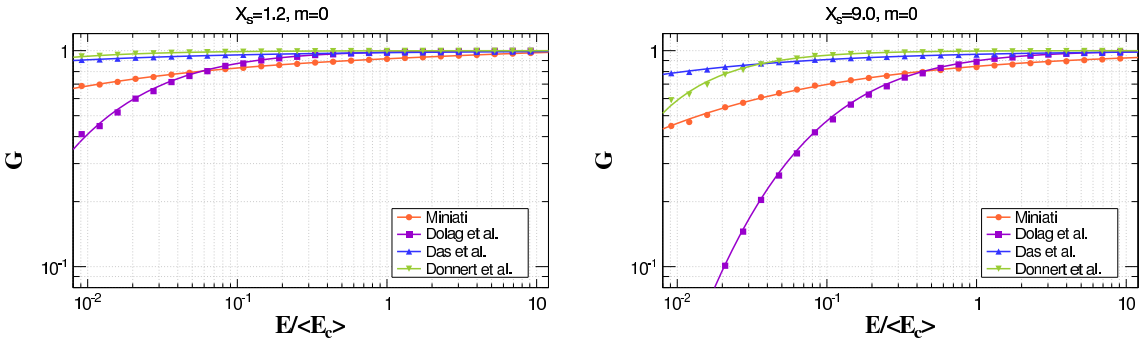

Figure 4.6: Suppression factor as a function of $x \equiv E/\langle E_{c,0}\rangle$. The markers are the suppression factors estimated using equation 4.14, whereas the lines correspond to the best fit values obtained using equation 4.15, for m=0.

4.4 Upper limits on the magnetic suppression

Using equation 4.15 the energy E_e at which the flux is suppressed to $e^{-1} \approx 0.37$ of its former value can be calculated. From equation 4.15 one can calculate $G(E_e/\langle E_{c,0}\rangle) = 1/e$, obtaining

$$E_e^{\alpha} + bE_e^{\beta}\langle E_{c,0}\rangle^{\alpha-\beta} = (aX_s\langle E_{c,0}\rangle)^{\alpha}. \tag{4.18}$$

Similarly one can find the coherence length the corresponding coherence length for E_e:

$$(ad_s cZe\langle B_0\rangle)^{\alpha} R_H^{-\alpha/2} l_{c,0}^{\alpha/2} - b(cZe\langle B_0\rangle)^{\alpha-\beta} E_e^{\beta} = E_e^{\alpha}. \tag{4.19}$$

In the particular case where $\alpha = \beta$, equations 4.18 and 4.19 are, respectively, reduced to:

$$E_e = aX_s\langle E_{c,0}\rangle\,(1+b)^{\frac{1}{\alpha}} \tag{4.20}$$

and

$$l_{c,0} = \frac{E_e}{ZeH_0\langle B_0\rangle}\left(\frac{4\pi n_s}{3}\right)^{\frac{1}{3}}(1+b)^{\frac{1}{\alpha}}\,. \tag{4.21}$$

Assuming that the sources are uniformly distributed, and that the extragalactic magnetic field strength is distributed according to one of the considered models, it is possible to calculate E_e, as a function of l_c. From equations 4.14 and 4.16 it is possible to see that the suppression is stronger for lower source densities. Thus, adopting the lower limit for the source density estimated by the Pierre Auger Collaboration [428], 6×10^{-6} Mpc^{-3}, it is possible to set an upper limit for the flux suppression. This is shown in figure 4.7 for the case of iron[5]. One should bear in mind that if nuclear photodisintegration occurs, and it very likely will, the curves displayed in this figure will be shifted to even lower energies. In this figure the upper limits for the cases of constant magnetic field are calculated with the best fit parameters from ref. [419].

The suppression is stronger for $l_c \sim$ Mpc. This dependence can be understood by analyzing the behavior of the diffusion coefficient, shown in equation 4.6, for different values of l_c. The critical energy E_c is proportional to l_c, as displayed in equation 4.8. Therefore, at a given energy, for small values of l_c, the

[5]As described in chapter 2, the measurements around 1 EeV favor a light composition. The choice to set the upper limit for the case of iron is meant to be the most conservative case. For realistic mass compositions at this energy the flux will be even less suppressed.

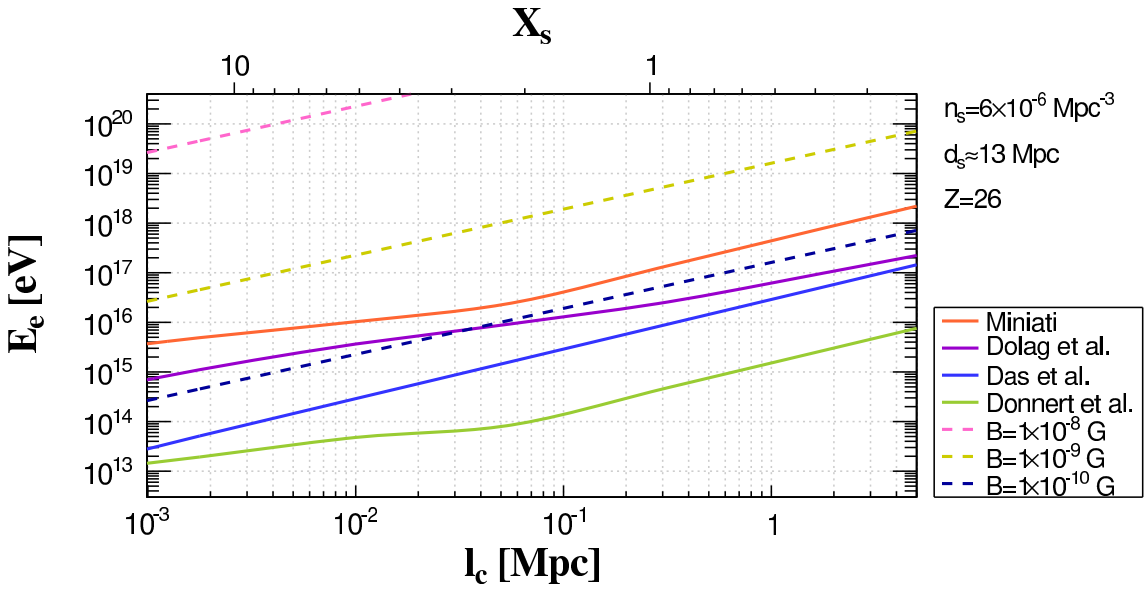

Figure 4.7: Energy for which the flux is suppressed to $1/e$ of its former value, as a function of the coherence length. Dashed lines correspond to the cases of constant magnetic field strength and solid lines to magnetic fields from the cosmological simulations indicated in the legend. This particular case is for n_s=6×10^{-6} Mpc^{-3} and Z=26.

term proportional to E^2 in equation 4.6 would dominate, implying $D \propto l_c^{-1}$, and thus $\lambda \propto l_c^{-1/2}$. This leads to a flux suppression and a critical energy both of which increase with l_c. Similarly, if l_c is large, $D \propto l_c^{2/3}$ and hence $\lambda \propto l_c^{1/3}$, implying that E_e should decrease with l_c. However, this last effect is not visible in figure 4.7, due to the limited range of parameters covered in our analysis, tuned to encompass typical values of l_c found in the literature, and allow an analytical description of the suppression through equation 4.15.

4.5 Discussion

The results presented in this chapter indicate a weak suppression of the flux of cosmic rays at 10^{18} eV, which starts to become more pronounced at $E \lesssim 10^{16}$ eV, depending on the magnetic field model, its coherence length, and the charge of the particle. This result is in qualitative agreement with ref. [279], in which three other MHD simulations were used and a similar analysis was performed. In this work the authors observed the presence of a magnetic horizon for energies below $\sim 10^{17}$ eV, which roughly corresponds to the upper limit for the energy the suppression sets in, for the most optimistic choice of parameters. Even though the MHD simulations used in this reference were not analyzed, their filling factors distributions are lower compared to the Miniati case, particularly for $B \gtrsim 100$ nG. Since a larger contribution from higher magnetic fields would spawn a stronger suppression, one can take the Miniati scenario as a limiting case for the ones presented in ref. [279].

A uniform source distribution was adopted, but other possibilities could be easily taken into account by changing equation 4.11, since the spectrum is the superposition of the fluxes of individual sources. At energies below 1 EeV, the spectrum is dominated by the contribution of distant sources. At cosmological distances the distribution of sources is probably close to uniform. Therefore, unless the sources are clustered and their distribution is highly non uniform, the results here obtained would not change significantly.

To have diffusion from the nearest source the diffusion length ($l_D = 3D/c$) should be smaller than the distance of this source, i. e., $l_D < d_s$. This effect may be dominant depending on the source distance and luminosity. Therefore, a more precise calculation of the suppression would need to take into account

the inhomogeneity of the magnetic field in scales comparable to the distance of the nearest source. As long as the filling factors distribution for a volume containing both the nearest source and Earth has the same shape as the ones considered, the results here presented will hold. This is not true in scales comparable to the size of the structures. Moreover it may not be valid if both the observer and the source lie within the same filament, due to the higher magnetic field strengths in these regions compared to the voids. This would change the magnetic field distribution, shifting its mean value toward higher values of B, possibly spawning a stronger suppression in the observed flux if the luminosity of the source is high enough.

Another assumption made in this work is that the coherence length is fixed, which is hardly realistic. The present analysis can be easily extended to incorporate coherence length distributions. However, the actual distribution of coherence lengths is not well known and can vary in different regions of the universe. In this work coherence lengths between $\sim 10^{-3}$ and 10 Mpc, which are typical values in the literature [131, 429,430], were analyzed. Regardless of the shape of this distribution, as long as the contribution of coherence lengths outside the studied range is negligible, E_e for l_c=10 Mpc can still be taken as an upper limit for the magnetic suppression.

Sigl [431] has shown that the confinement of particles around the source position may play a role in the low energy suppression. If this is true, there might be an additional contribution, due to the fact that the magnetic field would be much higher around the source than elsewhere. This would occur if the following condition were satisfied

$$B \gtrsim \sqrt{\frac{l_c}{10\ \mathrm{kpc}}} \left(\frac{L}{100\ \mathrm{kpc}}\right)\ \mu\mathrm{G}, \tag{4.22}$$

where L represents the characteristic scale of the magnetized region. If the magnetic fields have stochastic nature with a relatively low RMS value ($B \lesssim 100$ nG), this confinement would not be expected.

The neglected energy loss processes are not so relevant at $E \lesssim$ EeV, as mentioned earlier. At energies of a few EeV it has been shown in ref. [419] that the effect of pair production would be small, slightly shifting the low energy suppression to higher energies. This effect is also negligible for $E \lesssim$ EeV.

The results here obtained are for the range of $10^{-3} < \mathrm{x} \equiv E/\langle E_c \rangle < 10$. Although not systematically, the fit using equation 4.15 was tested in the range of $10^{-4} < x < 100$. For $x \sim 100$ the fit describes the suppression well. For $x \sim 10^{-4}$, however, equation 4.15 no longer fits satisfactorily the values calculated using equation 4.14.

In this work the diffusion approximation was used to describe the effects of extragalactic magnetic fields on the cosmic ray spectrum and composition. This approximation is not valid for $D \gtrsim cR_H$ because the diffusive propagation speed over a time scale $t_H \equiv R_H c^{-1}$ is of the order of $(D/t_H)^{1/2}$ which would then exceed the speed of light[6] and hence be unphysical. With D given by eq. 4.6 this typically happens for $B \lesssim 0.01$ nG. In summary, if $D \gtrsim R_H c$ and/or $D/\ell_D \gtrsim c$ the diffusion approximation can no longer be applied and one would have to adopt a full numerical Monte Carlo simulation of trajectories.

In ref. [419] it was argued that the low energy suppression could be relevant for the propagation of cosmic rays at $\sim$ EeV energies, which is in contrast with the results here presented. This discrepancy is due to the oversimplified assumption of a turbulent magnetic field with fixed $\langle B_{rms} \rangle$. In the case of inhomogeneous magnetic fields the contribution of the voids is dominant, lowering the average field strength.

Many authors [18, 433–435] have recently attempted to obtain models that can simultaneously describe the measured spectrum and mass composition of UHECRs. In ref. [435] it was shown that it is possible to perform combined spectrum-composition fits of the Auger data for $E \gtrsim 5 \times 10^{18}$ eV, due to the hard spectral indexes required ($\gamma \sim$1.0-1.6). Hard spectra are incompatible with the standard acceleration paradigm, in which particles are accelerated in non-relativistic shocks through Fermi-like mechanisms, pro-

[6] A phenomenological approach to the problem of superluminal diffusion of cosmic rays can be found in ref. [432].

cess which leads to $\gamma \sim 2 - 2.3$. Hard spectral indexes ($\gamma \lesssim 2$) are predicted in many other acceleration models such as the ones in which UHECRs are accelerated by magnetars [331] or young pulsars [338, 339].

Here it was shown that for the magnetic field models studied the low energy suppression of the extragalactic flux is mild at EeV energies, becoming more relevant at energies $\lesssim 10^{17}$ eV. Since the spectral index of the source and the existence of a magnetic horizon are connected, understanding the low energy suppression is important for identifying the sources of UHECRs. In terms of cosmic ray observables, harder spectral indexes could lead to an overproduction of secondary protons for $E \lesssim 10^{18}$ eV. This same effect could be mimicked by considering softer injection spectra which are effectively hardened during propagation by the effect of the magnetic suppression, as shown in ref. [419]. In the context of this work, if the scale of inhomogeneity of the cosmic web is of the order of the distance of the nearest sources, i. e., if there are no dominant nearby sources, the suppression is very low at EeV energies, as can be seen in figure 4.7. In the Miniati model, which has the higher mean magnetic field, the suppression would become significant only at $E \lesssim 10^{17}$ eV for the most optimistic choice of parameters. The main implication of this is that the combined spectrum-composition fits would again favor scenarios in which the sources have hard injection spectrum.

4.6 Remarks on the validity of the approximations

For the sake of numerical calculations only adiabatic energy losses due to the expansion of the universe were considered. Pair production starts to become relevant for energies $\gtrsim 3Z$ EeV and pion production above $\gtrsim 50$ EeV (for protons). Photodisintegration can also be neglected, for it conserves the Lorentz factor of the particles, hence keeping diffusion properties approximately unaltered. Therefore, it is a reasonable approximation to neglect all other energy loss processes for $E \lesssim Z$ EeV.

The volume averaged spectrum is formally not the same as the volume averaged diffusion coefficient, and both approaches could, in principle, be chosen. Nevertheless they give similar results, particularly for higher redshifts ($z > 0.5$), which correspond to most of the flux at $E \lesssim 1$ EeV. The relative difference between the factor F obtained through these two approaches is $\lesssim 6\%$ at 10^{16} eV and $\lesssim 0.02\%$ at 10^{18} eV. Therefore the choice of the spectrum over the diffusion coefficient for the calculation of the volume average, as shown in equation 4.13, is justified.

The diffusion equation is solved[7] assuming a spatially constant diffusion coefficient, which depends on time and on the energy of the cosmic ray. When writing the diffusion equation one has the following term:

$$\vec{\nabla}.\left[D(\vec{x},t)\vec{\nabla}n(\vec{x},t)\right] = D(\vec{x},t)\nabla^2 n(\vec{x},t) + \vec{\nabla}D(\vec{x},t).\vec{\nabla}n(\vec{x},t), \tag{4.23}$$

where $\vec{x}$ is the position vector in physical coordinates. If $D(t) = D(\vec{x},t)$ the diffusion coefficient is position independent, implying that only the first term in the right hand side of this equation remains, because $\vec{\nabla}n(\vec{x},t)$ can be neglected. This approximation is valid as long as $D(\vec{x},t)\nabla^2 n(\vec{x},t) \gg \vec{\nabla}D(\vec{x},t).\vec{\nabla}n(\vec{x},t)$. There is a convection-like term (second term in the right hand side) in the equation, which is a convection velocity (v_c). This is bounded by the speed of light, so that $v_c < c$ should be enforced. Therefore, the condition $D/\ell_D \ll c$ should hold, where ℓ_D is the length scale on which D varies. If there are no dominant effects such as magnetic or interaction horizons, then the average source distance for this uniform source distribution is of the order of a sizable fraction of the Hubble radius (R_H). Consequently, the contribution of the neglected convective term can be deemed trifling for sources farther than $\sim (D/\ell_D c)R_H \ll R_H$, which are responsible for most of the observed flux in the energy range in question. Equivalently, this condition

[7] Refer to appendix A for the complete solution.

assures that the first term in eq. 4.23 indeed dominates over the second, assuming that the cosmic ray density varies on a length scale ℓ_D in regions of significant variation of D.

For $E \sim$ EeV, the above condition is satisfied, for example, in galaxy clusters where $B \sim \mu$G and and $l_c \sim$kpc. This would imply, from eq. 4.8, that $E_c \sim$EeV, and using eq. 4.6 one obtains $D/c \sim 0.1$ kpc. Thus, with $\ell_D \sim 100$ kpc one has $D/\ell_D \sim 10^{-3} c$. Therefore, in the regions where the largest diffusion gradients are present, which are the edge of structures such as galaxy clusters, the approximation is sufficiently good. In the voids, if $B \gtrsim 0.1$ nG and $l_c \lesssim 10$ Mpc, one has $E_c \gtrsim 0.1(l_c/\text{Mpc})$ EeV and thus $D \lesssim 100(l_c/\text{Mpc})^{-1}$ Mpc. Therefore, with $\ell_D \sim 100$ Mpc on void scales one has $D/(c\ell_D) \lesssim 1$ such that for $B \lesssim 0.01$ nG and/or $l_c \lesssim 1$ Mpc the approximation here presented breaks down, implying a flattening of the spectrum due to the additional contribution of the convective term, which depends on the energy.

For $B \lesssim 0.01$ nG and $l_c \lesssim 1$ Mpc the condition that the scale on which D changes is small compared to the average source distance is violated. However, in this case the diffusion approach can no longer be applied, since the convective velocity would exceed the speed of light, i.e., $v_c > c$. Hence, if $B \gtrsim 0.01$ nG everywhere the approach here presented is valid and the lower limit of integration can be extended down to $B = 0$ without significant changes in the flux, as shown in figure 4.8.

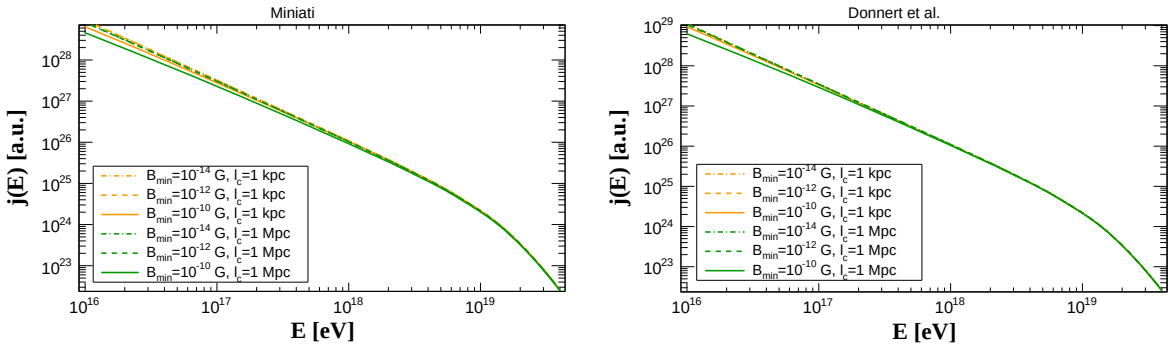

Figure 4.8: Calculated cosmic ray spectrum considering the extragalactic magnetic field models from Miniati (left) and Donnert *et al.* (right). Orange curves correspond to the case of l_c =1 kpc and green to l_c =1 Mpc. The legend indicates the lower integration limit, $B \equiv B_{min}$.

chapter 5

CRPropa 3.0

5.1 About the code

CRPropa 3 [7–9] is a public[1] Monte Carlo code for propagating UHECRs and secondary gamma rays and neutrinos in the universe. It includes all relevant interactions for the energy range of $6 \times 10^{16} \lesssim E\,[\mathrm{eV}] \lesssim \times 10^{22}$, as well as many magnetic field environments and source distribution possibilities. Currently the propagation can be done in one (1D), three (3D) or four dimensions (4D). This version consists on a completely redesign of the previous ones, CRPropa [5] and CRPropa 2 [6, 436], and is highly modular, with many new features, namely:

- parallel processing;
- Python steering;
- four-dimensional propagation;
- improved photodisintegration tables;
- redshift-dependent CIB;
- new models of CIB;
- propagation in the galactic magnetic field;
- galactic magnetic field lensing;
- enhanced calculation of interaction rates;
- extragalactic magnetic fields from SPH[2];
- modulated grids.

These features will be described in details in the following sections.

5.2 Technical aspects

CRPropa 3 is written in the C++, with optional Python bindings built via SWIG[3], for simplicity of usage. Therefore users are able to extend the code in Python to implement new functionalities for specific

[1] The code can be obtained from https://crpropa.desy.de.

[2] SPH (Smoothed Particle Hydrodynamics) is a lagrangian formalism for MHD simulations.

[3] SWIG is an interace compiler for cross-language polymorphism, making it possible for codes written, for example, in C++ to be extended to other language such as Python, allowing one to tailor the wrapping process as desired. It is available in http://swig.org.

purposes. Albeit Python is the recommended steering mode, XML inputs are also accepted, for backward compatibility with CRPropa 2.

The propagation of cosmic rays in CRPropa 3 can be done using shared memory parallel processing, through OpenMP[4]. Because the propagation of a large number of cosmic rays can be done on a particle-by-particle basis, meaning that each cosmic ray, in principle, does not affect others, the parallelization is convenient and the work load can be distributed among several threads. The bottleneck of this approach is that thread-safe objects and variables (with shared memory) cannot parallelized, affecting the performance of the parallelization, as shown in figure 5.1. These critical regions are the call of the SOPHIA code [369], for photopion production, and the output modules.

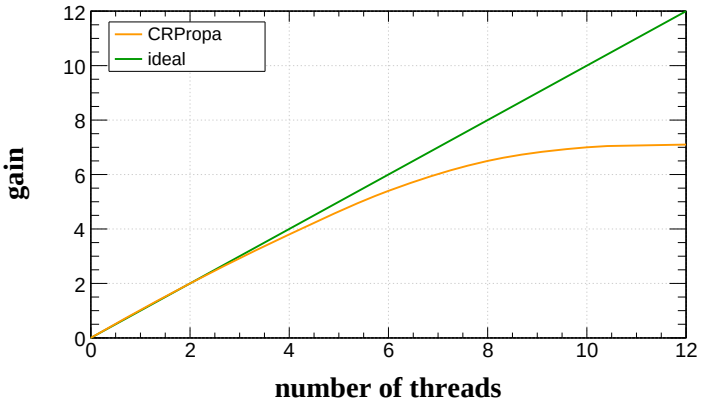

Figure 5.1: Performance of the parallelization in CRPropa 3. Ideally the gain of speed in using multiple threads would increase linearly with the number of threads (green curve), whereas in CRPropa critical processes limit this scaling (orange curve).

5.3 Code structure and propagation algorithm

In CRPropa 3 all relevant aspects for the propagation of UHECRs are contained in various modules (class 'Module'), gathered under the class 'ModuleList', which cojointly act to alter the information of a cosmic ray stored in the class 'Candidate'. This information includes the position of the cosmic ray at the previous, current and next (preliminary) step, the size of the step, the momentum, position, redshift and particle type, the interactions that are expected to occur in this step, and the status flag (e.g. 'Detected'). At each step of propagation the code checks for interactions with photon backgrounds and, in case they occur, the information of the candidate is updated. If the 'Redshift' module is included, adiabatic losses are also taken into account at each step. The propagation of a cosmic ray ends if one or more of the following conditions are met:

- particle reaches the observer;
- energy of the candidate drops below a given minimum energy;
- trajectory length exceeds the maximum propagation length allowed.

An schematic overview of the modular structure and the communication between modules is displayed in figure 5.2.

[4]OpenMP is a powerful tool that allows parallel programming in C, C++ and Fortran. More information can be found in http://openmp.org.

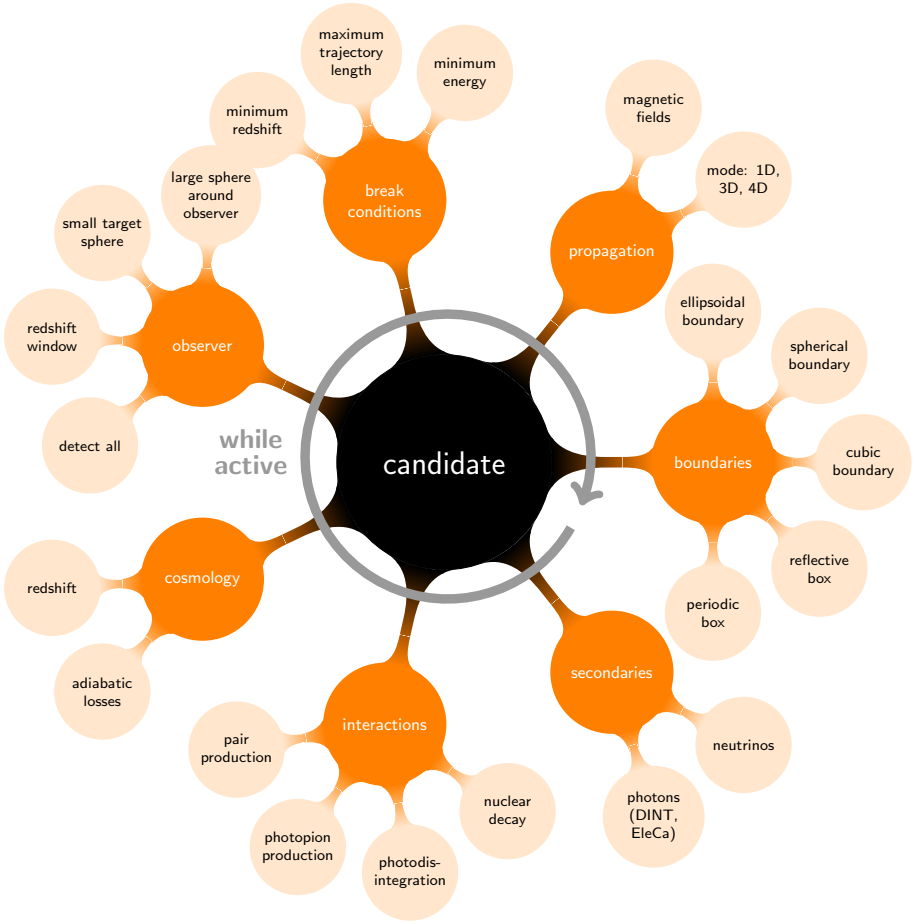

Figure 5.2: An overview of the modular structure of CRPropa. Each module acts independently on the 'Candidate' class. The procedure is repeated while the candidate is still active.

Starting at the source, at each step k with size Δx_k a random distance is dialed and compared with the mean free path (λ). It is assumed that λ is constant within each step, which is a good approximation for $\Delta x_k \ll \lambda$. Moreover, it is assumed that the energy losses due to different interactions can be factorized. If a cosmic ray has energy E_k at step k, for each interaction the probability of occurrence is drawn from a uniform distribution, and a distance x_r is calculated, as follows:

$$x_r = -\lambda \ln r, \tag{5.1}$$

where r is a random number in the interval [0,1]. If $x_r < \Delta x_k$ nothing occurs in this step and Δx_{k+1} (the next step size) is limited to a fraction of λ. Otherwise an interaction takes place within this step, and the information of the cosmic ray, including the energy lost due to the interaction in question, is updated in the 'Candidate' class. This occurs for all stochastic energy losses. In the continuous energy losses approximation the energy loss per step is calculated using the formula

$$\Delta E_k = \frac{dE}{dx} \Delta x_k, \tag{5.2}$$

where dE/dx is the energy loss length for the interaction. In CRPropa 3 pair production and the adiabatic expansion of the universe are considered continuous energy loss processes, whereas photopion production and photodisintegration are assumed to be stochastic. For each secondary nuclei stemmed by photodisintegration the above described algorithm is recursively applied.

Magnetic deflections are calculated in each step by integrating the equations of motion in the phase space $(\vec{r}, \vec{p})$, with $\vec{r}$ and $\vec{p}$ designating, respectively, the position and momentum. The equations of motion read

$$\begin{cases} |\vec{p}|\,\dot{\vec{r}} = c\vec{p} \\ \dot{\vec{p}} = q\left|\dot{\vec{r}} \times \vec{B}\right|. \end{cases} \tag{5.3}$$

where q is is the charge of the cosmic ray and $\vec{B}$ the magnetic field. These equations are solved using a 5th-order Runge-Kutta method with Cash-Karp coefficients [437]. This method is adequate for variable step size algorithms, as is the case. A minimum and maximum step size are provided by the user, and the maximum value is used whenever possible, for efficiency reasons. When controlling the step size a relative error is estimated and should be smaller than the designated tolerance.

To assess the relative errors introduced by the numerical solution of the equations of motion, the positional and directional errors were estimated in the simple scenario of a uniform magnetic field with magnetic field strength B and Larmor radius R_L. After propagating a distance D the directional $(\Delta\delta)$ and positional (R/R_L) errors were estimated, as a function of the propagated distance in units of Larmor length $(2\pi R_L)$. These are shown in figure 5.3, together with the number of steps required to achieve the desired precision. It is remarkable that the positional error is smaller than 10^{-3} for a tolerance smaller than $\sim 10^{-5}$, as shown in the right panel of this figure, indicating that CRPropa can handle trajectories with good precision.

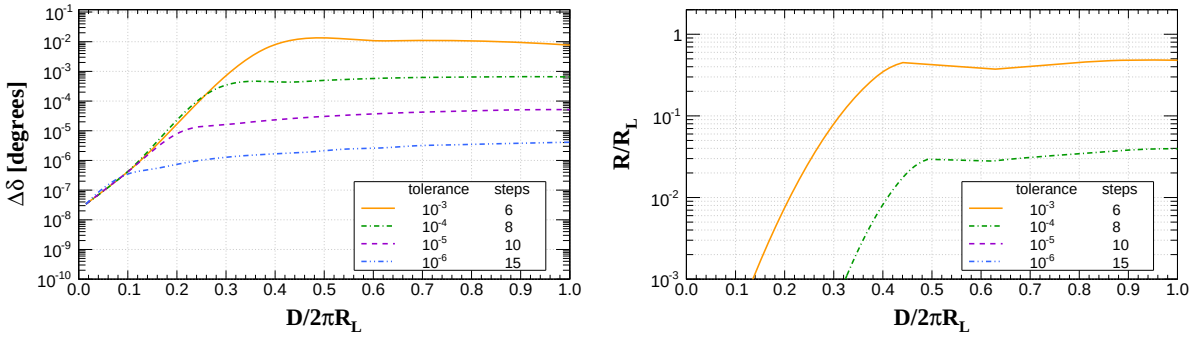

Figure 5.3: Directional (left panel) and positional (right) errors, as a function of the propagated distance (D) in units of Larmor length ($2\pi R_L$). Here $\Delta\delta$ designates the error in the deflection, and $R = |\vec{R}|$ the position. In the plots the number of steps required to achieve the results with the required tolerance are also indicated. In the right panel the curves for tolerances of 10^{-5} and 10^{-6} cannot be seen, although they are indicated in the legend, because they are below 10^{-12} in the whole interval displayed.

The algorithms for detection will be discussed in details in section 5.6.

5.4 Interaction and energy losses

5.4.1 Pair production

Let E be the energy of a nucleus of atomic number Z and mass A. The rate of energy loss of a given nucleus is the same rate at which electrons/positrons gain energy if the energy of the background photon is much smaller than the rest mass of electrons/positrons, so that it can be neglected. Hence

$$-\frac{dE}{dx} = \alpha r_0^2 Z^2 (m_e c^2)^2 \int_2^\infty d\xi n\left(\frac{\xi m_e c^2}{2\gamma}\right)\frac{\phi(\xi)}{\xi^2}, \tag{5.4}$$

where $\phi(\xi)$, displayed in figure 5.4, can be obtained from the cross section, as in ref. [358].

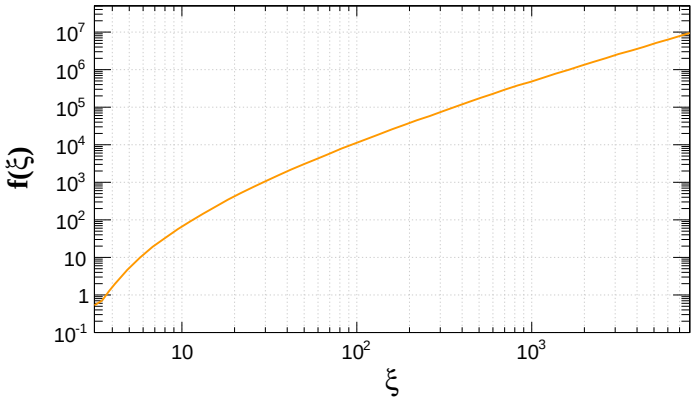

Figure 5.4: Function $f(\xi)$ show in equation 5.4, as defined in Blumenthal [358].

In the particular case of the CMB equation 5.4 reduces to

$$-\frac{dE}{dx} = \frac{\alpha 8\pi r_0^2 Z^2 (m_e c^2 k_B T)^2}{\hbar^3 c^3} f(\varepsilon), \tag{5.5}$$

with $f(\varepsilon)$ given by

$$f(\varepsilon) = \left(\frac{2\pi\varepsilon}{\hbar}\right)^2 \int_2^\infty d\xi \frac{\phi(\xi)}{e^{\varepsilon\xi/h} - 1}, \tag{5.6}$$

where ε is the energy of the background photon.

The threshold energy for pair production for a nucleus ${}^A_Z X$ is

$$E_{thr} = \frac{m_e(m_X + m_e)}{\varepsilon} \approx 4.8 \times 10^{14} A \frac{\text{eV}}{\varepsilon}\ \text{eV}, \tag{5.7}$$

where m_X can be directly obtained from the mass number A. Consequently, for a microwave photon with energy $\varepsilon \sim 1\,\text{meV}$, the threshold energy for this process is approximately $E_{thr} \approx 5 \times 10^{17}\,\text{eV}$.

Even though the mean free path for pair production is relatively small, so is the energy loss per interaction. Furthermore, the inelasticity is $\eta \sim 10^{-3}$. Consequently, in CRPropa this process is treated as a continuous energy loss.

The energy loss length, defined as $\left|\frac{1}{E}\frac{dE}{dx}\right|$, can be calculated for the case of protons using equation 5.4. For a nucleus ${}^A_Z X$ it can be rescaled as

$$\left(\frac{1}{E}\frac{dE}{dx}\right)_{{}^A_Z X} = \frac{Z^2}{A}\left(\frac{1}{E}\frac{dE}{dx}\right)_p. \tag{5.8}$$

5.4.2 Photopion production

Photopion production occurs when a nucleon scatters off a background photon. The two main interaction channels for protons are:

$$p + \gamma \to \Delta^+ \to \begin{cases} p + \pi^0 \\ n + \pi^+ \end{cases},$$

and for neutrons the dominant one is

$$n + \gamma \rightarrow \pi^- + p.$$

The energy threshold for photopion production is

$$E_{thr} = \begin{cases} \dfrac{m_{\pi^-}(m_n + 0.5 m_{\pi^-})}{2\varepsilon} \\ \dfrac{m_{\pi^0}(m_p + 0.5 m_{\pi^0})}{2\varepsilon} \end{cases} \approx 6 \times 10^{22} \dfrac{\text{eV}}{\varepsilon}\ \text{eV}. \tag{5.9}$$

Hence for a microwave photon of energy $\varepsilon \sim 1\,\text{meV}$, $E_{thr} \approx 6 \times 10^{19}\,\text{eV}$, which is roughly the energy of the GZK cutoff, described in chapter 2.

In CRPropa photopion production in handled by the SOPHIA code [369]. In this case the total cross sections for proton-gamma and neutron-gamma scattering[5] as a function of the energy of the photon in the nucleus rest frame (ϵ') are shown in figure 5.5. These cross sections are obtained from SOPHIA[6], and correspond to the sum of all relevant processes including baryon resonances, multipion production and diffractive scattering.

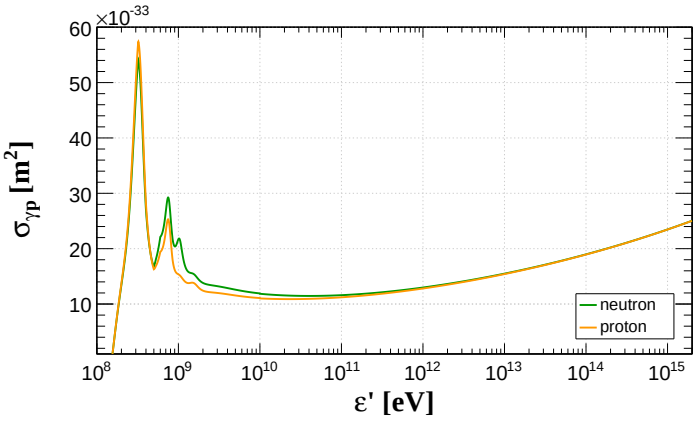

Figure 5.5: Total cross sections for $p\gamma$ and $n\gamma$ scattering, as a function of the photon energy in the nucleus rest frame.

The mean free path for photopion production by a nucleus of energy E, charge Ze and mass number A, $\lambda_{A,Z}$, is written in terms of the mean free path for protons (λ_p) and neutrons (λ_n):

$$\lambda_{A,Z} \approx 1.18 \left[\frac{Z^a}{\lambda_p(E/A)} + \frac{(A-Z)^a}{\lambda_n(E/A)} \right]^{-1}, \tag{5.10}$$

where $a = 2/3$ if $A \leq 8$, or $a = 1$ otherwise. This definition is the same as the one used in CRPropa 2. As discussed in ref. [6], this approximation does not take into account Fermi motion within the nucleus, nor spectral changes in the resonances. Nevertheless this approach introduces a bias in the cross sections smaller than 20% in the energy range of interest.

5.4.3 Photodisintegration

The interaction of atomic nuclei with background photons causes these nuclei to split into parts, through a photodisintegration process. Early studies of photon-nuclei interactions at high energies were

[5] For a more detailed review on production of mesons from nuclei-gamma interactions see ref. [438]

[6] In SOPHIA [369] the interactions can be interpreted in terms of reggeons and pomerons exchanges, following the cross sections parametrizations from ref. [439].

conducted by Danos and Fuller [440] and Hayward [441]. In the context of UHECRs, a pioneer work on photodisintegration of nuclei by Puget *et al.* [442] and later revisited by Kahn *et al.* [443].

In CRPropa 3 photonuclear cross sections are obtained from the TALYS 1.6 code [444], unlike CRPropa 2 which uses an older version of TALYS (1.0). TALYS can be used to predict photodisintegration products of the exclusive channels: proton (p), neutron (n), deuterium (^2H), tritium (^3H), helium-3 (^3He) and helium-4 (^4He, or alpha particle, α). Cross sections obtained in TALYS use the default setting suggested by ref. [443]. When available, experimental data containing relevant nuclear data are used. Otherwise theoretical models such as potentials for nucleon and alpha particle optical models, as well as global nuclear level descriptions are employed[7].

Nuclei with $A < 12$ (except for ^6Li and ^{8}Be) are not treated with TALYS. Their cross sections are taken from other references, summarized in table 5.1.

Table 5.1: References for the photodisintegration cross sections for nuclei with $A < 12$. Table extracted from ref. [447].

nucleus	reference	details
^2H	Rachen [448]	
^3H	Rachen [448]	rescaled by factor 1.7
^3He	Rachen [448]	rescaled by factor 0.66
^4He	Rachen [448]	
^7Li	measurements [449, 450]	interpolation of measured data
^8Li	GEANT 4 [451]	loss of neutron
^9Li	GEANT 4 [451]	loss of neutron
^7Be	GEANT 4 [451]	loss of proton
^9Be	Rachen [448], Ahrens [452]	parametrization from [448], refitted with data from [452]
^{10}Be	GEANT 4 [451]	loss of neutron
^{11}Be	GEANT 4 [451]	loss of neutron
^8B	GEANT 4 [451]	loss of proton
^{10}B	GEANT 4 [451]	loss of neutron and proton
^{11}B	GEANT 4 [451]	loss of neutron
^9C	GEANT 4 [451]	loss of proton
^{10}C	GEANT 4 [451]	loss of proton
^{11}C	GEANT 4 [451]	loss of proton

From the individual cross sections of exclusive channels the total cross sections are obtained, as well as the number of channels for each nucleus-photon interaction. The total number of disintegration channels obtained from TALYS output is then thinned aiming to optimize the computational performance by reducing memory consumption. Only channels with cross sections larger than 0.01 of the total cross section, for the whole energy range, are kept. Consequently, the total cross section is not significantly affected by this cut. In total 7649 channels are used. In figure 5.6 total cross sections for many nuclei, as a function of the photon energy in the nucleus rest frame (ε') are shown.

As expound in ref. [443], one of the main sources of uncertainties in the evaluation of photonuclear cross sections is the calculation of transmission coefficients, related to the probability of a given compound nucleus to be excited by photoabsorption. At ultra-high energies the transmission function is dominated by the E1 transition which is estimated based on the classical representation of the giant dipole resonance (GDR) as a lorentzian function, given by [443]

$$\mathcal{T}_{E1}(\varepsilon') = \frac{8Z(A-Z)}{3A}\frac{e^2(1+\chi)}{\hbar mc^3}\frac{\Gamma(\varepsilon')\varepsilon'^4}{\Gamma^2(\varepsilon')\varepsilon'^2 + (\varepsilon'^2 - \mathcal{E}_{GDR}^2)^2}, \tag{5.11}$$

[7] A detailed description of these models are presented in refs. [445, 446].

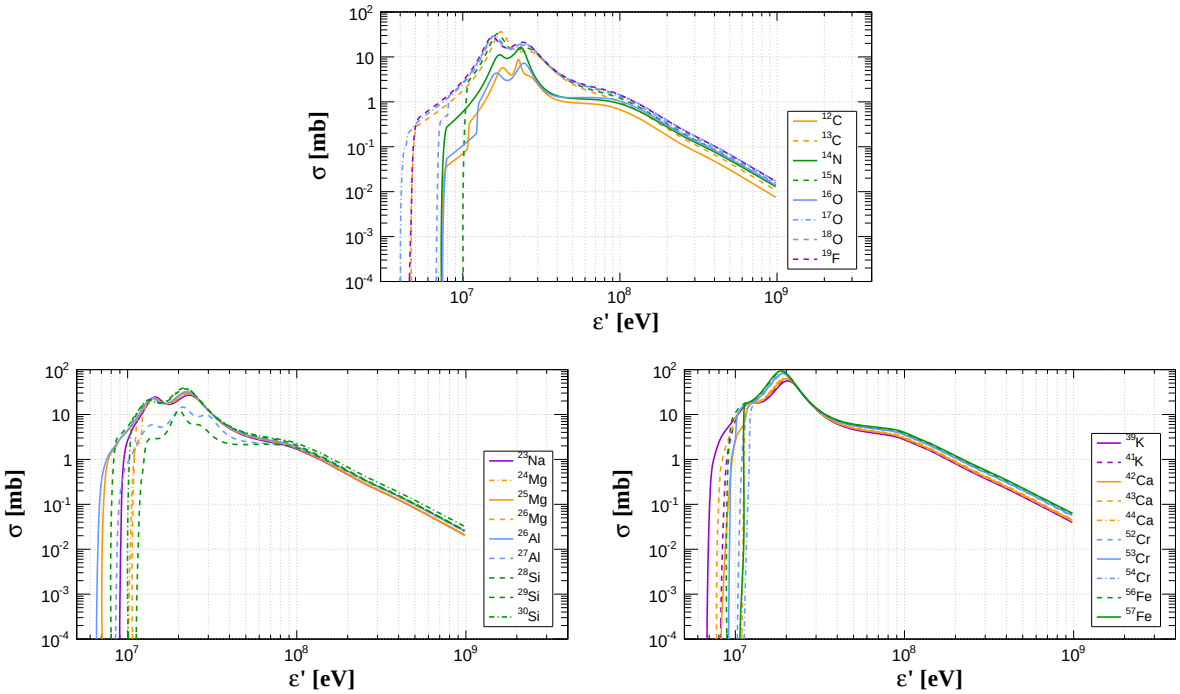

Figure 5.6: Total cross sections for nucleus-photon collisions for various isotopes, obtained from TALYS 1.6. Most of these isotopes are stable. The x-axis is the energy of the photon in the rest frame of the nucleus.

where

$$\Gamma(\varepsilon') = \Gamma_{GDR}\frac{\varepsilon'^2}{\mathcal{E}_{GDR}^2}, \tag{5.12}$$

with $\mathcal{E}_{GDR}$ and Γ_{GDR} designating, respectively, the energy and width of the GDR, and m the nucleon mass. $\chi \approx 0.2$ is introduced to account for exchange force contribution in the dipole sum calculation. This model[8] is an improved version from previous formulations [454] where $\Gamma(\varepsilon') = \Gamma_{GDR}$, and is presented in ref. [455]. A description of its shortcomings and possible refinements, as well as impact on photodisintegration rates, can be found in ref. [443].

Two processes are relevant for photonuclear interactions at ultra-high energies: the giant dipole resonance (GDR) and quasi-deuteron (QD) processes. The total cross section is essentially the combination of these two [456, 457], i.e.:

$$\sigma_t(\varepsilon') = \sigma_{GDR}(\varepsilon') + \sigma_{QD}(\varepsilon'), \tag{5.13}$$

where σ_{GDR} can be obtained from eq. 5.11 [453]

$$\sigma_{GDR}(\varepsilon') = \sum_{i=1}^{N}\sigma_{E1}\frac{\Gamma^2(\varepsilon')\varepsilon'^2}{\Gamma^2(\varepsilon')\varepsilon'^2 + (\varepsilon'^2 - \mathcal{E}_{GDR}^2)^2}, \tag{5.14}$$

where N is the total number of parts in which the GDR is split, and i the index corresponding to each part.

For E1 transitions, which dominate the GDR in the energy range of interest, the parameters for different nuclei are obtained from the standard TALYS database. For some nuclei no data for E1 transitions

[8] The complete description includes a term which depends on the nuclear temperature, as shown in ref. [453]. However, as pointed out in ref. [443], in the case of photoabsorption these terms essentially vanish because the temperature can be deemed as null.

exist. In this case TALYS adopts the parametrization for the cross section from ref. [453]:

$$\sigma_{E1} = 144\frac{(A-Z)Z}{A}\frac{1}{\pi\Gamma_{E1}}\,\text{mb}. \tag{5.15}$$

The E1 transition energy ($\mathcal{E}_{GDR}$) is

$$\mathcal{E}_{E1} = (31.2A^{-1/3} + 20.6A^{-1/6})\,\text{MeV}, \tag{5.16}$$

and Γ_{E1} is

$$\Gamma_{E1} = 0.026\mathcal{E}_{E1}^{1.91}\,\text{MeV}. \tag{5.17}$$

Notice that if the GDR is not split, then $\mathcal{E}_{E1} = \mathcal{E}_{GDR}$, and $\Gamma_{E1} = \Gamma_{GDR}$. Formulas for transition radiation for higher order multipoles are presented in ref. [453], following ref. [458].

The cross section for the quasi-deuteron component (σ_{QD}) is given by

$$\sigma_{QD}(\varepsilon') = L\frac{(A-Z)Z}{A}\sigma_d(\varepsilon')f(\varepsilon'), \tag{5.18}$$

where $L = 6.5$ is the Levinger parameter, and σ_d is the deuteron photodisintegration cross section, parametrized to match experimental data. Above a threshold energy of 2.224 MeV, the cross section is approximated by

$$\sigma_d(\varepsilon') = 61.2\left(\frac{\text{MeV}}{\varepsilon'}\right)^3\left(\frac{\varepsilon'}{\text{MeV}} - 2.224\right)^{\frac{3}{2}}\,\text{mb}, \tag{5.19}$$

being 0 below this threshold. The function $f(\varepsilon')$ is the Pauli-blocking function, whose parametrization is also given in ref. [453] for different energy ranges, and reads:

$$f(\varepsilon') = \begin{cases} \exp\left(-q_1/\varepsilon'\right) & \text{if } E < 20\,\text{MeV} \\ p_0 + p_1\varepsilon' + p_2\varepsilon'^2 + p_3\varepsilon'^3 + p_4\varepsilon'^4 & \text{if } 20 < E < 140\,\text{MeV} \\ \exp\left(-q_2/\varepsilon'\right) & \text{if } E > 140\,\text{MeV} \end{cases}, \tag{5.20}$$

with $q_1 = 24.2348$, $q_2 = -73.30$, $p_0 = 8.3714 \times 10^{-2}$, $p_1 = -9.8343 \times 10^{-3}$, $p_2 = 4.122 \times 10^{-4}$, $p_3 = -3.4762 \times 10^{-6}$ and $p_4 = 9.3537 \times 10^{-9}$.

There are significant differences in the interaction rates obtained from these two versions of TALYS, as can be seen in figure 5.7. These differences are more relevant for stable intermediate mass nuclei such as ^{12}C, ^{14}N, ^{16}O, ^{27}Al, and small for other isotopes of these elements, as can also be seen in this figure.

One of the main differences from TALYS 1.0, used in CRPropa 2, and TALYS 1.6, used in CRPropa 3, are the higher energy extensions. Previous version were limited to a photon energy (in the nucleus rest frame) of $\varepsilon' \lesssim 250\,\text{MeV}$. As described in ref. [459], the extension to $\varepsilon' \sim 1\,\text{GeV}$ requires further improvements in the description of the optical model potential, as well as adequate binning for residual nuclides in the reaction chain.

5.4.4 Nuclear decay

At ultra-high energies unstable nuclei can be produced through photodisintegration or photopion production. The typical distance (ℓ) that a nucleus propagate before decaying depends on its lifetime (τ) and Lorentz factor (γ), as follows:

$$\ell = \gamma\tau. \tag{5.21}$$

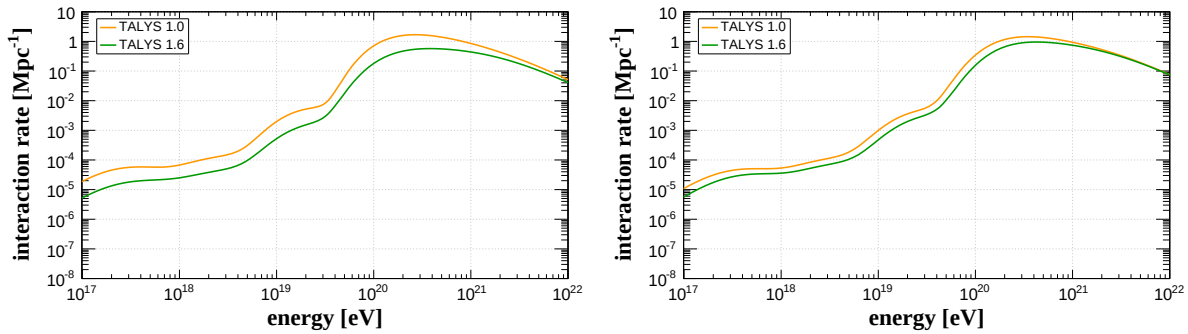

(a) ^{12}C (b) ^{14}N

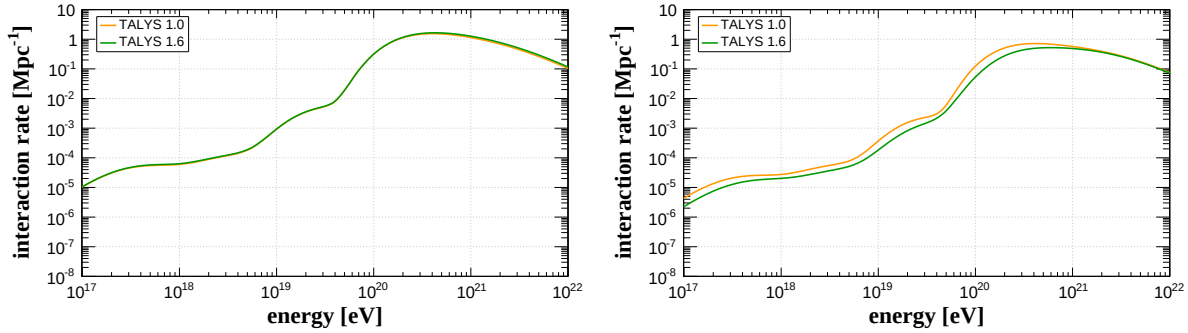

(c) ^{15}N (d) ^{16}O

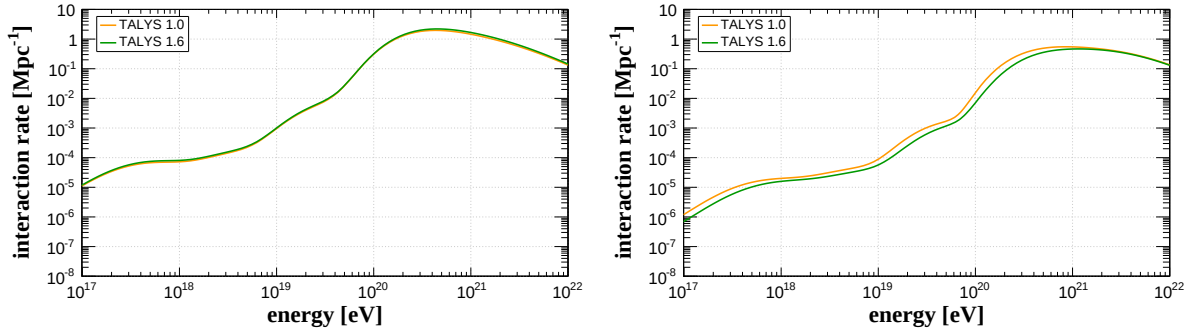

(e) ^{17}O (f) ^{27}Al

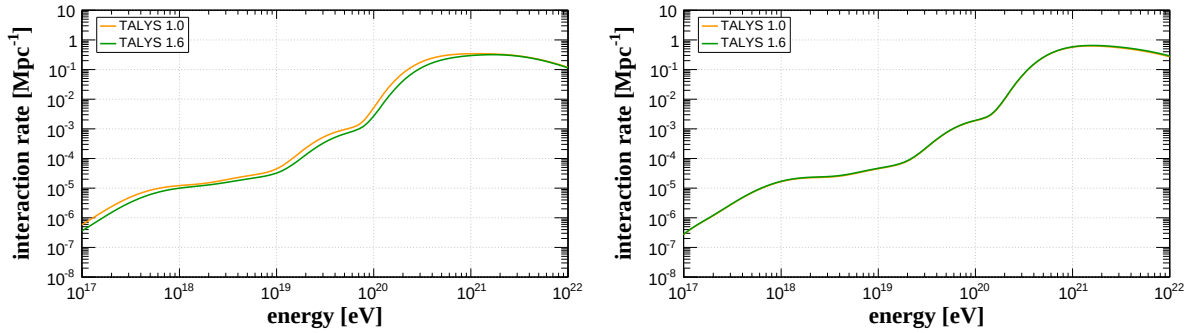

(g) ^{28}Si (h) ^{56}Fe

Figure 5.7: Comparison of the interaction rates for different nuclei obtained with TALYS 1.0 (orange curves) and TALYS 1.6 (green curves). These rates are combined from the individual rates IRB model of ref. [45], and the CMB.

Some nuclei have a finite and often small lifetime, as shown in figure 5.8.

The main processes through which a nucleus of atomic number Z and mass A decay are nucleon

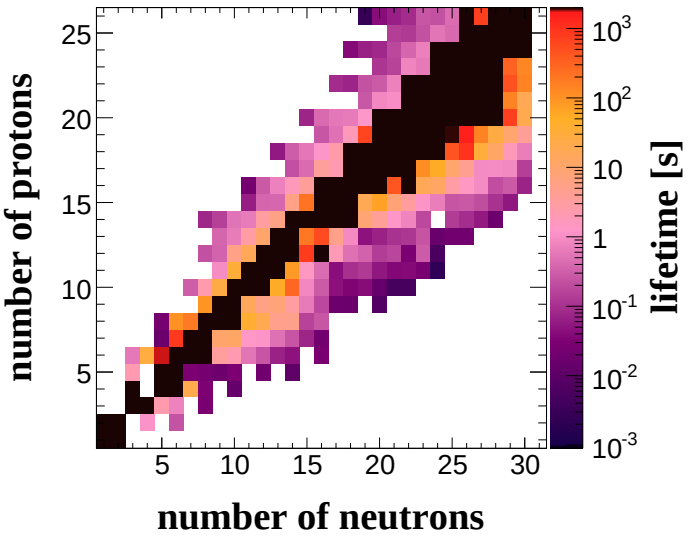

Figure 5.8: Lifetime of nuclei. Stable nuclei are indicated in black. Data taken from NuDat 2.6 database.

dripping, beta decays (both beta plus and beta minus), and alpha decay. The combination of number of neutrons and protons which stems each of these processes is shown in figure 5.9.

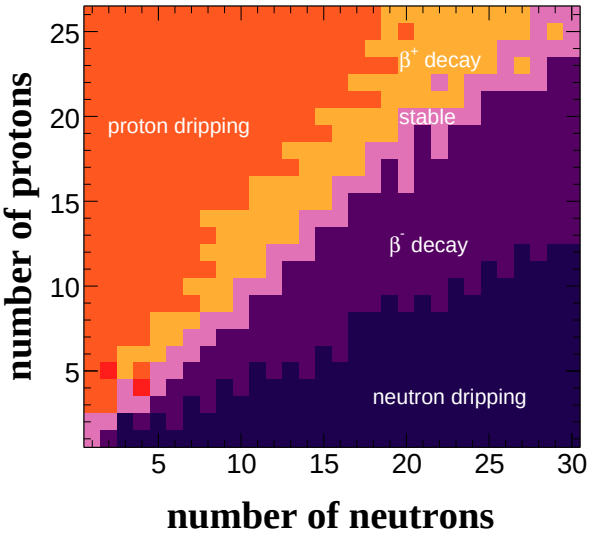

Figure 5.9: Nuclear decay modes for different combinations of proton and neutron numbers.

Alpha decay is the well-known radioactive process which consists on the emission of an alpha particle (or a helium-4 nucleus) by a nucleus. For a generic nucleus ${}^{A}_{Z}X$ it can be written as

$$ {}^{A}_{Z}X \rightarrow {}^{A-4}_{Z-2}X' + {}^{4}_{2}\alpha, $$

where X' symbolizes the new nucleus, and ${}^{4}_{2}\alpha$ is an alpha particle. In this case the daughter-nucleus is assumed to have the same Lorentz factor as the parent-nucleus, which is a good approximation if the binding energy per nucleon is small compared to the rest energies of the decay products.

Beta decays are typically characterized by the conversion of a neutron into a proton (beta plus decay):

$$ {}^{A}_{Z}X \rightarrow {}^{A}_{Z+1}X' + e^{-} + \bar{\nu}_e, $$

or the conversion of a proton into a neutron (beta minus decay):

$$ {}^{A}_{Z}X \rightarrow {}^{A}_{Z-1}X' + e^{+} + \nu_e. $$

Arbitrary combinations of atomic mass (A) and atomic number (Z) are, in principle, possible, despite the fact that they do not necessarily result in stable nuclei. These undergo virtually immediate decay for some combinations of number of protons and number of neutrons, emitting a proton or neutron of same isospin. This process is called nucleon dripping (or leaking). Also, as in the case of alpha decay, it is assumed to conserve the Lorentz factor of the parent-nucleus.

In CRPropa the treatment of nuclear decays is based on tabulated values obtained from the NuDat 2.6 database[9], which provides data for nuclear lifetimes, as shown in figure 5.8, as well as number of decay channels (figure 5.10), and binding energies (figure 5.11).

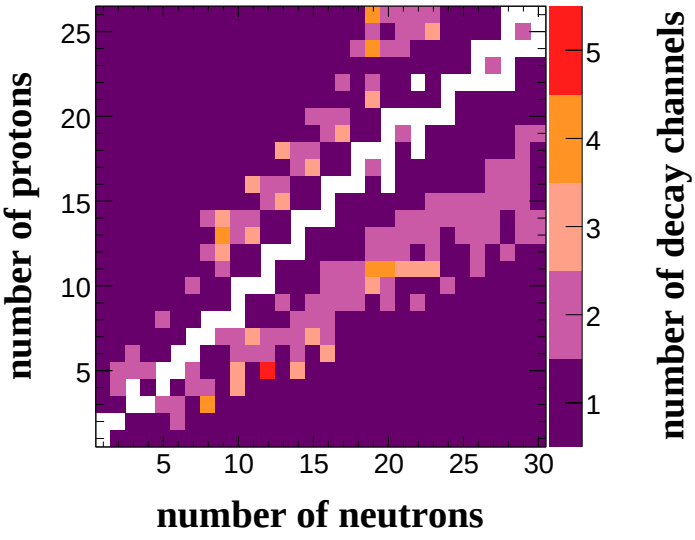

Figure 5.10: Multiplicity of the decay (color scale) for different combinations of number of protons and neutrons. White regions correspond to stable nuclei, thus having no decay channels.

5.5 Adiabatic energy losses

The expansion of the universe itself is another source of energy loss, as described in chapter 2. The change in redshift (dz) is related to the propagated distance (dx) as follows:

$$ dz = \frac{H(z)}{c} dx, \tag{5.22} $$

where H(z) is the redshift dependent Hubble constant. In numerical simulations the distance is discretized in units of $dx \approx \Delta x$, which should be much smaller than all lengths involved. In this case the change in the redshift ($dz \approx \Delta z$) is also a finite value.

[9] For details refer to the website http://www.nndc.bnl.gov/nudat2/.

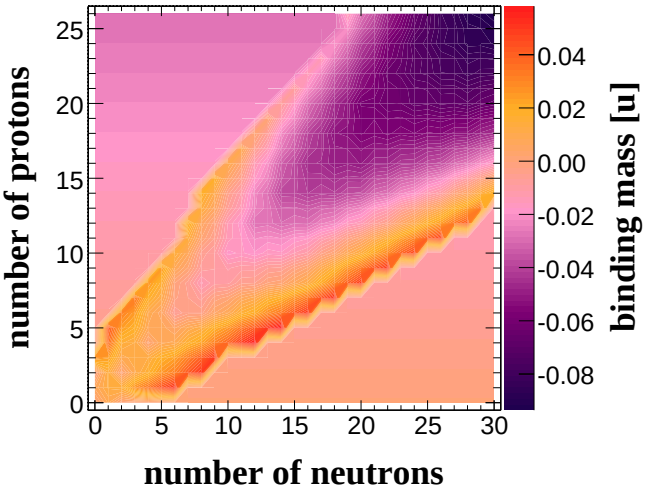

Figure 5.11: Binding energies for different nuclei.

In CRPropa this energy loss is calculated at each step. Let E_i be the energy of the particle at redshift z_k, after propagating a distance Δx_k, corresponding to redshift Δz_k. In the next step, where z_{k+1}, the new energy E_{k+1} is given by

$$\Delta E_{k+1} = E_k \frac{1 - \Delta z_k}{1 + z_k}, \tag{5.23}$$

with the condition $\Delta z_k < z_k$ strictly enforced.

5.6 Sources and Observers

In CRPropa the sources are implemented within the 'Source' class. There are seven pre-defined types of sources, namely: uniform distributions within a sphere, a box or in 1D; uniform distributon on the surface of a sphere; grid containing density of sources in each cell; individual sources; list of individual sources. These sources can emit particles in a specific direction, within a cone with a given opening angle, or isotropically. The cosmic rays are emitted with a monochromatic or power law spectrum, and one or multiple particle types can be defined. It is also possible to fix the redshift of the source(s) or dial this quantity from a uniform distribution of redshifts.

There are three types of observers implemented, one designed for detection in the 1D mode, and the others for 3D and 4D. In 3D the observer can be defined as a sphere of a given radius R_{obs}. In the 'ObserverSmallSphere' module the cosmic ray is flagged as detected if it crosses this sphere from the outside to the inside, i.e., if the position of the particle ($\vec{r}$) and the center of the observer sphere ($\vec{r}_{obs}$) satisfy the following condition

$$|\vec{r} - \vec{r}_{obs}| < R_{obs}. \tag{5.24}$$

At each step the next step size is limited to avoid overshooting. In the module 'ObserverLargeSphere' the particle is detected if

$$|\vec{r} - \vec{r}_{obs}| > R_{obs}. \tag{5.25}$$

In the 4D mode the 3D observer is used, and another detection condition has to be added. This other condition is a redshift window, which flags a particle as detected if the particle reaches the 3D observer within a given redshift interval[10].

[10] The 4D mode is a novel feature of CRPropa, and will be explained in further details in section 5.7.

5.7 The 4D mode

The interaction rates for different processes depend on the redshift at which cosmic rays interact with the pervasive photon backgrounds, because the number density of these radiation fields are evolving with the expansion of the universe. In the case of the CMB the redshift dependence can be scaled by a factor $(1+z)^2$ from its value at present time. However, for the CIB this dependence is not so simple. Unlike CRPropa 2, in which the interaction rates with the CIB at a given redshift were obtained by rescaling their present values in a similar way to the CMB, in CRPropa 3 interaction rates with the CIB are obtained through two-dimensional interpolation of tabulated values of energy and redshift. By doing so, the proper redshift evolution of this background is taken into account according to the different CIB models.

The calculation of adiabatic energy losses requires an *a priori* knowledge of the propagation length, thus the redshift. In a one-dimensional environment it is trivial, since the redshift can be directly obtained from the distance of the source to the observer. In a three-dimensional environment, however, the situation is more complex because the effective propagation length can change due to deflections caused by intervening magnetic fields and due to the redshift dependence of the photon backgrounds. In order to simultaneously take into account cosmological effects as well as deflections by magnetic fields, in CRPropa 3 a new propagation environment was introduced, which will henceforth be called the '4D mode'[11]. This new feature extends the notion of three-dimensional observer to four-dimensions, so that the observer is considered a hypervolume composed by a sphere of a given radius R_{obs} and a time (actually redshift) window of size Δz_{obs} around $z = 0$. The choice of a symmetric interval around $z = 0$ guarantees its convergence for different window sizes, compared to a simple redshift window between 0 and Δz_{obs}. Relevant values such as photon number density for $z < 0$ are obtained by extrapolation of the corresponding quantities down to the desired value.

When using the 4D mode the redshift of the sources can be set by hand, or randomly picked from a uniform distribution. The redshift window (Δz_{obs}, corresponding to Δt_{obs}) has to be smaller than all relevant time scales in which the cosmic flux could vary, unless one is interested in studies of time variability of sources, in which case the window should be as small as possible. This means that if the Hubble time is expressed by t_H, then $\Delta t_{obs}/t_H \sim 0.1$ is already a sufficient constraint if the density of background photons vary slowly within the redshift interval. Moreover, at the extreme high energy part of the spectrum ($E \gtrsim 10\,\mathrm{EeV}$) one is limited by interaction horizons, which are $\lesssim 100\,\mathrm{Mpc}$, corresponding to a small redshift ($z \lesssim 0.02$). For $E \lesssim 1\,\mathrm{EeV}$ adiabatic losses are much larger than the others, and that is the region where effects of the redshift window would be more pronounced. Aiming to check the convergence of the spectrum for different Δz_{obs} some tests were performed. The differences between $\Delta z_{obs} = 0.05$ and $\Delta z_{obs} = 0.20$ are of the order of 10^{-5} at 1 EeV and 10^{-6} at 0.1 EeV, suggesting a convergence of the spectrum for smaller Δz_{obs}.

5.8 Magnetic Fields

5.8.1 Extragalactic magnetic fields

CRPropa 3 supports a variety of pre-defined magnetic field configurations, including a uniform magnetic field, turbulent (e.g. Kolmogorov), magnetic field grid, and the novel support to large scale structure simulations through the spherical particle formalism (SPH), with the MHD code Gadget [460].

[11] "4D mode" may be a garbled nomenclature, for it is a mere generalization of the 3D tracking of particles to encompass the time dimension, not referring to 4D in the context of general relativity.

5.8.2 Galactic magnetic fields

CRPropa 3 offers, for the first time, the possibility of propagating UHECRs in the galactic space, considering deflections due to the galactic magnetic field. For now only a few models are implemented such as the logarithmic spiral by Tinyakov and Tkachev [167] (see section 1.5.4.2), and the toroidal halo field by Prouza and Šmida [168] (see section 1.5.4.3). The Jansson-Farrar model (JF12) [183, 184], previously described in section 1.5.4.4, is one of the most up-to-date models for the galactic magnetic field and is also available.

The typical scale for galactic propagation is $\sim$ kpc, which is much smaller than the extragalactic distance scale ($\gtrsim$ Mpc). In such small distances interactions can be neglected, for their typical mean free paths at energies $\gtrsim 10^{17}$ eV is $\gtrsim 1$ Mpc. When propagating cosmic rays from extragalactic sources to Earth it is not convenient to define an observer as small as Earth to account for both galactic and extragalactic propagation, because very few events would be detected. Since there are no stochastic processes involved in the propagation of cosmic rays with such high energies in the galaxy, lookup tables correcting the incoming arrival direction and momentum of the cosmic ray can be constructed. These "lenses" will be subject of the next section.

5.8.3 Galactic lensing

Due to the inherent difficulty in combining galactic and extragalactic propagation within a single framework, an *a posteriori* solution to account for the effects of the galactic magnetic field in the arrival direction of UHECRs is through the use of lenses. This way, the cosmic rays do not necessarily have to propagate over cosmological distances and reach a small observer in the galaxy. When they reach a $\sim$ Mpc size spherical target (observer) their arrival direction can be corrected to account for galactic deflections. For this reason in CRPropa 3 a lensing technique is applied to account for this effect. It is based on the implementation previously used in the PARSEC code [461].

Let E_i be the energy of a cosmic ray indexed by n entering the galaxy at point $\vec{P}_{eg}$ and direction $(\varphi_{eg}, \theta_{eg})$, being designated by $Q_{eg} \equiv (\vec{P}_{eg}, \varphi_{eg}, \theta_{eg})$. Let $Q_g \equiv (\vec{P}_g, \varphi_g, \theta_g)$ be the point in phase space where is observed. Let m be indexes denoting the observed direction. The directions at the edge of the galaxy and observed at Earth are represented by spheres and therefore can be pixelated into a HEALPix[12] map, so that each point $Q_{eg,n}$ can be mapped into several points of the phase space $Q_{g,m}$. The probability of a cosmic ray $Q_{eg,n}$ arriving at Earth at the phase space point $Q_{g,m}$ is denoted by ℓ_{mn}, which forms a matrix $\overleftrightarrow{\mathcal{L}}_i$, representing the lens for a cosmic ray with energy E_i. A lens for a given model is described by $\left\{\overleftrightarrow{\mathcal{L}}_1, ..., \overleftrightarrow{\mathcal{L}}_N\right\}$, with $i = 1, 2, ..., N$.

Lenses are generated by backtracking (isotropic) cosmic rays from the observer to the edge of the galaxy. The counting of all trajectories leads to a matrix $\overleftrightarrow{L}_i$ with elements l_{mn}. $\overleftrightarrow{\mathcal{L}}_i$ and $\overleftrightarrow{L}_i$ are related as follows:

$$\overleftrightarrow{\mathcal{L}}_i = \frac{1}{\max \left\| \overleftrightarrow{L}_i \right\|} \overleftrightarrow{L}_i , \tag{5.26}$$

where $\max \left\| \overleftrightarrow{L}_i \right\|$ is the maximum of unity norms.

As pointed out in ref. [461], the lensing technique leads to an uncertainty in the arrival directions inferior to 23% for a 3 EeV cosmic ray, and to 1% at 30 EeV. The uncertainty for each individual pixel is inferior to 2%.

[12] HEALPix [462] stands for Hierarchical Equal Area isoLatitude Pixelation, and is a tessellation scheme which divides the sphere in pixels of equal area. It can be obtained from http://healpix.sourceforge.net.

5.9 CIB: models and redshift dependence

CRPropa 3 provides several options CIB models. The user can choose between several predefined models, namely:

- Kneiske *et al.*(2004) [45];
- Stecker *et al.* (2006) [46];
- Dole *et al.* (2006) [47];
- Franceschini *et al.* (2008) [48];
- Kneiske *et al.*(2010) [49];
- Finke *et al.* (2010) [50];
- Gilmore *et al.* (2012) [51].

A comparison between the spectral photon density of these models can be seen in figure .

A new feature in CRPropa 3 is the redshift dependence of the infrared background. As discussed in section 1.4.2, the CIB does not scale with redshift as the CMB, since it is affected by diverse processes during structure formation. In CRPropa 2 the redshift dependence of the CIB was assumed to be similar to that of CMB, implying that interaction rates were written as

$$\frac{1}{E}\frac{dE}{dt}(E,z) = (1+z)^3 \frac{1}{E}\frac{dE}{dt}(E(1+z),0), \tag{5.27}$$

which is satisfactory as a first approach, but can induce to errors in the treatment of various photohadronic processes involving infrared photons. In a recent work by Kalashev and Kido [463], it was shown that the interaction rates can be significantly altered by this assumption. Therefore, in CRPropa 3 the treatment is complete and the photon density at redshift z is obtained by a two-dimensional interpolation of a table containing the CIB number density for different energies and redshifts. An example of the redshift dependence of the CIB can be seen in figure 5.12

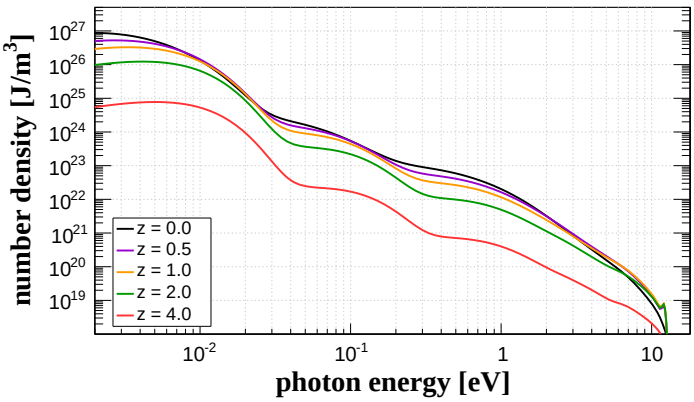

Figure 5.12: Example of redshift dependent CIB for the model by Finke *et al.* [50].

5.10 Applications

5.10.1 1D propagation with secondaries

As an application of CRPropa within a multimessenger approach, the propagation of UHECRs and the photon and neutrino counterparts is simulated. It is assumed a uniform distribution of sources emitting UHE protons with spectrum $dN/dE \propto E^{-2}$. The infrared background model assumed is the one by Kneiske *et al.* [45]. The secondary photons and neutrinos spectra produced from the interaction of protons with background photons were also computed. The spectra for cosmic rays and secondaries are shown in figure 5.13. In this figure data from the Pierre Auger Observatory [252] are displayed for the sake of comparison.

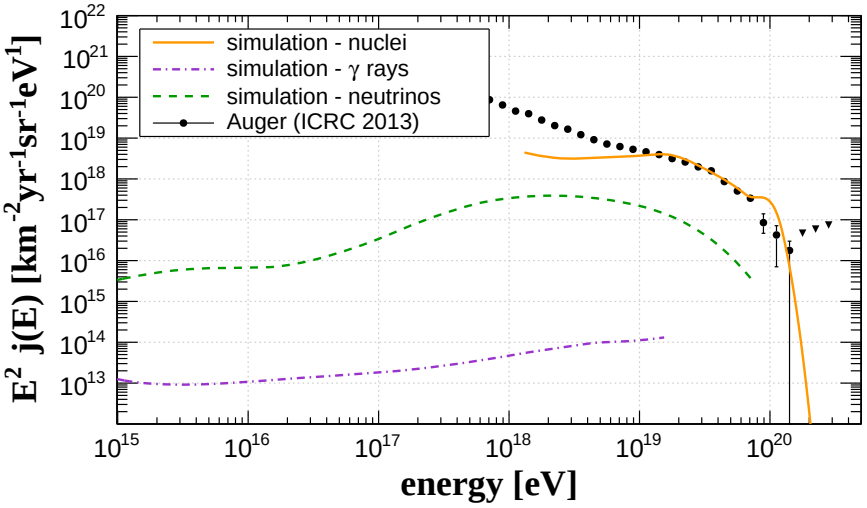

Figure 5.13: Simulated UHECR (solid line) and secondary gamma ray (dot-dashed line) and neutrino (dashed line) spectra. The markers correspond to the Auger 2013 spectrum [252].

5.10.2 3D propagation

To exemplify the propagation of cosmic rays in a three-dimensional environment a "benchmark" scenario is used [464]. In this scenario cosmological simulations from refs. [424, 425, 465] are adopted. The results of a three-dimensional simulation are presented. The large scale matter distribution from Dolag *et al.* [425, 465], constrained in such a way as to reproduce the observational data from cosmological surveys, namely the PSCz catalog [466]. This box, henceforth called matter distribution grid, is a cubic grid of approximately 132 Mpc with a spacing of ∼300 kpc. Instead of using the magnetic field distribution from this MHD simulation, the one from Miniati [424][13] is used for the propagation of UHECRs. The Miniati model has a higher magnetic field strength compared to Dolag *et al.*. The profile magnetic field-density distributions from the Miniati simulation is used to obtain a relation between magnetic field and density, which is then written into a modulation grid by replicating the matter distribution grid, replacing the density in each cell by the corresponding magnetic field strength obtained from the profile. The modulation grid has 256^3 cells covering a volume of approximately $(132\ \mathrm{Mpc})^3$. It is used to modulate another 256^3 grid with volume $\approx(13.2\ \mathrm{Mpc})^3$ containing a realization of a turbulent Kolmogorov field with coherence length 500 kpc, periodically repeated to cover the complete simulation volume.

[13] This MHD simulation has been used in several other works e.g. [467, 468].

To illustrate the propagation including effects of magnetic fields and matter distribution it is assumed a scenario composed by four species of atomic nuclei, namely hydrogen, helium, nitrogen and iron, with fractions 1, 0.5, 0.25 and 0.125, respectively. The sources follow the large scale distribution from Dolag *et al.* [425] (model 'mhdz'), and emit particles with a differential spectrum proportional to $E^{-1.8}$. The maximum rigidity of the source is $\mathcal{R}_{max} = 10^{19.8}$ V. The maximum trajectory length considered was 2 Gpc.

In figure 5.14 the cosmic ray spectrum above 10^{18} eV is shown.

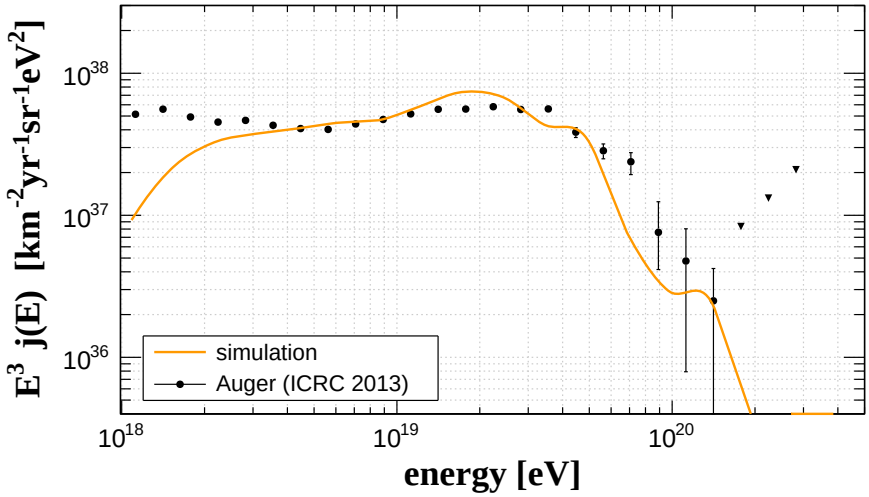

Figure 5.14: UHECR spectrum for the simulated scenario. The line correspond to the simulated scenario, and the markers to measurements from the Pierre Auger Observatory [252].

The mass composition of the observed particles is expected to be different from the injected one, due to photodisintegration. In terms of experimental observables, a change in composition implies a change in the depth of the shower maximum ($\langle X_{max} \rangle$). In figure 5.15 the values of $\langle X_{max} \rangle$ and $\sigma(X_{max})$ for this scenario are shown. They were estimated using the parametrization from ref. [469], assuming the EPOS-LHC hadronic interaction model [301].

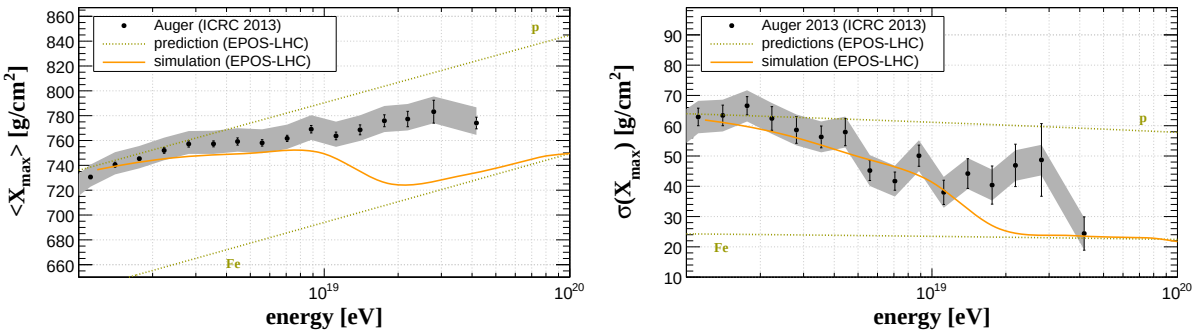

Figure 5.15: Estimated X_{max} and $\sigma(X_{max})$ for the simulated data (orange line). Black markers correspond to data measured by the Pierre Auger Observatory [252], and gray regions are systematics uncertainties. Dotted lines are the predicted composition for pure proton and pure iron scenarios, according to the EPOS-LHC hadronic interaction model.

The skymaps containing the arrival directions of the simulated events are shown in figure 5.16 considering only extragalactic deflections and including effects of the galactic magnetic field according to the model by Jansson & Farrar [183, 184].

The 4D mode will be illustrated in chapter 7.

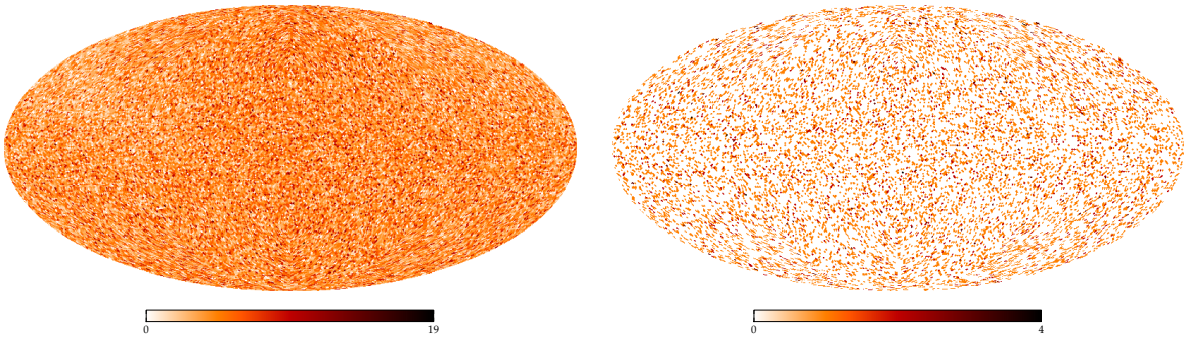

Figure 5.16: Skymaps for the simulated scenario without (top) and with (bottom) the effects of the galactic magnetic field. The color scale indicates the number of events per pixel.

chapter 6

Propagation of UHECRs in the cosmic web

In this chapter results of numerical simulations of ultra-high energy cosmic ray propagation in the magnetized cosmic web, obtained through magnetohydrodynamical simulations of structure formation, are shown. The goal is not to present the simulations in details, but rather to use them to study UHECR propagation. The impact of different magnetic field seeds on the distribution of magnetic fields and trajectories of the cosmic rays is analyzed. The prospects for ultra-high energy cosmic ray astronomy are discussed in light of these results.

6.1 The simulated cosmic web

Small fluctuations in the early universe can generate a cosmic web composed by voids, filaments, sheets and clustered halos. Based on a set of initial conditions, grid-based magnetohydrodynamics can be solved with gravitational evolution, including the most relevant astrophysical processes. MHD simulations using RAMSES [470] were performed. RAMSES is a multiresolution adaptive mesh refinement (AMR) code which allows higher resolution in regions where the density is higher.

The simulation code can be divided essentially in two parts. The dynamical core ensures the conservation of relevant quantities (energy, momentum) and the no monopole condition ($\vec{\nabla} \cdot \vec{B} = 0$), and at the same time provides a framework to solve ideal MHD. The second part is related to the parameterizations of physical processes, including source and sink terms, heating and cooling, as well as other relevant terms. Grid scale processes such as chemical reactions, convection and others are included in this part, as well as subgrid processes such as formation of astrophysical objects, feedback, turbulence, dynamos, and others.

Five MHD simulations were done [471], changing the initial conditions of the magnetic fields and the resolution. The size of the comoving simulation volume is $(200\mathrm{h}^{-1}\ \mathrm{Mpc})^3$, where $h \approx 0.7$ is the normalized Hubble constant. The initial number of dark matter particles of the grids are 256^3 and 512^3, and the resolution of each cell is refined up to 10 levels. This implies a minimum cell size of approximately 760 pc/h for a 256^3 grid, and 380 pc/h for a 512^3 grid. The details of the grids are shown below:

- grid A: fiducial run with 256^3 dark matter particles;
- grid B: run with 256^3 dark matter particles with magnetic field seed 10^5 times higher than model A;
- grid C: run with 256^3 dark matter particles and power on small scales;
- grid D: run with 256^3 dark matter particles and power on large scales;

- grid E: fiducial-like run with 512^3 dark matter particles.

In figure 6.1 the filling factors[1] of these models, together with the ones from Miniati [424] (also used in ref. [467]), Dolag *et al.* [425] and Kotera & Lemoine [279] are displayed. In figure 6.1 one can notice that

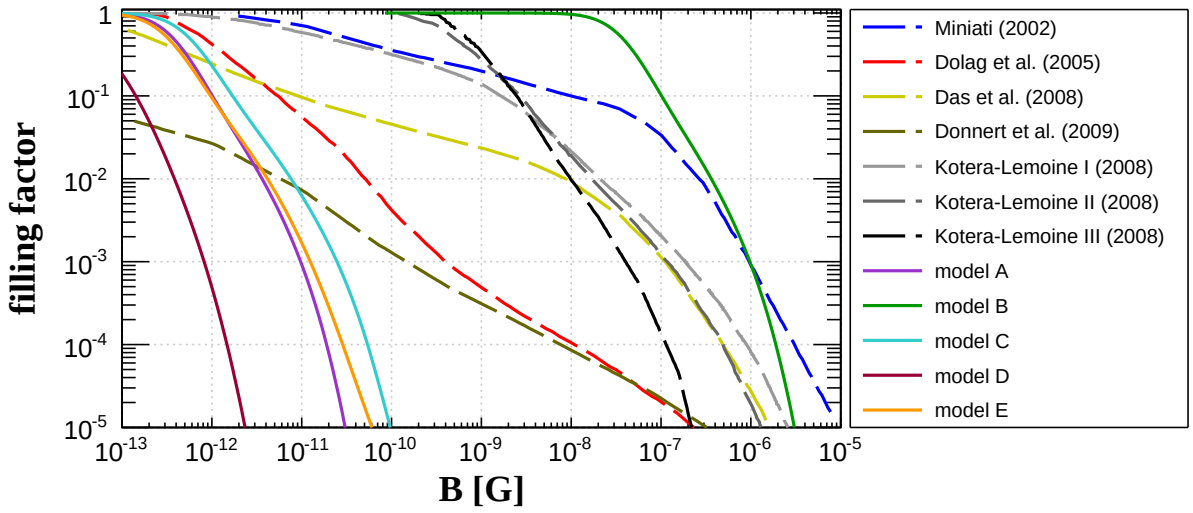

Figure 6.1: Filling factors distributions for the five models here presented (solid curves) and some others found in the literature (dashed lines). Grids A, C, D and E are normalized by a factor 10^7 of their original value, for the sake of comparison with other models, and grid B by a factor 10^5.

the discrepancy in the filling factors of different MHD simulations are huge. By comparing grids A, C and D one can see how different initial conditions for the magnetic field seed affect the distribution of magnetic field strengths. The comparison between grids A and E indicate that the increase in the resolution of the MHD simulations does not change the distribution of magnetic fields significantly. The shape of the filling factors distributions of grids A, B, C, D and E are roughly consistent with one of the models by Kotera & Lemoine [279], displayed in figure 6.1, in which $B \propto \rho^{2/3}$, where ρ is the gas density. Furthermore, by comparing the curves corresponding to the models by Miniati and Dolag *et al.* one can understand the conclusions obtained in refs. [467] and [425] regarding the possibility of UHECR astronomy. The fraction of the volume filled by magnetic fields with strengths larger than nG is much smaller in the simulation of Dolag *et al.* than in Miniati's, implying that the deflections will be much larger in the later case.

Another factor that affects the filling factors distribution is the normalization of the simulations. The normalizations can be done, for instance, using limits from primordial magnetic fields from Big Bang Nucleosynthesis (BBN) or the cosmic microwave background (CMB) implying $B_{primordial} \lesssim 1$ nG [472], or using the measured magnetic field strength in clusters of galaxies, which results on $B_{clusters} \sim 1\ \mu$G, or in the voids, through estimates based on electromagnetic cascades[2] [2], which imply that $B_{voids} \gtrsim 10^{-16}$ G. These different possibilities provide many options for normalizing filling factors distributions, but also reflect our poor knowledge of cosmic magnetic fields.

6.1.1 Checking the impact of the magnetic field normalization

Different seed magnetic fields at earlier times result on different magnetic field strengths at present time. Because the strength of cosmic magnetic fields is unknown, it would be computationally expensive to

[1] Filling factors are here defined as the fraction of the volume filled with magnetic fields larger than the reference value. This is equivalent to the complementary cumulative distribution.

[2] These constrains, however, are questioned since they rely on the existence of electromagnetic cascades in the intergalactic medium, which may not occur if plasma instabilities suppress their development [3, 4, 473].

run different simulations for different magnetic field seeds and span a large range of parameters, as would be ideal. For this reason, a test to assess the impact of the normalization of the magnetic field strength was done. Grids A and B were obtained from the same initial conditions, except for the magnetic field seed which is 10^5 times stronger in grid B. In figure 6.2 it can be clearly seen that by scaling the magnetic field by a constant factor the magnetic field in the whole simulation is essentially unaltered. In the case of UHECR propagation, which is the goal of this work, this allows the rescaling of the entire volume by a scaling factor, making it possible to study the impact of uncertainties in the magnetic field strength on the propagation of UHECRs, as shown in section 6.5.

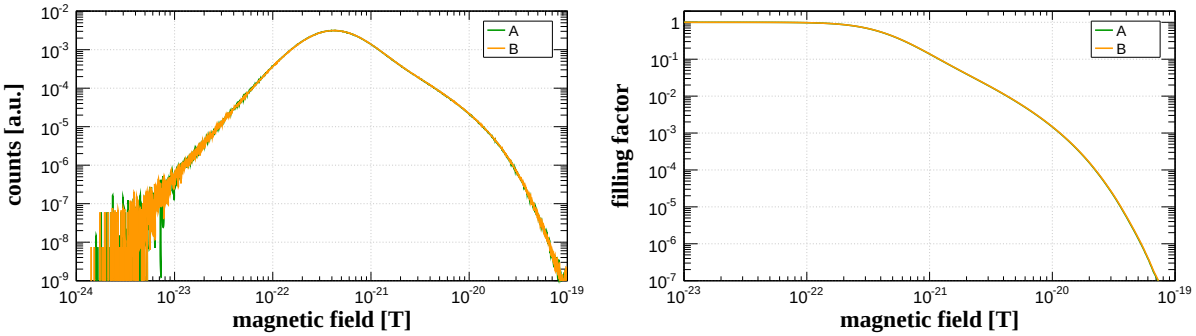

Figure 6.2: Comparison of the magnetic field distributions (left panel) and the corresponding cumulative distributions (right panel) for grids A (green line) and B (orange line).

6.1.2 Checking the convergence of the MHD simulations

A standing problem in numerical simulations of the cosmic web is related to the resolution of the grids, since a good description of some processes such as turbulent dynamo requires large resolutions [474, 475][3].

It is important to determine the required resolutions for a given task. For this reason, it is of paramount importance to analyze the convergence of grids with different resolutions, aiming to optimize the computational time (resolution should not be larger than needed) and simultaneously include all relevant physical processes that might affect the simulation outcome. A comparison of the magnetic field distributions of models A and E allow the study of the convergence of the grid, and is shown in figure 6.3. It should

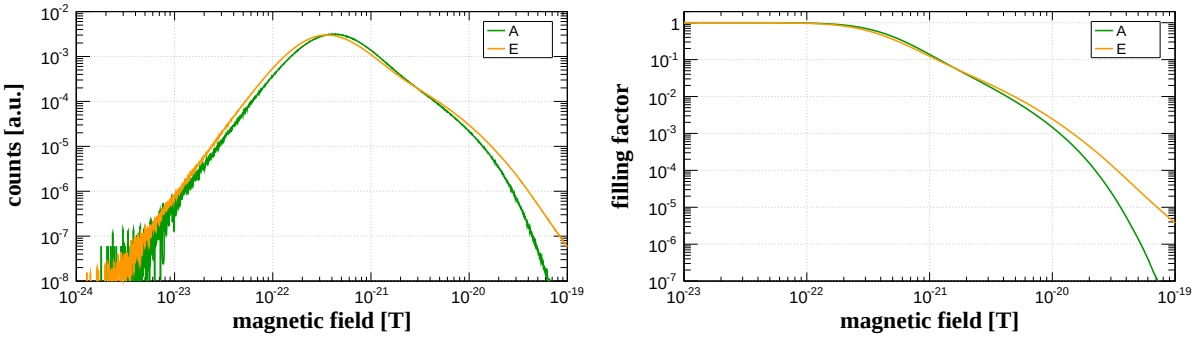

Figure 6.3: Comparison of the magnetic field distributions (left panel) and the corresponding cumulative distributions (right panel) for grids A (green line) and E (orange line).

be stressed that both simulations have the same initial conditions, the only difference being the resolution of the grids. In grids A and E, as can be seen in figure 6.3, the magnetic field distributions depend on the

[3] For a study on the impact of different resolutions on the magnetization of filaments see e.g. ref. [146].

resolution of the grids. However, as shown in the right panel, the discrepancies are visible only for filling factors smaller than 10^{-3}, and below 10^{-5}. Therefore, for the purposes of cosmic ray propagation, only for a number of events considerably larger than $\sim 10^5$ the discrepancy between the grids is relevant.

6.2 Handling AMR grids in CRPropa

The final goal of the work presented in this chapter is to use a high resolution constrained grid for UHECR propagation. The advantage of AMR over uniform-spaced grids is the very high resolution that can be achieved in relevant regions (in this case around structures). Typically a 256^3 grid with ten levels of refinement has a size ~ 20 GB. For the 512^3 grid the size is ~ 160 GB. In principle, this large memory requirement limits the usage of these grids to computers with a lot of memory. Moreover, the structure of mesh refined grid makes it rather complex to search for cells corresponding to specific locations. For this reason a new method to access AMR grids was devised. It is based on SQLite[4] databases with the information stored using R-tree structures.

R-trees [476] are data structures very useful for methods requiring multi-dimensional indexing for spatial access. They are usually used to store maps, locations, etc. Its structure also provides a fast method for neighbor searches, as shown in ref. [477].

The simulated large scale structure AMR grids obtained with RAMSES are converted into an SQLite 3 database with R-tree structure. Once the file is in SQL format, a library called SAGA[5] (SQL for AMR Grids Application) handles the grid. If CRPropa is installed with support for SAGA, then an appropriate call of the corresponding function will allow CRPropa to read and access the SQL database as any other magnetic field grid.

6.3 UHECR "tomography" of the cosmic web

A remarkable capability of UHECRs is their potential to probe the large scale structure of the universe. Whereas a true tomography of the magnetized cosmic web requires a detailed knowledge of the sources of UHECRs and the magnetization of the medium which is practically unattainable, from the simulational point of view one can grasp valuable insights on how the trajectories of charged cosmic rays are related to the distribution of magnetic fields. For instance, the deflection suffered by UHECRs over a given distance depends on the probability of these particles crossing highly magnetized regions (e.g filaments, clusters) and on the intensity of the magnetic fields pervading the intergalactic space.

As an example of UHECR "tomography" the propagation of UHE protons with energies 10^{20} eV was simulated using CRPropa. The sources were placed at the center of the grid, and the particles were flagged as detected when they crossed the sphere inscribed in these cubes from the inside to the outside. The source was assumed to emit UHECRs within a cone of angle θ, in an arbitrary direction. For this study 100 protons are emitted within each cone, and the average deflection is defined as

$$\delta = \cos^{-1}\left(\vec{p}_i \cdot \vec{p}_f\right), \tag{6.1}$$

where $\vec{p}_i$ and $\vec{p}_f$ are respectively the initial and final momenta of the particle. The magnetic field strength in the simulation volume was scaled by a factor 10^6 with respect to that of the original grid. The results are shown in figure 6.4. In figure 6.4 one can notice that by changing the value of θ the deflections of

[4] SQLite is an open source engine to handle databases. More information can be found in http://www.sqlite.org/.
[5] The code is available in https://github.com/rafaelab/saga.

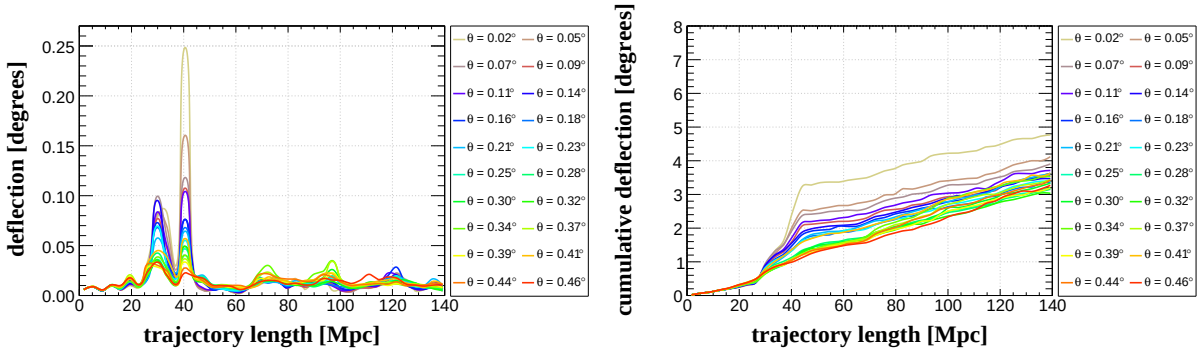

Figure 6.4: Example of UHECR tomography of the structures. The plots show the deflections (left panel) and cumulative deflections (right panel) as a function of the propagated length. UHE protons of 100 EeV are emitted within each cone with a given opening angle θ. The results are the average of the deflections of 100 particles in random directions within these cones. This particular example corresponds to grid A with magnetic field strengths scaled up by a factor 10^6.

the cosmic rays slightly change. If the source is far from the scattering centers where deflections should be larger, then the average deflection of the 100 cosmic rays will increase with θ, and vice-versa. The inclusion of energy losses will obviously change the results, but the qualitative analysis remains unaltered.

The goal of this example was to illustrate how UHECRs deflect in inhomogeneous extragalactic magnetic fields. Their deflection clearly depends on the actual contribution of regions highly magnetized such as clusters, and the average field in the voids, which fill most of the volume.

6.4 Effects of primordial magnetic field seeds

The origin of cosmic magnetic fields is still an open problem. Many magnetogenesis scenarios predict a seed magnetic field generated during processes taking place in the early universe, which are later amplified by dynamos. The distribution of magnetic fields today depends on the shape of the power spectrum of the seed magnetic fields, on the amplification mechanism, and on the redistribution of magnetic energy during structure formation, hence potentially affecting the propagation of UHECRs.

Three scenarios for the power spectrum of primordial magnetic fields were used, namely grids A, C and D. The magnetic field was normalized as in figure 6.1. In figure 6.5 the power spectra of the magnetic field seeds injected at $z = 20$ are shown, together with their values at $z = 0$.

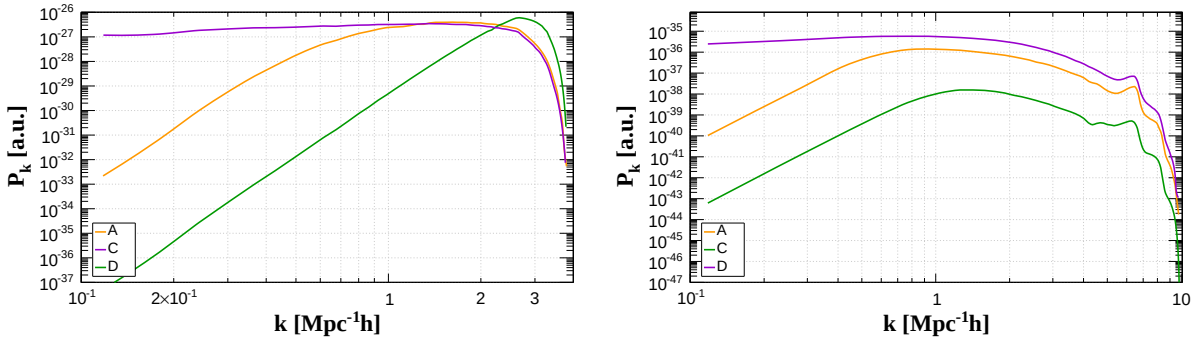

Figure 6.5: Power spectrum of injected magnetic field seed at $z \sim 20$ (left) and $z \approx 0$ (right) as a function of the comoving wave number k.

These three cosmological simulations are used for the propagation of UHE protons. As a first study all interactions and energy loss processes were neglected. The introduction of interactions and energy losses

in this analysis would quantitatively change the results, but qualitatively the conclusions would hold.

Protons are injected by sources with a differential spectrum $\propto E^{-2}$ with energies between 10^{18} and 10^{21} eV. The sources follow the large scale distribution of matter in the simulated volume, and are placed in regions with density larger than 10^{28} kg/m^3. Because the exact position of the observer is unknown, i.e. the simulation is unconstrained, the ambiguity induced by this choice of the position is removed by considering 10 observers in random located in the grids, and averaging over them. Hence the obtained results are related to the actual magnetic field distribution of these cosmological simulations rather than spurious effects of the magnetization near the observer. It is worth stressing that the redshift evolution of the simulation volume is neglected, and instead its value for $z \approx 0$ is used. Although grids A to E have high resolution, the magnetic fields are not high enough to require step sizes as small as ~ 0.1 kpc. Therefore, the step sizes used were 1 kpc (minimum) and 1 Mpc (maximum).

Using the previously described parameters simulations using CRPropa were made. The distributions of deflections for these scenarios are shown in figure 6.6. Comparing figures 6.5 and 6.6 it can be clearly

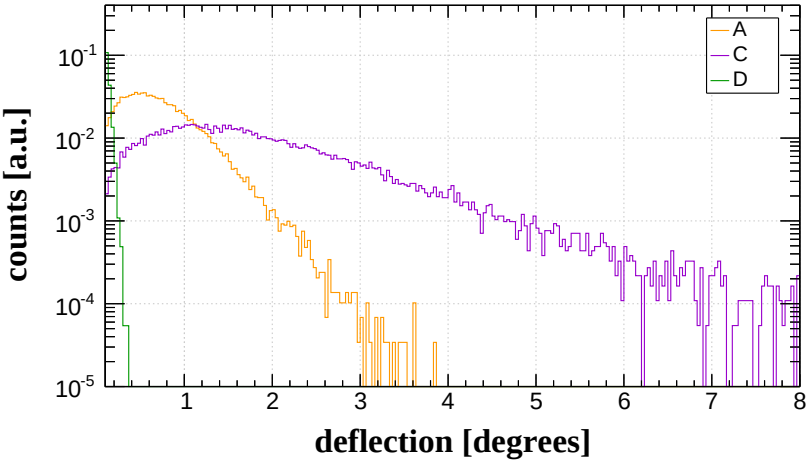

Figure 6.6: Average deflections of UHE protons in tgrids A, C and D.

seen that the heavier the small-k tail in the power spectra are, the higher are the deflections of cosmic rays and the broader its distribution. In this particular example one can see that the identification of sources of UHECRs in the case of grid D would be possible, since the deflections would be $\lesssim 10°$, which is not necessarily true for grid C due to the considerable fraction of events with deflections larger than 3°, which implies even higher deflections in the case of nuclei.

The results from figure 6.6 can be better understood by comparing the panels displayed in figure 6.7. In this figure transverse sections of grids A, C and D are shown. It can be seen that whereas in grid C structures are well-resolved, in grid D structures are not sharp. Furthermore, magnetic fields do not strongly concentrate around structures in the case of grid D. Grid A is an intermediate case, and structures can be clearly seen for this range of magnetic field strengths.

6.5 Impact of the normalization choice

6.5.1 Choice of the magnetic field normalization

In section 6.1.1 it was shown that the magnetic field strength can be scaled by an arbitrary factor without altering the distribution of magnetic fields in the simulation volumes. Because of the uncertainties

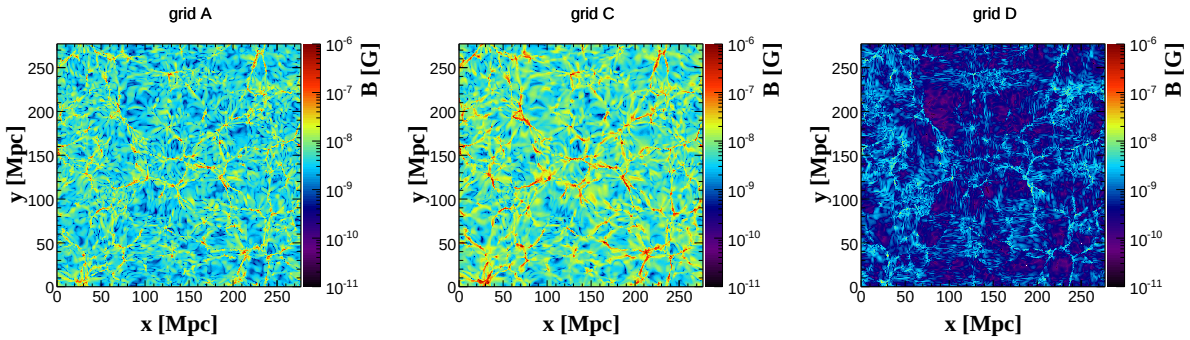

Figure 6.7: Transverse section of grids A (left), B (center) and D (right). The color scale indicates the strength of the magnetic field, and is the same for the three cases.

in the strength of magnetic fields in different regions of the universe[6], it is important to analyze the effects of different normalizations, spanning the whole parameter space. For this reason the effects of three normalizations of grid E on the propagation of UHECRs were analyzed. These three scenarios will be henceforth referred to as E_1, E_2 and E_3 (or collectively E_i) and have, respectively, the following scaling factors with respect to the original magnetic fields from grid E: 10^6, 10^8 and 10^{10}.

The choice of normalizations has to be consistent with observational constraints (see section 1.5). Using CMB data intergalactic magnetic fields have upper limits $B \lesssim 4\,\mathrm{nG}$ [81]. For the general case in which the primordial power spectrum has different spectral indexes, the most extreme constraint is $B \lesssim 50\,\mathrm{nG}$ [478]. Other constraints from spectral distortions of the CMB imply $B \lesssim 30\,\mathrm{nG}$ for coherence lengths $l_c \sim 0.5\,\mathrm{Mpc}$. Magnetic fields in the center of galaxy clusters can reach values as high as $B \sim 0.01\,\mathrm{mG}$ [130].

One can normalize magnetic field distributions using the filling factors, which indicate the fraction of the total volume filled with magnetic fields higher than a given value. Studies using data of the Sloan Digital Sky Survey (SDSS) suggest that the voids fill roughly 80% of the volume of the universe [479, 480]. This provides the first constrain for choosing the normalization: for a filling factor of 0.8, $B \lesssim 50\,\mathrm{nG}$.

The second possibility is to constrain using the filling factors and estimated magnetic field in filaments. Some constraints from MHD simulations place the strength of the field in these regions in the interval $\sim 0.1 - 10\,\mu\mathrm{G}$ [1, 145, 146], although there are some indications of the existence of filaments with fields $\sim 1\,\mu\mathrm{G}$ [144, 481]. Analysis of SDSS data indicate that filaments fill about 1–10% [482, 483] of the volume.

A third constraint for the choice of normalization is the observed magnetic field in clusters of galaxies. Although this quantity is well-constrained by synchrotron and Faraday rotation measurements, the filling factors of clusters of galaxies are poorly known. Typical values for the strength of the field in these regions are $B \sim 0.05 - 30\,\mu\mathrm{G}$ in the center, and $\sim 10^{-8}\,\mathrm{G}$ in away from central regions, as suggested by synchrotron measurements of radio relics. Analyses of SDSS data [482] indicate that the filling fraction of knots in the cosmic web are $\sim 3 \times 10^{-3}$. Nevertheless, one should bear in mind that the central regions of clusters, where the magnetic fields are higher, have much smaller volume filling fraction than this, and that the magnetic field strengths radially decreases away from the central regions of clusters.

These bounds combined indicate the regions of the parameter space corresponding to clusters, filaments and voids. E_1 is a minimum magnetic field scenario, which however fails to satisfy the observational and theoretical constraints of magnetic fields in clusters and filaments. It is analyzed only for the sake of comparison. Scenarios E_2 and E_3 satisfy all constraints and can be deemed as realistic descriptions of the cosmic web, although E_3 is an extreme case, with very strong magnetic fields. The filling factors distribution for these scenarios are shown in figure 6.8.

[6] For a discussion on this topic the reader can refer to section 1.5.

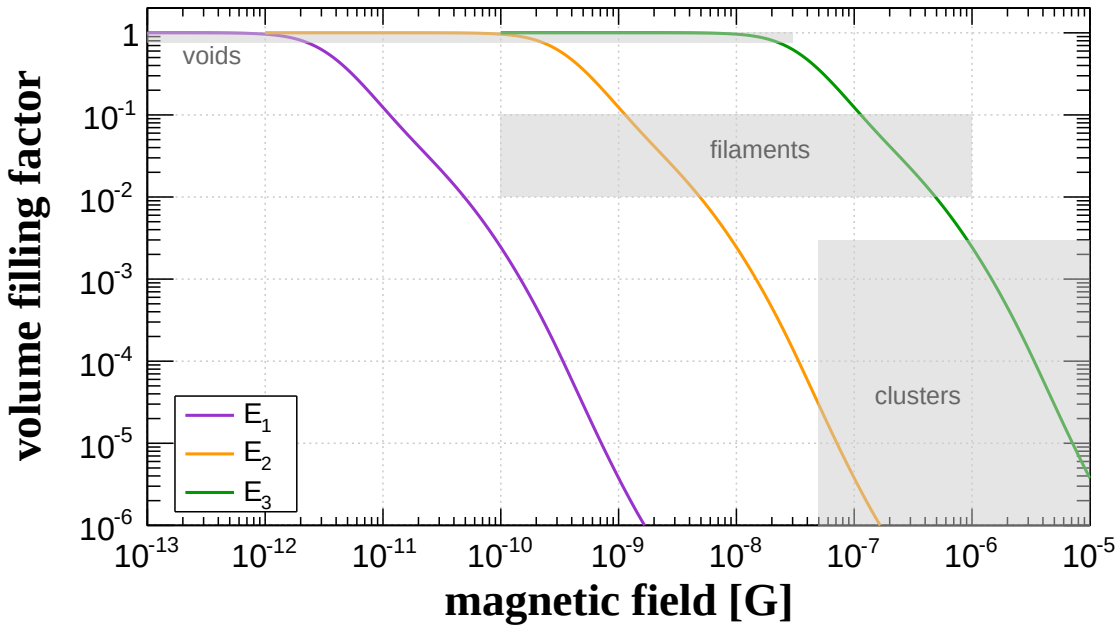

Figure 6.8: Volume filling factors for scenarios E_i. Gray areas are regions of the parameter space corresponding to clusters, filaments and voids.

6.5.2 Setup of the simulation

To understand the impact of different normalizations on the propagation of UHECRs, a few scenarios were studied using simulations performed with CRPropa 3. A single source was placed at the center of the grid (coordinates (139, 139, 139) Mpc). Large spheres inscribed in the grids E_i were used as observers. The source emits particles isotropically with the following injection spectrum

$$\frac{dN}{dE} \propto E^{-2} \cosh\left(\frac{E}{Ze\mathcal{R}_{max}}\right), \tag{6.2}$$

where $\mathcal{R}_{max} = 200\,\mathrm{EV}$ is the maximum rigidity for a nucleus with charge Ze. The hyperbolic cosine used here guarantees a smooth and relatively slow cutoff of the acceleration spectrum, as argued in ref. [419]. This study was done in the rigidity range $3 \leq E/\mathrm{EV} < 1000$. Two compositions were assumed: pure proton (Z=1) and pure iron (Z=26). The energy loss processes taken into account were photopion production, pair production and photodisintegration (in the iron scenario). Energy losses caused by the adiabatic expansion of the universe were not taken into account in this approach. Particles are propagated until one of the following break conditions is met:

(i) they reach the observer;

(ii) their energy drops below the minimum energy threshold, set to $E_{min} = 3 \times 10^{18}\,\mathrm{eV}$;

(iii) the propagation time of the cosmic rays is larger than a predefined value, $T_{max} = 2000\,\mathrm{Mpc}$.

Deflections due to the magnetic field were handled by CRPropa using steps of size between 1 kpc and 500 kpc, which should suffice to obtain the trajectories of the cosmic rays. Usually larger values are used ($\sim 1\,\mathrm{Mpc}$), but herein one can profit from the high resolution of the grids for a detailed study.

Although a large number of primaries ($N = 500000$) were injected, many of them did not reach the observer due to the break conditions (ii) and (iii). Moreover, the computational time required for running

simulations with such small step sizes is very large, thus limiting the number of events to be simulated within a reasonable time frame.

6.5.3 Results and discussion

The cosmic ray spectrum and composition are shown in figure 6.9 for both compositions studied (iron and proton). As can be seen in the left panel of figure 6.9 for the proton case, the shape of the spectrum is

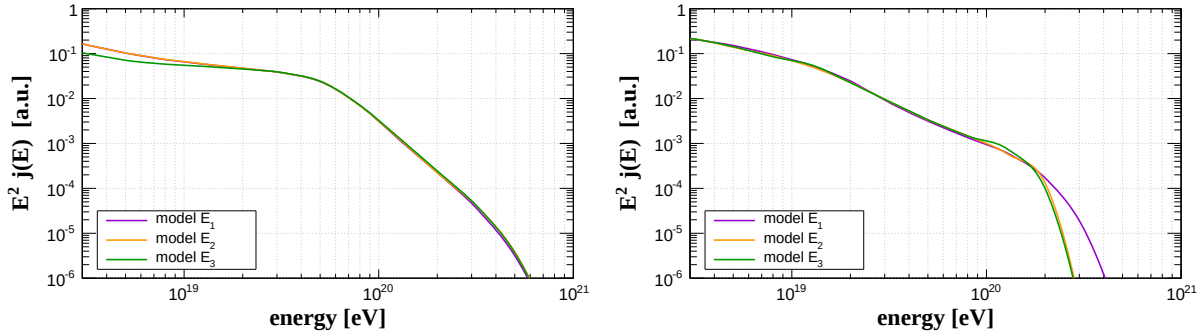

Figure 6.9: The spectrum obtained for the simulations in the proton (left) and iron (right) scenarios.

affected by magnetic fields. For $E \lesssim 10^{19}$ eV the flux of protons propagating through the magnetic field grid E_3 is slightly suppressed, which is expected to occur depending on the strength of the magnetic field and the size of the observer ($R_{obs} \approx 139$ Mpc). This suppression can be understood through an analogy with the magnetic horizon effect discussed in chapter 4. The larger the magnetic field, the longer the cosmic ray has to travel to the observer, and eventually this flux will be comparable to some distance scale (e.g. age of the universe).

Strictly speaking, the magnetic horizon is defined as the maximum distance that a cosmic ray can travel away from the source within one Hubble time. In this analysis cosmological effects were neglected, and hence this suppression can be explained by one or both of these hypotheses: (i) the energy of the cosmic rays dropped below the threshold ($E < E_{min}$); (ii) the time traveled is larger than the maximum propagation time allowed ($T > T_{max}$). Condition (ii) is roughly equivalent to the strict definition of magnetic horizon. The most likely explanation for the flux suppression is that the cosmic rays never reach the observer. This occurs if the Larmor radius (R_L) is much smaller than the distance to the observer (R_{obs}). From this condition one can derive the maximum magnetic field for which the cosmic ray flux is not suppressed due to confinement around the source:

$$B_{max} \ll \frac{E}{\text{EeV}} \frac{\text{Mpc}}{R_{obs}} \text{ nG}. \tag{6.3}$$

Therefore, for $R_{obs} \sim 100$ Mpc, in order not to have a flux suppression at 10 EeV the magnetic field should on average be smaller than 10^{-10} G, which is true for models E_1 and E_2. This is consistent with figure 6.9, in which the proton flux propagated in grid E_3 is suppressed. Similar effect has been observed by the authors of ref. [431], but not ref. [279]. As noted by Lemoine [278], this confinement effect occurs if

$$B \geq \sqrt{\frac{\ell_c}{10 \text{ kpc}} \frac{L}{100 \text{ kpc}}} \ \mu\text{G}, \tag{6.4}$$

where ℓ_c is the coherence length of the magnetic field and L is the length over which the magnetic field is spread around the source.

In the right panel of figure 6.9, which depicts the simulated spectrum for iron primaries, no suppression

at lower energies is observed. Nevertheless the position of the cutoffs at the highest energies are different. With the current number of events in this simulation it is not clear whether the observed cutoff at the highest energies is a genuine effect of the magnetic field on the maximal acceleration energy, or rather a spurious statistical fluctuation. Therefore, no conclusion can be reached and further studies are required to answer this question.

In the proton case there is obviously no change in the mass composition of the cosmic rays. For the iron scenario, however, signatures of cosmic magnetic fields can be imprinted in the composition, since photodisintegration occurs. In figure 6.10 it can be seen that for model E_3, which has the highest magnetic field strength, the average mass at energies $E \lesssim 10^{19}\,\mathrm{eV}$ is lower than in model E_1, which has relatively low magnetic field strength everywhere. This effect can be understood in terms of propagation length: the higher the magnetic field, the larger the deflection, the longer the cosmic ray takes to reach the observer and consequently the more likely it is for photodisintegration to occur, causing a decrease in the average mass.

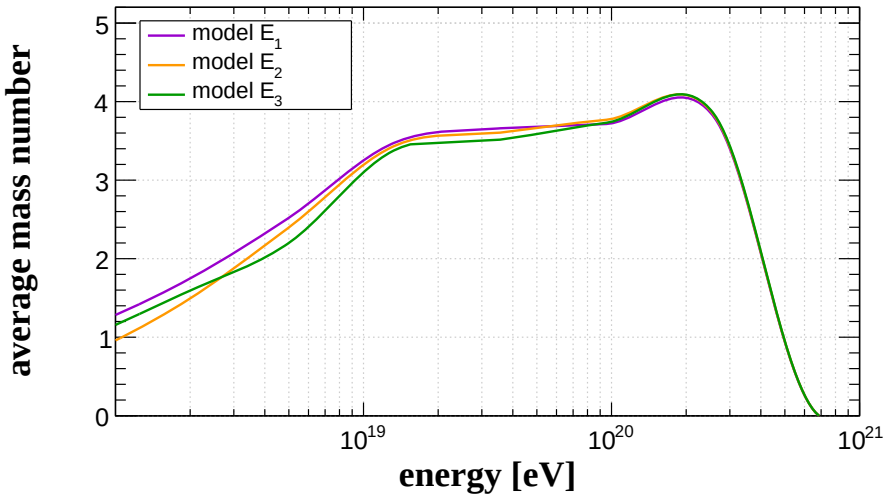

Figure 6.10: Average of the logarithm of the mass number ($\langle ln(A) \rangle$) as a function of the energy for the simulated scenarios, assuming a pure iron composition.

Skymaps containing the arrival directions of the UHECRs from these simulation are shown in figure 6.11, for the proton scenario, and figure 6.12 for the iron scenario. The galactic magnetic field (GMF) model of Jansson and Farrar [183, 184] is taken into account by using the lensing technique described in chapter 5.

It is also possible to estimate the deflections of the cosmic rays in the different scenarios. This is shown in figure 6.13 for both cases (proton and iron composition).

In figure 6.13 it can be seen that for model E_3 the deflections are large even at the highest energies ($E \sim 100\,\mathrm{EeV}$), whereas for model E_1 they are overall small in both composition scenarios. The galactic magnetic field causes an increase in the average deflection at all energies, but this effect is only visible for model E_3.

6.6 Further remarks

In this chapter several studies of the impact of extragalactic magnetic fields on the propagation of UHECRs were presented. Although rather simple, these analyses provided valuable insights on horizons of

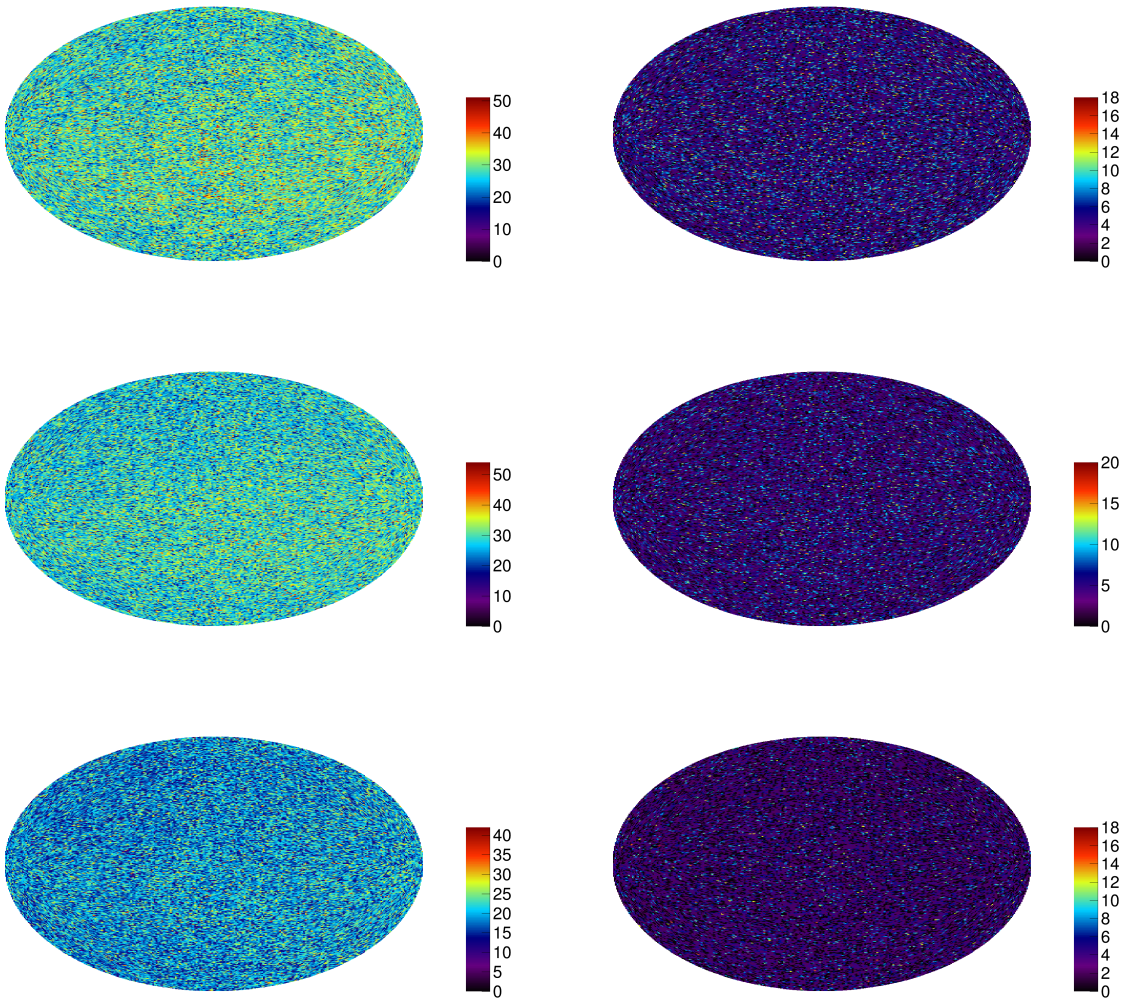

Figure 6.11: Skymaps depicting the arrival directions of cosmic rays at the border of the galaxy (left column) and at Earth (right column), after correcting for the GMF. Each row corresponds to a magnetic field model: E_1 (top), E_2 (middle) and E_3 (bottom). These skymaps correspond to the scenario in which only protons are injected. The color scale indicates the number of events in each bin.

cosmic rays and the actual impact of uncertainties on extragalactic magnetic fields on cosmic ray observables.

A remarkable result here obtained is that the shape of the power spectrum of the magnetic field seed leads to very different configurations of magnetic fields at present time, thus potentially affecting the propagation of UHECRs, as shown in figure 6.6. In the work of Dolag *et al.* [425, 465] a uniform magnetic field seed with strength $B \sim 1$–5 nG (at $z = 20$) was used to perform a constrained simulation of the local universe. In spite of the fact that different normalizations for this seed were studied, and the final one chosen in such a way as to match observations of clusters, the effects of non uniform seeds were not analyzed, although this is acknowledged as a potential source of uncertainty [425]. These authors argue that the uniform magnetic field results on the largest deflections for a given magnetic field strength, hence being regarded as an upper limit. Here gaussian magnetic seeds were used.

If deflections are not too large and cosmic ray astronomy is possible, as advocated by Dolag *et al.* [425, 465], then it is possible to use UHECRs as probes of EGMFs, by comparing theoretical models with measurements. Since the power spectrum of the magnetic field is intrinsically related to the magnetogenic mechanism, the study of deflections of UHECRs in different models can provide constraints to the magnetic

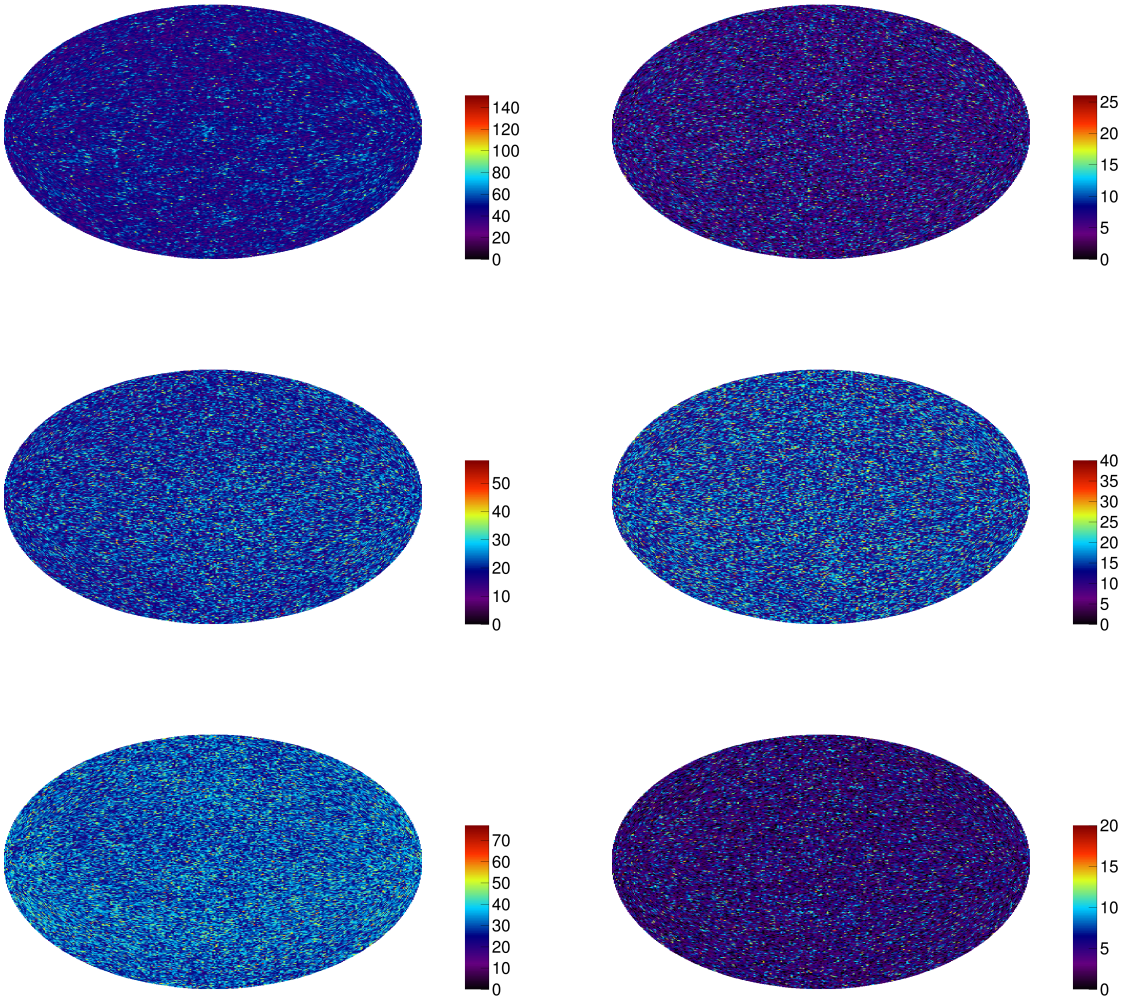

Figure 6.12: Skymaps depicting the arrival directions of cosmic rays at the border of the galaxy (left column) and at Earth (right column), after correcting for the GMF. Each row corresponds to a magnetic field model: E_1 (top), E_2 (middle) and E_3 (bottom). These skymaps correspond to the scenario in which only iron nuclei are injected. The color scale indicates the number of events in each bin.

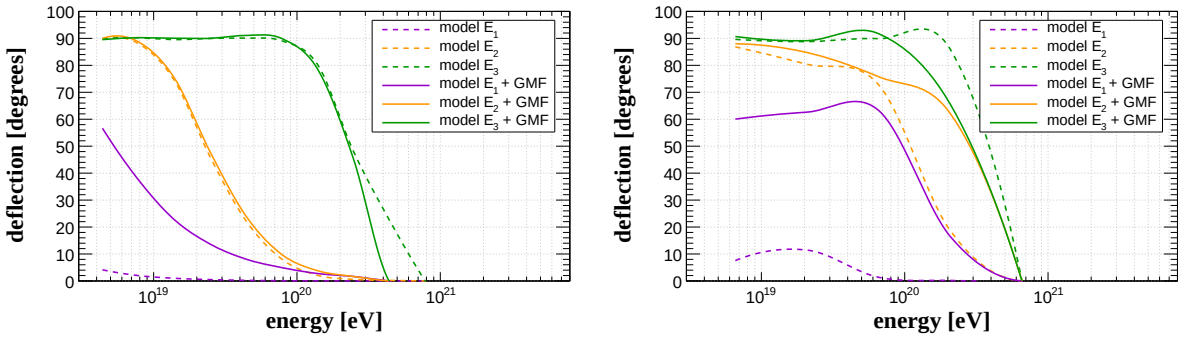

Figure 6.13: Average deflection per energy bin for the case of proton (left panel) and iron (right panel) primaries. Dashed lines correspond to only extragalactic deflections, and solid lines includes also deflections due to the GMF model of Jansson and Farrar [183, 184].

fields at present and earlier times.

Three scenarios (models E_1, E_2 and E_3) for the magnetic field were considered. Two of them are

possible, albeit some are hardly realistic. Model E_1, for instance, does not match the measured magnetic field strength in clusters of galaxies, and model E_3 almost exceeds the constraints imposed by BBN[7]. Model E_2 is an intermediate case and probably more realistic. With these scenarios the interesting effect of confinement of UHECRs around the source was studied. Moreover, it was possible to have a general overview of the behavior of cosmic rays propagating in these grids.

For the referred studies here presented only one source in a fixed position was used. If the source is located in a strongly magnetized environment, with a magnetic field that satisfies the condition imposed by equation 6.3 then the flux suppression observed at the lowest energies (for protons) can be attributed to the confinement of cosmic rays around the source. The study of the environment around the sources by using gamma ray and neutrino counterparts allows one to impose limits on this type of effect.

An interesting conclusion that can be drawn from this analysis concerns the possibility of UHECR astronomy. As can be seen in figure 6.13, the deflection in the proton scenarios are rather high for energies $E \lesssim 10^{19}\,\mathrm{eV}$ in all three magnetic field models studied, if one considers both galactic and extragalactic deflections. The GMF does not increase the average deflection for model E_2 and E_3, for they were already high. For model E_1, however, the average deflection increases drastically from a few degrees to 30° at 10 EeV. Obviously, for the iron scenarios the deflections are higher than the proton case. The only model in which UHECR astronomy with iron nuclei would be possible is in the case of model E_1 if the galactic magnetic field is weaker than in the Jansson-Farrar model. For models E_2 and E_3 the results are inconsistent with the ones by Dolag *et al.* [425], which predict deflections smaller than 1° (for protons) for a source 110 Mpc away from Earth.

Usually the prospects for UHECR astronomy are discussed in the context of models with a given source distribution, which is often uniform or follows the distribution of matter in the local universe. In this particular analysis a single source was used, and therefore the results here obtained must be cautiously interpreted. For the source analyzed, distant approximately 139 Mpc from the observer, UHECR astronomy is hardly possible at energies $\lesssim 10\,\mathrm{EeV}$. A complete analysis for a given source distribution would actually allow the proper comparison with the literature. In refs. [467, 468, 484, 485] which uses the MHD simulation by Miniati [424], the authors found that UHECR astronomy is not possible in the whole sky, and that deflections are large ($\sim 20°$) at 10^{20} eV (for protons). In ref. [426] the authors have found deflections $\sim 15°$ at 60 EeV, which are rather large considering the assumed protonic composition. On the other hand, in ref. [425, 465] the deflections were smaller than 1° covering 99% of the sky. These discrepancies are mainly due to the different methods adopted to perform the cosmological simulation of structure formation, which imply very distinct filling factor distributions, as shown in figure 6.1.

[7] The reader can refer to figure 1.7 for constraints on the strength and coherence length of EGMFs. A detailed discussion on the topic is presented in section 1.5.3.

chapter 7

Propagation of UHECRs over cosmological distances

7.1 Introduction

High energy particles can propagate over cosmological distances, albeit the existence of pervasive photon fields potentially limit the distance they can travel (or interaction horizon). A realistic simulation of the propagation of high energy particles such as cosmic and gamma rays should take into account all the relevant energy loss processes due to interactions with astrophysical backgrounds, as well as the intervening cosmic magnetic fields. Cosmological effects such as the redshift dependence of the photon backgrounds, evolution of the sources over time, and the adiabatic expansion of the universe, can play an important role in the aforementioned processes.

In the case of UHECRs, in spite of their relatively small interaction horizon, at energies $\sim 10^{18}$ eV there may be a dominant contribution of distant sources. At energies above ~ 50 EeV the contribution of sources farther than ~ 100 Mpc is virtually negligible.

A problem in the simulation of the propagation of UHECRs in the universe is the difficulty to account for cosmological effects in three-dimensional simulations with magnetic fields. This problem occurs due to the fact that the redshift of a particle is not known *a priori*, since it can be deflected by intervening magnetic fields, changing the effective length of the trajectory. The solution is to perform a complete four-dimensional simulation including the time dimension, which is computationally expensive. In this chapter *a posteriori* methods to account for cosmological effects in three-dimension simulations are presented, and their limitations discussed. At the end an application of the four-dimensional propagation is discussed.

7.2 Cosmological effects in three-dimensional simulations of propagation of UHECRs

7.2.1 First attempt: redshift correction

In chapter 1 an equation relating the redshift and time in a flat two component universe was presented (eq. 1.21). For the sake of completeness it is transcribed below:

$$\frac{dt}{dz} = \frac{1}{H_0(1+z)} \frac{1}{\sqrt{\Omega_m(1+z)^3 + \Omega_\Lambda}}. \tag{7.1}$$

Equation 7.1 can be analytically solved, yielding

$$z(t) = \left(\frac{\Omega_\Lambda}{\Omega_m}\right)^{\frac{1}{3}} \left[\left(\tanh\left(\frac{1}{2} \ln\left(\frac{\sqrt{1+\frac{\Omega_m}{\Omega_\Lambda}}+1}{\sqrt{1+\frac{\Omega_m}{\Omega_\Lambda}}-1} \right) - \frac{3}{2}\sqrt{\Omega_\Lambda} H_0 t \right) \right)^2 - 1 \right]^{-\frac{1}{3}} - 1. \tag{7.2}$$

As a first attempt, one might try to correct the observed energy of the particle by the effective propagation time using the simple relation

$$E = \frac{E_0}{1+z}, \tag{7.3}$$

where E_0 is the energy of the emitted particle.

This energy correction was applied to 3D simulations in a scenario without magnetic fields, for sources uniformly distributed between 0 and 4 Gpc, emitting protons with a power law spectrum with spectral index -2.2, propagating through the CMB and CIB, assuming the CIB model from ref. [45]. If the correction is effective, it is expected that the spectrum for a 1D simulation including redshift losses, and a 3D simulation without magnetic fields would be similar. The relative difference between the 1D and 3D spectra, given by $(j_{1D} - j_{3D})/j_{1D}$, should be zero if the correction worked perfectly. Figure 7.1 shows the spectra for the 1D simulation, the 3D simulation and its correction, as well as the relative differences for both cases (corrected and non corrected). A simple fit of the relative difference with a function $f(\log E) = a$, where a is a constant,

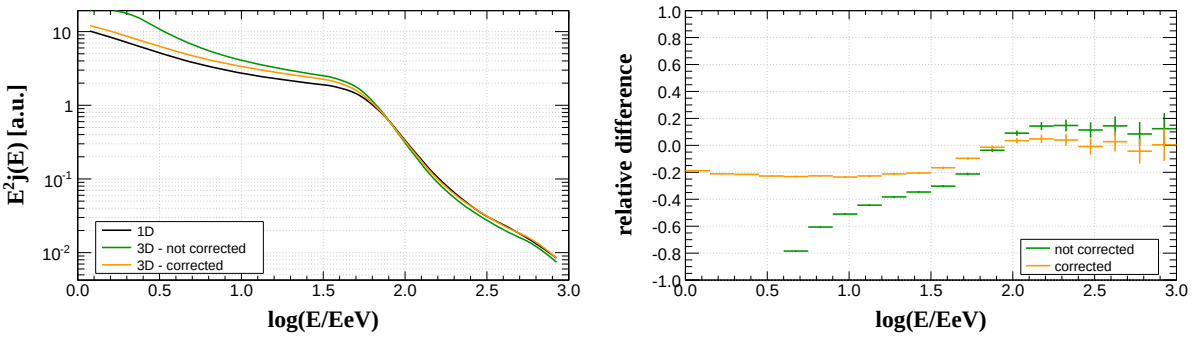

Figure 7.1: In the left panel it is shown the spectra for the 1D simulation with redshift losses (black curve), the 3D simulation without redshift losses (green) and the attempted correction using the formula (orange). The relative differences between 1D and 3D, as well as 1D and corrected 3D are shown in the right panel, for different energy bins.

provides a good estimate of the efficiency of the correction. Performing this fit to the relative difference for the corrected case, one obtains $a = 0.012 \pm 0.001$. Therefore, this approach introduces an error of $\approx 1.2\%$ in the overall correction. Notice, however, that in individual energy bins the discrepancies can be $\approx 20\%$.

This method of correction does provide good results in the case considered, as can be seen in figure 7.1. However, there are still some differences that can affect the spectrum. One of the reasons for these differences is that using equation 7.3 is equivalent to assume that the total energy losses can be completely factorized in terms of the other processes (pair and photopion production) and redshift losses. Another possible reason is that this correction changes only the observed energy of the simulated particles in 3D, and does not consider the contribution of the redshift scaling of the background photon fields.

7.2.2 A novel approach: correction table

7.2.2.1 The method

The energy losses of ultra-high energy particles depend on their initial energy and trajectory length. Hence, to correct the energy of the particle in a 3D simulation considering redshift losses, these should be taken into account. For that, binned tables containing these quantities were built. In these tables the y-axis is the injected energy, the x-axis the trajectory length, and the z-axis the observed energy. They are shown in figures 7.2 for the 1D and 3D cases.

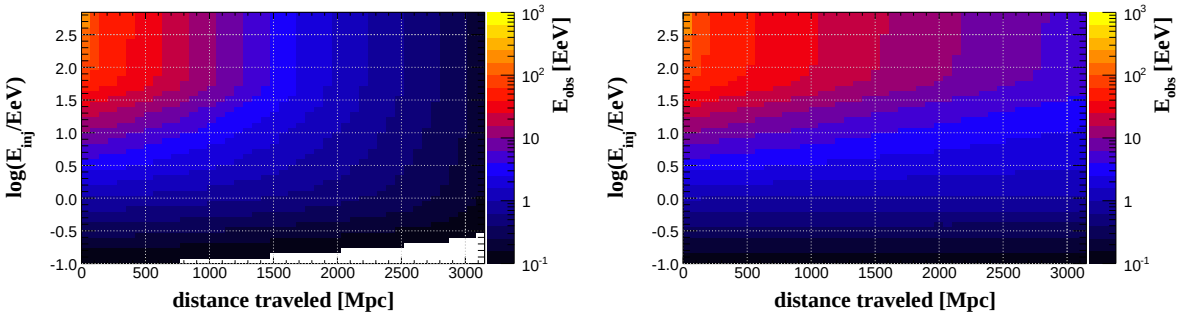

Figure 7.2: Observed energy (z axis) for a given propagation time (x axis) and injected energy (y axis) for the 1D simulation taking into account redshift losses (left) and the 3D case without cosmological effects and magnetic fields (right). The sources are assumed to be uniformly distributed with spectral indexes -2.2.

If the 3D model took into account redshift losses, as the 1D model does, for a scenario without any magnetic fields present, the observed energy of the particles for the same injected energy and trajectory length should be approximately the same. Therefore, a reasonable assumption is that the ratio of the observed energies in the 1D and 3D simulations (shown in figure 7.3), for a given injected energy and trajectory length, could be used as a correction factor for the observed energy of the 3D simulations.

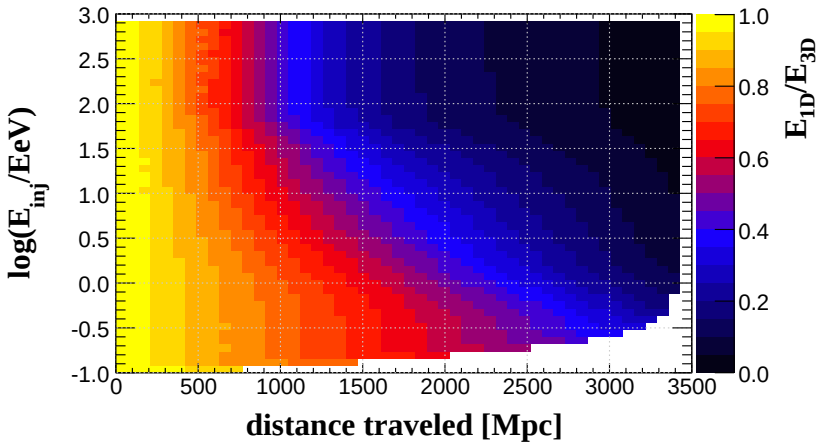

Figure 7.3: Correction factor obtained by the ratio between the observed energies in the 1D and 3D simulations (z-axis) for a given propagation time (x-axis) and injected energy (y-axis).

To check the efficiency of this approach, a procedure similar to the one described in the previous section was adopted. The spectra for a uniform source distribution for the 1D and 3D with and without corrections were plotted and are shown in figure 7.4. The dataset used here was the same one used to generate the tables shown in figure 7.2. The correction seems to yield excellent results, as can be seen in figure 7.4.This can be better assessed by estimating the relative difference between the 1D case and

the 3D, both with and without the correction, also shown in the referred figure. By fitting a function of the form $f(\log E) = a$ to the relative difference between the 1D and the 3D corrected spectra, one finds $a = 0.002 \pm 0.001$, which might be a result of the choice of normalization. Notice that the maximum relative difference occurs for higher energies ($\log(E/\mathrm{EeV}) \gtrsim 2.5$), but nevertheless is still inferior to 10%.

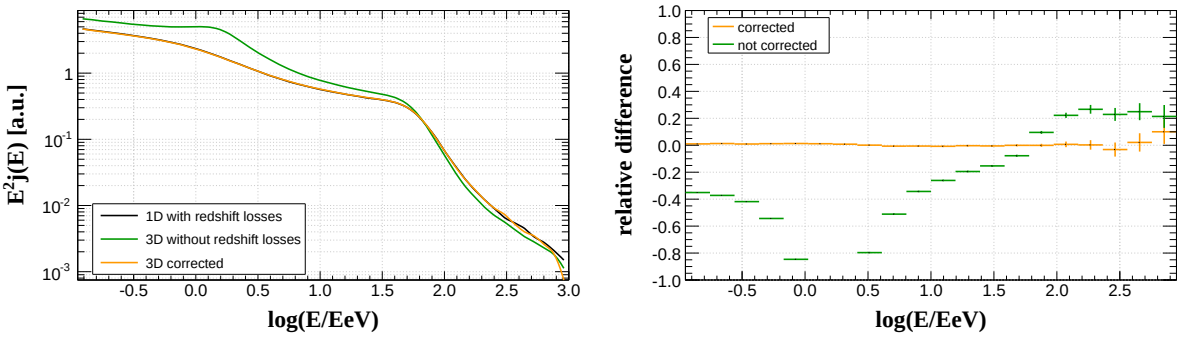

Figure 7.4: In the left panel the spectra for the 1D simulation with redshift losses (black), the 3D simulation without redshift losses (green) and the attempted correction using the correction table (orange) are shown. In the right panel the relative difference between the 1D and 3D simulations without the correction (green) and with the correction (orange) can be seen. This scenario is the same one used to generate the correction table shown in figure 7.3.

7.2.2.2 Applications

As an example of application of this correction, further simulations were performed. The simulated particles were propagated in three different scenarios with different magnetic field assumptions. The first case is a uniform magnetic field of 10 pG oriented along the z direction. The second scenario is a turbulent Kolmogorov magnetic field with $\langle B_{rms} \rangle = 2\,\mathrm{nG}$ and coherence length given by ref. [88]:

$$L_c = \frac{L_{max}}{2} \frac{\alpha - 1}{\alpha} \frac{1 - \left(\frac{L_{min}}{L_{max}}\right)^{\alpha}}{1 - \left(\frac{L_{min}}{L_{max}}\right)^{\alpha - 1}}, \tag{7.4}$$

where $\alpha = -11/3$ for a Kolmogorov field, $L_{min}^{-1} = 0.5\ \mathrm{Mpc}^{-1}$ is the maximum wave number and $L_{max}^{-1} = 0.03125\ \mathrm{Mpc}^{-1}$ is the minimum wave number. Therefore $L_c \approx 11\,\mathrm{Mpc}$. The spectrum and relative differences for both scenarios are show in figures 7.5 and 7.6

The calculation of the difference between the 1D and 3D spectra both for the corrected and non corrected cases allows the estimation of the performance of the correction for these scenarios. The relative difference between the spectra for the case without magnetic field is already displayed in figure 7.4. The examples corresponding to the cases with magnetic fields are shown in figures 7.5 and 7.6, for the uniform magnetic field and for the Kolmogorov turbulent field, respectively. Adjusting these relative differences between the 1D and corrected 3D cases with $f(\log E) = a$, one obtains $a = 0.0090 \pm 0.0009$, for the first case (no magnetic field), $a = 0.017 \pm 0.001$ for the second (uniform magnetic field), and $a = 0.016 \pm 0.002$ for the third case (Kolmogorov turbulent field). In all these scenarios the simulation setup assumes a uniform distribution of sources with spectral index -2.2.

One should notice that these are the only scenarios that allow a proper test of the correction and comparison with the 1D case, for the propagation theorem holds. Since the correction relies on the initial and final energies, as well as the total path length of the trajectory, and these observables are independent

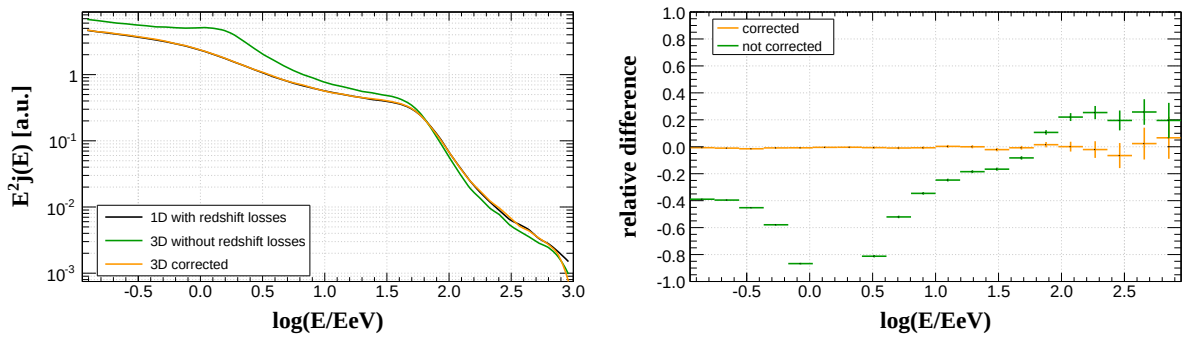

Figure 7.5: Relative difference between the 1D and 3D simulations without the correction (green) and with the correction (orange) for the scenario with a uniform magnetic field of 10 pG oriented along the z direction.

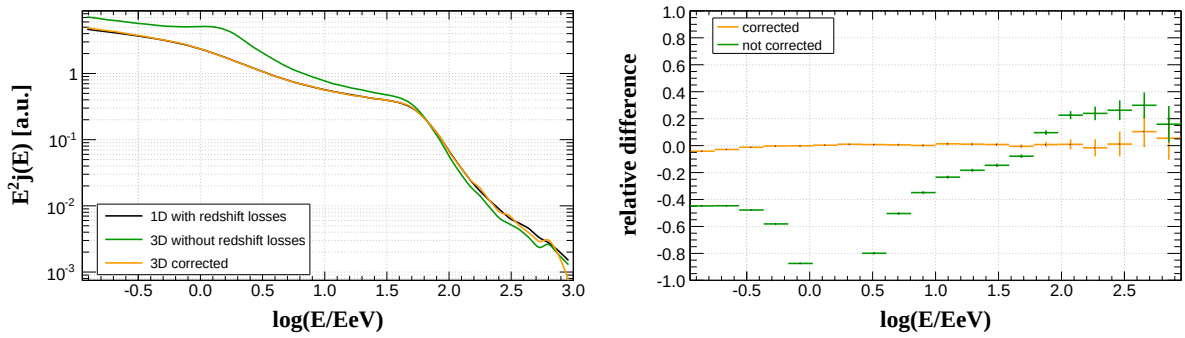

Figure 7.6: Relative difference between the 1D and 3D simulations without the correction (blue) and with the correction (red) for the Kolmogorov turbulence scenario, with $\langle B_{rms} \rangle \approx 1\ nG$.

of assumptions such as source distribution and intervening magnetic fields, it is reasonable to assume that they will also hold for other scenarios such as a single source in a structured magnetic field, for example.

7.2.2.3 General remarks

A computational problem in Monte Carlo simulations of the propagation of UHECRs in the universe is the difficulty to account for cosmological effects in 3D scenarios, in which magnetic fields are present. This problem occurs due to the fact that it is impossible to have a prior knowledge of the redshift of the particle, which is subject to constant deflection. This can only be achieved by adding an extra dimension to the problem, as done in the 4D mode of CRPropa 3, described in chapter 5, which increases the complexity of the code, and hence the required computational time.

In the previous subsections two approaches to account for cosmological effects in three dimensions *a posteriori* were described. The correction table provided better results than the simple adiabatic correction of the energy, using equation 7.3. This correction introduces an overall average bias inferior to 10% in the regions of the energy spectrum between 10^{17} eV and 10^{21} eV. These results indicate that the correction has an excellent performance for the typical energy ranges of interest, below a few hundred EeV.

Because this correction is obtained from a binned table, it is subject to statistical fluctuations. The results do not depend on the spectral index of the source, for the only relevant quantities are the initial and final energies, and the propagated distance. This correction was tested for cases in which propagation theorem holds (uniform source distribution with separation between sources much smaller than the characteristic propagation lengths). The tests assumed certain models for the photon fields, namely the CIB model by Kneiske *et al.* [45]. Changes in relevant interaction quantities such as cross sections, photon densities

and others may affect the spectrum, thus requiring different correction tables. Nevertheless, the method to obtain these tables can be easily applied to other cases.

The results here presented hold only for protons, not being valid for nuclei. In this case the dominant radiation field for the interactions between background photons and protons at these energies is the CMB. Therefore, the correction table here obtained can be applied to other scenarios with different CIB models without introducing considerable errors.

A generalization of this method for the case of nuclei is not straightforward, since the correction would have to account not only for the spectrum, but also the mass composition, which is not trivial due to photodisintegration processes. The search for a unified method to account for cosmological effects in 3D simulations that can be applied to any nuclei will be the subject of the following section.

7.2.3 A "hybrid" approach

7.2.3.1 The method

As discussed before, the redshift dependence of the photon backgrounds, namely the CMB and CIB, and the evolution of the sources can affect the spectrum and composition of the detected cosmic rays. Also, the expansion of the universe causes energy losses.

Relevant quantities obtained from a three-dimensional simulation are the initial (E_i^{3D}) and final (E_f^{3D}) energy of the particle, initial (A_i^{3D}, Z_i^{3D}) and final (A_f^{3D}, Z_f^{3D}) particle species, initial (x_i, y_i, z_i) and final particle position (x_f, y_f, z_f), effective propagation time (T^{3D}), among others. The "hybrid" mode is a tentative solution to generalize the *a posteriori* correction for nuclei and is presented in ref. [21], and is so called because it blends 3D simulations with 1D, speeding up the simulation time in comparison with the 4D simulation.

Each individual particle from a 3D simulation is resimulated in 1D, using the following quantities: E_i^{3D}, (A_i^{3D}, Z_i^{3D}) and T^{3D}. A set of subproducts from the photodisintegration of the parent-nucleus is obtained for individual daughter-nuclei, where the index k is associated to each one of these subproducts. The final energy ($E_{f,k}^{1D}$) and particle type ($A_{f,k}^{1D}, Z_{f,k}^{1D}$) can be obtained from the output of the 1D simulation. As a first approximation one can choose k uniformly among all daughter-nuclei. Finally, the final energy and type of particle in the former 3D dataset are replaced by the corresponding ones obtained from the 1D simulation, by setting $E_f^{3D} = E_{f,k}^{1D}$ and $(A_f^{3D}, Z_f^{3D}) = (A_{f,k}^{1D}, Z_{f,k}^{1D})$.

To verify the validity of the method the trivial case of a 3D simulation without magnetic fields was tested. Sources with spectral index -2.2 were assumed to be uniformly distributed up to 4000 Mpc. At first, only protons were considered, whereas in the second only iron was considered. The parameters of the 1D and 3D simulations are exactly the same, so that the only difference between these cases arise from the consideration of cosmological effects. The simulated spectra in 1D and 3D, as well as the corrected one, can be seen in figure 7.7 for pure proton and pure iron scenarios.

7.2.3.2 Application

In this subsection the method is applied to a realistic scenario of extragalactic magnetic field. For the simulations it was assumed the magnetic field distribution from ref. [484] according to a differential energy spectrum that follows a power law of spectral index $\gamma = -1$, reweighted afterwards to $\gamma = -2.2$. The observer is treated as a sphere of radius 0.5 Mpc, lying within a cubic box of approximately (75 Mpc)^3, periodically and smoothly concatenated with copies of itself up to a distance of 2000 Mpc. The propagation was performed with CRPropa, considering pion production, photodisintegration and pair production. Redshift

losses were only considered in the 1D mode. The astrophysical backgrounds used were the CMB and CIB, namely the model by Kneiske *et al.* [45] for the latter.

Simulations with and without magnetic field were performed in order to understand the effects of cosmic magnetic fields on the spectrum. A side view of this magnetic field box is shown in figure 7.8. All the simulations were performed for two mass compositions, namely pure iron and pure proton. The results of these simulations are shown in figure 7.9, together with the corresponding universal spectra and the experimental spectrum measured by the Pierre Auger Observatory [287], for the sake of comparison.

For a non uniform source distribution the propagation theorem does not necessarily hold, and deviations from universality may occur. This can be seen in figure 7.10. As expected, the effects of magnetic fields on the spectrum are much larger in the iron than in the proton scenario, due to the fact that iron nuclei have a charge 26 times larger than protons, which implies deflection angles up to 26 times larger.

In figure 7.10 a comparison between the original 3D spectrum with the one corrected for cosmological effects is shown. There are visible effects of cosmology for both simulated mass compositions scenarios. This happens because when the correction is applied, many events from the lower energy tail of the spectrum (~ 1 EeV) will suffer another energy loss process not present in the original 3D simulation, dropping below the minimum energy threshold, set to 1 EeV in this simulation. In the iron case, however, the discrepancy between the corrected and non-corrected spectra is larger, because for energies ~EeV the main contribution comes from secondary nuclei, originated from the photodisintegration of primary iron.

Another relevant analysis is the change in mass composition, namely the $\langle X_{max} \rangle$ observable, due to magnetic fields and cosmological effects. This is analysis is presented only for the iron scenario, since the proton case is trivial. Besides the depth of the shower maximum ($\langle X_{max} \rangle$), its variance ($\sigma(X_{max})$) is also estimated, using the parametrization from ref. [469]. The values of $\langle X_{max} \rangle$ and $\sigma(X_{max})$ for different energy ranges are shown in figure 7.11, together with the experimental values measured by the Pierre Auger Observatory [469] and the theoretical predictions assuming the EPOS1.99 hadronic interaction model. In this figure it can be seen that even though cosmological effects are relevant, magnetic fields are responsible for the largest change in composition at lower energies.

In figure 7.12 the mean deflection as a function of the energy is shown. It is clear that there are no significant differences in the energy dependence of the deflections. In the case of isotropy, the mean value

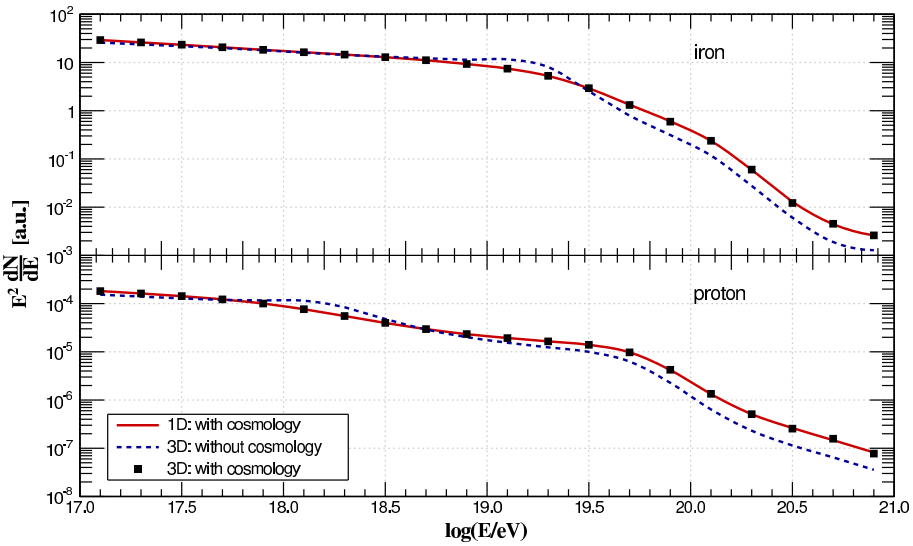

Figure 7.7: Spectra for the 1D simulation (solid line), the 3D without cosmology (dashed line) and the 3D corrected for cosmology (squares) for the a pure iron (top) and pure proton (bottom) composition. The spectra are normalized to the total number of events times 100 for iron, and 0.01 for proton.

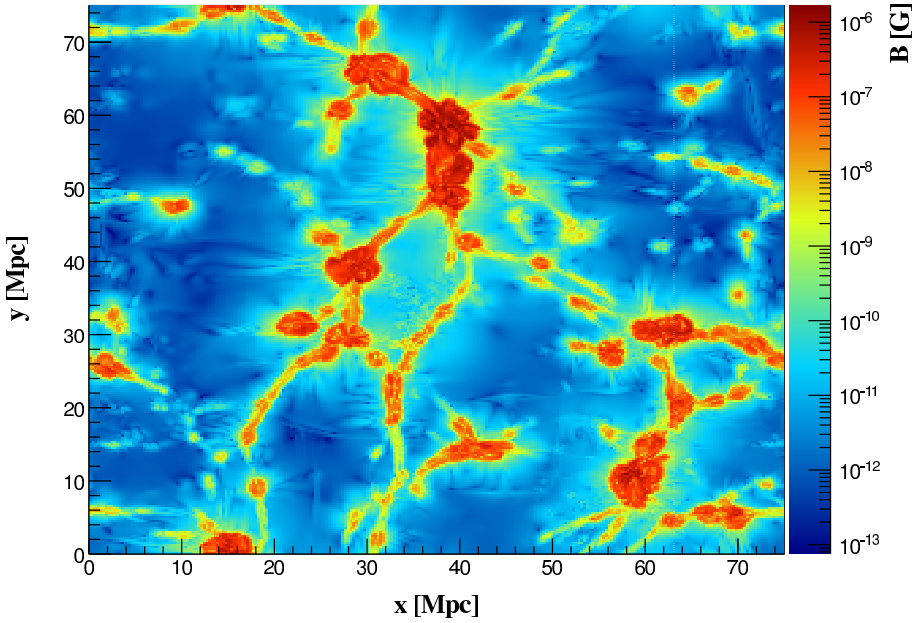

Figure 7.8: Two-dimensional cut through the magnetic field box. The color scale indicates the strength of this field.

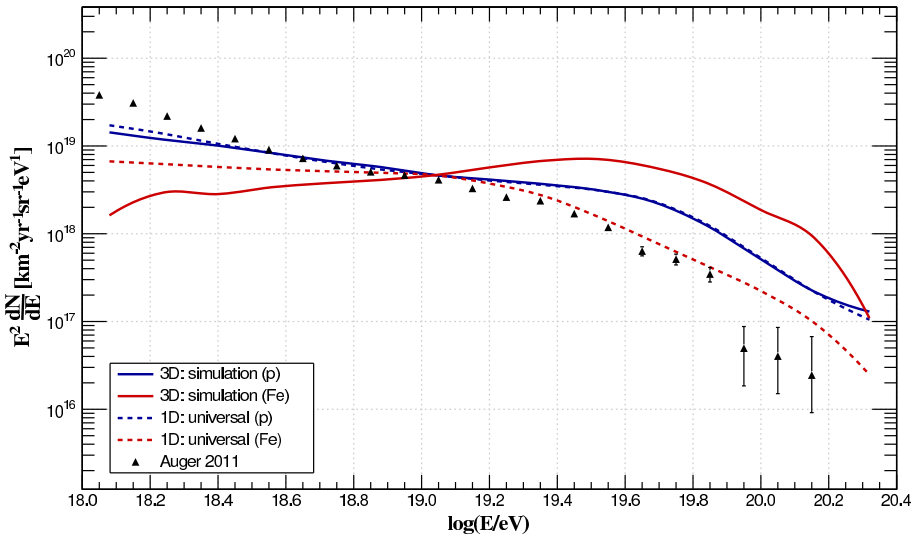

Figure 7.9: Simulated spectra corrected for cosmology (solid lines), universal spectrum (dashed lines) for a proton (blue) and iron (red) compositions. The dots correspond to the hybrid Auger spectrum, taken from ref. [287]. The spectra here presented are normalized to the Auger '2011 spectrum at $10^{19.1}$ eV.

of the deflection would be 90°. Thus one can notice that for lower energies the simulated data sets are highly isotropic, becoming more anisotropic as energy increases.

7.2.3.3 General remarks and setbacks of the method

In some cases the method here presented cannot be applied. As an example a scenario with a single source emitting helium nuclei with spectrum E^{-2} was considered. This source was placed at distances 200 Mpc, 500 Mpc and 1000 Mpc from Earth, and the 4D mode of CRPropa was used to obtain a dataset for comparison. The magnetic field was completely switched off, so that the 1D and 4D modes should behave in the same way, and the hybrid mode similarly. The results for the spectrum and average of the logarithmic mass composition are shown in figure 7.13.

In figure 7.13 one notices that the hybrid mode approximately corrects the shape of the spectrum, but

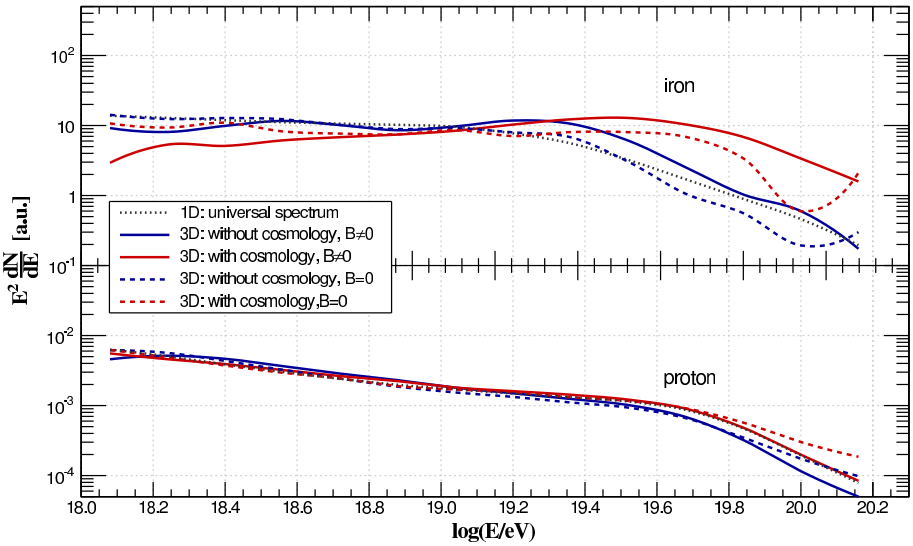

Figure 7.10: Simulated spectra corrected for cosmology (red lines), not corrected (blue lines), for the case with (solid lines) and without (dashed lines) magnetic field. The universal spectrum is represented by the black dotted lines, for comparison. The spectra are normalized to the total number of events times a factor of 100 for the iron case, and 0.01 for the proton case.

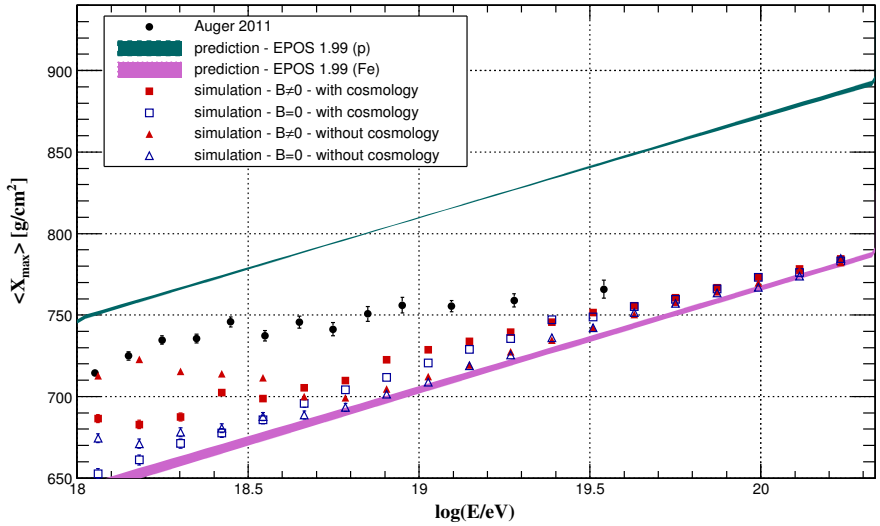

Figure 7.11: Mean value of the $\langle X_{max} \rangle$ for the simulated data (for the iron scenario), compared to measurements of the Pierre Auger Observatory (black circles) and the theoretical predictions according to the EPOS 1.99 model (filled area) for protons (green filled area) and iron (pink filled area). The scenarios without magnetic field are represented by empty markers, whereas the scenarios with magnetic fields are represented by filled markers. Squares correspond to the simulated data set with the cosmology correction, and the triangles without it.

not the composition. In spite of the fact that this correction improves the predictions for a 3D simulation and is much faster than the 4D case, its quantitative predictions are not reliable and therefore the method in general is not viable.

The hybrid mode is a useful tool to include cosmological effects in scenarios in which the propagation theorem holds, since in this case the spectrum is universal. This means that this approach is applicable only if the sources are approximately uniformly distributed, and if their average separation is much smaller than the typical lengths involved. For instance, UHE nuclei whose photodisintegration mean free paths are small compared to the average source separation are not well described by this approach, for the propagation theorem is not applicable.

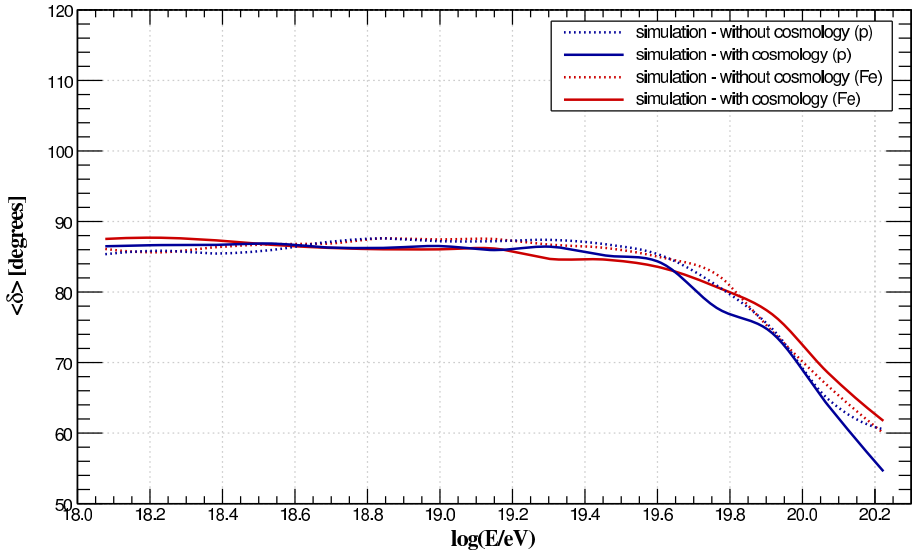

Figure 7.12: Mean value of the deflection as a function of the energy for an iron (red) and proton (blue) composition. The dotted lines correspond to the original 3D simulation, whereas the solid lines correspond to the simulation including cosmological effects.

The aforementioned condition is necessary but not sufficient. Other effects have to be carefully considered when applying this method. One problem is related to the multiplicity of particles reaching the observer. In a realistic situation essentially only one daughter-nucleus from a parent-nucleus reaches the observer. In the hybrid mode when the cosmic ray is resimulated in 1D all daughter-nuclei which do not drop below the minimum energy threshold are kept, implying high multiplicities for the same parent-nucleus. This may introduce a bias which affects the spectrum and composition. Aiming to solve this issue a tentative method was applied, and consisted on randomly choosing one of the daughter-nuclei from a uniform distribution. However, this did not improve the results.

If the problem of the multiplicity is solved, there is still another factor that should be taken into account, which is the elongation of the trajectories described by UHECRs in the presence of magnetic fields. The expected deflection for a particle of energy E under the action of a magnetic field[1] of strength B can be written as

$$\delta(E, D) \approx \frac{qcBD}{E}, \tag{7.5}$$

where q is the charge of the particle, c the speed of light and D the distance of the genitor source. This deflection causes an elongation of the path length given by [461]

$$\Delta X \approx 0.1 Z^2 \left(\frac{B}{\text{nG}}\right)^2 \left(\frac{D}{\text{Mpc}}\right)^2 \left(\frac{\text{EeV}}{E}\right)^2 \left(\frac{\ell_c}{\text{kpc}}\right) \text{ kpc}, \tag{7.6}$$

where ℓ_c is the coherence length of the turbulent magnetic field. If $\Delta X \ll \lambda_{pd}$, where λ_{pd} is the mean free path of photodisintegration, then the hybrid mode should be a reasonable approximation for the complete propagation. This condition can be written in a more clear way as follows:

$$B \ll \frac{1}{10Z} \left(\frac{\text{Mpc}}{D}\right) \left(\frac{E}{\text{EeV}}\right) \sqrt{\frac{\lambda_{pd}}{\ell_c}} \text{ nG}. \tag{7.7}$$

At 100 EeV $\lambda_{pd} \sim 300$ Mpc for iron (see figure 2.4). For a coherence length of ~ 300 kpc, and a source located at a distance ~ 100 Mpc, using equation 7.7 one obtains the following condition: $B \ll 100$ pG

[1] A detailed analytical description of the deflection, its variance and the elongation of the trajectories can be found in ref. [461].

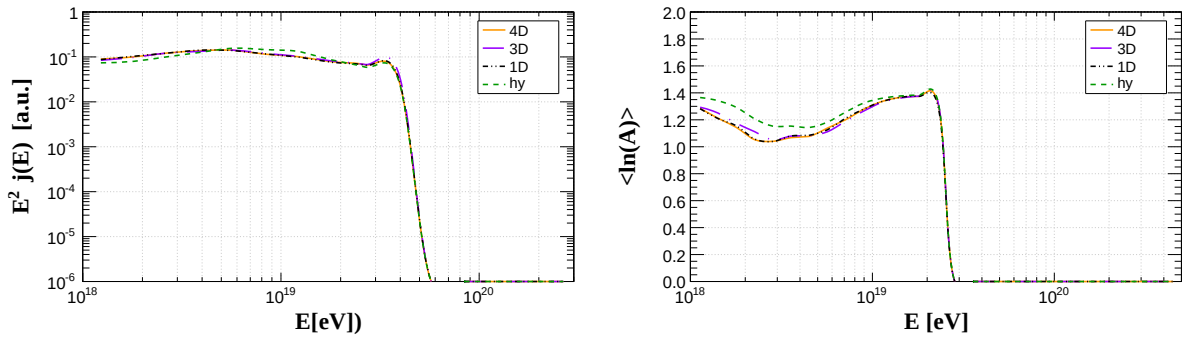

(a) D=200 Mpc

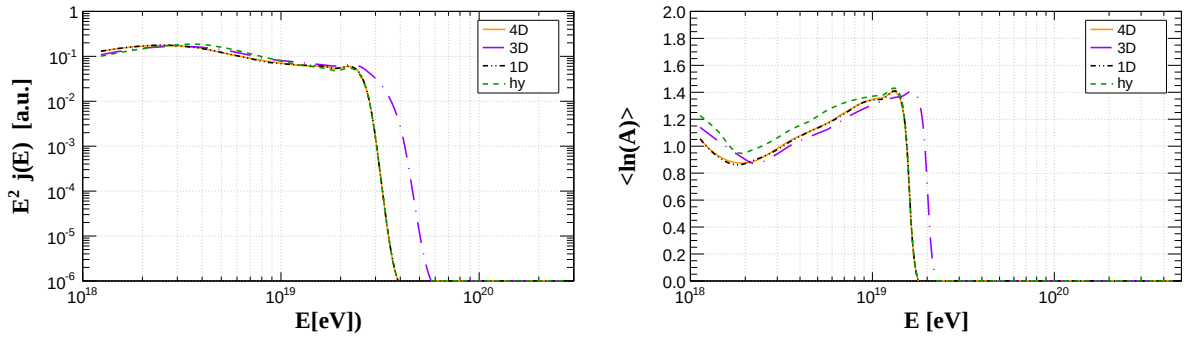

(b) D=500 Mpc

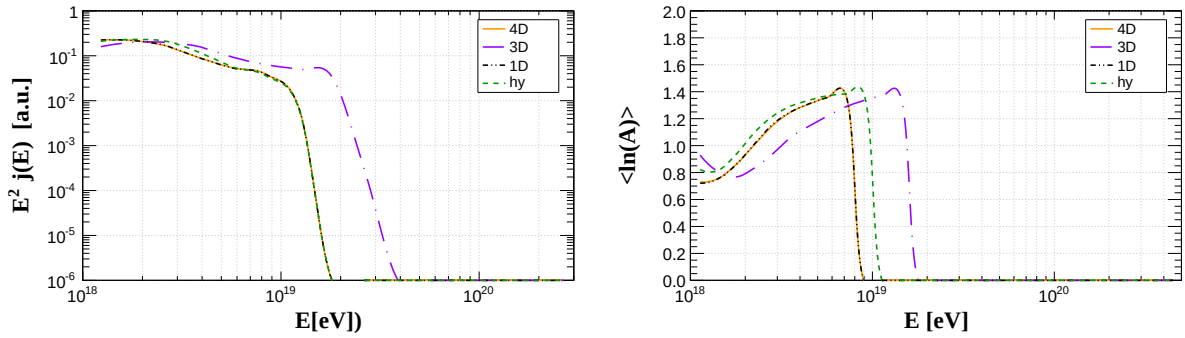

(c) D=1000 Mpc

Figure 7.13: Spectrum (left column) and composition (right column) for a scenario with a single source located at the indicated distances emitting helium with a spectrum E^{-2}.

(for iron primaries). For a distance $D = 1000\,\text{Mpc}$ this condition is even smaller: $B \ll 1\,\text{pG}$. In this case the conditions start to become too strict and the method cannot be applied, since over large distances the probability of the cosmic ray crossing a region with higher magnetic field strength is relatively high.

7.3 4D propagation of UHECRs

7.3.1 Simulation setup

To illustrate the propagation of UHECRs over cosmological distances the benchmark scenario described in section 5.10.2 was used. The composition was assumed to be "galactic", to match the abundance of cosmic rays in the galaxy [486], and is shown in table 7.1.

In order to identify the main factors that affect the spectrum and composition of cosmic rays, four

Table 7.1: Abundance (energy per nucleon) of cosmic rays in the "galactic" composition scenario. The abundances with asterisks are upper limits.

nucleus	abundance
^{1}H	92000
^{3}He	13000
^{9}Be	4.5*
^{11}B	4.5*
^{12}C	447.4
^{14}N	34.2
^{16}O	526.3
^{19}F	0.3*
^{20}Ne	58
^{23}Na	3.2
^{24}Mg	108
^{27}Al	7.8
^{28}Si	100
^{32}S	13.1
^{40}Ar	2.2
^{40}Ca	6.5
^{45}Sc	0.97*
^{48}Ti	0.97*
^{51}V	0.97*
^{52}Cr	1.5
^{55}Mn	1.1
^{56}Fe	97

simulations using variations of the benchmark scenario were done. These scenarios are the following:

- 3D simulation without magnetic fields ($B = 0$), and without cosmological effects;
- 4D simulation without magnetic fields ($B = 0$), including cosmological effects;
- 3D simulation with magnetic fields ($B \neq 0$), and without cosmological effects;
- 4D simulation with magnetic fields ($B \neq 0$), including cosmological effects.

They all have the same source distribution, observer position and injection spectrum, of the form

$$\frac{dN_{inj}}{dE} \propto E^{-\alpha_{src}} \exp\left(-\frac{E}{Ze\mathcal{R}_c}\right), \tag{7.8}$$

where $\mathcal{R}_c$ is the cutoff rigidity.

7.3.2 Results and discussion

In figure 7.14 (left) the energy spectrum is shown for all four scenarios, as well as the corresponding universal spectrum (1D). In the right panel of this figure the relative difference between the spectra are shown. Effects of the magnetic field and cosmology are separately identified. One can clearly see that in this simulation magnetic fields do not affect the shape of the spectrum, for the relative difference is compatible with zero. However, neglecting cosmological effects can introduce errors as large as 30%.

In figure 7.15 the inferred $\langle X_{max}\rangle$ and $\sigma(X_{max})$ are shown. Effects of magnetic fields are negligible, but the inclusion of cosmological effects causes a slight change in the average mass (increase in $\langle X_{max}\rangle$), although it is very small ($\sim$5%).

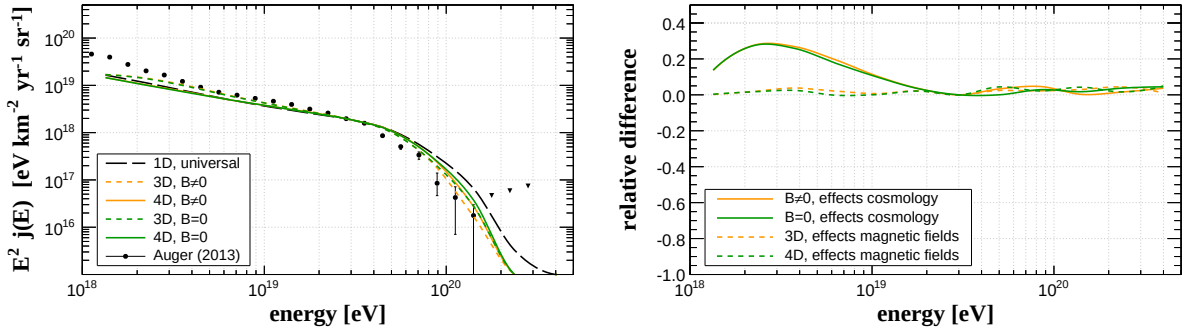

Figure 7.14: Spectrum (left panel) and relative difference (right panel) for the different scenarios considered.

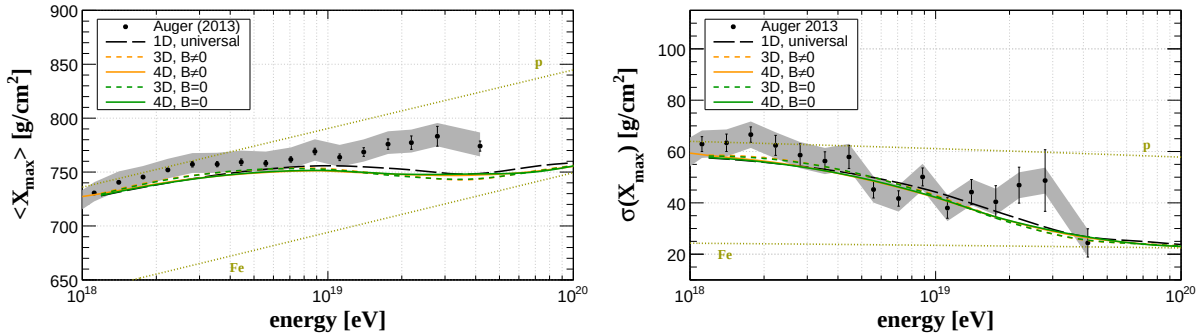

Figure 7.15: Infered $\langle X_{max} \rangle$ and $\sigma(X_{max})$ for the different scenarios. The hadronic interaction model considered is EPOS-LHC.

Another quantity that is significantly affected by cosmological effects is the average deflection as a function of the energy, shown in figure 7.16. One notices that around 50 EeV the deflection for the scenario that does not include these effects is slightly higher than the 4D scenario. The effects of the galactic magnetic field were not included in the analysis.

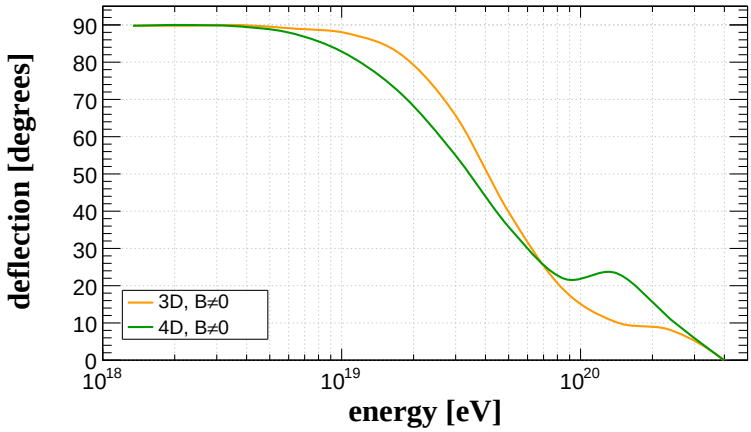

Figure 7.16: Deflection-energy profile for the simulation using the benchmark scenario. Here only the cases in which $B \neq 0$ are displayed, since for $B = 0$ it is trivial. Above 10^{20} eV the low number of events may be responsible for some artificial effects, such as the bump in the curve for the 4D simulation (green curve).

In the scenario studied here the inclusion of cosmological effects significantly altered the spectrum, and in a smaller degree the composition and average deflection per energy. The benchmark scenario contains rather weak turbulent magnetic fields, and therefore their effects are not as large as it would be for a

structured field such as the MHD simulation by Miniati [424], for example.

chapter 8

GRPropa 1.0

8.1 Introduction

There are some notorious works on the propagation of VHE gamma ray-induced electromagnetic cascades. Most of them rely on the small angle approximation, assuming that the opening angle of the cascade is small [2, 18, 19, 152, 430, 487–489]. Few works [16, 490–492] have fully addressed the problem of propagation of electromagnetic cascades in three dimension, including arbitrarily large angles. In these works, however, the adiabatic energy losses due to the expansion of the universe, as well as the cosmological evolution of the photon backgrounds, are not usually taken into account.

The well-known cascade propagation code Elmag[1] [19] is extremely powerful for the one dimensional case, but fails to treat the problem in three dimensions. Moreover, most of the aforementioned works use crude approximations for the intergalactic magnetic fields, which may affect the result considerably, specially if there are regions with very high magnetic field strengths along the line of sight.

In order to properly treat the problem in three spatial dimensions plus time a Monte Carlo code was developed. It is based on the CRPropa code, described in chapter 5, modified to allow the propagation of primary gamma rays in an arbitrary extragalactic magnetic field model considering also cosmological effects. This code will be henceforth called GRPropa.

8.2 An overview of the code

GRPropa is a Monte Carlo code based on the structure of CRPropa 3 [7–9], hence being written in C++. It is designed for the energy range between 10^9 eV and 10^{15} eV. The interactions are handled in a similar fashion to Elmag [19], but with the particle-by-particle approach of CRPropa, without thinning.

The interactions implemented in GRPropa are pair production and inverse Compton scattering. In the energy range in question the dominant background for pair production is the EBL[2], whereas the interaction between electrons[3] and CMB is much larger than the one with the CIB. Nevertheless both backgrounds can be simultaneously taken into account to perform interactions. Synchrotron losses of electrons due to the presence of magnetic fields are also taken into account. Adiabatic energy losses due to the expansion of the universe are relevant for distant sources and are included in the treatment.

As the energy increases the number of secondaries grows exponentially. Above 10^{15} eV the CPU time required for the simulations makes the particle-by-particle approach inviable. Hence, all the interaction rate

[1] Available in http://elmag.sourceforge.net/.

[2] In this chapter CIB and EBL are often used interchangeably. Strictly speaking, the EBL encompasses a much wider range of the electromagnetic spectrum, but the CIB is the dominant component in this case.

[3] In this chapter the term 'electrons' will be used to refer both to electrons and positrons.

tables are available to energies up to 10^{15} eV, although they can easily be extended to higher energies and a "brute force" approach adopted, tracking all particles regardless of the CPU consumption.

8.3 Interactions and energy losses

8.3.1 Pair production

To compute kinematic quantities at each step of propagation it is important to know the mean free path (λ). For a gamma ray of energy E at redshift z propagating through a background of photons with energy ε, the pair production mean free path (λ_{PP}) can be written as

$$\lambda_{PP}^{-1}(E,z) = \frac{1}{8E^2}\int_{s_{min}}^{s_{max}}\int_{\varepsilon_{min}}^{\infty}\sigma_{PP}(s)s\frac{n(\varepsilon,z)}{\varepsilon^2}dsd\varepsilon, \tag{8.1}$$

where the center of mass energy square is given by

$$s = 2E\varepsilon(1-\cos\theta). \tag{8.2}$$

From this equation follows that $s_{max} = 4E\varepsilon_{max}$, with $\varepsilon_{max} \approx 14\,\text{eV}$ being the cutoff energy for the EBL. The threshold energy for this process in the center of mass frame is $s_{min} = 2m_e^2c^4$. The cross section for this process, shown in figure 8.1, can be written as

$$\sigma_{PP}(s) = \frac{\pi r_e^2}{2}(1-\beta^2)\left[(3-\beta^4)\ln\left(\frac{1+\beta}{1-\beta}\right) - 2\beta(2-\beta^2)\right], \tag{8.3}$$

with $r_e = e^2/m_ec^2 \approx 2.818\times10^{-15}\,\text{m}$ designating the classical electron radius, and

$$\beta = \sqrt{1-\frac{4m_e^2c^4}{s}}. \tag{8.4}$$

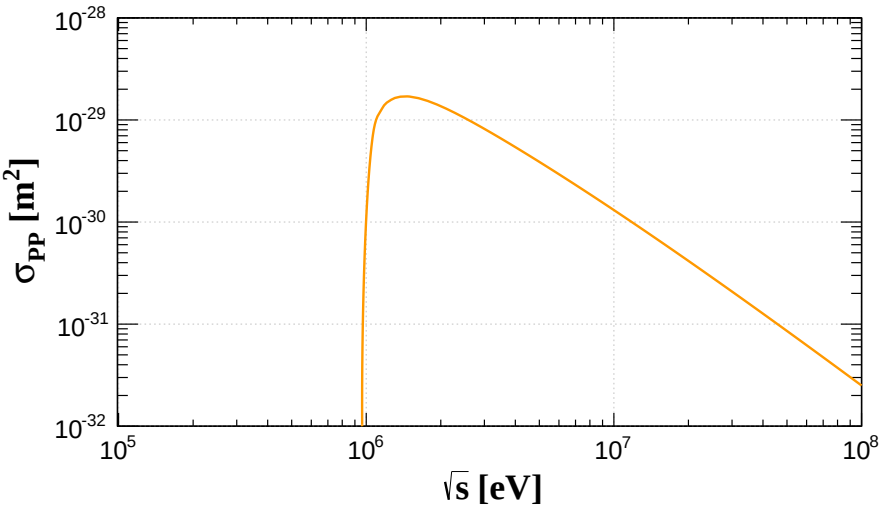

Figure 8.1: Cross section for pair production as a function of s.

During pair production the energy of the electrons produced is $\sim E_\gamma/2$. However, in the limit

$s \gg m_e^2c^4$ this energy is not approximately equally divided[4]. The energy fraction (y) of each secondary lepton is given by [19]

$$\frac{d\sigma_{PP}(s,y)}{dy} \propto y^{-1}\left[\frac{y^2}{1-y} + 1 - y + \frac{(1-\beta^2)^2}{4y(1-y)^2}\right]\left[1 + 2\beta^2 - 2\beta^4\right]^{-1}. \tag{8.5}$$

The other secondary particle will then receive a fraction $1-y$ of the energy of the progenitor photon.

8.3.2 Inverse Compton scattering

The mean free path for the inverse Compton scattering is

$$\lambda_{ICS}^{-1}(E,z) = \frac{1}{8\beta E^2}\int_0^\infty \int_{s_{min}}^{s_{max}} \frac{n(\varepsilon,z)}{\varepsilon^2}\sigma_{ICS}(s)(s - m_e^2c^4)ds d\varepsilon, \tag{8.6}$$

where E is the energy of the incident photon, ε the energy of the background photon and β is given by

$$\beta = \sqrt{1 - \frac{m_e^2c^4}{E^2}}, \tag{8.7}$$

and s is

$$s = m_e^2c^4 + 2E\varepsilon(1 - \beta\cos\theta). \tag{8.8}$$

The minimum and maximum values of s are written as $s_{min} = m_e^2c^4$ and $s_{max} = m_e^2c^4 + 2E\varepsilon_{max}(1+\beta)$, following ref. [19].

The cross section for this interaction is given by [494]

$$\sigma_{ICS}(s) = \frac{3\sigma_T}{8\xi}\frac{m_e^2c^4}{s}\left[\frac{2}{\xi(1+\xi)}(2 + 2\xi - \xi^2 - 2\xi^3) - \frac{1}{\xi^2}(2 - 3\xi^2 - \xi^3)\ln\left(\frac{1+\xi}{1-\xi}\right)\right], \tag{8.9}$$

where

$$\xi = \frac{s - m_e^2c^4}{s + m_e^2c^4}. \tag{8.10}$$

At lower energies $\sigma_{ICS} = \sigma_T$, recovering the classical regime, as shown in figure 8.2.

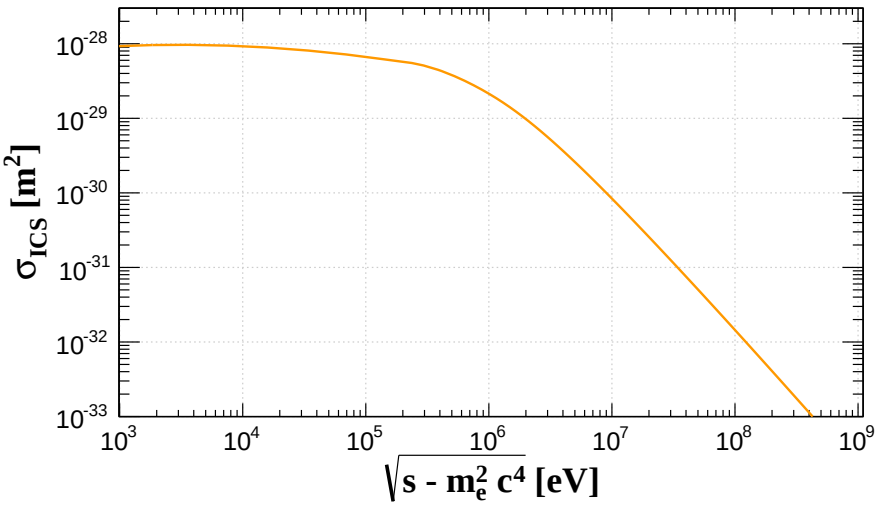

Figure 8.2: Cross section for inverse Compton scattering, as a function of s.

[4] This limit is known as the Klein-Nishima limit [493]. Thomson's classical limit can be recovered if $s \ll m_e^2c^4$.

The change in energy of a photon in the direct Compton scattering, in which the electron is at rest in the laboratory frame, is given by

$$\varepsilon_f = \varepsilon \left[1 + \frac{\varepsilon}{m_e c^2}(1 - \cos\theta)\right], \tag{8.11}$$

where ε is the initial energy of the photon, and

For $E \lesssim 10^{13}$ eV, plugging the CMB number density (equation 1.22) into eq. 8.6, one can easily show that the mean free path does not depend on the energy and can be written as

$$\lambda_{ICS}(E, z) = \lambda(z) = \frac{\pi^2 \hbar^2 c^3}{2\sigma_T} \frac{1}{\varepsilon^3 \zeta(3)(1+z)^2}. \tag{8.12}$$

8.3.3 Synchrotron emission

Synchrotron losses are implemented following Elmag [19] and ref. [495], in which the energy loss per unit distance is

$$\frac{dE}{dx} \approx \frac{m_e^2 c^4 \chi^2}{\hbar c \left(1 + a_1(1+\chi)\ln(1 + a_2\chi) + a_3\chi^2\right)^{\frac{2}{3}}}, \tag{8.13}$$

where the parameters a_i are: $a_1 = 4.8$, $a_2 = 1.7$ and $a_3 = 3.44$. Here χ is given by

$$\chi = \frac{\left|\vec{p} \times \vec{B}\right|}{m_e c B_{cr}}, \tag{8.14}$$

where $B_{cr} = 4.14 \times 10^{13}$ G is the critical magnetic field. Because the synchrotron radiation emitted has energy typically $\lesssim$ GeV, it can be neglected for studies in the GeV - PeV energy range.

8.3.4 Adiabatic losses

The adiabatic losses are simply given by equation 2.27, the same used in CRPropa. The standard cosmological parameters used by default in the code are: $\Omega_m = 0.318$, $\Omega_\Lambda = 0.682$ and $H_0 = 67.1$ km/s/Mpc.

8.4 Detection methods

The motivation for the development of GRPropa was the possibility of studying extended emission of very-high energy gamma rays from objects at cosmological distances. The main propagation modes are:

- 1D mode: the propagation is performed in one dimension taking into account only the interactions between the particles and photon backgrounds;
- 3D mode: in this mode pair production and inverse Compton scattering are taken into account, considering also magnetic deflections of electrons; adiabatic losses are not considered;
- 4D mode: this mode is the same one used in CRPropa 3 (see chapter 5), and considers the redshift dependence of the photon backgrounds as well as adiabatic losses due to the expansion of the universe and effects of extragalactic magnetic fields.

For complete studies the recommended mode is the 4D. In this mode a particle is flagged as detected when it reaches a sphere with a given radius (R_{obs}), within a time window Δt. The value of R_{obs} should be chosen in such a way that it mimics the field of view of a given gamma ray telescope. To optimize the

number of events detected, the standard detection mode is a sphere with radius $R_{obs} = D$, where D is the distance of the source located at redshift $z = z_{src}$. This way, essentially all particles which do not drop below the arbitrarily chosen energy threshold are detected. The actual selection of events which would be detected by a telescope with a given point spreading function θ_{psf} has to be made by the user *a posteriori*. This post processing is done in a similar fashion to ref. [16], in which a patch about the size of the field of view of the telescope is chosen and approximated by a plane[5].

8.5 Comparisons with Elmag

The first test to validate the implementation was a comparison between the fluxes obtained by Elmag and GRPropa in the absence of magnetic fields. This comparison is shown in figure 8.3.

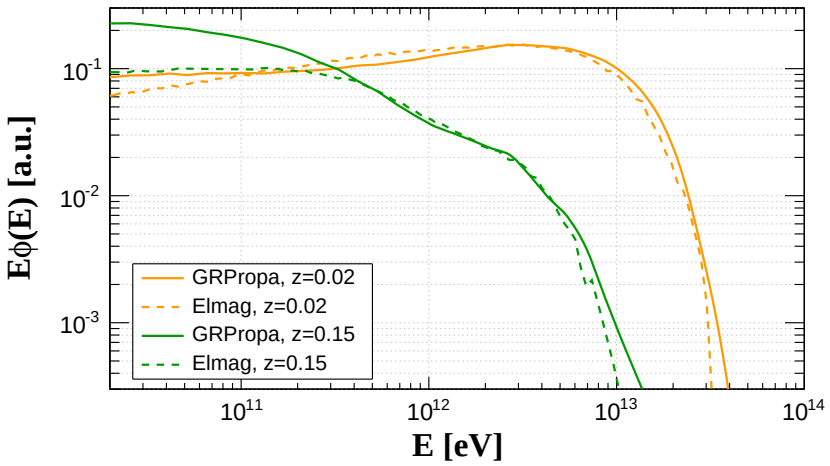

Figure 8.3: Diffuse flux of gamma rays for a source injecting 100 TeV gamma rays at redshifts $z = 0.02$ (orange curves) and $z = 0.15$ (green curves). Dashed lines are the corresponding flux estimated by Elmag and solid curves by GRPropa.

In this figure a small discrepancy between Elmag and GRPropa can be noticed at energies $\lesssim$ TeV. This difference can, in principle, be explained by the choice and implementation of different EBL models. For the GRPropa simulation the model by Finke *et al.* [50] was used, whilst the Elmag simulation was done with a default model (Kneiske & Dole [49] lower limit). Therefore, due to the lower density of background photons, in the Elmag simulation less interactions occur, compared to GRPropa, decreasing the amount of secondary particles in the region between 10 and 100 GeV. Moreover, Elmag adopts a weighted sampling procedure, thinning the resulting secondaries. In GRPropa the full three-dimensional Monte Carlo particle-by-particle approach without thinning is adopted yielding more precise results, although in this example the propagation is essentially one-dimensional due to the absence of magnetic fields.

[5] Even though the cascades can be extended, their angular sizes are small, and so this (small angle) approximation is valid. For very large angular sizes a small sphere which mimics the properties of the detector has to be used, since the curvature of the large sphere would become relevant and the tangent plane approximation would be inaccurate.

8.6 Applications

8.6.1 Spectrum of the blazar 1ES 0229+200

An example of an application is the study of the spectrum of the blazar 1ES 0229+200, a BL Lacertae object with hard spectrum extending up to energies ~ 10 TeV. It is located at $z \approx 0.14$ ($D \approx 580$ Mpc). This object was thoroughly studied in several wavelengths and has been used by many authors [2, 17, 18, 152, 430] to estimate the strength of intergalactic magnetic fields. Its estimated spectral index is rather hard (~ 1.3) and the cutoff energy is $E_{max} \sim 6$ TeV. It has been measured by the HESS telescope [496] in the TeV energy range.

Its spectrum was simulated with GRPropa, assuming the parameters previously described and is shown in figure 8.4. One can clearly the set of parameters chosen are adequate for describing the spectrum. Moreover, the spectral shape obtained with the simulation is in accordance with other works (see e.g. ref. [152]).

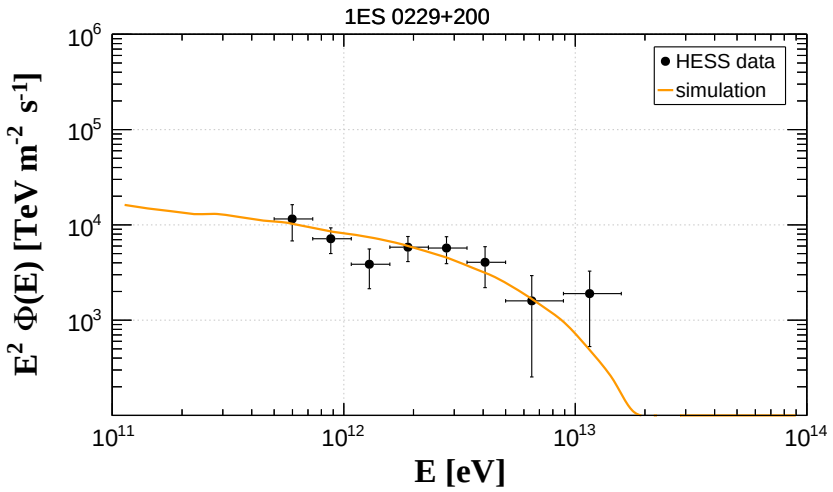

Figure 8.4: Spectrum of the blazar 1ES 0229+200 as measured by the HESS telescope, and simulated by GRPropa.

8.6.2 Extended emission at E$\gtrsim$10 TeV

The computational setup of GRPropa is the same as CRPropa's in what concerns magnetic fields (see section 5.8 for details). The effect of magnetic field on cascades is the increase in the opening angle of pairs, creating an extended emission around a point-like source. This effect can be clearly seen in figure 8.5, in which a source located at redshift $z = 0.2$ emits gamma rays with 100 TeV, within a jet with opening angle $\Psi = 5°$. This angle is typical in blazars, and is of the same order of the inverse of the Lorentz factor of the jet. Three magnetic field configurations are compared in this example, all of them being Kolmogorov turbulent fields with coherence length $\ell_c \sim 0.5$ Mpc, and RMS values 0.1, 1.0 and 10 pG.

Defining a (tangent) plane of detection, as described in section 8.4, it is possible to estimate the angular size of the extended emission of the cascades shown in figure 8.6. The arrival directions of gamma rays on this plane of detection are shown in figure 8.6. To generate this figure all events which did not drop below the minimum energy threshold (set to 10 GeV) were collected and no posterior cuts to mimic the point spreading function and field of view of the detector were made.

In figure 8.6 it is clear that the size of the halo around the source increases with the magnetic field. This relation allows one to constrain intergalactic magnetic fields, topic which will be explored in details in

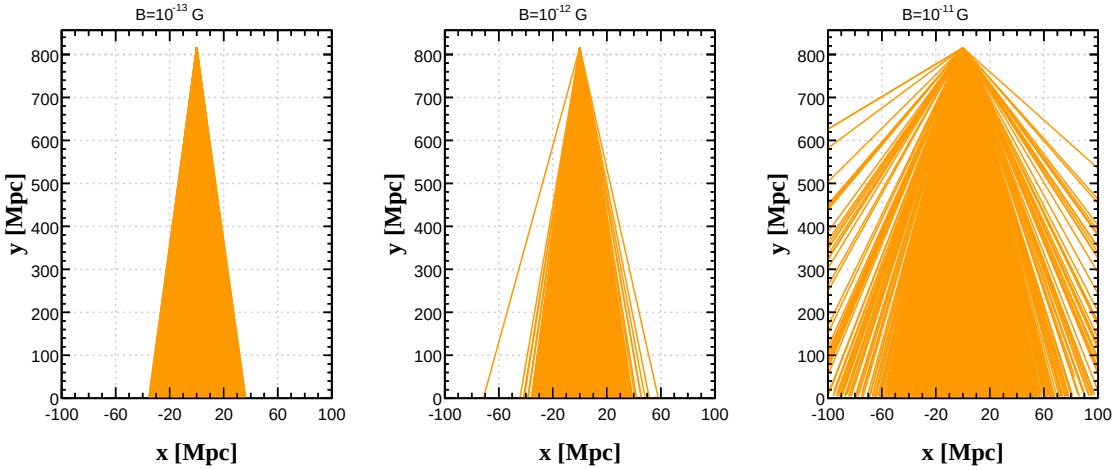

Figure 8.5: Cascades induced by gamma rays with energies $E = 100\,\mathrm{TeV}$ in turbulent Kolmogorov magnetic fields with coherence length 500 kpc and root mean square magnetic field strengths 0.1 (left), 1.0 (middle) and 10 pG (right panel). The source is located at $z = 0.2$ and emits particles within an angle of 5°.

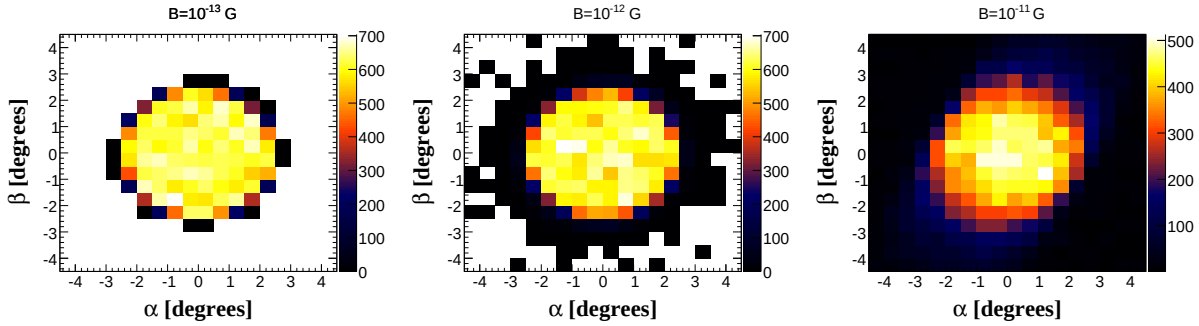

Figure 8.6: Observed arrival directions of secondary gamma rays induced by primaries with energies $E = 100\,\mathrm{TeV}$ in turbulent Kolmogorov magnetic fields with coherence length 500 kpc and root mean square magnetic field strengths 0.1 pG (left), 1.0 pG (middle) and 10 pG (right panel). The source is located at $z = 0.2$ and emits particles within an angle of 5°.

chapter 9.

chapter 9

Blazar pair halos and EGMFs

9.1 Overture

With the advent of the imaging air Cherenkov telescopes (IACTs) very high energy processes involving gamma rays can be studied with unprecedented precision. A great advantage of IACTs is that they provide good angular resolution ($\theta_{psf} \sim 0.1°$), making VHEGR astronomy possible.

Spectral, angular and temporal properties of astrophysical objects are affected by the interactions between gamma rays and the pervasive photon fields and consequently the development of the electromagnetic cascade. Furthermore the presence of intervening IGMF can interfere with the development of the cascade causing point sources to appear extended. This phenomenon has been studied by several authors [16, 489–491, 497].

Recently the Fermi Large Area Telescope (Fermi-LAT) observed and cataloged many blazars. At higher energies IACTs have detected TeV emission by several blazars. Interestingly some of them such as 1ES 0229+200 [496], 1ES 1101-232 [498], 1ES 0347-121 [499] and RGB J0710+591 [500], among others, present unusually hard spectra. As a matter of fact, the intrinsic spectra of gamma ray sources is poorly known and cannot be easily disentangled from other effects such as magnetic deflections of the charged leptonic component of the electromagnetic cascade.

Blazar pair halos are useful to probe magnetic fields, for they can be larger than the typical point spread function of the detectors. Their size is roughly inversely proportional to the maximal energy of the gamma ray emitted by the source, the strength of the intervening magnetic fields, and the geometry of detection. In this chapter the relation between blazar pair halos and intergalactic magnetic fields is studied. The analytical description of the formation of pair halos follows Neronov & Semikoz [487, 488].

9.2 An analytical description of the formation of pair halos

TeV gamma rays emitted by distant sources such as blazars interact with ambient radiation fields. The typical mean free path for this process is given by equation 8.1, which is transcribed below for the sake of completeness:

$$\frac{1}{\lambda'_{PP}(E(z),z)} = \frac{1}{8E^2(z)} \int_{s_{min}}^{s_{max}} \int_{\varepsilon_{min}}^{\infty} \sigma_{PP}(s) s \frac{n(\varepsilon,z)}{\varepsilon^2} ds d\varepsilon, \tag{9.1}$$

where E is the energy of the gamma ray, ε the energy of the background photon. The pair production cross section is shown in equation 8.3. The main photon field which contributes to this process is the EBL, which is model dependent. As discussed in section 1.4.2, the redshift evolution of the CIB, the dominant

component of the EBL, is not trivial. As a first approximation one can assume that

$$n_{EBL}(\varepsilon, z) = n_{EBL}(\varepsilon, z = 0)(1 + z)^2. \tag{9.2}$$

The mean free path for pair production can then be rewritten using the approximation [488]

$$\lambda'_{PP}(E(z), z) = \frac{800\kappa(E(z), z)}{(1 + z)^2} \left(\frac{\text{TeV}}{E(z)}\right) \text{Mpc}, \tag{9.3}$$

where κ is a parameter to account for model uncertainties of EBL models, E_g is the energy of the gamma ray at generation time (redshift z_g).

The optical depth (τ) for pair production has the following temporal dependence:

$$\frac{d\tau(E(z), z)}{dt} = \frac{c}{\lambda'_{PP}(E(z), z)}. \tag{9.4}$$

One can show that $\tau(t_{PP}) = 1$, with t_{PP} designating the instant when electrons were created.

It is convenient to work with the mean free path in comoving coordinates, which is

$$\lambda_{PP}(E(z), z) = c \int_{t_{PP}}^{t_g} \frac{dt'}{a(t')}, \tag{9.5}$$

where t_g is the time of emission of the gamma ray. If $z_{PP} \equiv z_{PP}(t_{PP})$ and $z_g \equiv z_g(t_g)$ have approximately the same value[1], i.e, if $z_{PP} \approx z_g$, then the optical depth can be written as

$$\tau(E(z), z) = \int_0^{z_g} dz \frac{dt}{dz} \frac{c}{\lambda'_{PP}(E_g, z)}, \tag{9.6}$$

thence yielding [488]

$$\tau(E(z), z_g) = \frac{2c}{3} \frac{\sqrt{\Omega_m(1 + z_g)^3 + \Omega_\Lambda} - 1}{H_0 \Omega_m \lambda'_{PP}(E, 0)} \tag{9.7}$$

if one adopts the approximation from equation 9.3.

Another relevant result can be obtained by integrating equation 9.6 from $z = z_{PP} \approx z_g$ to $z = 0$. At TeV energies the relation

$$\tau(E, z) = \frac{D'}{\lambda'_{PP}}, \tag{9.8}$$

is a satisfactory approximation, since $z_{PP} \approx z_g$. Here the source distance D' is expressed in physical coordinates.

Let $j(E)$ be the observed flux of gamma rays of energy E, and $j_0(E_g)$ the injected spectrum. The production of pairs due to the interaction of gamma rays with the EBL stems a reduction of the flux. This reduction of the flux is an exponential attenuation of the form

$$j(E) = j_0(E_g) \exp\left(-\tau(E(z), z)\right), \tag{9.9}$$

where z_g is the redshift of the generation of gamma rays with energy E_g. The inverse Compton scattering

[1] This assumption is a good approximation for energies $\sim$ TeV. For lower energies ($E \lesssim 10$ GeV) it does not hold.

between electrons and the CMB generates secondary gamma rays with typical energies

$$E = \frac{4\varepsilon}{3(1+z_{PP})}\left(\frac{E_g}{m_e c^2}\right)^2 \approx 0.8\left(\frac{E_g}{\mathrm{TeV}}\right)^2 \mathrm{GeV}. \tag{9.10}$$

Here E_g is the energy of the primary gamma ray at the source. Notice that $\varepsilon = \varepsilon(z_{PP}) \sim 0.6(1+z_{PP})\,\mathrm{meV}$ (typical energy of microwave photon). For the sake of calculation it is assumed that electrons and positrons carry half of the energy of the incident gamma ray, which is enough for rough analytical estimates, but can be improved in Monte Carlo simulations (see chapter 8 for the exact treatment). It is worth stressing that the typical mean free path for inverse Compton scattering is $\lambda_{ICS} \sim$ kpc, which is much smaller than λ_{PP}. Hence it is a good approximation to consider prompt emission of secondary photons once the pairs are created.

The mean free path for electrons interacting with the CMB can, at first order, be approximated by

$$\lambda_{ICS}(E(z), z) = \frac{3m_e^2 c^3}{4\sigma_T n_{CMB}(z) E_e(z)} \approx \frac{300}{(1+z_{PP})^4}\left(\frac{\mathrm{TeV}}{E_e(z)}\right)\ \mathrm{kpc}, \tag{9.11}$$

where the energy of the electron E_e is at redshift z, and σ_T is the Thomson cross section.

9.2.1 Extended emission around point sources

In this work the focus will be extended emissions of TeV gamma rays by blazars. As discussed in ref. [487], the naive expectation that the gamma ray flux will be suppressed due to production of pairs which will likely not reach Earth is not accurate. Deflections of electrons whose initial momenta do not point to Earth can contribute for the production of secondary photons which reach the observer, as shown in figure 9.1.

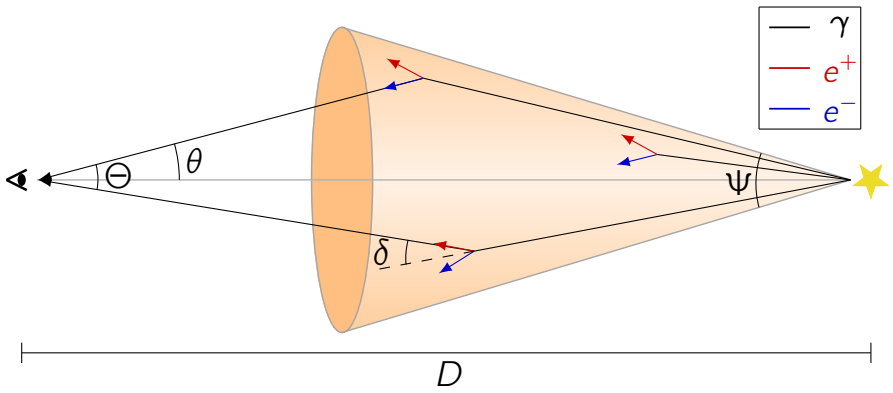

Figure 9.1: General scheme of the development of an electromagnetic cascade. Gamma rays (black) emitted by a source (yellow star) through a jet of opening angle Ψ interacts with the EBL producing electrons (blue) and positrons (red). The pairs are split due to the presence of a magnetic field forming an angle 2δ, and scatter CMB photons via inverse Compton scattering. These secondary photons may reach Earth. The splitting of the pairs cause a point-like source to appear extended with an angular size Θ. Here θ denotes an observation angle.

The typical separation between the electrons and positrons which compose the pair depends on the magnetic field strength (B). Two regimes are possible, depending on the coherence length (ℓ_c) of the field. If the electrons cool down in scales much smaller than the coherence length of the magnetic field, i.e., if $\ell_c \ll \lambda_{ICS}$, then the propagation is diffusive and δ is

$$\delta = \frac{\sqrt{\lambda_{ICS}\ell_c}}{R_L}. \tag{9.12}$$

In the ballistic regime $\ell_c \gg \lambda_{ICS}$ and therefore

$$\delta \approx \frac{\lambda_{ICS}}{R_L}. \tag{9.13}$$

Hence δ can be written as

$$\delta(E(z), z) = \begin{cases} 1.2 \left(\frac{\text{TeV}}{E(z)}\right)^2 \left(\frac{B(z)}{\text{pG}}\right) & \ell_c \gg \lambda_{ICS} \\ 44.7 \left(\frac{\text{TeV}}{E(z)}\right)^{\frac{3}{2}} \left(\frac{B(z)}{\text{pG}}\right) \left(\frac{\ell_c(z)}{kpc}\right) & \ell_c \ll \lambda_{ICS} \end{cases}, \tag{9.14}$$

where E is the energy the primary gamma ray at redshift z. Here $B(z) = B_0(1+z)^2$, where B_0 is the magnetic field strength at $z = 0$, and $\ell_c(z) = \ell_{c,0}/(1+z)$ the coherence length at the indicated redshift.

By analyzing figure 9.1 one can see that for the top-most pair the angle θ can be written as

$$\frac{\sin\theta}{\sin\delta} = \frac{\lambda_{PP}}{D}. \tag{9.15}$$

In this two-dimensional analogy the actual extension of the source (Θ) is simply the sum of the angle θ for the pair at the top, and the bottom-most pair. If they are symmetric and if $\lambda_{PP} \ll D$, then one has

$$\Theta(E_0, z_g) \approx 2\frac{\lambda_{PP}(E_g, z_g)}{D}\delta(E_g, z_g), \tag{9.16}$$

where all the distances considered are assumed to be comoving for simplicity, and $E_0 \equiv E(0)$ is the observed energy. Using equation 9.8 this expression reduces to

$$\Theta(E_g, z_g) = \frac{2\delta(E_g, z_g)}{\tau(E_g, z_g)}. \tag{9.17}$$

Combining the equation above with equations 9.3 and 9.14 one can see that the source will appear extended with angular size [488]

$$\Theta(E(z), z) \approx \begin{cases} 50^\circ \left(\frac{\text{TeV}}{E(z)}\right) \left(\frac{B(z)}{\text{pG}}\right) \tau(E(z), z) & \ell_c \gg \lambda_{ICS} \\ 12^\circ \left(\frac{\text{TeV}}{E(z)}\right)^{\frac{1}{2}} \left(\frac{B(z)}{\text{pG}}\right) \left(\frac{\ell_c(z)}{\text{kpc}}\right)^{\frac{1}{2}} \tau(E(z), z) & \ell_c \ll \lambda_{ICS}, \end{cases} \tag{9.18}$$

where E is the energy of the primary gamma ray.

9.2.2 Time delay

The elongation of the trajectory of the particles due to magnetic deflections leads to a time delay in the arrival of the cascade signal. From figure 9.1 one can choose one of the cascades to calculate the time delays (Δt). The resulting geometry of this process is shown in figure 9.2.

The time delay can be written as

$$\Delta t = t_g - (t_{PP} + t_{sec}), \tag{9.19}$$

where t_{PP} is the lookback time at redshift z_{PP}, t_{sec} is the propagation time of the gamma rays produced via ICS, and t_g is the lookback time of emission of the primary gamma ray.

The angle χ can be calculated using simple trigonometry and reads $\chi = \delta - \theta$. The distance propagated

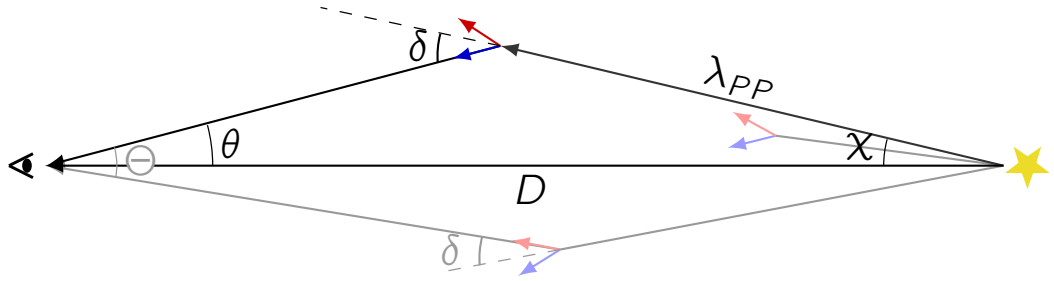

Figure 9.2: Schematic representation of the geometry of the electromagnetic cascade. The lines follow the same color convention from figure 9.1.

by the secondary gamma can be obtained by applying the law of cosines to the triangle shown in figure 9.2. Thence one has

$$(ct'_{sec})^2(E,z) = \sqrt{D^2 + \lambda_{PP}^2(E,z) - 2\lambda_{PP} D\cos\chi}, \tag{9.20}$$

where t' denotes the conformal time, since all distances are assumed to be comoving. To work with time delays one has to convert everything into light travel time, which yields the implicit equation

$$\int_0^{z_{pp}} dz \frac{dt}{dz}(1+z) = \int_{t_0 - t_{sec}}^{t_0} \frac{dt'}{a(t')} = \sqrt{D^2 + \lambda_{PP}^2(E,z) - 2\lambda_{PP}(E,z) D\cos\left(\delta(E,z) - \frac{1}{2}\Theta(E,z)\right)}, \tag{9.21}$$

with t_0 indicating the present time, and Θ being the angular size of the cascade assuming that it develops approximately symmetrically with respect to the line which connects the source and observer.

Using the assumption that the opening angle of the pairs is small and that $z_{PP} \approx z_g$ one can write the time delay in a suitable form:

$$\Delta t(E,z) \approx \frac{1}{2}\lambda(E(z),z)\delta(E(z),z)\left[1 - \frac{\lambda_{PP}(E(z),z)}{D}\right]. \tag{9.22}$$

Finally, substituting eq. 9.14 into this equation one obtains

$$\Delta t = \begin{cases} 2\times 10^9 \dfrac{\kappa(E_g,z_g)}{(1+z_g)^5}\left(1 - \dfrac{1}{\tau(E_g,z_g)}\right)\left(\dfrac{\mathrm{TeV}}{E_0}\right)^{\frac{5}{2}}\left(\dfrac{B_0}{\mathrm{fG}}\right)^2 \mathrm{s} & \lambda_{PP} \ll l_c \\ 3\times 10^7 \dfrac{\kappa(E_g,z_g)}{(1+z_g)}\left(1 - \dfrac{1}{\tau(E_g,z_g)}\right)\left(\dfrac{\mathrm{TeV}}{E_0}\right)^{2}\left(\dfrac{B_0}{\mathrm{fG}}\right)^2\left(\dfrac{l_{c,0}}{\mathrm{kpc}}\right) \mathrm{s} & \lambda_{PP} \gg l_c \end{cases}. \tag{9.23}$$

9.3 Setup of simulations

The formation of pair halos in two blazars was studied: 1ES 0229+200 [17, 152, 496] and 1ES 2344+514 [501–503]. Simulations using GRPropa were performed, using the parameters shown in table 9.1.

Table 9.1: Parameters used in the simulations. Here α_{src} is the source spectrum, E_{max} the maximum energy, z the redshift, D the comoving source distance, and Ψ the jet angle.

object	α_{src}	E_{max} [TeV]	z	D [Mpc]	Ψ
1ES 2344+514	2.55	300	0.044	194.7	5.0°
1ES 0229+200	1.50	300	0.140	604.9	5.0°

The magnetic fields used in these simulations is a Kolmogorov turbulent field grid with coherence length $\ell_c \approx 1.2\,\mathrm{Mpc}$, with maximum scale 5 Mpc and root mean square (RMS) values 10^{-10} G, 10^{-12} G,

10^{-14} G and 10^{-16} G. The exact same realization was used for the whole analysis, except for the RMS value of the field. The EBL model adopted was the one by Finke *et al.* [50].

The opening angles of the blazar jets (Ψ), assumed to be pointing toward Earth with no misalignment, were set to $\Psi = 5°$, which is the minimal possible angle for a jet with bulk Lorentz factor $\gamma_{jet} \sim 10$ [16].

The detection method is the one described in chapter 8, previously used in ref. [16]. Particles are detected when reaching a sphere with a radius equal to the distance to the source. The coordinate system adopted is conveniently chosen to be such that Earth is located at (0,0,0) and the source at (D,0,0). The plane of detection is formed by two angles, α and β, which are respectivelly the angles formed between the y and z components of the arrival direction and the imaginary line connecting the source and the observer.

9.4 Result of analysis

The simulated halos for 1ES 0229+200 for magnetic fields with RMS values 10^{-10} G, 10^{-12} G and 10^{-14} G are shown in figure 9.3, for three energy ranges: $E > 10$ GeV, $E > 1$ TeV and $E > 10$ TeV. One clearly notices the existence the formation of a glow around the source which increases with the magnetic field strength. A significant fraction of the total number of events start to fall outside the area which correspond to the source extension. For $B \lesssim 10^{-14}$ G no halos were formed.

Notice that in figure 9.3 the events were injected uniformly within a cone with opening angle $\Psi = 5°$, hence explaining the plateau for $\alpha < 2.5°$ and $\beta < 2.5°$. In a realistic case the point spread function of the detector would have to be taken into account. In this case the halos shown in the figure would be convoluted with the point spread function of the detector, which is usually assumed to be a two-dimensional gaussian. The approximation of a top-hat distribution might not be realistic but is enough for the purposes of this first analysis. Here the binning chosen was approximately the size of the typical PSF of IACTs ($\sim 0.1°$).

For $B = 10^{-10}\,G$ and $E > 300$ GeV the halo is not symmetric around the source (figure 9.3, bottom row, second panel). This might be explained by a conjunction of effects. First, pair production generates approximately the same number of electrons and positrons, explaining why the excesses are diametrically opposed. Second, turbulent field modes varying in scales much larger than the Larmor radius of electrons are responsible for anisotropic diffusion, an effect similar to what has been shown in refs. [504, 505] for the case of cosmic rays. Moreover, the field near the observer may also play an important role. Other magnetic field configurations may not result in this anisotropic behavior. Systematic analyses spanning a wider parameter space for the field and detailed studies of the trajectories of particles may provide further insights about the morphology of the halos.

Similarly, for 1ES 2344+514 maps containing the arrival directions in the plane of detection were obtained and are shown in figure 9.4. The formation of the halo proceeds in a similar fashion to the case of 1ES 0229+200, already discussed.

The surface brightness ($S(\theta)$) in terms of $\theta = \sqrt{\alpha^2 + \beta^2}$ is shown in figure 9.5, for $B = 10^{-12}$ G and different energy ranges, for both blazars. One can see that for an observation angle $\theta < \Psi$ the curve is approximately constant, which reflects the assumption of a jet with initial momenta uniformly distributed within $\Psi = 5°$. Furthermore, the high-θ tail of the distributions is heavier for higher energies, as expected according to the behavior of figures 9.3 and 9.4.

9.5 Discussion

In ref. [16] extended emission from the blazar Mrk 421 was studied. Similar parameters such as the jet opening angle were used, and the results were similar to the ones here presented. In this reference the

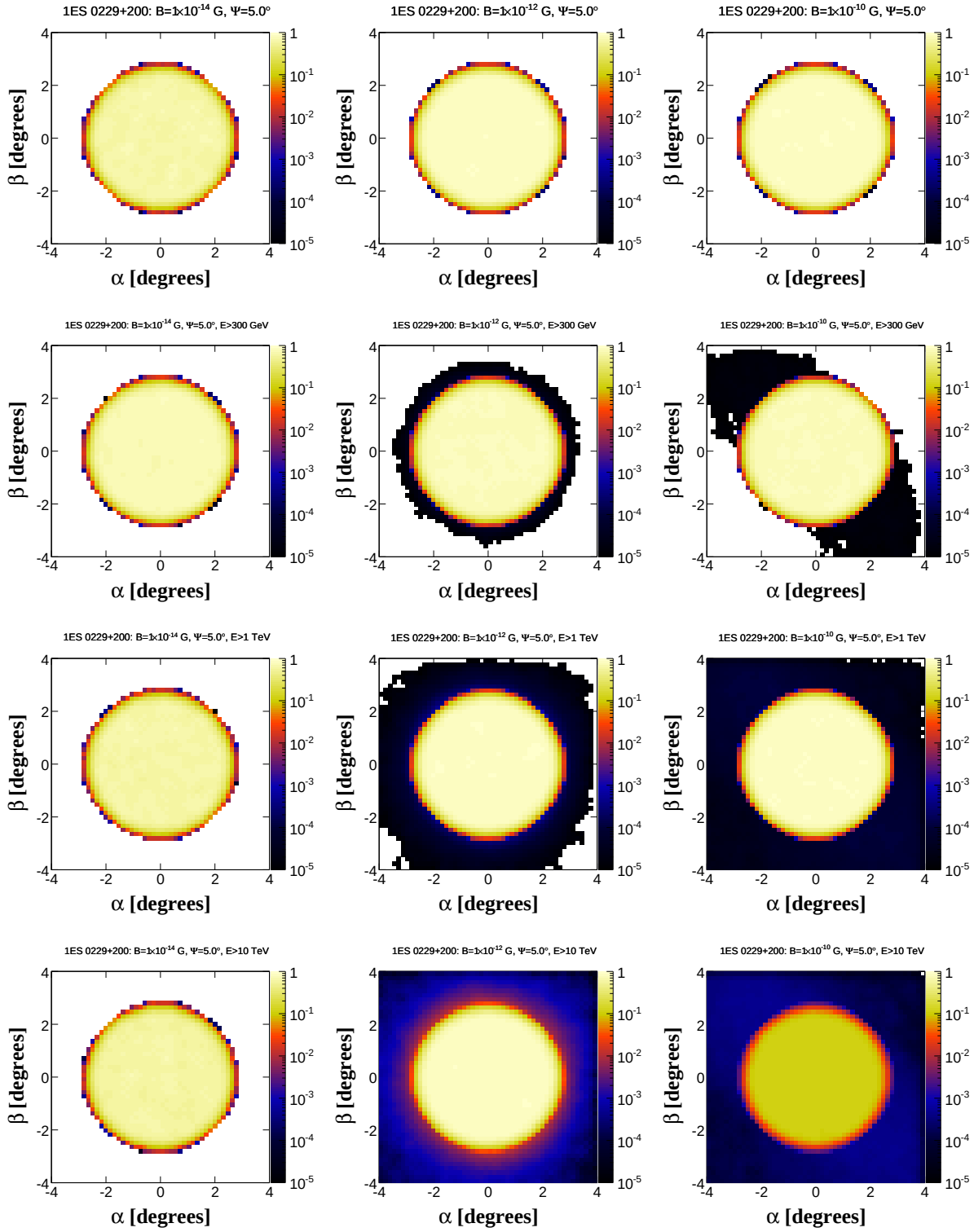

Figure 9.3: Simulated pair halos for 1ES 0229+200 for three magnetic field strengths 10^{-14} G (left column), 10^{-12} G (middle column), 10^{-10} G (right column), for the the following energy ranges: $E > 10$ GeV, $E > 300$ GeV, $E > 1$ TeV and $E > 10$ TeV (from top to bottom). The color scale indicates the number of events per bin, where each bin has a size of approximately 0.1°.

authors devised a method for inferring the strength of the IGMF based on the extension of the halo, which can be applied in the range $10^{-12} \leq B[\mathrm{G}] \leq 10^{-16}$. For $B \gtrsim 10^{-10}$ G their method does not work. From figures 9.3 and 9.4 one can see that for this magnetic field strength the morphology of the halo is different,

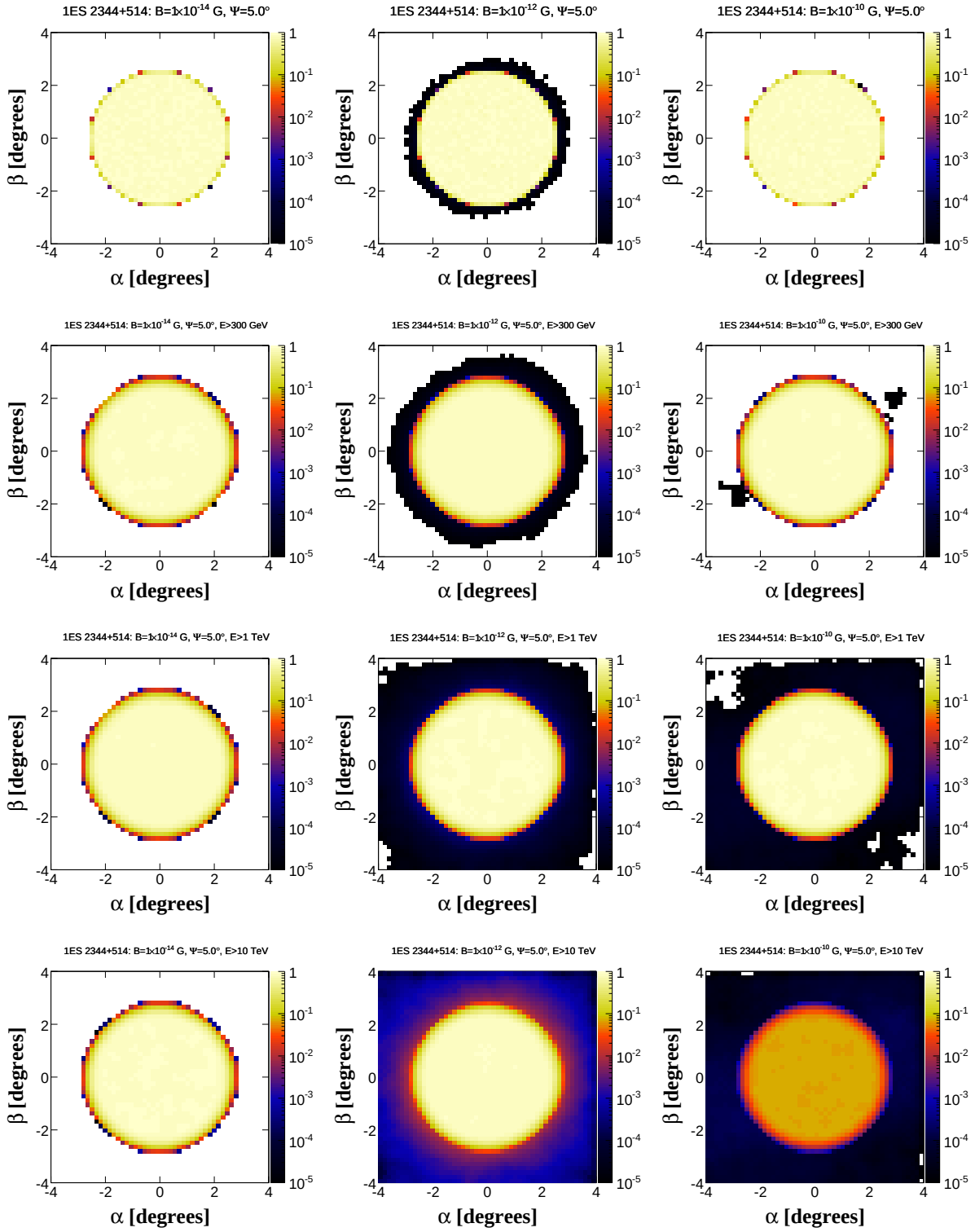

Figure 9.4: Simulated pair halos for 1ES 2344+514 for three magnetic field strengths: 10^{-14} G (top row), 10^{-12} G (middle row), 10^{-10} G (bottom row) and 10^{-10} G (bottom right). The color scale indicates the number of events per bin, where each bin has a size of approximately 0.1°.

implying that the strength of the IGMF would not be trivially obtained simply from the extension of the source (Θ_{ext}).

A similar analysis was also performed by the authors of ref. [491]. In this case, however, the authors use a more realistic magnetic field distribution along the line of sight, obtained from MHD simulations, namely

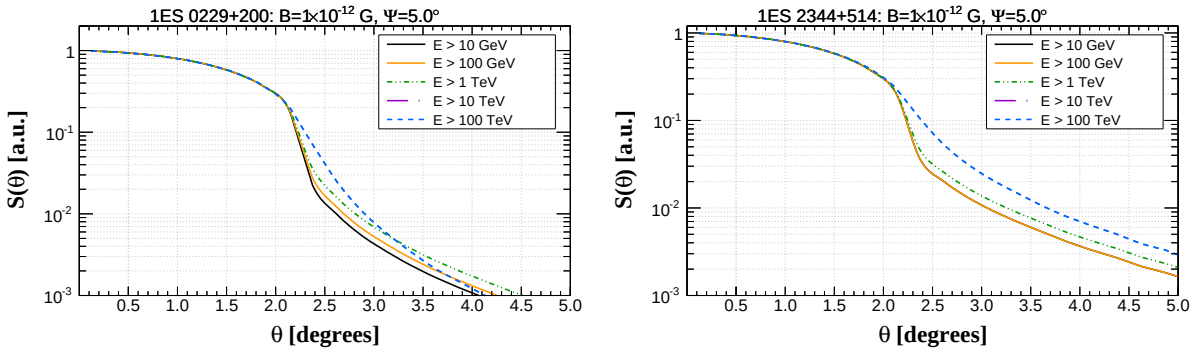

Figure 9.5: Surface brightness of 1ES 0229+200 (left) and 1ES 2344+514 (right) for different energy ranges as a function of the the observation angle. This case is for $B = 10^{-12}$ G.

the ones by Dolag *et al.* [465]. Their conclusion is that pair halos can (optimistically) be detected or excluded by the current generation of IACT facilities. This is somehow in agreement with results here obtained, which indicate that in this particular configuration of parameters pair halos for $B \sim 1\,\mathrm{pG}$, $\ell_c \sim 1.2\,\mathrm{Mpc}$ could be detected in the TeV energy range.

For this analysis the EBL model by Finke *et al.* [50] was used. By using other models the size of the halos could decrease. For instance, in the lower limit model from ref. [49] the surface brightness ($S(\theta)$) would decrease faster with θ compared to what is shown figure 9.5.

There is a clear relationship between the maximal energy of gamma rays emitted by a source (E_{max}) and the formation of halos, as can be seen in figures 9.3, 9.4 and 9.5. The radial profile of the surface brightness is affected by the energy of the gamma rays. This means that the size of the extended regions (Θ) is roughly proportional to the inverse of the energy for a given magnetic field and optical depth, as shown in equation 9.18. As pointed out in ref. [16], halos could be detected by IACTs as an extended energy dependent glow around the point-like source. As suggested by the results of the simulations here performed, for primary gamma rays with $E \gtrsim 10 - 100\,\mathrm{TeV}$ the extension of the halos is larger than the typical point spread function of the detectors ($\Theta > \theta_{psf}$), meaning that the observation of halos would imply a source spectrum extending up to or above these energies.

In a realistic simulation the intrinsic spectrum of the source is not known *a priori*, and it can be obtained by means of fits including magnetic field effects. Furthermore, the point spread function of the detector has also to be taken into account.

Often TeV blazars have strong time variability. This property cannot be properly studied with pair halos, since time delays caused by deflections of the charged component of the cascade can be as large as or even larger than the intrinsic variability time.

Pair halos can also be generated through the interaction of gamma rays emitted by the source with ambient photons, electrons and hadrons, if the surrounding environment is dense enough. This effect was neglected here but may play an important role in the formation of halos, hence requiring further studies. If blazar pair halos are ever detected by gamma ray observatories, before constraining the strength of EGMFs the impact of "source halos" would have to be carefully assessed, including counterparts in other wavelengths, and neutrinos.

chapter 10

Conclusions

In this work it was explored the connection between cosmic magnetic fields and high energy particles, particularly ultra-high energy cosmic rays and very-high energy gamma rays.

First, it was obtained an analytical approximation for the magnetic suppression of the cosmic ray flux from distant sources for energies $\sim 10^{18}$ eV. This suppression can be understood as a magnetic horizon, which occurs if the propagation time of cosmic rays is comparable to the age of the universe. Furthermore model dependent upper limits for the flux suppression due to magnetic horizons were obtained, suggesting that in the absence of nearby dominant sources the extragalactic component of the UHECR flux can be significantly suppressed only for $E \lesssim 10^{17}$ eV, provided that the coherence length of the extragalactic magnetic fields is smaller than a few Mpc, hence implying an almost inexistent magnetic horizon for UHECRs at EeV energies. This approximation, however, is volume averaged and does not reflect local effects such as the nearby distribution of magnetic fields. For instance, if both the source and the observer lie within the same filament or if the source is in a highly magnetized region this approach may no longer be valid. In this case full three-dimensional Monte Carlo simulations are needed.

An important phenomenological consequence of the inexistence[1] of a magnetic horizon effect at EeV energies is related to combined spectrum-composition fits of experimental data of the Pierre Auger Observatory. In these fits hard spectral indexes ($\gamma \sim 1.0$) are found, contradicting the current acceleration paradigm via diffusive shocks, in which $\gamma \sim 2.0 - 2.3$. By invoking magnetic horizon effects the fits again yield the conventional spectral indexes. Nevertheless, as shown in this work, the upper limit on the energy at which the magnetic horizon effect sets in is $E \lesssim 10^{17}$ eV implying that magnetic horizon effects at energies ~ 1 EeV should be negligible. As a consequence, if combined fits actually favor hard spectral indexes, this might be an evidence of acceleration mechanisms other than diffusive shocks, favoring source candidates such as magnetars or young pulsars.

With the goal of confronting the available experimental data with theoretical models the CRPropa code has been developed. The newest version, CRPropa 3, is its final stages of development and about to be released. It allows parallel processing, python steering, and the inclusion of custom modules. The main new features are cosmological effects in three-dimensional simulations (four-dimensional propagation), galactic magnetic fields, new extragalactic magnetic field techniques and improved interaction tables, and new CIB models. The code was used for several studies presented in this thesis.

An analysis using magnetohydrodynamical simulations of structure formation was performed, using CRPropa. First, it was studied the impact of different power spectra of seed magnetic fields on the trajectories of UHECRs. These seeds have the same total magnetic energy, the only difference being how this energy is distributed over different scales. It was shown that the heavier the small-k tail of the power

[1] Strictly speaking, the suppression has an asymptotic behavior for $E \sim Z \times 10^{18}$ eV, and for practical purposes it can be deemed null.

spectrum of the primordial magnetic field seed, the larger the induced deflections of UHECRs, and the wider this distribution. Even though this effect was already expected, this conclusion was achieved using high resolution cosmological simulations, which are supposedly realistic, hence demonstrating the feasibility of using UHECRs to constrain the power spectra and strength of IGMFs.

There are many uncertainties on the strength of cosmic magnetic fields. The impact of these uncertainties on the propagation of UHECRs was studied using the cosmological simulations of the magnetized cosmic web. A single realization of the large scale structure was used, with different normalizations of the magnetic field. By doing so the typical range of uncertainties of the strength of IGMFs was encompassed. The propagation of UHECRs from a single source was studied. It was shown that for IGMFs with strength $\sim 10^{-9} - 10^{-8}$ G there is a strong magnetic horizon effect due to confinement of cosmic rays around the source. Moreover, it was shown that these uncertainties are a limiting factor for identifying sources of UHECRs, due to the fact that high deflections might spoil all prospects for correlating arrival directions of UHECRs with astrophysical sources. For these particular cosmological simulations the identification of the single source studied at energies $\gtrsim 10^{19}$ eV would be possible only if the strength of IGMFs was $\lesssim 10^{-12}$ G and the galactic magnetic field weaker than in the Jansson-Farrar model. This analysis was performed for a single source located in a specific position. Therefore, effects of the magnetization around the source and magnetic confinement of UHECRs can play an important role on the propagation of cosmic rays and explain the high deflections obtained for this particular case of study. A thorough analysis including several source candidates using constrained cosmological simulations could verify if the results here obtained are due to local features of the magnetic field, or if it occurs for other sources as well, which would answer the question about the feasibility of UHECR astronomy in general.

The sources of UHECRs are unknown and so is the distance they are located. At energies above 10 EeV interaction horizons strongly limit the distance of sources that can be detected. However, for energies $\lesssim 1$ EeV, sources located at cosmological distances can significantly contribute to the observed flux. Usually when simulating the propagation of UHECRs sources are assumed to be local and cosmological effects are neglected. The main difficulty in accounting for cosmological effects in three-dimensional simulations is the computational time required, for it is impossible to know *a priori* the redshift of a particle, since it can be deflected by intervening magnetic fields, changing the effective path length. The solution is to simulate particles starting off at different redshifts and consider as detected only the ones which reach the observer within a given time (or conversely redshift) interval. Some methods for accounting for cosmological effects in three-dimensional simulations of the propagation of UHECRs were investigated.

One computationally efficient method was developed and can be applied to include cosmological effects in simulations of the propagation of UHE protons. It consists in a lookup table containing the initial and final energy of the cosmic rays, as well as the propagated distance in 3D and 1D simulations. A correction factor defined as the ratio between the observed energy in 3D and 1D simulations can be extracted from the table and applied to three-dimensional simulations, in order to account for cosmological effects. This correction table is not universal and has to be calculated for different parameters. This method introduces an overall average bias inferior to 10% in the energy range of 10^{17} eV and 10^{21} eV. The treatment for heavy nuclei is not straightforward, since photodisintegration can occur, and the original nuclei are not the same as the observed ones. In this case, this method cannot be applied and other methods were sought. The "hybrid" approach is one of them. It consists in the resimulation of an UHECR detected in a three-dimensional simulation in one dimension using the trajectory lengths and energy from the former as input for the later simulation. This method works well for protons and in some cases for nuclei, if the magnetic field strengths are relatively low and if the average separation between sources is much smaller than the typical distances involved, which in this case is the photodisintegration mean free path. However, as for the correction table, this method is

still not general. The only general method, although it is not very efficient from the computational point of view, is the complete four-dimensional propagation including the time dimension, feature which has been implemented in CRPropa 3.

The second part of the work concerns the propagation of gamma rays in the universe, focusing on their relation with cosmic magnetic fields. First, a Monte Carlo code for three-dimensional propagation of gamma rays with energies between 1 GeV and 1 PeV was developed. The GRPropa code includes all relevant interactions for this energy range, as well as cosmological effects.

Using GRPropa the formation of pair halos around the blazars 1ES 0229+200 and 1ES 2344+514 was studied. A dependence on the angular size of the halo for higher energies was observed, suggesting that the size of halos can be used to constrain the maximal acceleration energy attainable by a source. Furthermore, it was shown that halos tend to be formed if the strength of IGMFs is high enough. In this work the typical strength that allows the formation of halos was found to be $B \gtrsim 0.1\,\mathrm{pG}$. Moreover, the energy dependence of the extension of the halo was verified. It was found that halos are detectable for $B \gtrsim 0.1\,\mathrm{pG}$ for energies $\gtrsim 1\,\mathrm{TeV}$.

Epilogue

This thesis comes to an end, but that does not mean that the work here started is concluded. As a matter of fact, it has just started. Now powerful computational tools (CRPropa and GRPropa) are available and many new studies which were not possible can now be done. The work of this thesis can be further developed in many directions.

There are still many open issues in the fields of astroparticle physics and cosmology that require further studies. The reader may ask how did the landscape of these fields, presented in the introductory chapters, changed in light of the results obtained.

The origin and nature of the UHECRs remain an unsolved problem. There may be a problem with the description of hadronic interactions, and therefore the composition might not be increasingly heavier, as predicted by Auger, or purely protonic, as TA's results seem to suggest. How will these results change with the new LHC data? How will the hadronic interaction models change? Is the muon deficit problem a consequence of the poor knowledge of hadronic interactions at the highest energies or a hint of new physics? These questions will hopefully be answered in the near future with the new run of LHC at higher energies, which will allow the improvement of hadronic interaction models, and the foreseen upgrades for the Pierre Auger Observatory, which will provide more accurate estimates of the mass composition.

The uncertainties related to hadronic interaction models can have even more profound implications. Measurements suggest that at the highest energies are mostly heavy nuclei, then the observed flux suppression around 5×10^{19} eV is not the Greisen-Zatsepin-Kuz'min cutoff, but possibly a signature of the maximum acceleration energy of the sources. Therefore at the current stage the existence of a cutoff has been firmly established but no consensual interpretation has been reached.

Not much progress has been made in what concerns the sources of UHECRs. Today, perhaps the most important result in this field is the observation of an intermediate scale hotspot by the Telescope Array Collaboration. The main question is: will this signal perdure or will it fade away as did the AGN correlation signal observed by Auger a few years ago? Also, what are the sources generating this excess?

A crucial question is related to the possibility of identifying individual sources of UHECRs. This depends, naturally, on the nature of the highest energy cosmic rays and the strength of cosmic magnetic fields. The strength of IGMFs may be such that cosmic rays are considerably deflected, hence spoiling all prospect for UHECR astronomy. Moreover the power spectrum and strength of IGMFs are poorly known and a huge source of uncertainties. In particular, in this thesis it was shown that the measured spectrum and composition of UHECRs are significantly affected by different magnetic field configurations. Moreover, in light of the results here obtained using magnetohydrodynamical simulations of the cosmic web, the prospects for UHECR astronomy are, in general, not promising. New studies using constrained MHD simulations are required and are currently underway, and may shed new light on these issues.

Nevertheless one should bear in mind that some UHECR sources may be nearby, as indicated by results of the Pierre Auger Observatory, which observes a small excess toward the nearest AGN, Centaurus

A. Even with the next generation of UHECR observatories UHECR astronomy may not be possible for the whole sky, depending on the strength of IGMFs.

VHEGRs provide an interesting perspective on the strength of these fields, since only the short-living charged component of the electromagnetic cascade is affected. The current lower limits on IGMFs suggest that they are larger than 10^{-16} G. Observation of halos around sources of TeV gamma rays may provide better estimates for the strength of these fields, as discussed in this work, and may be, under certain conditions, observed with the current generation of IACTs. With the next generation of IACTs it may be possible to observe extended VHE emissions and exclude or confirm the existence of pair halos.

The non observation of pair halos, if confirmed in the future, may indicate that IGMFs have negligible strength. Another interesting possibility is that gamma rays can oscillate into axion-like particles (ALPs), which are dark matter candidates, decreasing the expected size of pair halos. If confirmed, systematic studies can provide information about magnetogenic mechanisms that took place in the early universe.

This is an exciting moment for the field of astroparticle physics. There is still much to be done both theoretically and experimentally. By combining information from multiple messengers such as gamma rays, cosmic rays, neutrinos and gravitational waves, it is possible to study the universe with unprecedented precision, addressing many open issues such as the origin and nature of UHECRs, existence of IGMFs, nature of dark matter, baryonic asymmetry, among others. On a more fundamental level, it is possible to probe the fundamental laws of physics and look for signatures of quantum gravity using complementary information from multiple messengers.

appendix A

Diffusive cosmic ray spectrum in an expanding universe

A.1 Diffusion equation in an expanding universe

In this section the diffusion equation in an expanding universe is derived, following Berezinsky and Gazizov [418]. Throughout the calculations r is used to designate comoving and $x(t) = a(t)r$ physical coordinates, with scale factor given by $a(z) = (1+z)^{-1}$.

Let r be the radius of an expanding sphere at time t. In physical coordinates the diffusive flux through this sphere is:

$$\vec{j} = -D(\vec{x}, t)\vec{\nabla}_x n(\vec{x}, t), \tag{A.1}$$

where $D(\vec{x}, t)$ is the diffusion coefficient at position $\vec{x}$ and time t, and the subscript x indicates that the operator $\vec{\nabla}$ is written in the basis x.

The continuity equation in its integral form is

$$\frac{d}{dt}\int\limits_{V(t)} dV n(\vec{x}, t) = -\oint\limits_{S(t)} \vec{j}\cdot d\vec{S}, \tag{A.2}$$

where $V(t)$ is the volume of the sphere at time t and $S(t)$ its surface. At this stage of the calculations it is assumed that the number of particles is changing only due to diffusion.

Substituting the value of $\vec{j}$ in eq. A.2 by eq. A.1 and applying Gauss's divergence theorem, this equation reduces to:

$$\frac{d}{dt}\int\limits_{V(t)} dV n(\vec{x}, t) = \int\limits_{V(t)} dV \vec{\nabla}_x \cdot \left[D(\vec{x}, t)\vec{\nabla}_x n(\vec{x}, t)\right]. \tag{A.3}$$

The left-hand side is a time derivative of a volume integral of an expanding sphere. At a time t the volume is $V(t)$ and at a time $t + \delta t$ the volume is $V(t) + \delta V(t)$. Let $\mathcal{V} = a^{-3}(t)V(t)$ be the comoving volume. Calculating the left-hand side of equation A.3 one has

$$\frac{d}{dt}\int\limits_{V(t)} dV n(\vec{x}, t) = \int\limits_{V(t)} dV n(\vec{x}, t) + n(\vec{x}, t)\left[\frac{d}{dt}(V + \delta V) - \frac{dV}{dt}\right] = \int\limits_{V(t)} dV n(\vec{x}, t) + n(\vec{x}, t)\frac{d}{dt}\delta V. \tag{A.4}$$

Calculating the second term in the right-hand side of this equation, one obtains:

$$n(\vec{x}, t)\frac{d}{dt}(\delta V) = n(\vec{x}, t)\frac{d}{dt}\left(a^3(t)\delta\mathcal{V}\right) = 3n(\vec{x}, t)H(t)a^3(t)\delta\mathcal{V} = 3H(t)n(\vec{x}, t)\delta V, \tag{A.5}$$

with $H(t)$ designating the time-dependent Hubble constant. The substitution of this equation in eq. A.3 yields:

$$\int_{V(t)} dV n(\vec{x},t) + 3H(t)n(\vec{x},t)\delta V = \int_{V(t)} dV \vec{\nabla}_x \cdot \left[D(\vec{x},t)\vec{\nabla}_x n(\vec{x},t)\right]. \tag{A.6}$$

The right-hand side term can be explicitly written, in comoving coordinates, as:

$$\begin{aligned}\vec{\nabla}_x \cdot \left[D(\vec{x},t)\vec{\nabla}_x n(\vec{r},t)\right] &= \vec{\nabla}_x D(\vec{x},t)\cdot\vec{\nabla}_x n(\vec{x},t) + D(\vec{x},t)\nabla_x^2 n(\vec{x},t) \\ &= \frac{1}{a^2(t)}\vec{\nabla}_r D(\vec{r},t)\cdot\vec{\nabla}_r n(\vec{r},t) + \frac{1}{a^2(t)}D(\vec{r},t)\nabla_r^2 n(\vec{r},t).\end{aligned} \tag{A.7}$$

A reasonable assumption is that $D(\vec{r},t)\nabla^2 n(\vec{r},t) \gg \vec{\nabla}D(\vec{r},t)\cdot\vec{\nabla}n(\vec{r},t)$, i. e., the diffusion coefficient is position independent. This first approximation can be deemed valid if the convection velocity ($\vec{\nabla}D(\vec{x},t)$) is much smaller than the speed of light. In other words, $D/\ell_D \ll c$ everywhere, where ℓ_D is the scale on which D varies. If the magnetic field is such that cosmic rays are not confined around the source, then the average source distance will be of the order of a sizable fraction of the Hubble radius (R_H), implying that convective effects will only be relevant for sources with distances less than $D/c\ell_D$, which is much smaller than 1. Furthermore, the contribution of these sources to the total flux is small.

Substituting eq. A.7 in eq. A.6, and writing it in comoving coordinates, one obtains the explicit form of the (incomplete) diffusion equation

$$\frac{\partial n(\vec{r},t)}{\partial t} + 3H(t)n(\vec{r},t) = \vec{\nabla}_r D(\vec{r},t)\cdot\vec{\nabla}_r n(\vec{r},t) + \frac{1}{a^2(t)}D(\vec{r},t)\nabla_r^2 n(\vec{r},t). \tag{A.8}$$

The particle density due to the injection of cosmic rays by the source. Hence a source term ($Q(E,t)a^{-3}(t)\delta^3(\vec{r}-\vec{r}_g)$) has to be added, together with another one that accounts for the energy losses ($\frac{\partial}{\partial E}[n(E,\vec{r},t)b(E,t)]$), as shown below:

$$\begin{aligned}&\frac{\partial}{\partial t}n(E,\vec{r},t) - \frac{\partial}{\partial E}\left[n(E,\vec{r},t)b(E,t)\right] + 3H(t)n(E,\vec{r},t) - \vec{\nabla}D(E,\vec{r},t) \\ &\cdot\vec{\nabla}n(E,\vec{r},t) - \frac{D(E,\vec{r},t)}{a^2(t)}\nabla^2 n(E,\vec{r},t) = \frac{Q(E,t)}{a^3(t)}\delta^3(\vec{r}-\vec{r}_g).\end{aligned} \tag{A.9}$$

Henceforth we will use the subscript 'g' to refer to the corresponding quantities at generation time, i. e., when the particles were first emitted by the source. In this case the source has comoving coordinates $\vec{r}_g = \vec{r} - \vec{r}_s$, where $\vec{r}_s$ is the position vector with respect to the observer. $b(E,t) = -\frac{dE}{dt}$ describes the total energy losses, both collisional and due to the adiabatic expansion of the universe.

A.2 The diffusive cosmic ray spectrum

The convection-like term from equation A.9 ($\vec{\nabla}D(\vec{r},t)\cdot\vec{\nabla}n(\vec{r},t)$) can be taken as zero, for the reasons previously discussed. This equation will now be solved following again Berezinsky and Gazizov [418].

The diffusion equation can be rewritten in Fourier space by calculating the Fourier transform of each term individually. Let $f(E,t)$ be the Fourier transform of $n(\vec{r},t,E)$. Then

$$n(\vec{r},E,t) = \frac{1}{(2\pi)^3}\int d\vec{k} f(E,t)\exp\left(i\vec{k}\cdot(\vec{r}-\vec{r}_g)\right), \tag{A.10}$$

and the Fourier representation of the Dirac delta function is

$$\delta^3(\vec{r}-\vec{r}_g) = \frac{1}{(2\pi)^3}\int d\vec{k}\exp\left(i\vec{k}\cdot(\vec{r}-\vec{r}_g)\right). \tag{A.11}$$

In Fourier space the laplacian operator applied on $n(\vec{r}, t, E)$ will have eigenvalue $-k^2$. The Fourier transform will have no effect on the time derivatives whatsoever. Therefore, with $f = f(E,t)$ and $b = b(E,t)$ the diffusion equation reads:

$$\frac{\partial f}{\partial t} - b(E,t)\frac{\partial f}{\partial E} + \left[3H(t) - \frac{\partial b}{\partial E} + k^2\frac{D(E,t)}{a^2(t)}\right] f = \frac{Q(E,t)}{a^3(t)}. \tag{A.12}$$

By definition $b(E,t) = -dE/dt$ is defined as the total energy losses. Because f depends on E and t, its total derivative can be expressed as

$$df(E,t) = \frac{\partial f(E,t)}{\partial t}dE + \frac{\partial f(E,t)}{\partial t}dt. \tag{A.13}$$

Dividing this equation by dt, the partial differential equation from eq. A.12 can be written as a first order linear and inhomogeneous differential equation, as follows:

$$\frac{df}{dt} + \left[3H(t) - \frac{\partial b}{\partial E} + k^2\frac{D(E,t)}{a^2(t)}\right] f = \frac{Q(E,t)}{a^3(t)}. \tag{A.14}$$

The solution of the homogeneous equation is

$$f_h(E(t),t) = \exp\left\{-\int_{t'}^{t} dt' \left[3H(t') - \frac{\partial b(E(t'),t')}{\partial E(t')} + k^2\frac{D(E(t'),t')}{a^2(t')}\right]\right\}, \tag{A.15}$$

where the notation $E(t)$ is explicitly written to indicate that the cosmic ray generated with energy E_g at time t has energy $E(t)$. Multiplying eq. A.12 by eq. A.15 one can show that

$$\frac{d}{dt}\left[f(E,t)f_h(E,t)\right] = \frac{Q(E,t)f_h(E,t)}{a^3(t)}. \tag{A.16}$$

The general solution of this equation is

$$\begin{aligned} f(E,t) = &\int_{t_g}^{t} dt' \left[f(E(t_g),t_g)\delta(t'-t_g) + \frac{Q(E(t'),t')}{a^3(t')}\right] \\ &\exp\left\{-\int_{t'}^{t} dt'' \left[3H(t'') - \frac{\partial b(E(t''),t'')}{\partial E(t'')} + k^2\frac{D(E(t''),t'')}{a^2(t'')}\right]\right\}. \end{aligned} \tag{A.17}$$

The quantity

$$\lambda^2(E,t') \equiv \int_{t'}^{t} dt'' \frac{D(E(t''),t'')}{a^2(t'')} \tag{A.18}$$

is similar to the the solution obtained in ref. [421]. Henceforth this variable will be called Syrovatskii variable[1]
.

It is now possible to calculate the integral inside the exponential term, which results in

$$\ln\left[\left(\frac{1+z(t')}{1+z(t)}\right)^3\right] + k^2\lambda^2(E(t'),t') - \mathcal{B}(t,t'), \tag{A.19}$$

[1]The definition used here differs from Syrovatskii's by a square. In its original work [421] Syrovatskii defined the left side of equation A.18 simply as λ. The same was done by Berezinsky and Gazizov [418].

with $a(t) = 1 + z(t)$ and

$$\mathcal{B}(t, t') \equiv \int_{t'}^{t} dt'' \frac{\partial b(E(t''), t'')}{\partial E(t'')}. \tag{A.20}$$

The number density can be obtained from f through a Fourier transform, yielding

$$n(\vec{r}, t, E) = \frac{1}{(2\pi)^3} \int_{t_g}^{t} dt' \frac{Q(E(t'), t')}{a^3(t')} \frac{a^3(t')}{a^3(t)} \exp(\mathcal{B}(t, t')) \int d\vec{k} \exp\left\{ i\vec{k} \cdot (\vec{r} - \vec{r}_g) - k^2 \lambda^2(E(t'), t') \right\} \tag{A.21}$$

Analyzing the integral in the power of the exponential, one can complete squares to transform it into a gaussian integral, whose result yields a factor $(\sqrt{\pi}/\lambda)^3 \exp\{-(\vec{r} - \vec{r}_g)^2/4\lambda^2\}$.

Therefore, the solution to the diffusion equation in Fourier space is

$$n(\vec{r}, t, E) = \frac{\pi^3}{(2\pi)^3} \int_{t_g}^{t} \frac{Q(E(t'), t')}{a^3(t')} \frac{\exp(\mathcal{B}(t, t'))}{\lambda^3(E(t'), t')} \exp\left\{ -\frac{(\vec{r} - \vec{r}_g)^2}{4\lambda^2(E(t'), t')} \right\}. \tag{A.22}$$

Rewriting this equation as a function of the redshift using the relation from eq. 1.21 and dE_g/dE, as presented in ref. [420], one has

$$n(\vec{r}, t, E) = \int_{0}^{z_g} dz \left| \frac{dt}{dz} \right| \frac{dE_g}{dE} Q(E_g(E, z), z) \frac{\exp\left\{ -\frac{(\vec{r} - \vec{r}_g)^2}{4\lambda^2(E, z)} \right\}}{(4\pi\lambda^2(E, z))^{3/2}}, \tag{A.23}$$

where dE_g/dE is given by [420]

$$\frac{dE_g}{dE} = (1 + z) \exp\left(\int_{0}^{z} dz' \left| \frac{dt'}{dz'} \right| \frac{\partial}{\partial E_g} b_{int}(E_g, z') \right), \tag{A.24}$$

with b_{int} designating the energy losses due to interactions. Notice that in the limit where there are no interactions, and the only energy loss process is the adiabatic expansion of the universe, this result reduces to to the well-known result $E = E_g/(1 + z)$.

appendix B

Magnetic suppression: best fit parameters

In this appendix the tables for the best fit parameters obtained by fitting the suppression factor (eq. 4.14 with the equation 4.15 are shown. For the sake of clarity eq. 4.15 is transcribed below:

$$G(x) = \exp\left[-\frac{(aX_s)^\alpha}{x^\alpha + bx^\beta}\right]. \tag{B.1}$$

Even though the fit parameters are not sensitive to the maximum acceleration energy of the source (E_{max}) nor the spectral index (γ), they are sensitive to the evolution parameter m. Here the complete tables for the parameters $m = 0$, $m = 1$ and $m = 2$ are shown.

Table B.1: Best fit parameters for $m = 0$.

	Miniati				Dolag *et al.*				Das *et al.*				Donnert *et al.*			
X_s	α	β	a	b	α	β	a	b	α	β	a	b	α	β	a	b
0.2	0.31	1.02	0.0001	0.61	1.15	0.59	0.0210	0.15	0.33	1.16	0.0000	0.23	0.84	0.60	0.0021	2.18
0.4	0.31	1.26	0.0002	0.33	1.17	0.64	0.0283	0.24	0.31	1.37	0.0000	0.09	0.66	0.66	0.0003	1.72
0.6	0.30	1.36	0.0003	0.20	1.16	0.65	0.0294	0.29	0.32	1.66	0.0000	0.03	0.68	0.68	0.0004	1.78
0.8	0.30	1.44	0.0003	0.12	1.14	0.64	0.0276	0.30	0.32	2.01	0.0000	0.01	0.70	0.70	0.0005	1.65
1.0	0.31	1.50	0.0003	0.08	1.11	0.63	0.0250	0.28	0.33	2.45	0.0000	0.00	0.73	0.73	0.0006	1.40
1.2	0.31	1.55	0.0003	0.06	1.09	0.61	0.0226	0.26	0.33	0.33	0.0000	0.66	0.77	0.77	0.0006	1.35
1.4	0.31	1.60	0.0004	0.04	1.07	0.59	0.0207	0.23	0.33	0.33	0.0000	0.79	0.80	0.80	0.0006	0.95
1.6	0.31	1.66	0.0004	0.03	1.05	0.57	0.0191	0.20	0.34	0.34	0.0001	0.90	0.83	0.83	0.0007	0.90
1.8	0.31	1.72	0.0004	0.02	1.04	0.55	0.0179	0.19	0.34	0.34	0.0000	0.69	0.86	0.86	0.0007	0.86
2.0	0.31	1.79	0.0004	0.02	1.03	0.54	0.0170	0.17	0.34	0.34	0.0000	0.66	0.89	0.89	0.0008	0.83
2.2	0.31	1.87	0.0004	0.01	1.02	0.52	0.0162	0.16	0.34	0.34	0.0000	0.64	0.92	0.92	0.0008	0.80
2.4	0.31	1.95	0.0004	0.01	1.01	0.51	0.0156	0.15	0.34	0.34	0.0000	0.60	0.94	0.94	0.0009	0.78
2.6	0.31	2.04	0.0004	0.01	1.00	0.49	0.0151	0.14	0.35	0.35	0.0000	0.62	0.96	0.96	0.0009	0.77
3.0	0.32	2.26	0.0004	0.00	0.99	0.47	0.0143	0.12	0.35	0.35	0.0003	1.90	0.99	0.99	0.0008	0.47
3.5	0.32	2.62	0.0004	0.00	0.98	0.44	0.0135	0.11	0.35	0.35	0.0003	1.90	1.02	1.02	0.0006	0.08
4.0	0.32	3.15	0.0004	0.00	0.97	0.42	0.0130	0.10	0.36	0.36	0.0003	1.90	1.03	1.03	0.0007	0.21
4.5	0.32	0.32	0.0057	1.27	0.97	0.40	0.0126	0.10	0.36	0.36	0.0003	1.90	1.05	1.05	0.0008	0.26
5.0	0.33	0.33	0.0060	1.30	0.96	0.39	0.0123	0.09	0.37	0.37	0.0003	1.90	1.05	1.05	0.0008	0.26
5.5	0.33	0.33	0.0059	1.28	0.95	0.37	0.0120	0.09	0.37	0.37	0.0004	1.98	1.05	1.05	0.0008	0.26
6.0	0.33	0.33	0.0059	1.27	0.95	0.36	0.0118	0.08	0.37	0.37	0.0004	1.98	1.06	1.06	0.0008	0.27
6.5	0.33	0.33	0.0061	1.29	0.95	0.35	0.0116	0.08	0.38	0.38	0.0004	1.99	1.05	1.05	0.0008	0.27
7.0	0.33	0.33	0.0060	1.29	0.94	0.34	0.0115	0.08	0.38	0.38	0.0004	1.99	1.05	1.05	0.0008	0.28
8.0	0.33	0.33	0.0059	1.26	0.94	0.32	0.0112	0.08	0.38	0.38	0.0004	1.97	1.04	1.04	0.0008	0.29
9.0	0.33	0.33	0.0058	1.23	0.93	0.30	0.0110	0.08	0.39	0.39	0.0004	1.97	1.04	1.04	0.0008	0.36
10.0	0.34	0.34	0.0057	1.22	0.93	0.29	0.0109	0.07	0.39	0.39	0.0004	1.95	1.03	1.03	0.0009	0.54

Table B.2: Best fit parameters for $m = 1$.

	Miniati				Dolag *et al.*				Das *et al.*				Donnert *et al.*			
X_s	α	β	a	b	α	β	a	b	α	β	a	b	α	β	a	b
0.2	0.31	0.98	0.0001	0.69	1.13	0.56	0.0177	0.12	0.33	1.14	0.0000	0.25	0.95	0.64	0.0162	9.24
0.4	0.31	1.18	0.0002	0.42	1.13	0.58	0.0204	0.16	0.32	1.28	0.0000	0.13	0.67	0.67	0.0003	2.02
0.6	0.30	1.23	0.0002	0.29	1.10	0.56	0.0191	0.16	0.32	1.46	0.0000	0.06	0.69	0.69	0.0004	2.01
0.8	0.30	1.26	0.0002	0.21	1.08	0.53	0.0172	0.15	0.32	1.67	0.0000	0.03	0.72	0.72	0.0005	1.63
1.0	0.30	1.30	0.0002	0.16	1.06	0.50	0.0158	0.13	0.33	1.92	0.0000	0.01	0.75	0.75	0.0005	1.52
1.2	0.30	1.33	0.0002	0.12	1.04	0.48	0.0146	0.12	0.33	2.21	0.0000	0.00	0.78	0.78	0.0006	1.44
1.4	0.31	1.36	0.0002	0.10	1.03	0.45	0.0138	0.11	0.34	0.34	0.0000	0.76	0.81	0.81	0.0007	1.36
1.6	0.31	1.39	0.0003	0.08	1.02	0.44	0.0132	0.11	0.34	0.34	0.0000	0.79	0.84	0.84	0.0007	1.29
1.8	0.31	1.42	0.0003	0.06	1.01	0.42	0.0127	0.10	0.34	0.34	0.0000	0.88	0.86	0.86	0.0007	1.21
2.0	0.31	1.46	0.0003	0.05	1.00	0.41	0.0123	0.10	0.34	0.34	0.0000	0.92	0.88	0.88	0.0008	1.15
2.2	0.31	1.50	0.0003	0.04	1.00	0.39	0.0120	0.10	0.34	0.34	0.0000	0.92	0.90	0.90	0.0008	1.10
2.4	0.31	1.54	0.0003	0.03	0.99	0.38	0.0118	0.09	0.34	0.34	0.0000	0.72	0.92	0.92	0.0008	1.02
2.6	0.31	1.58	0.0003	0.03	0.99	0.38	0.0115	0.09	0.34	0.34	0.0000	0.74	0.93	0.93	0.0008	0.98
3.0	0.31	1.68	0.0003	0.02	0.98	0.36	0.0112	0.09	0.35	0.35	0.0000	0.71	0.95	0.95	0.0008	0.92
3.5	0.32	1.81	0.0003	0.01	0.98	0.35	0.0109	0.09	0.35	0.35	0.0000	0.70	0.97	0.97	0.0008	0.85
4.0	0.32	1.95	0.0003	0.01	0.97	0.34	0.0107	0.10	0.35	0.35	0.0000	0.66	0.98	0.98	0.0008	0.84
4.5	0.32	2.12	0.0003	0.00	0.97	0.33	0.0106	0.10	0.36	0.36	0.0000	0.66	0.98	0.98	0.0008	0.87
5.0	0.32	2.32	0.0003	0.00	0.97	0.33	0.0105	0.10	0.36	0.36	0.0000	0.64	0.98	0.98	0.0008	0.87
5.5	0.32	2.55	0.0003	0.00	0.96	0.32	0.0104	0.10	0.36	0.36	0.0000	0.63	0.98	0.98	0.0009	0.87
6.0	0.33	0.33	0.0048	1.40	0.96	0.32	0.0103	0.11	0.37	0.37	0.0000	0.61	0.98	0.98	0.0009	0.88
6.5	0.33	0.33	0.0037	1.19	0.96	0.32	0.0102	0.11	0.37	0.37	0.0000	0.60	0.98	0.98	0.0009	0.88
7.0	0.33	0.33	0.0049	1.41	0.96	0.31	0.0102	0.12	0.37	0.37	0.0001	0.59	0.98	0.98	0.0009	0.90
8.0	0.33	0.33	0.0050	1.41	0.96	0.31	0.0101	0.12	0.38	0.38	0.0001	0.58	0.97	0.97	0.0013	1.84
9.0	0.33	0.33	0.0049	1.39	0.96	0.31	0.0101	0.13	0.38	0.38	0.0001	0.57	0.96	0.96	0.0018	3.01
10.0	0.33	0.33	0.0044	1.31	0.96	0.31	0.0100	0.14	0.38	0.38	0.0001	0.58	1.00	0.94	0.0058	9.59

Bibliography

[1] J. P. Vallée, *Magnetic fields in the galactic Universe, as observed in supershells, galaxies, intergalactic and cosmic realms*, *New Astronomy Reviews* **55** (2011) 91–154. [Cited on pages 1, 17, 20, 21, and 91.]

[2] A. Neronov and I. Vovk, *Evidence for Strong Extragalactic Magnetic Fields from Fermi Observations of TeV Blazars*, *Science* **328** (2010) 73–, [arXiv:1006.3504]. [Cited on pages 1, 2, 21, 22, 86, 113, and 118.]

[3] A. E. Broderick, P. Chang, and C. Pfrommer, *The Cosmological Impact of Luminous TeV Blazars. I. Implications of Plasma Instabilities for the Intergalactic Magnetic Field and Extragalactic Gamma-Ray Background*, *The Astrophysical Journal* **752** (2012) 22, [arXiv:1106.5494]. [Cited on pages 1 and 86.]

[4] R. Schlickeiser, D. Ibscher, and M. Supsar, *Plasma Effects on Fast Pair Beams in Cosmic Voids*, *The Astrophysical Journal* **758** (2012) 102. [Cited on pages 1 and 86.]

[5] E. Armengaud, G. Sigl, T. Beau, and F. Miniati, *CRPropa: A numerical tool for the propagation of UHE cosmic rays, γ-rays and neutrinos*, *Astroparticle Physics* **28** (2007) 463–471, [astro-ph/0603675]. [Cited on pages 2 and 65.]

[6] K.-H. Kampert, J. Kulbartz, L. Maccione, N. Nierstenhoefer, P. Schiffer, G. Sigl, and A. R. van Vliet, *CRPropa 2.0 - A public framework for propagating high energy nuclei, secondary gamma rays and neutrinos*, *Astroparticle Physics* **42** (2013) 41–51, [arXiv:1206.3132]. [Cited on pages 2, 39, 65, and 70.]

[7] R. Alves Batista, M. Erdmann, C. Evoli, K.-H. Kampert, D. Kuempel, G. Müller, P. Schiffer, G. Sigl, A. van Vliet, D. Walz, and T. Winchen, *CRPropa 3.0 - a Public Framework for Propagating UHE Cosmic Rays through Galactic and Extragalactic Space*, in *Proceedings of the 33rd International Cosmic Ray Conference*, (Rio de Janeiro), (2013). arXiv:1307.2643. [Cited on pages 2, 3, 65, and 113.]

[8] R. Alves Batista, M. Erdmann, C. Evoli, K.-H. Kampert, D. Kuempel, G. Müller, G. Sigl, A. van Vliet, D. Walz, and T. Winchen, *CRPropa: a public framework to propagate UHECRs in the universe*, *ArXiv e-prints* (2014) [arXiv:1411.2259]. [Cited on pages 2, 3, 65, and 113.]

[9] R. Alves Batista, M. Erdmann, C. Evoli, K.-H. Kampert, D. Kuempel, G. Mueller, G. Sigl, A. Van Vliet, D. Walz, and T. Winchen, *Cosmic ray propagation with CRPropa 3*, *ArXiv e-prints* (2014) [arXiv:1410.5323]. [Cited on pages 2, 3, 65, and 113.]

[10] R. Aloisio, D. Boncioli, A. F. Grillo, S. Petrera, and F. Salamida, *SimProp: a simulation code for ultra high energy cosmic ray propagation*, *Journal of Cosmology and Astroparticle Physics* **10** (2012) 7, [arXiv:1204.2970]. [Cited on page 2.]

[11] M. De Domenico, *HERMES: Simulating the propagation of ultra-high energy cosmic rays*, *European Physical Journal Plus* **128** (2013) 99, [arXiv:1305.4364]. [Cited on page 2.]

[12] Pierre Auger Collaboration, *Depth of maximum of air-shower profiles at the Pierre Auger Observatory. I. Measurements at energies above $10^{17.8}$ eV*, *Physical Review D* **90** (2014) 122005, [arXiv:1409.4809]. [Cited on pages 2 and 34.]

[13] High Resolution Fly's Eye Collaboration, *Indications of Proton-Dominated Cosmic-Ray Composition above 1.6 EeV*, *Physical Review Letters* **104** (2010) 161101, [arXiv:0910.4184]. [Cited on pages 2 and 34.]

[14] P. Tinyakov and for the Telescope Array Collaboration, *Latest results from the Telescope Array*, *Nuclear Instruments and Methods in Physics Research A* **742** (2014) 29–34. [Cited on pages 2 and 34.]

[15] Pierre Auger Collaboration, *Muons in air showers at the Pierre Auger Observatory: Mean number in highly inclined events*, *Phys.Rev.D* **D91** (2015) 032003, [arXiv:1408.1421]. [Cited on pages 2 and 34.]

[16] A. Elyiv, A. Neronov, and D. V. Semikoz, *Gamma-ray induced cascades and magnetic fields in the intergalactic medium*, *Physical Review D* **80** (2009) 023010, [arXiv:0903.3649]. [Cited on pages 2, 113, 117, 121, 126, and 129.]

[17] F. Tavecchio, G. Ghisellini, L. Foschini, G. Bonnoli, G. Ghirlanda, and P. Coppi, *The intergalactic magnetic field constrained by Fermi/Large Area Telescope observations of the TeV blazar 1ES 0229+200*, *Monthly Notices of the Royal Astronomical Society* **406** (2010) L70–L74, [arXiv:1004.1329]. [Cited on pages 2, 21, 118, and 125.]

[18] A. M. Taylor, I. Vovk, and A. Neronov, *Extragalactic magnetic fields constraints from simultaneous GeV-TeV observations of blazars*, *Astronomy & Astrophysics* **529** (2011) A144, [arXiv:1101.0932]. [Cited on pages 2, 21, 62, 113, and 118.]

[19] M. Kachelrieß, S. Ostapchenko, and R. Tomàs, *ELMAG: A Monte Carlo simulation of electromagnetic cascades on the extragalactic background light and in magnetic fields*, *Computer Physics Communications* **183** (2012) 1036–1043, [arXiv:1106.5508]. [Cited on pages 2, 113, 115, and 116.]

[20] R. Alves Batista and G. Sigl, *Diffusion of cosmic rays at EeV energies in inhomogeneous extragalactic magnetic fields*, *Journal of Cosmology and Astroparticle Physics* **11** (2014) 31, [arXiv:1407.6150]. [Cited on pages 3, 53, and 58.]

[21] R. Alves Batista, P. Schiffer, and G. Sigl, *Propagation of UHECRs in the universe*, *Nuclear Instruments and Methods in Physics Research A* **742** (2014) 245–249, [arXiv:1308.1530]. [Cited on pages 3 and 104.]

[22] A. Friedmann, *Über die Krümmung des Raumes*, *Zeitschrift fur Physik* **10** (1922) 377–386. [Cited on page 6.]

[23] A. Friedmann, *Über die Möglichkeit einer Welt mit konstanter negativer Krümmung des Raumes*, *Zeitschrift fur Physik* **21** (1924) 326–332. [Cited on page 6.]

[24] P. J. E. Peebles, *Principles of Physical Cosmology*. Princeton University Press, 1993. [Cited on page 6.]

[25] D. W. Hogg, *Distance measures in cosmology*, *ArXiv Astrophysics e-prints* (1999) [astro-ph/9905116]. [Cited on page 6.]

[26] Planck Collaboration, *Planck 2013 results. XVI. Cosmological parameters*, *Astronomy & Astrophysics* **571** (2014) A16, [arXiv:1303.5076]. [Cited on page 8.]

[27] A. Liddle, *An Introduction to Modern Cosmology, Second Edition*. Wiley-VCH, 2nd ed., (2003). [Cited on page 8.]

[28] B. W. Carroll and D. A. Ostlie, *An introduction to modern astrophysics and cosmology*. Addison-Wesley, San Francisco, 2nd ed., (2006). [Cited on page 8.]

[29] A. Loeb, *First Light*, pp. 1–160. Springer-Verlag, Berlin, 2008. [Cited on page 8.]

[30] A. V. Kravtsov and S. Borgani, *Formation of Galaxy Clusters*, *Annual Review of Astronomy and Astrophysics* **50** (2012) 353–409, [arXiv:1205.5556]. [Cited on page 8.]

[31] J. R. Bond, S. Cole, G. Efstathiou, and N. Kaiser, *Excursion set mass functions for hierarchical Gaussian fluctuations*, *The Astrophysical Journal* **379** (1991) 440–460. [Cited on page 8.]

[32] R. B. Tully, H. Courtois, Y. Hoffman, and D. Pomarède, *The Laniakea supercluster of galaxies*, *Nature* **513** (2014) 71–73, [arXiv:1409.0880]. [Cited on page 8.]

[33] S. Weinberg, *Oxford Astronomy Encyclopedia*. John Wiley & Sons, 1972. [Cited on page 9.]

[34] R. H. Dicke, R. Beringer, R. L. Kyhl, and A. B. Vane, *Atmospheric Absorption Measurements with a Microwave Radiometer*, *Physical Review* **70** (1946) 340–348. [Cited on page 9.]

[35] V. S. Alpher, *Ralph A. Alpher, George Antonovich Gamow, and the Prediction of the Cosmic Microwave Background Radiation*, *Asian Journal of Physics* **23** (2014) 17, [arXiv:1411.0172]. [Cited on page 9.]

[36] G. Gamow, *The Evolution of the Universe*, *Nature* **162** (1948) 680–682. [Cited on page 9.]

[37] R. A. Alpher and R. Herman, *Evolution of the Universe*, *Nature* **162** (1948) 774–775. [Cited on page 9.]

[38] R. A. Alpher and R. C. Herman, *Theory of the Origin and Relative Abundance Distribution of the Elements*, *Reviews of Modern Physics* **22** (1950) 153–212. [Cited on page 9.]

[39] G. Gamow, *Origin of protogalaxies.*, *Astronomical Journal* **58** (1953) 39. [Cited on page 9.]

[40] A. A. Penzias and R. W. Wilson, *A Measurement of Excess Antenna Temperature at 4080 Mc/s.*, *The Astrophysical Journal* **142** (1965) 419–421. [Cited on page 9.]

[41] R. H. Dicke, P. J. E. Peebles, P. G. Roll, and D. T. Wilkinson, *Cosmic Black-Body Radiation.*, *The Astrophysical Journal* **142** (1965) 414–419. [Cited on page 9.]

[42] M. G. Hauser and E. Dwek, *The Cosmic Infrared Background: Measurements and Implications*, *Annual Review of Astronomy and Astrophysics* **39** (2001) 249–307, [astro-ph/0105539]. [Cited on page 10.]

[43] A. Kashlinsky, *Cosmic infrared background and early galaxy evolution*, *Physics Reports* **409** (2005) 361–438, [astro-ph/0412235]. [Cited on page 10.]

[44] G. Lagache, J.-L. Puget, and H. Dole, *Dusty Infrared Galaxies: Sources of the Cosmic Infrared Background*, *Annual Review of Astronomy and Astrophysics* **43** (2005) 727–768, [astro-ph/0507298]. [Cited on page 10.]

[45] T. M. Kneiske, T. Bretz, K. Mannheim, and D. H. Hartmann, *Implications of cosmological gamma-ray absorption. II. Modification of gamma-ray spectra*, *Astronomy & Astrophysics* **413** (2004) 807–815, [astro-ph/0309141]. [Cited on pages 10, 41, 74, 80, 81, 100, 103, and 105.]

[46] F. W. Stecker, M. A. Malkan, and S. T. Scully, *Intergalactic Photon Spectra from the Far-IR to the UV Lyman Limit for $0 \leq z \leq 6$ and the Optical Depth of the Universe to High-Energy Gamma Rays*, *The Astrophysical Journal* **648** (2006) 774–783, [astro-ph/0510449]. [Cited on pages 10 and 80.]

[47] H. Dole, G. Lagache, J.-L. Puget, K. I. Caputi, N. Fernández-Conde, E. Le Floc'h, C. Papovich, P. G. Pérez-González, G. H. Rieke, and M. Blaylock, *The cosmic infrared background resolved by Spitzer. Contributions of mid-infrared galaxies to the far-infrared background*, *Astronomy & Astrophysics* **451** (2006) 417–429, [astro-ph/0603208]. [Cited on pages 10 and 80.]

[48] A. Franceschini, G. Rodighiero, and M. Vaccari *Astronomy & Astrophysics* **487** (2008) 837–852, [arXiv:0805.1841]. [Cited on pages 10 and 80.]

[49] T. M. Kneiske and H. Dole, *A lower-limit flux for the extragalactic background light*, *Astronomy & Astrophysics* **515** (2010) A19, [arXiv:1001.2132]. [Cited on pages 10, 80, 117, and 129.]

[50] J. D. Finke, S. Razzaque, and C. D. Dermer, *Modeling the Extragalactic Background Light from Stars and Dust*, *The Astrophysical Journal* **712** (2010) 238–249, [arXiv:0905.1115]. [Cited on pages 10, 80, 117, 126, and 129.]

[51] R. C. Gilmore, R. S. Somerville, J. R. Primack, and A. Domínguez, *Semi-analytic modelling of the extragalactic background light and consequences for extragalactic gamma-ray spectra*, *Monthly Notices of the Royal Astronomical Society* **422** (2012) 3189–3207, [arXiv:1104.0671]. [Cited on pages 10 and 80.]

[52] D. J. Fixsen, A. Kogut, S. Levin, M. Limon, P. Lubin, P. Mirel, M. Seiffert, J. Singal, E. Wollack, T. Villela, and C. A. Wuensche, *ARCADE 2 Measurement of the Absolute Sky Brightness at 3-90 GHz*, *The Astrophysical Journal* **734** (2011) 5. [Cited on page 11.]

[53] M. Seiffert, D. J. Fixsen, A. Kogut, S. M. Levin, M. Limon, P. M. Lubin, P. Mirel, J. Singal, T. Villela, E. Wollack, and C. A. Wuensche, *Interpretation of the ARCADE 2 Absolute Sky Brightness Measurement*, *The Astrophysical Journal* **734** (2011) 6. [Cited on page 11.]

[54] R. Subrahmanyan and R. Cowsik, *Is there an Unaccounted for Excess in the Extragalactic Cosmic Radio Background?*, *The Astrophysical Journal* **776** (2013) 42, [arXiv:1305.7060]. [Cited on page 11.]

[55] R. J. Protheroe and P. L. Biermann, *A new estimate of the extragalactic radio background and implications for ultra-high-energy γ-ray propagation*, *Astroparticle Physics* **6** (1996) 45–54, [astro-ph/9605119]. [Cited on page 11.]

[56] W. A. Hiltner, *Polarization of Light from Distant Stars by Interstellar Medium*, *Science* **109** (1949) 165. [Cited on page 12.]

[57] W. A. Hiltner, *On the Presence of Polarization in the Continuous Radiation of Stars. II.*, *The Astrophysical Journal* **109** (1949) 471. [Cited on page 12.]

[58] J. S. Hall and A. H. Mikesell, *Observations of polarized light from stars.*, *Astronomical Journal* **54** (1949) 187–188. [Cited on page 12.]

[59] L. Davis Jr. and L. Greenstein, *The Polarization of Starlight by Aligned Dust Grains.*, *The Astrophysical Journal* **114** (1951) 206. [Cited on page 12.]

[60] L. M. Widrow, *Origin of galactic and extragalactic magnetic fields*, *Rev. Mod. Phys.* **74** (2002) 775–823. [Cited on pages 12, 14, 15, 17, 18, 20, and 22.]

[61] G. B. Rybicki and A. P. Lightman, *Radiative Processes in Astrophysics*. Wiley-VCH, (1986). [Cited on pages 12, 13, and 44.]

[62] N. Duric, *Equipartition - Fact or Fiction*, in *Galactic and Intergalactic Magnetic Fields* (R. Beck, R. Wielebinski, and P. P. Kronberg, eds.), vol. 140 of *IAU Symposium*, p. 235, 1990. [Cited on page 12.]

[63] R. Beck and M. Krause, *Revised equipartition and minimum energy formula for magnetic field strength estimates from radio synchrotron observations*, *Astronomische Nachrichten* **326** (2005) 414–427, [astro-ph/0507367]. [Cited on page 12.]

[64] P. P. Kronberg, *Extragalactic magnetic fields*, *Reports on Progress in Physics* **57** (1994) 325–382. [Cited on page 12.]

[65] J. G. Bolton and J. P. Wild, *On the Possibility of Measuring Interstellar Magnetic Fields by 21-cm Zeeman Splitting.*, *The Astrophysical Journalj* **125** (1957) 296. [Cited on page 13.]

[66] R. S. Davies, R. D. Booth and A. J. Wilson, *Interstellar Magnetic Fields determined from Zeeman Effect Measurements*, *Nature* **220** (1968) 1207–1210. [Cited on page 13.]

[67] G. L. Verschuur, *Positive Determination of an Interstellar Magnetic Field by Measurement of the Zeeman Splitting of the 21-cm Hydrogen Line*, *Physical Review Letters* **21** (1968) 775–778. [Cited on page 13.]

[68] P. P. Kronberg and J. J. Perry, *Absorption lines, Faraday rotation, and magnetic field estimates for QSO absorption-line clouds*, *The Astrophysical Journal* **263** (1982) 518–532. [Cited on page 14.]

[69] D. Grasso and H. R. Rubinstein, *Magnetic fields in the early Universe*, *Physics Reports* **348** (2001) 163–266, [astro-ph/0009061]. [Cited on pages 14, 17, 18, and 19.]

[70] K. S. Thorne, *Primordial Element Formation, Primordial Magnetic Fields, and the Isotropy of the Universe*, *The Astrophysical Journal* **148** (1967) 51. [Cited on page 14.]

[71] G. Greenstein, *Primordial Helium Production in "Magnetic" Cosmologies*, *Nature* **223** (1969) 938–939. [Cited on page 14.]

[72] J. J. Matese and R. F. O'Connell, *Neutron Beta Decay in a Uniform Constant Magnetic Field*, *Physical Review* **180** (1969) 1289–1292. [Cited on page 14.]

[73] R. F. O'Connell and J. J. Matese, *Effect of a Constant Magnetic Field on the Neutron Beta Decay Rate and its Astrophysical Implications*, *Nature* **222** (1969) 649–650. [Cited on page 14.]

[74] J. J. Matese and R. F. O'Connell, *Production of Helium in the Big-Bang Expansion of a Magnetic Universe*, *The Astrophysical Journal* **160** (1970) 451. [Cited on page 14.]

[75] D. Grasso and H. R. Rubinstein, *Limits on possible magnetic fields at nucleosynthesis time*, *Astroparticle Physics* **3** (1995) 95–102, [astro-ph/9409010]. [Cited on page 14.]

[76] D. Grasso and H. R. Rubinstein, *Effects of Magnetic Fields on Primordial Nucleosynthesis*, *Nuclear Physics B Proceedings Supplements* **43** (1995) 303–307. [Cited on page 14.]

[77] B. Cheng, D. N. Schramm, and J. W. Truran, *Interaction rates at high magnetic field strengths and high degeneracy*, *Physics Letters B* **316** (1993) 521–527, [astro-ph/9308035]. [Cited on page 14.]

[78] P. J. Kernan, G. D. Starkman, and T. Vachaspati, *Big bang nucleosynthesis constraints on primordial magnetic fields*, *Physical Review D* **54** (1996) 7207–7214, [astro-ph/9509126]. [Cited on page 14.]

[79] I. B. Zeldovich and I. D. Novikov, *Relativistic astrophysics. Volume 2 - The structure and evolution of the universe*, vol. 2. University of Chicago Press, Chicago, IL, USA, 1983. [Cited on pages 14 and 15.]

[80] M. S. Madsen, *Magnetic fields in cosmology*, *Monthly Notices of the Royal Astronomical Society* **237** (1989) 109–117. [Cited on page 14.]

[81] J. D. Barrow, P. G. Ferreira, and J. Silk, *Constraints on a Primordial Magnetic Field*, *Physical Review Letters* **78** (1997) 3610–3613, [astro-ph/9701063]. [Cited on pages 14, 15, and 91.]

[82] A. Kosowsky and A. Loeb, *Faraday Rotation of Microwave Background Polarization by a Primordial Magnetic Field*, *The Astrophysical Journal* **469** (1996) 1, [astro-ph/9601055]. [Cited on page 15.]

[83] K. Jedamzik, V. Katalinić, and A. V. Olinto, *Limit on Primordial Small-Scale Magnetic Fields from Cosmic Microwave Background Distortions*, *Physical Review Letters* **85** (2000) 700, [astro-ph/9911100]. [Cited on page 15.]

[84] M. S. Turner and L. M. Widrow, *Inflation-produced, large-scale magnetic fields*, *Physical Review D* **37** (1988) 2743–2754. [Cited on pages 15, 18, and 19.]

[85] R. Jansson, G. R. Farrar, A. H. Waelkens, and T. Ensslin, *Large scale magnetic field of the Milky Way from WMAP3 data*, *International Cosmic Ray Conference* **2** (2008) 223–226, [arXiv:0708.2714]. [Cited on page 15.]

[86] R. Alves Batista, M. Zimbres, and E. Kemp, *Identifying Patterns on Cosmic Ray Maps with Wavelets on the Sphere*, in *Physicæ Proceedings*, vol. 1, 2012. arXiv:1201.2183. [Cited on page 15.]

[87] M. Zimbres, R. Alves Batista, and E. Kemp, *Using spherical wavelets to search for magnetically-induced alignment in the arrival directions of ultra-high energy cosmic rays*, *Astroparticle Physics* **54** (2014) 54–60, [arXiv:1305.0523]. [Cited on page 15.]

[88] D. Harari, S. Mollerach, E. Roulet, and F. Sánchez, *Lensing of ultra-high energy cosmic rays in turbulent magnetic fields*, *Journal of High Energy Physics* **3** (2002) 45, [astro-ph/0202362]. [Cited on pages 16 and 102.]

[89] Pierre Auger Collaboration, *Search for signatures of magnetically-induced alignment in the arrival directions measured by the Pierre Auger Observatory*, *Astroparticle Physics* **35** (2012) 354–361, [arXiv:1111.2472]. [Cited on page 15.]

[90] R. Plaga, *Detecting intergalactic magnetic fields using time delays in pulses of γ-rays*, *Nature* **374** (1995) 430–432. [Cited on pages 15 and 16.]

[91] K. Subramanian, *Magnetizing the universe*, in *From Planets to Dark Energy: the Modern Radio Universe*, (2008). arXiv:0802.2804. published by PoS; PoS MRU:071,2007. [Cited on page 17.]

[92] R. M. Kulsrud and E. G. Zweibel, *On the origin of cosmic magnetic fields*, *Reports on Progress in Physics* **71** (2008) 046901, [arXiv:0707.2783]. [Cited on pages 17 and 18.]

[93] A. Kandus, K. E. Kunze, and C. G. Tsagas, *Primordial magnetogenesis*, *Physics Reports* **505** (2011) 1–58, [arXiv:1007.3891]. [Cited on pages 17 and 18.]

[94] L. Biermann, *Über den Ursprung der Magnetfelder auf Sternen und im interstellaren Raum*, *Zeitschrift Naturforschung Teil A* **5** (1950) 65. [Cited on page 17.]

[95] L. Biermann and A. Schlüter, *Cosmic Radiation and Cosmic Magnetic Fields. II. Origin of Cosmic Magnetic Fields*, *Physical Review* **82** (1951) 863–868. [Cited on page 17.]

[96] E. R. Harrison, *Generation of magnetic fields in the radiation era*, *Monthly Notices of the Royal Astronomical Society* **147** (1970) 279. [Cited on page 18.]

[97] I. N. Mishustin and A. A. Ruzmajkin, *Formation of "priming" magnetic fields during the formation of protogalaxies.*, *Zhurnal Eksperimentalnoi i Teoreticheskoi Fiziki* **61** (1971) 441–444. [Cited on page 18.]

[98] E. R. Harrison, *Origin of Magnetic Fields in the Early Universe*, *Physical Review Letters* **30** (1973) 188–190. [Cited on page 18.]

[99] G. Davies and L. M. Widrow, *A Possible Mechanism for Generating Galactic Magnetic Fields*, *The Astrophysical Journal* **540** (2000) 755–764. [Cited on page 18.]

[100] J. Silk and M. Langer, *On the first generation of stars*, *Monthly Notices of the Royal Astronomical Society* **371** (2006) 444–450, [astro-ph/0606276]. [Cited on page 18.]

[101] H. Xu, B. W. O'Shea, D. C. Collins, M. L. Norman, H. Li, and S. Li, *The Biermann Battery in Cosmological MHD Simulations of Population III Star Formation*, *The Astrophysical Journal Letters* **688** (2008) L57–L60, [arXiv:0807.2647]. [Cited on page 18.]

[102] R. M. Kulsrud, R. Cen, J. P. Ostriker, and D. Ryu, *The Protogalactic Origin for Cosmic Magnetic Fields*, *The Astrophysical Journal* **480** (1997) 481–491, [astro-ph/9607141]. [Cited on page 18.]

[103] J. A. Stamper and B. H. Ripin, *Faraday-rotation measurements of megagauss magnetic fields in laser-produced plasmas*, *Physical Review Letters* **34** (1975) 138–141. [Cited on page 18.]

[104] F. Miniati and A. R. Bell, *Resistive Magnetic Field Generation at Cosmic Dawn*, *The Astrophysical Journal* **729** (2011) 73, [arXiv:1001.2011]. [Cited on page 18.]

[105] F. Hoyle, *Magnetic Fields and Highly Condensed Objects*, *Nature* **223** (1969) 936. [Cited on page 18.]

[106] R. A. Daly and A. Loeb, *A possible origin of galactic magnetic fields*, *The Astrophysical Journal* **364** (1990) 451–455. [Cited on page 18.]

[107] E. G. Zweibel and C. Heiles, *Magnetic fields in galaxies and beyond*, *Nature* **385** (1997) 131–136. [Cited on page 18.]

[108] R. Durrer and A. Neronov, *Cosmological magnetic fields: their generation, evolution and observation*, *The Astronomy and Astrophysics Review* **21** (2013) 62, [arXiv:1303.7121]. [Cited on page 18.]

[109] B. Ratra, *Cosmological 'seed' magnetic field from inflation*, *The Astrophysical Journal Letters* **391** (1992) L1–L4. [Cited on page 18.]

[110] J. Martin and J. Yokoyama, *Generation of large scale magnetic fields in single-field inflation*, *Journal of Cosmology and Astroparticle Physics* **1** (2008) 25, [arXiv:0711.4307]. [Cited on page 18.]

[111] K. Subramanian, *Magnetic fields in the early Universe*, *Astronomische Nachrichten* **331** (2010) 110, [arXiv:0911.4771]. [Cited on page 18.]

[112] K. E. Kunze, *Large scale magnetic fields from gravitationally coupled electrodynamics*, *Physical Review D* **81** (2010) 043526, [arXiv:0911.1101]. [Cited on page 18.]

[113] L. Motta and R. R. Caldwell, *Non-Gaussian features of primordial magnetic fields in power-law inflation*, *Physical Review D* **85** (2012) 103532, [arXiv:1203.1033]. [Cited on page 18.]

[114] R. K. Jain and M. S. Sloth, *Consistency relation for cosmic magnetic fields*, *Physical Review D* **86** (2012) 123528, [arXiv:1207.4187]. [Cited on page 18.]

[115] C. J. Hogan, *Magnetohydrodynamic effects of a first-order cosmological phase transition*, *Physical Review Letters* **51** (1983) 1488–1491. [Cited on page 19.]

[116] J. M. Quashnock, A. Loeb, and D. N. Spergel, *Magnetic field generation during the cosmological QCD phase transition*, *The Astrophysical Journal Letters* **344** (1989) L49–L51. [Cited on page 19.]

[117] Y. Aoki, G. Endrődi, Z. Fodor, S. D. Katz, and K. K. Szabó, *The order of the quantum chromodynamics transition predicted by the standard model of particle physics*, *Nature* **443** (2006) 675–678, [hep-lat/0611014]. [Cited on page 19.]

[118] B. Cheng and A. V. Olinto, *Primordial magnetic fields generated in the quark-hadron transition*, *Physical Review D* **50** (1994) 2421–2424. [Cited on page 19.]

[119] G. Sigl, A. V. Olinto, and K. Jedamzik, *Primordial magnetic fields from cosmological first order phase transitions*, *Physical Review D* **55** (1997) 4582–4590, [astro-ph/9610201]. [Cited on page 19.]

[120] J. Ahonen and K. Enqvist, *Magnetic field generation in first order phase transition bubble collisions*, *Physical Review D* **57** (1998) 664–673, [hep-ph/9704334]. [Cited on page 19.]

[121] T. Vachaspati, *Magnetic fields from cosmological phase transitions*, *Physics Letters B* **265** (1991) 258–261. [Cited on page 19.]

[122] D. Grasso and A. Riotto, *On the nature of the magnetic fields generated during the electroweak phase transition*, *Physics Letters B* **418** (1998) 258–265, [hep-ph/9707265]. [Cited on page 19.]

[123] A. Díaz-Gil, J. García-Bellido, M. García Pérez, and A. González-Arroyo, *Magnetic Field Production during Preheating at the Electroweak Scale*, *Physical Review Letters* **100** (2008) 241301, [arXiv:0712.4263]. [Cited on page 20.]

[124] G. B. Field and S. M. Carroll, *Cosmological magnetic fields from primordial helicity*, *Physical Review D* **62** (2000) 103008, [astro-ph/9811206]. [Cited on page 20.]

[125] R. Banerjee and K. Jedamzik, *Evolution of cosmic magnetic fields: From the very early Universe, to recombination, to the present*, *Physical Review D* **70** (2004) 123003, [astro-ph/0410032]. [Cited on page 20.]

[126] A. Saveliev, K. Jedamzik, and G. Sigl, *Evolution of helical cosmic magnetic fields as predicted by magnetohydrodynamic closure theory*, *Physical Review D* **87** (2013) 123001, [arXiv:1304.3621]. [Cited on page 20.]

[127] F. Govoni and L. Feretti, *Magnetic Fields in Clusters of Galaxies*, *International Journal of Modern Physics D* **13** (2004) 1549–1594, [astro-ph/0410182]. [Cited on page 20.]

[128] T. Enßlin, C. Vogt, and C. Pfrommer, *Magnetic Fields in Clusters of Galaxies*, in *The Magnetized Plasma in Galaxy Evolution* (K. T. Chyzy, K. Otmianowska-Mazur, M. Soida, and R.-J. Dettmar, eds.), pp. 231–238, (2005). astro-ph/0501338. [Cited on page 20.]

[129] M. A. G. Willson, *Radio observations of the cluster of galaxies in Coma Berenices - the 5C4 survey*, *Monthly Notices of the Royal Astronomic Society* **151** (1970) 1–44. [Cited on page 20.]

[130] A. Bonafede, L. Feretti, M. Murgia, F. Govoni, G. Giovannini, and V. Vacca, *Galaxy cluster magnetic fields from radio polarized emission*, in *Proceedings of ISKAF2010 Science Meeting "A Golden Age for radio astronomy"*, (2010). arXiv:1009.1233. [Cited on pages 20 and 91.]

[131] C. L. Carilli and G. B. Taylor, *Cluster Magnetic Fields*, *Annual Review of Astronomy and Astrophysics* **40** (2002) 319–348, [astro-ph/0110655]. [Cited on pages 20, 21, and 62.]

[132] K. Dolag, S. Schindler, F. Govoni, and L. Feretti, *Correlation of the magnetic field and the intra-cluster gas density in galaxy clusters*, *Astronomy & Astrophysics* **378** (2001) 777–786, [astro-ph/0108485]. [Cited on page 20.]

[133] V. Vacca, M. Murgia, F. Govoni, L. Feretti, G. Giovannini, E. Orrã, and A. Bonafede, *The intracluster magnetic field power spectrum in Abell 665*, *Astronomy & Astrophysics* **514** (2010) A71. [Cited on page 20.]

[134] F. Govoni, M. Murgia, L. Feretti, G. Giovannini, K. Dolag, and G. B. Taylor, *The intracluster magnetic field power spectrum in Abell 2255*, *Astronomy & Astrophysics* **460** (2006) 425–438, [astro-ph/0608433]. [Cited on page 20.]

[135] M. Murgia, F. Govoni, M. Markevitch, L. Feretti, G. Giovannini, G. B. Taylor, and E. Carretti, *Comparative analysis of the diffuse radio emission in the galaxy clusters A1835, A2029, and Ophiuchus*, *Astronomy & Astrophysics* **499** (2009) 679–695, [arXiv:0901.1943]. [Cited on page 20.]

[136] L. Feretti and M. Johnston-Hollitt, *Magnetic fields in clusters of galaxies*, *New Astronomy Reviews* **48** (2004) 1145–1150, [astro-ph/0409462]. [Cited on page 20.]

[137] L. Feretti, D. Dallacasa, G. Giovannini, and A. Tagliani, *The magnetic field in the Coma cluster.*, *Astronomy & Astrophysics* **302** (1995) 680, [astro-ph/9504058]. [Cited on page 20.]

[138] G. B. Taylor, F. Govoni, S. W. Allen, and A. C. Fabian, *Magnetic fields in the 3C 129 cluster*, *Monthly Notices of the Royal Astronomical Society* **326** (2001) 2–10, [astro-ph/0104223]. [Cited on page 20.]

[139] J. P. Vallée, J. M. MacLeod, and N. W. Broten, *Magnetic field excess observed in a cluster of galaxies*, *Astrophysical Letters* **25** (1987) 181–186. [Cited on page 21.]

[140] C. Vogt and T. A. Enßlin, *Measuring the cluster magnetic field power spectra from Faraday rotation maps of Abell 400, Abell 2634 and Hydra A*, *Astronomy & Astrophysics* **412** (2003) 373–385, [astro-ph/0309441]. [Cited on page 21.]

[141] J. P. Vallée, *A possible excess rotation measure and large-scale magnetic field in the Virgo Supercluster of galaxies*, *Astronomical Journal* **99** (1990) 459–462. [Cited on page 21.]

[142] J. P. Vallée, *Faraday Screen and Reversal of Rotation Measure in the Local Supercluster Plane*, *Astronomical Journal* **124** (2002) 1322–1327. [Cited on page 21.]

[143] D. Hutsemékers, R. Cabanac, H. Lamy, and D. Sluse, *Mapping extreme-scale alignments of quasar polarization vectors*, *Astronomy & Astrophysics* **441** (2005) 915–930, [astro-ph/0507274]. [Cited on page 21.]

[144] J. Bagchi, T. A. Enßlin, F. Miniati, C. S. Stalin, M. Singh, S. Raychaudhury, and N. B. Humeshkar, *Evidence for shock acceleration and intergalactic magnetic fields in a large-scale filament of galaxies ZwCl 2341.1+0000*, *New Astronomy* **7** (2002) 249–277, [astro-ph/0204389]. [Cited on pages 21 and 91.]

[145] M. Brüggen, M. Ruszkowski, A. Simionescu, M. Hoeft, and C. Dalla Vecchia, *Simulations of Magnetic Fields in Filaments*, *The Astrophysical Journal Letters* **631** (2005) L21–L24, [astro-ph/0508231]. [Cited on pages 21 and 91.]

[146] F. Vazza, M. Brüggen, C. Gheller, and P. Wang, *On the amplification of magnetic fields in cosmic filaments and galaxy clusters*, *Monthly Notices of the Royal Astronomical Society* **445** (2014) 3706–3722, [arXiv:1409.2640]. [Cited on pages 21, 87, and 91.]

[147] K.-T. Kim, P. P. Kronberg, G. Giovannini, and T. Venturi, *Discovery of intergalactic radio emission in the Coma-A1367 supercluster*, *Nature* **341** (1989) 720–723. [Cited on page 21.]

[148] T. A. Enßlin, P. P. Kronberg, R. A. Perley, and N. E. Kassim, *74 MHz-VLA-Observation of Coma Berenices with Subarcminute Resolution-Observation Data Reduction, and Preliminary Results*, in *Diffuse Thermal and Relativistic Plasma in Galaxy Clusters* (H. Boehringer, L. Feretti, and P. Schuecker, eds.), p. 21, 1999. astro-ph/9906422. [Cited on page 21.]

[149] T. A. Ensslin, P. Simon, P. L. Biermann, U. Klein, S. Kohle, P. P. Kronberg, and K.-H. Mack, *Signatures in a Giant Radio Galaxy of a Cosmological Shock Wave at Intersecting Filaments of Galaxies*, *The Astrophysical Journal Letters* **549** (2001) L39–L42, [astro-ph/0012404]. [Cited on page 21.]

[150] J. P. Vallée, *Upper limits to the magnetism of the shell around the Bootes Void*, *Astrophysics and Space Science* **178** (1991) 41–44. [Cited on pages 21 and 23.]

[151] S. Ando and A. Kusenko, *Evidence for Gamma-ray Halos Around Active Galactic Nuclei and the First Measurement of Intergalactic Magnetic Fields*, *The Astrophysical Journal Letters* **722** (2010) L39–L44, [arXiv:1005.1924]. [Cited on page 21.]

[152] I. Vovk, A. M. Taylor, D. Semikoz, and A. Neronov, *Fermi/LAT Observations of 1ES 0229+200: Implications for Extragalactic Magnetic Fields and Background Light*, *The Astrophysical Journal Letters* **747** (2012) L14, [arXiv:1112.2534]. [Cited on pages 21, 113, 118, and 125.]

[153] K. Takahashi, M. Mori, K. Ichiki, and S. Inoue, *Lower Bounds on Intergalactic Magnetic Fields from Simultaneously Observed GeV-TeV Light Curves of the Blazar Mrk 501*, *The Astrophysical Journal Letters* **744** (2012) L7, [arXiv:1103.3835]. [Cited on page 21.]

[154] O. Gerhard, *Mass distribution in our Galaxy*, *Space Science Reviews* **100** (2002) 129–138, [astro-ph/0203110]. [Cited on page 21.]

[155] J. P. Vallée, *New Velocimetry and Revised Cartography of the Spiral Arms in the Milky Way – A Consistent Symbiosis*, *The Astronomical Journal* **135** (2008) 1301–1310. [Cited on page 22.]

[156] R. Beck and R. Wielebinski, *Magnetic Fields in Galaxies*, p. 641. Springer, 2013. [Cited on page 22.]

[157] M. Simard-Normandin and P. P. Kronberg, *New large-scale magnetic features of the Milky Way*, *Nature* **279** (1979) 115–118. [Cited on page 22.]

[158] A. W. Clegg, J. M. Cordes, J. M. Simonetti, and S. R. Kulkarni, *Rotation measures of low-latitude extragalactic sources and the magnetoionic structure of the Galaxy*, *The Astrophysical Journal* **386** (1992) 143–157. [Cited on page 22.]

[159] R. J. Rand and A. G. Lyne, *New Rotation Measures of Distant Pulsars in the Inner Galaxy and Magnetic Field Reversals*, *Monthly Notices of the Royal Astronomical Society* **268** (1994) 497. [Cited on page 22.]

[160] J. L. Han, R. N. Manchester, and G. J. Qiao, *Pulsar rotation measures and the magnetic structure of our Galaxy*, *Monthly Notices of the Royal Astronomical Society* **306** (1999) 371–380, [astro-ph/9903101]. [Cited on page 22.]

[161] M. Simard-Normandin and P. P. Kronberg, *Rotation measures and the galactic magnetic field*, *The Astrophysical Journal* **242** (1980) 74–94. [Cited on page 22.]

[162] J. P. Vallée, *Large-scale magnetic field in the Perseus spiral arm*, *Astronomy & Astrophysics* **124** (1983) 147–150. [Cited on page 22.]

[163] Y. Sofue and M. Fujimoto, *A bisymmetric spiral magnetic field and the spiral arms in our Galaxy*, *The Astrophysical Journal* **265** (1983) 722–729. [Cited on page 23.]

[164] T. Stanev, *Ultra-high-energy Cosmic Rays and the Large-scale Structure of the Galactic Magnetic Field*, *The Astrophysical Journal* **479** (1997) 290–295, [astro-ph/9607086]. [Cited on page 23.]

[165] D. Harari, S. Mollerach, and E. Roulet, *The toes of the ultra high energy cosmic ray spectrum*, *Journal of High Energy Physics* **8** (1999) 22, [astro-ph/9906309]. [Cited on page 23.]

[166] J. L. Han, *Magnetic Fields in our Galaxy: How Much Do We Know?*, *Astrophysics and Space Science* **278** (2001) 181–184, [astro-ph/0010537]. [Cited on page 23.]

[167] P. G. Tinyakov and I. I. Tkachev, *Tracing protons through the Galactic magnetic field: a clue for charge composition of ultra-high-energy cosmic rays*, *Astroparticle Physics* **18** (2002) 165–172, [astro-ph/0111305]. [Cited on pages 23 and 79.]

[168] M. Prouza and R. Šmída, *The Galactic magnetic field and propagation of ultra-high energy cosmic rays*, *Astronomy & Astrophysics* **410** (2003) 1–10, [astro-ph/0307165]. [Cited on pages 23, 24, and 79.]

[169] M. Kachelrieß, P. D. Serpico, and M. Teshima, *The Galactic magnetic field as spectrograph for ultra-high energy cosmic rays*, *Astroparticle Physics* **26** (2007) 378–386, [astro-ph/0510444]. [Cited on page 23.]

[170] L. Page, G. Hinshaw, E. Komatsu, M. R. Nolta, D. N. Spergel, C. L. Bennett, C. Barnes, R. Bean, O. Doré, J. Dunkley, M. Halpern, R. S. Hill, N. Jarosik, A. Kogut, M. Limon, S. S. Meyer, N. Odegard, H. V. Peiris, G. S. Tucker, L. Verde, J. L. Weiland, E. Wollack, and E. L. Wright, *Three-Year Wilkinson Microwave Anisotropy Probe (WMAP) Observations: Polarization Analysis*, *The Astrophysical Journal Supplement Series* **170** (2007) 335–376, [astro-ph/0603450]. [Cited on page 23.]

[171] X. H. Sun, W. Reich, A. Waelkens, and T. A. Enßlin, *Radio observational constraints on Galactic 3D-emission models*, *Astronomy & Astrophysics* **477** (2008) 573–592, [arXiv:0711.1572]. [Cited on pages 23 and 24.]

[172] M. S. Pshirkov, P. G. Tinyakov, P. P. Kronberg, and K. J. Newton-McGee, *Deriving the Global Structure of the Galactic Magnetic Field from Faraday Rotation Measures of Extragalactic Sources*, *The Astrophysical Journal* **738** (2011) 192, [arXiv:1103.0814]. [Cited on page 23.]

[173] M. Tosa and M. Fujimoto, *The Configuration of Magnetic Fields in the Spiral Galaxy M 51*, *Publications of the Astronomical Society of Japan* **30** (1978) 315–326. [Cited on page 23.]

[174] A. Poezd, A. Shukurov, and D. Sokoloff, *Global Magnetic Patterns in the Milky-Way and the Andromeda Nebula*, *Monthly Notices of the Royal Astronomical Society* **264** (1993) 285. [Cited on page 23.]

[175] B. Ruiz-Granados, J. A. Rubiño-Martín, and E. Battaner, *Constraining the regular Galactic magnetic field with the 5-year WMAP polarization measurements at 22 GHz*, *Astronomy & Astrophysics* **522** (2010) A73, [arXiv:1006.5573]. [Cited on page 23.]

[176] J. L. Han and G. J. Qiao, *The magnetic field in the disk of our Galaxy*, *Astronomy & Astrophysics* **288** (1994) 759–772. [Cited on page 23.]

[177] J. P. Vallée, *Magnetic field reversals in the Milky Way- "cherchez le champ magnetique"*, *Astronomy & Astrophysics* **308** (1996) 433–440. [Cited on page 23.]

[178] H. Men, K. Ferrière, and J. L. Han, *Observational constraints on models for the interstellar magnetic field in the Galactic disk*, *Astronomy & Astrophysics* **486** (2008) 819–828, [arXiv:0805.3454]. [Cited on page 23.]

[179] A. Noutsos, S. Johnston, M. Kramer, and A. Karastergiou, *New pulsar rotation measures and the Galactic magnetic field*, *Monthly Notices of the Royal Astronomical Society* **386** (2008) 1881–1896, [arXiv:0803.0677]. [Cited on page 23.]

[180] J. P. Vallée, *Pulsar-based Galactic Magnetic Map: A Large-Scale Clockwise Magnetic Field with an Anticlockwise Annulus*, *The Astrophysical Journal* **619** (2005) 297–305. [Cited on page 23.]

[181] J. P. Vallée, *An Improved Magnetic Map of the Milky Way, with the Circularly Orbiting Gas and Magnetic Field Lines Crossing the Dusty Stellar Spiral Arms*, *The Astrophysical Journal* **681** (2008) 303–310. [Cited on page 23.]

[182] R. Jansson, G. R. Farrar, A. H. Waelkens, and T. A. Enßlin, *Constraining models of the large scale Galactic magnetic field with WMAP5 polarization data and extragalactic rotation measure sources*, *Journal of Cosmology and Astroparticle Physics* **7** (2009) 21, [arXiv:0905.2228]. [Cited on page 23.]

[183] R. Jansson and G. R. Farrar, *A New Model of the Galactic Magnetic Field*, *The Astrophysical Journal* **757** (2012) 14, [arXiv:1204.3662]. [Cited on pages 24, 79, 82, 94, and 96.]

[184] R. Jansson and G. R. Farrar, *The Galactic Magnetic Field*, *The Astrophysical Journal Letters* **761** (2012) L11, [arXiv:1210.7820]. [Cited on pages 24, 79, 82, 94, and 96.]

[185] M. C. Beck, A. M. Beck, R. Beck, K. Dolag, A. W. Strong, and P. Nielaba, *A new prescription for the random magnetic field of the Milky Way*, *ArXiv e-prints* (2014) [arXiv:1409.5120]. [Cited on page 25.]

[186] V. Cirkel-Bartelt, *History of Astroparticle Physics and its Components*, *Living Reviews in Relativity* **11** (2008), no. 2 2008. [Cited on pages 27, 28, and 43.]

[187] M. Walter and A. W. Wolfendale, *Early history of cosmic particle physics*, *The European Physical Journal H* **358** (2012) 323–358. [Cited on page 27.]

[188] Q. Xu, *The early history of cosmic ray research*, *American Journal of Physics* **55** (1987), no. 1 23. [Cited on page 27.]

[189] W. F. G. Swann, *The history of cosmic rays*, *American Journal of Physics* **29** (1961), no. 12 811–816. [Cited on page 27.]

[190] R. A. Millikan, *Electrons (+ and -), protons, photons, neutrons, mesotrons, and cosmic rays*. The University of Chicago Press, 2nd ed., 1934. [Cited on page 27.]

[191] O. Ravel, *Early cosmic ray research in France*, *AIP Conference Proceedings* **1516** (2013) 67–71. [Not cited.]

[192] P. Spillantini, *Early cosmic ray research in Italy*, *AIP Conference Proceedings* **1516** (2013) 61–66. [Cited on page 27.]

[193] J. R. Hörandel, *Early cosmic-ray work published in German*, in *American Institute of Physics Conference Series* (J. F. Ormes, ed.), vol. 1516 of *American Institute of Physics Conference Series*, pp. 52–60, (2013). arXiv:1212.0706. [Cited on page 27.]

[194] C. T. R. Wilson, *On the Leakage of Electricity through Dust-free Air*, *Proceedings of the Cambridge Philosophical Society* **11** (1900) 32. [Cited on page 27.]

[195] J. Elster and H. Geitel, *Weitere Versuche über die Elektrizitätszerstreuung in abgeschlossenen Luftmengen*, *Physikalische Zeitschrift* **2** (1901) 560. [Cited on page 27.]

[196] H. Geitel, *Über die Elektrizitätszerstreuung in abgeschlossenen Luftmengen*, *Physikalische Zeitschrift* **2** (1901) 116. [Cited on page 27.]

[197] G. A. Cline, *On the Penetrating Radiation at the Surface of the Earth*, *Physical Review Series I* **30** (1910) 35–52. [Cited on page 27.]

[198] K. Kurz, *Die radioaktiven Stoffe in Erde und Luft als Ursache der durchdringenden Strahlung in der Atmosphäre*, *Physikalische Zeitschrift* **10** (1909) 834. [Cited on page 27.]

[199] T. Wulf, *Über die in der Atmosphäre vorhandene Strahlung von hoher Durchdringungsfähigkeit*, *Physikalische Zeitschrift* **10** (1909) 152. [Cited on page 27.]

[200] T. Wulf, *Beobachtungen über die Strahlung hoher Durchdringungsfähigkeit auf dem Eiffelturm*, *Physikalische Zeitschrift* **11** (1910) 811. [Cited on page 27.]

[201] A. Gockel, *Die Luftelektrizität. Methoden und Resultate der neueren Forschung*. S. Hirzel, Leipzig, 1908. [Cited on page 27.]

[202] V. F. Hess, *Über Beobachtungen der durchdringenden Strahlung bei sieben Freiballonfahrten*, *Physikalische Zeitschrift* **13** (1912) 1084. [Cited on page 27.]

[203] W. Kohlhörster, *Über eine Neukonstruktion des Apparates zur Messung der durchdringenden Strahlung nach Wulf und die damit bisher gewonnen Ergebnisse*, *Physikalische Zeitschrift* **14** (1913) 21. [Cited on page 27.]

[204] R. A. Millikan and G. H. Cameron, *High Frequency Rays of Cosmic Origin III. Measurements in Snow-Fed Lakes at High Altitudes*, *Physical Review* **28** (1926) 851–868. [Cited on page 28.]

[205] D. V. Skobeltzyn, *The early stage of cosmic particle research*, in *Early History of Cosmic Ray Studies: Personal Reminiscences with Old Photographs* (Y. Sekido and H. Elliot, eds.), vol. 118 of *Astrophysics and Space Science Library*, p. 47. D. Reidel, Dordrecht, Netherlands; Boston, U.S.A., 1985. [Cited on page 28.]

[206] J. Clary, *[unknown title]*, in *Proceedings of the Section of Sciences*, vol. 30, (Amsterdam, Netherlands), p. 633, Koninklijke Akademie van Wetenschappen te Amsterdam, 1927. [Cited on page 28.]

[207] A. H. Compton, *A Geographic Study of Cosmic Rays*, *The Scientific Monthly* **36** (1933) 75–87. [Cited on page 28.]

[208] A. H. Compton, *The Significance of Recent Measurements of Cosmic Rays*, *Science* **77** (1933) 480–482. [Cited on page 28.]

[209] A. H. Compton, *Nature of Cosmic Rays*, *Nature* **131** (1933) 713–715. [Cited on page 28.]

[210] B. Rossi and S. De Benedetti, *Una nuova componente della radiazione cosmica*, *La Ricerca Scientifica (Supplement)* **2** (1934) 119–122. [Cited on page 28.]

[211] P. Auger, R. Maze, and T. Grivet-Meyer, *Extensive cosmic showers in the atmosphere containing ultra-penetrating particles*, *Comptes Rendus de l'Académie des Sciences. Série II* **206** (1938) 1721–1722. [Cited on page 28.]

[212] P. Auger, P. Ehrenfest, R. Maze, J. Daudin, and R. A. Fréon, *Extensive Cosmic-Ray Showers*, *Reviews of Modern Physics* **11** (1939) 288–291. [Cited on page 28.]

[213] K. Strobach, *Zur Geschichte der Geophysik*, *Naturwissenschaften* **67** (1980) 321–331. [Cited on page 28.]

[214] J. A. van Allen, *Radiation belts around the earth*. Freeman, San Francisco, 1958. [Cited on page 28.]

[215] J. A. van Allen, *Direct Detection of Auroral Radiation with Rocket Equipment*, *Proceedings of the National Academy of Science* **43** (1957) 57–62. [Cited on page 28.]

[216] J. A. van Allen, *Cosmic Rays and the Sun's Magnetic Field: Apparent Absence of Low-energy Cosmic-ray Primaries*, *Nature* **170** (1952) 62–63. [Cited on page 28.]

[217] C. D. Anderson, *The Positive Electron*, *Physical Review* **43** (1933) 491–494. [Cited on page 28.]

[218] C. M. G. Lattes, G. P. S. Occhialini, and C. F. Powell, *Observations on the Tracks of Slow Mesons in Photographic Emulsions*, *Nature* **160** (1947) 453–456. [Cited on page 28.]

[219] G. W. Clark, J. Earl, W. L. Kraushaar, J. Linsley, B. B. Rossi, F. Scherb, and D. W. Scott, *Cosmic-Ray Air Showers at Sea Level*, *Physical Review* **122** (1961) 637–654. [Cited on page 29.]

[220] J. Linsley, *Evidence for a Primary Cosmic-Ray Particle with Energy 10^{20} eV*, *Physical Review Letters* **10** (1963) 146–148. [Cited on page 29.]

[221] K. Greisen, *Highlights in air shower studies, 1965.*, *International Cosmic Ray Conference* **2** (1965) 609. [Cited on page 29.]

[222] D. Westervelt and H. Hoerlin, *The los alamos air fluorescence detection system*, *Proceedings of the IEEE* **53** (1965) 2067–2072. [Cited on page 29.]

[223] T. Donahue, *Detection of high-altitude explosions by observation of air fluorescence*, *Proceedings of the IEEE* **53** (1965) 2072–2078. [Cited on page 29.]

[224] L. G. Porter, J. C. Earnshaw, e. Tielsch-Cassel, J. C. Ahlstrom, and K. Greisen, *A space-time detector for cosmic ray showers*, *Nuclear Instruments and Methods* **87** (1970), no. 1 87 – 92. [Cited on page 29.]

[225] T. Hara, F. Ishikawa, S. Kawaguchi, Y. Miura, M. Nagano, K. Suga, and G. Tanahashi, *Detection of the atmospheric scintillation light from air showers*, *International Cosmic Ray Conference* **3** (1970) 369. [Cited on page 29.]

[226] M. A. Lawrence, R. J. O. Reid, and A. A. Watson, *The cosmic ray energy spectrum above $4*10^{17}$ eV as measured by the Haverah Park array*, *Journal of Physics G* **17** (1991) 733–757. [Cited on pages 29 and 31.]

[227] M. Ave, L. Cazón, J. A. Hinton, J. Knapp, J. Lloyd-Evans, and A. A. Watson, *Mass composition of cosmic rays in the range 2×10^{17}-3×10^{18} eV measured with the Haverah Park array*, *Astroparticle Physics* **19** (2003) 61–75, [astro-ph/0203150]. [Cited on page 29.]

[228] M. Ave, J. Knapp, J. Lloyd-Evans, M. Marchesini, and A. A. Watson, *The energy spectrum of cosmic rays in the range 3×10^{17}-4×10^{18} eV as measured with the Haverah Park array*, *Astroparticle Physics* **19** (2003) 47–60, [astro-ph/0112253]. [Cited on page 29.]

[229] M. M. Winn, J. Ulrichs, L. S. Peak, C. B. A. McCusker, and L. Horton, *The cosmic-ray energy spectrum above 10^{17} eV*, *Journal of Physics G* **12** (1986) 653–674. [Cited on page 29.]

[230] M. M. Winn, J. Ulrichs, L. S. Peak, C. B. A. McCusker, and L. Horton, *The arrival directions of cosmic rays above 10^{17} eV*, *Journal of Physics G* **12** (1986) 675–686. [Cited on page 29.]

[231] Fly's Eye Collaboration, *Detection of a cosmic ray with measured energy well beyond the expected spectral cutoff due to cosmic microwave radiation*, *The Astrophysical Journal* **441** (1995) 144–150, [astro-ph/9410067]. [Cited on page 29.]

[232] Fly's Eye Collaboration, *Evidence for correlated changes in the spectrum and composition of cosmic rays at extremely high energies*, *Physical Review Letters* **71** (1993) 3401–3404. [Cited on page 29.]

[233] Fly's Eye Collaboration, *The cosmic-ray energy spectrum observed by the Fly's Eye*, *The Astrophysical Journal* **424** (1994) 491–502. [Cited on pages 29, 31, and 33.]

[234] AGASA Collaboration, *Extension of the cosmic ray energy spectrum beyond the predicted Greisen-Zatsepin-Kuz'min cutoff*, *Physical Review Letters* **81** (1998) 1163–1166, [astro-ph/9807193]. [Cited on pages 29 and 33.]

[235] W. Heitler, *The Quantum Theory of Radiation*. Oxford University Press, Oxford, 3rd ed., 1944. [Cited on page 30.]

[236] T. K. Gaisser, *Cosmic rays and particle physics*. 1990, Cambridge and New York, 1990. [Cited on page 30.]

[237] M. Lemoine and G. Sigl, eds., *Physics and astrophysics of ultra-high-energy cosmic rays*, vol. 576 of *Lecture Notes in Physics*, (Berlin), Springer Verlag, 2001. [Cited on page 30.]

[238] J. Blümer, R. Engel, and J. R. Hörandel, *Cosmic rays from the knee to the highest energies*, *Progress in Particle and Nuclear Physics* **63** (2009) 293–338, [arXiv:0904.0725]. [Cited on page 30.]

[239] T. Stanev, *High Energy Cosmic Rays*. Springer, Berlin, 2nd ed., 2010. [Cited on page 30.]

[240] R. Engel, D. Heck, and T. Pierog, *Extensive Air Showers and Hadronic Interactions at High Energy*, *Annual Review of Nuclear and Particle Science* **61** (2011) 467–489. [Cited on page 30.]

[241] J. Engel, T. K. Gaisser, P. Lipari, and T. Stanev, *Nucleus-nucleus collisions and interpretation of cosmic-ray cascades*, *Physical Review D* **46** (1992) 5013–5025. [Cited on page 31.]

[242] N. L. Grigorov, Y. V. Gubin, B. M. Jakovlev, I. D. Rapoport, I. A. Savenko, V. V. Akimov, and V. E. Nesterov, *Energy Spectrum of Primary Cosmic Rays in the 10^{11}-10^{15} eV According to the Data of Proton-4 Measurements*, *Proceedings of the 12th International Cosmic Ray Conference* **1** (1971) 170. [Cited on page 31.]

[243] M. Nagano, T. Hara, Y. Hatano, N. Hayashida, S. Kawaguchi, K. Kamata, T. Kifune, and Y. Mizumoto, *Energy spectrum of primary cosmic rays between $10^{14.5}$ and 10^{18} eV*, *Journal of Physics G* **10** (1984) 1295–1310. [Cited on page 31.]

[244] E. S. Seo, J. F. Ormes, R. E. Streitmatter, S. J. Stochaj, W. V. Jones, S. A. Stephens, and T. Bowen, *Measurement of cosmic-ray proton and helium spectra during the 1987 solar minimum*, *The Astrophysical Journal* **378** (1991) 763–772. [Cited on page 31.]

[245] M. Nagano, M. Teshima, Y. Matsubara, H. Y. Dai, T. Hara, N. Hayashida, M. Honda, H. Ohoka, and S. Yoshida, *Energy spectrum of primary cosmic rays above 10^{17} eV determined from extensive air shower experiments at Akeno*, *Journal of Physics G: Nuclear and Particle Physics* **18** (1992), no. 2 423. [Cited on pages 31 and 32.]

[246] CASA-BLANCA Collaboration, *A measurement of the cosmic ray spectrum and composition at the knee*, *Astroparticle Physics* **15** (2001), no. 1 49 – 64. [Cited on pages 31 and 32.]

[247] D. B. Kieda, C. Larsen, and S. P. Swordy, *Reanalysis of Energy Spectrum and Composition in the DICE Experiment*, *Proceedings of the 27th International Cosmic Ray Conference* **1** (2001) 134. [Cited on page 31.]

[248] V. P. Egorova, A. V. Glushkov, A. A. Ivanov, S. P. Knurenko, V. A. Kolosov, A. D. Krasilnikov, I. T. Makarov, A. A. Mikhailov, V. V. Olzoyev, M. I. Pravdin, A. V. Sabourov, I. Y. Sleptsov, and G. G. Struchkov, *Spectrum of Cosmic Rays with Energy above 10^{17} EV*, *International Journal of Modern Physics A* **20** (2005) 6878–6880, [astro-ph/0411484]. [Cited on page 31.]

[249] K. Yoshida, R. Ohmori, T. Kobayashi, Y. Komori, Y. Sato, and J. Nishimura, *Cosmic-ray spectra of primary protons and high altitude muons deconvolved from observed atmospheric gamma rays*, *Physical Review D* **74** (2006) 083511, [astro-ph/0610009]. [Cited on page 31.]

[250] H. R. F. E. Collaboration, *First Observation of the Greisen-Zatsepin-Kuzmin Suppression*, *Physical Review Letters* **100** (2008) 101101, [astro-ph/0703099]. [Cited on pages 31 and 33.]

[251] KASCADE-Grande Collaboration, *The spectrum of high-energy cosmic rays measured with KASCADE-Grande*, *Astroparticle Physics* **36** (2012), no. 1 183 – 194, [arXiv:1206.3834]. [Cited on pages 31, 32, 33, and 34.]

[252] A. Letessier-Selvon and the Pierre Auger Collaboration, *Highlights from the Pierre Auger Observatory*, *Brazilian Journal of Physics* **44** (2014) 560–570, [arXiv:1310.4620]. [Cited on pages 31, 81, and 82.]

[253] G. Khristiansen and G. Kulikov, *[unknown title]*, *Zhurnal Eksperimental noi i Teoreticheskoi Fiziki* **35** (1958) 635. [Cited on page 32.]

[254] EAS-TOP Collaboration, *The EAS size spectrum and the cosmic ray energy spectrum in the region 10^{15}-10^{16} eV*, *Astroparticle Physics* **10** (1999), no. 1 1 – 9. [Cited on page 32.]

[255] HEGRA Collaboration, *Energy spectrum and chemical composition of cosmic rays between 0.3-PeV and 10-PeV determined from the Cherenkov light and charged particle distributions in air showers*, *Astronomy & Astrophysics* **359** (2000) 682–694, [astro-ph/9908202]. [Cited on page 32.]

[256] EAS-TOP Collaboration, *The cosmic ray primary composition between 10^{15} and 10^{16} eV from Extensive Air Showers electromagnetic and TeV muon data*, *Astroparticle Physics* **20** (2004), no. 6 641 – 652, [astro-ph/0305325]. [Cited on page 32.]

[257] EAS-TOP Collaboration, *The cosmic ray primary composition in the "knee" region through the EAS electromagnetic and muon measurements at EAS-TOP* , *Astroparticle Physics* **21** (2004), no. 6 583 – 596. [Cited on pages 32, 33, and 34.]

[258] Tibet ASγ Collaboration, *Are protons still dominant at the knee of the cosmic-ray energy spectrum?*, *Physics Letters B* **632** (2006), no. 1 58 – 64. [Cited on page 32.]

[259] GAMMA Collaboration, *Rigidity-dependent cosmic ray energy spectra in the knee region obtained with the GAMMA experiment*, *Astroparticle Physics* **28** (2007), no. 2 169 – 181, [arXiv:0704.3200]. [Cited on pages 32, 33, and 34.]

[260] TUNKA Collaboration, *The Cosmic Ray Mass Composition in the Energy Range 10^{15}-10^{18} eV measured with the Tunka Array: Results and Perspectives*, *Nuclear Physics B Proceedings Supplements* **190** (2009) 247–252, [arXiv:0902.3156]. [Cited on page 32.]

[261] GRAPES-3 Collaboration, *Studies of the energy spectrum and composition of the primary cosmic rays at 100–1000 tev from the grapes-3 experiment*, *Journal of Physics G: Nuclear and Particle Physics* **39** (2012), no. 2 025201. [Cited on page 32.]

[262] TUNKA Collaboration, *Tunka-25 air shower cherenkov array: The main results*, *Astroparticle Physics* **50-52** (2013) 18 – 25. [Cited on page 32.]

[263] KASCADE Collaboration, *KASCADE measurements of energy spectra for elemental groups of cosmic rays: Results and open problems*, *Astroparticle Physics* **24** (2005), no. 1 1 – 25. [Cited on pages 32, 33, and 34.]

[264] KASCADE-Grande Collaboration, *Kneelike structure in the spectrum of the heavy component of cosmic rays observed with kascade-grande*, *Physical Review Letters* **107** (2011) 171104, [arXiv:1107.5885]. [Cited on pages 32, 33, and 34.]

[265] KASCADE-Grande Collaboration, *KASCADE-Grande measurements of energy spectra for elemental groups of cosmic rays*, *ArXiv e-prints* (2013) [arXiv:1306.6283]. [Cited on pages 32, 33, and 34.]

[266] B. Peters, *Primary cosmic radiation and extensive air showers*, *Il Nuovo Cimento* **22** (1961), no. 4 800–819. [Cited on page 32.]

[267] P. L. Biermann, *Cosmic rays. 1. The cosmic ray spectrum between 10 TeV and 3 EeV*, *Astronomy & Astrophyiscs* **271** (1993) 649, [astro-ph/9301008]. [Cited on page 33.]

[268] T. Stanev, P. L. Biermann, and T. K. Gaisser, *Cosmic rays. IV. The spectrum and chemical composition above 10' GeV*, *Astronomy & Astrophysics* **274** (1993) 902, [astro-ph/9303006]. [Cited on page 33.]

[269] B. Wiebel-Sooth, P. L. Biermann, and H. Meyer, *Cosmic rays. VII. Individual element spectra: prediction and data*, *Astronomy & Astrophysics* **330** (1998) 389–398, [astro-ph/9709253]. [Cited on page 33.]

[270] P. L. Biermann, N. Langer, E.-S. Seo, and T. Stanev, *Cosmic rays IX. Interactions and transport of cosmic rays in the Galaxy*, *Astronomy & Astrophysics* **369** (2001) 269–277. [Cited on page 33.]

[271] T. K. Gaisser, T. Stanev, and S. Tilav, *Cosmic ray energy spectrum from measurements of air showers*, *Frontiers of Physics* **8** (2013) 748–758, [arXiv:1303.3565]. [Cited on page 33.]

[272] T. Stanev, T. K. Gaisser, and S. Tilav, *High energy cosmic rays: sources and fluxes*, *Nuclear Instruments and Methods in Physics Research A* **742** (2014) 42–46. [Cited on page 33.]

[273] V. L. Ginzburg and S. I. Syrovatskii, *The Origin of Cosmic Rays*. Macmillan, New York, 1964. [Cited on pages 33 and 45.]

[274] V. S. Ptuskin, S. I. Rogovaya, V. N. Zirakashvili, L. G. Chuvilgin, G. B. Khristiansen, E. G. Klepach, and G. V. Kulikov, *Diffusion and drift of very high energy cosmic rays in galactic magnetic fields*, *Astronomy & Astrophysics* **268** (1993) 726–735. [Cited on page 33.]

[275] J. Candia, L. N. Epele, and E. Roulet, *Cosmic ray photodisintegration and the knee of the spectrum*, *Astroparticle Physics* **17** (2002) 23–33, [astro-ph/0011010]. [Cited on page 33.]

[276] J. Candia and E. Roulet, *Rigidity dependent knee and cosmic ray induced high energy neutrino fluxes*, *Journal of Comology and Astroparticle Physics* **9** (2003) 5, [astro-ph/0306632]. [Cited on page 33.]

[277] G. Giacinti, M. Kachelrieß, and D. V. Semikoz, *Explaining the spectra of cosmic ray groups above the knee by escape from the Galaxy*, *Physical Review D* **90** (2014) 041302, [arXiv:1403.3380]. [Cited on page 33.]

[278] M. Lemoine, *Extragalactic magnetic fields and the second knee in the cosmic-ray spectrum*, *Physical Review D* **71** (2005) 083007, [astro-ph/0411173]. [Cited on pages 33, 53, and 93.]

[279] K. Kotera and M. Lemoine, *Inhomogeneous extragalactic magnetic fields and the second knee in the cosmic ray spectrum*, *Physical Review D* **77** (2008) 023005, [arXiv:0706.1891]. [Cited on pages 33, 53, 61, 86, and 93.]

[280] O. Deligny, *Cosmic rays around : Implications of contemporary measurements on the origin of the ankle feature*, *Comptes Rendus Physique* **15** (2014) 367–375, [arXiv:1403.5569]. [Cited on page 33.]

[281] J. Linsley, *Primary cosmic rays of energy 10^{17} to 10^{20} eV, the energy spectrum and arrival directions*, *Proceedings of the 8th International Cosmic Ray Conference* **4** (1963) 77. [Cited on page 33.]

[282] M. A. Lawrence, R. J. O. Reid, and A. A. Watson, *The cosmic ray energy spectrum above 4*10 17 ev as measured by the haverah park array*, *Journal of Physics G: Nuclear and Particle Physics* **17** (1991), no. 5 733. [Cited on page 33.]

[283] AGASA Collaboration, *The cosmic ray energy spectrum above 3×10^{18} eV measured by the Akeno Giant Air Shower Array*, *Astroparticle Physics* **3** (1995), no. 2 105 – 123. [Cited on page 33.]

[284] P. A. Collaboration, *Observation of the suppression of the flux of cosmic rays above 4×10^{19} eV*, *Physical Review Letters* **101** (2008) 061101, [arXiv:0806.4302]. [Cited on page 33.]

[285] High Resolution Fly'S Eye Collaboration, *Measurement of the flux of ultra high energy cosmic rays by the stereo technique*, *Astroparticle Physics* **32** (2009) 53–60, [arXiv:0904.4500]. [Cited on page 33.]

[286] Pierre Auger Collaboration, *Measurement of the energy spectrum of cosmic rays above 10^{18} eV using the Pierre Auger Observatory*, *Physics Letters B* (2010) 239–246, [arXiv:1002.1975]. [Cited on page 33.]

[287] M. Settimo *for the* Pierre Auger Collaboration, *Measurement of the Cosmic Ray Energy Spectrum Using Hybrid Events of the Pierre Auger Observatory*, *European Physical Journal Plus* **127** (2012) 87, [arXiv:1208.6574]. [Cited on pages 33, 105, and 106.]

[288] Telescope Array Collaboration, *The Cosmic-Ray Energy Spectrum Observed with the Surface Detector of the Telescope Array Experiment*, *The Astrophysical Journal Letters* **768** (2013) L1, [arXiv:1205.5067]. [Cited on page 33.]

[289] KASCADE-Grande Collaboration, *Ankle-like Feature in the Energy Spectrum of Light Elements of Cosmic Rays Observed with KASCADE-Grande*, *Physical Review D* **87** (2013) 081101, [arXiv:1304.7114]. [Cited on page 33.]

[290] V. Berezinsky, A. Z. Gazizov, and S. I. Grigorieva, *Dip in UHECR spectrum as signature of proton interaction with CMB*, *Physics Letters B* **612** (2005) 147–153, [astro-ph/0502550]. [Cited on page 33.]

[291] Pierre Auger Collaboration, *Measurement of the depth of maximum of extensive air showers above 10^{18} eV.*, *Physical Review Letters* **104** (2010) 091101, [arXiv:1002.0699]. [Cited on pages 33 and 39.]

[292] K. Greisen, *End of the Cosmic-Ray Spectrum?*, *Physical Review Letters* **16** (1966), no. 17 748–750. [Cited on page 33.]

[293] G. T. Zatsepin and V. A. Kuz'min, *Upper Limit of the Spectrum of Cosmic Rays*, *Journal of Experimental and Theoretical Physics* **4** (1966), no. 3 114–117. [Cited on page 33.]

[294] R. Aloisio, V. Berezinsky, and A. Gazizov, *Ultra high energy cosmic rays: The disappointing model*, *Astroparticle Physics* **34** (2011) 620–626, [arXiv:0907.5194]. [Cited on page 33.]

[295] R. S. Fletcher, T. K. Gaisser, P. Lipari, and T. Stanev, *sibyll: An event generator for simulation of high energy cosmic ray cascades*, *Physical Review D* **50** (1994) 5710–5731. [Cited on page 34.]

[296] S. Ostapchenko, *QGSJET-II: towards reliable description of very high energy hadronic interactions*, *Nuclear Physics B Proceedings Supplements* **151** (2006) 143–146, [hep-ph/0412332]. [Cited on page 34.]

[297] S. Ostapchenko, *QGSJET-II: results for extensive air showers*, *Nuclear Physics B Proceedings Supplements* **151** (2006) 147–150, [astro-ph/0412591]. [Cited on page 34.]

[298] S. Ostapchenko, *Monte Carlo treatment of hadronic interactions in enhanced Pomeron scheme: QGSJET-II model*, *Physical Review D* **83** (2011) 014018, [arXiv:1010.1869]. [Cited on page 34.]

[299] K. Werner and T. Pierog, *Extended Air Shower Simulations Using EPOS*, in *Collicers to Cosmic Rays* (M. Tripathi and R. E. Breedon, eds.), vol. 928 of *American Institute of Physics Conference Series*, pp. 111–117, (2007). arXiv:0707.3330. [Cited on page 34.]

[300] T. Pierog and K. Werner, *EPOS Model and Ultra High Energy Cosmic Rays*, *Nuclear Physics B Proceedings Supplements* **196** (2009) 102–105, [arXiv:0905.1198]. [Cited on page 34.]

[301] T. Pierog, I. Karpenko, J. M. Katzy, E. Yatsenko, and K. Werner, *EPOS LHC : test of collective hadronization with LHC data*, *ArXiv e-prints* (2013) [arXiv:1306.0121]. [Cited on pages 34 and 82.]

[302] V. N. Gribov, *A Reggeon Diagram Technique*, *Soviet Journal of Experimental and Theoretical Physics* **26** (1968) 414. [Cited on page 34.]

[303] V. N. Gribov, *Glauber Corrections and the Interaction between High-energy Hadrons and Nuclei*, *Soviet Journal of Experimental and Theoretical Physics* **29** (1969) 483. [Cited on page 34.]

[304] D. d'Enterria, R. Engel, T. Pierog, S. Ostapchenko, and K. Werner, *Constraints from the first LHC data on hadronic event generators for ultra-high energy cosmic-ray physics*, *Astroparticle Physics* **35** (2011) 98–113, [arXiv:1101.5596]. [Cited on page 34.]

[305] R. D. Parsons, C. Bleve, S. S. Ostapchenko, and J. Knapp, *Systematic uncertainties in air shower measurements from high-energy hadronic interaction models*, *Astroparticle Physics* **34** (2011) 832–839, [arXiv:1102.4603]. [Cited on page 34.]

[306] A. Fedynitch, J. Becker Tjus, and P. Desiati, *Influence of hadronic interaction models and the cosmic ray spectrum on the high energy atmospheric muon and neutrino flux*, *Physical Review D* **86** (2012) 114024, [arXiv:1206.6710]. [Cited on page 34.]

[307] J. Allen, A. Castellina, R. Engel, K. Kasahara, S. Knurenko, T. Pierog, A. Sabourov, B. T. Stokes, R. Ulrich, T. Sako, and S. Ostapchenko, *Air shower simulation and hadronic interactions*, in *European Physical Journal Web of Conferences*, vol. 53 of *European Physical Journal Web of Conferences*, p. 1007, (2013). arXiv:1306.6090. [Cited on page 34.]

[308] P. Lipari, *Cosmic rays and hadronic interactions*, *Comptes Rendus Physique* **15** (2014) 357–366. [Cited on page 34.]

[309] E. Fermi, *On the Origin of the Cosmic Radiation*, *Physical Review* **75** (1949) 1169–1174. [Cited on page 34.]

[310] R. J. Protheroe, *Acceleration and interaction of ultra high energy cosmic rays*, in *Topics in Cosmic-Ray Astrophysics* (M. A. Duvernois, ed.), p. 247, 1999. astro-ph/9812055. [Cited on pages 35 and 36.]

[311] M. S. Longair, *High Energy Astrophysics*. Cambridge University Press, Cambridge, UK, (2011). [Cited on pages 35 and 36.]

[312] W. I. Axford, E. Leer, and G. Skadron, *The acceleration of cosmic rays by shock waves*, *Proceedings of the 15th International Cosmic Ray Conference* **11** (1977) 132–137. [Cited on page 36.]

[313] G. F. Krymskii, *A regular mechanism for the acceleration of charged particles on the front of a shock wave*, *Soviet Physics Doklady* **22** (1977) 327. [Cited on page 36.]

[314] A. R. Bell, *The acceleration of cosmic rays in shock fronts. I*, *Monthly Notices of the Royal Astronomical Society* **182** (1978) 147–156. [Cited on page 36.]

[315] A. R. Bell, *The acceleration of cosmic rays in shock fronts. II*, *Monthly Notices of the Royal Astornomical Society* **182** (1978) 443–455. [Cited on page 36.]

[316] R. D. Blandford and J. P. Ostriker, *Particle acceleration by astrophysical shocks*, *The Astrophysical Journal Letters* **221** (1978) L29–L32. [Cited on page 36.]

[317] L. O. Drury, *An introduction to the theory of diffusive shock acceleration of energetic particles in tenuous plasmas*, *Reports on Progress in Physics* **46** (1983) 973–1027. [Cited on page 36.]

[318] R. Blandford and D. Eichler, *Particle acceleration at astrophysical shocks: A theory of cosmic ray origin*, *Physics Reports* **154** (1987) 1–75. [Cited on page 36.]

[319] A. R. Bell, *Turbulent amplification of magnetic field and diffusive shock acceleration of cosmic rays*, *Monthly Notices of the Royal Astronomical Society* **353** (2004) 550–558. [Cited on page 36.]

[320] A. Achterberg, Y. A. Gallant, J. G. Kirk, and A. W. Guthmann, *Particle acceleration by ultrarelativistic shocks: theory and simulations*, *Monthly Notices of the Royal Astronomical Society* **328** (2001) 393–408, [astro-ph/0107530]. [Cited on page 36.]

[321] M. Lemoine and G. Pelletier, *Particle Transport in Tangled Magnetic Fields and Fermi Acceleration at Relativistic Shocks*, *The Astrophysical Journal Letters* **589** (2003) L73–L76, [astro-ph/0304058]. [Cited on page 36.]

[322] J. Niemiec, M. Ostrowski, and M. Pohl, *Cosmic-Ray Acceleration at Ultrarelativistic Shock Waves: Effects of Downstream Short-Wave Turbulence*, *The Astrophysical Journal* **650** (2006) 1020–1027, [astro-ph/0603363]. [Cited on page 36.]

[323] J. Niemiec and M. Ostrowski, *Cosmic Ray Acceleration at Ultrarelativistic Shock Waves: Effects of a "Realistic" Magnetic Field Structure*, *The Astrophysical Journal* **641** (2006) 984–992, [astro-ph/0510811]. [Cited on page 36.]

[324] G. Pelletier, M. Lemoine, and A. Marcowith, *On Fermi acceleration and magnetohydrodynamic instabilities at ultra-relativistic magnetized shock waves*, *Monthly Notices of the Royal Astronomical Society* **393** (2009) 587–597, [arXiv:0807.3459]. [Cited on page 36.]

[325] M. Lemoine, G. Pelletier, and B. Revenu, *On the Efficiency of Fermi Acceleration at Relativistic Shocks*, *The Astrophysical Journal Letters* **645** (2006) L129–L132, [astro-ph/0606005]. [Cited on page 36.]

[326] Y. A. Gallant and A. Achterberg, *Ultra-high-energy cosmic ray acceleration by relativistic blast waves*, *Monthly Notices of the Royal Astronomical Society* **305** (1999) L6–L10, [astro-ph/9812316]. [Cited on page 36.]

[327] D. Gialis and G. Pelletier, *Which acceleration process for ultra high energy cosmic rays in gamma ray bursts?*, *Astronomy & Astrophysics* **425** (2004) 395–403, [astro-ph/0402586]. [Cited on page 36.]

[328] C. D. Dermer and S. Razzaque, *Acceleration of Ultra-high-energy Cosmic Rays in the Colliding Shells of Blazars and Gamma-ray Bursts: Constraints from the Fermi Gamma-ray Space Telescope*, *The Astrophysical Journal* **724** (2010) 1366–1372, [arXiv:1004.4249]. [Cited on page 36.]

[329] N. Globus, D. Allard, R. Mochkovitch, and E. Parizot, *UHECR acceleration at GRB internal shocks*, *ArXiv e-prints* (2014) [arXiv:1409.1271]. [Cited on page 36.]

[330] P. Blasi, R. I. Epstein, and A. V. Olinto, *Ultra-High-Energy Cosmic Rays from Young Neutron Star Winds*, *The Astrophysical Journal Letters* **533** (2000) L123–L126, [astro-ph/9912240]. [Cited on pages 36 and 37.]

[331] J. Arons, *Magnetars in the Metagalaxy: An Origin for UltraHigh?Energy Cosmic Rays in the Nearby Universe*, *The Astrophysical Journal* **589** (2003) 871–892, [astro-ph/0208444]. [Cited on pages 36, 38, and 63.]

[332] P. Blasi, *Theoretical challenges in acceleration and transport of ultra high energy cosmic rays: A review*, in *European Physical Journal Web of Conferences*, vol. 53 of *European Physical Journal Web of Conferences*, p. 1002, (2013). arXiv:1208.1682. [Cited on page 37.]

[333] E. M. de Gouveia Dal Pino and A. Lazarian, *Ultra-High-Energy Cosmic-Ray Acceleration by Magnetic Reconnection in Newborn Accretion-induced Collapse Pulsars*, *The Astrophysical Journal Letters* **536** (2000) L31–L34, [astro-ph/0002155]. [Cited on page 37.]

[334] Pierre Auger Collaboration, *Upper limit on the cosmic-ray photon flux above 10^{19} eV using the surface detector of the Pierre Auger Observatory*, *Astroparticle Physics* **29** (2008) 243–256, [arXiv:0712.1147]. [Cited on page 37.]

[335] Pierre Auger Collaboration, *Upper limit on the cosmic-ray photon fraction at EeV energies from the Pierre Auger Observatory*, *Astroparticle Physics* **31** (2009) 399–406, [arXiv:0903.1127]. [Cited on page 37.]

[336] D. F. Torres and L. A. Anchordoqui, *Astrophysical origins of ultrahigh energy cosmic rays*, *Reports on Progress in Physics* **67** (2004) 1663–1730, [astro-ph/0402371]. [Cited on pages 37 and 39.]

[337] A. M. Hillas, *The Origin of Ultra-High-Energy Cosmic Rays*, *Annual Reviews of Astronomy and Astrophysics* **22** (1984) 425–444. [Cited on page 37.]

[338] K. Fang, K. Kotera, and A. V. Olinto, *Newly Born Pulsars As Sources of Ultrahigh Energy Cosmic Rays*, *The Astrophysical Journal* **750** (2012) 118, [arXiv:1201.5197]. [Cited on pages 37 and 63.]

[339] K. Fang, K. Kotera, and A. V. Olinto, *Ultrahigh energy cosmic ray nuclei from extragalactic pulsars and the effect of their Galactic counterparts*, *Journal of Cosmology and Astroparticle Physics* **2013** (2013) 010–010, [arXiv:1302.4482]. [Cited on pages 37 and 63.]

[340] K. Fang, K. Kotera, K. Murase, and A. V. Olinto, *Testing the newborn pulsar origin of ultrahigh energy cosmic rays with EeV neutrinos*, *Physical Review D* **90** (2014) 103005, [arXiv:1311.2044]. [Cited on page 37.]

[341] Pierre Auger Collaboration, *A Targeted Search for Point Sources of EeV Neutrons*, *The Astrophysical Journal Letters* **789** (2014) L34, [arXiv:1406.4038]. [Cited on page 38.]

[342] M. Vietri, *The Acceleration of Ultra–High-Energy Cosmic Rays in Gamma-Ray Bursts*, *The Astrophysical Journal* **453** (1995) 883, [astro-ph/9506081]. [Cited on page 38.]

[343] E. Waxman, *High-Energy Particles from γ-Ray Bursts*, in *Physics and Astrophysics of Ultra-High-Energy Cosmic Rays* (M. Lemoine and G. Sigl, eds.), vol. 576 of *Lecture Notes in Physics*, (Berlin, Germany), p. 122, Springer Verlag, 2001. astro-ph/0103186. [Cited on page 38.]

[344] E. Waxman, *Gamma-Ray Bursts: The Underlying Model*, in *Supernovae and Gamma-Ray Bursters* (K. Weiler, ed.), vol. 598 of *Lecture Notes in Physics*, (Berlin, Germany), pp. 393–418, Springer Verlag, 2003. astro-ph/0303517. [Cited on page 38.]

[345] K. Murase, K. Ioka, S. Nagataki, and T. Nakamura, *High-energy cosmic-ray nuclei from high- and low-luminosity gamma-ray bursts and implications for multimessenger astronomy*, *Physical Review D* **78** (2008) 023005, [arXiv:0801.2861]. [Cited on page 38.]

[346] G. R. Farrar and P. L. Biermann, *Correlation between Compact Radio Quasars and Ultrahigh Energy Cosmic Rays*, *Physical Review Letters* **81** (1998) 3579–3582, [astro-ph/9806242]. [Cited on page 39.]

[347] G. Sigl, D. F. Torres, L. A. Anchordoqui, and G. E. Romero, *Testing the correlation of ultrahigh energy cosmic rays with high redshift sources*, *Physical Review D* **63** (2001) 081302, [astro-ph/0008363]. [Cited on page 39.]

[348] P. G. Tinyakov and I. I. Tkachev, *BL Lacertae are Probable Sources of the Observed Ultrahigh Energy Cosmic Rays*, *Soviet Journal of Experimental and Theoretical Physics Letters* **74** (2001) 445–448, [astro-ph/0102476]. [Cited on page 39.]

[349] D. F. Torres, S. Reucroft, O. Reimer, and L. A. Anchordoqui, *On the Cross-Correlation between the Arrival Direction of Ultra-High-Energy Cosmic Rays, BL Lacertae Objects, and EGRET Detections: A New Way to Identify EGRET Sources?*, *The Astrophysical Journal Letters* **595** (2003) L13–L16, [astro-ph/0307079]. [Cited on page 39.]

[350] Pierre Auger Collaboration, *Correlation of the Highest-Energy Cosmic Rays with Nearby Extragalactic Objects*, *Science* **318** (2007) 938–, [arXiv:0711.2256]. [Cited on page 39.]

[351] Pierre Auger Collaboration, *Update on the correlation of the highest energy cosmic rays with nearby extragalactic matter*, *Astroparticle Physics* **34** (2010) 314–326, [arXiv:1009.1855]. [Cited on page 39.]

[352] M. Kachelrieß, S. Ostapchenko, and R. Tomàs, *Multi-Messenger Astronomy with Centaurus a*, *International Journal of Modern Physics D* **18** (2009) 1591–1595, [arXiv:0904.0590]. [Cited on page 39.]

[353] M. Kachelrieß, S. Ostapchenko, and R. Tomàs, *High energy radiation from Centaurus A*, *New Journal of Physics* **11** (2009) 065017, [arXiv:0805.2608]. [Cited on page 39.]

[354] F. M. Rieger and F. A. Aharonian, *Centaurus A as TeV γ-ray and possible UHE cosmic-ray source*, *Astronomy & Astrophysics* **506** (2009) L41–L44, [arXiv:0910.2327]. [Cited on page 39.]

[355] H. Yüksel, T. Stanev, M. D. Kistler, and P. P. Kronberg, *The Centaurus A Ultrahigh-energy Cosmic-Ray Excess and the Local Extragalactic Magnetic Field*, *The Astrophysical Journal* **758** (2012) 16, [arXiv:1203.3197]. [Cited on page 39.]

[356] H. B. Kim, *Centaurus A as a Point Source of Ultrahigh Energy Cosmic Rays*, *The Astrophysical Journal* **764** (2013) 121, [arXiv:1206.3839]. [Cited on page 39.]

[357] A. Keivani, G. R. Farrar, and M. Sutherland, *Magnetic deflections of ultra-high energy cosmic rays from Centaurus A*, *Astroparticle Physics* **61** (2015) 47–55, [arXiv:1406.5249]. [Cited on page 39.]

[358] G. R. Blumenthal, *Energy Loss of High-Energy Cosmic Rays in Pair-Producing Collisions with Ambient Photons*, *Physical Review D* **1** (1970) 1596–1602. [Cited on pages 39 and 69.]

[359] R. d. A. Martins, *Como Becquerel não descobriu a radioatividade*, *Caderno Catarinense de Ensino de Física* **7** (1990) 27–45. [Cited on page 43.]

[360] L. Badash, *The discovery of radioactivity*, *Physics Today* **49** (1996) 21–27. [Cited on page 43.]

[361] R. d. A. Martins, *Henri becquerel and radioactivity: A critical revision*, in *Brazilian Studies in Philosophy and History of Science* (D. Krause and A. Videira, eds.), vol. 290 of *Boston Studies in the Philosophy of Science*, pp. 107–117. Springer, Netherlands, 2011. [Cited on page 43.]

[362] A. H. Becquerel, *The Discovery of Radioactivity*, vol. 1, p. 402. Basic Books, New York, 1966. [Cited on page 43.]

[363] R. A. Millikan and G. H. Cameron, *New Results on Cosmic Rays*, *Nature* **121** (1928) 19–26. [Cited on page 43.]

[364] K. R. Lang and O. Gingerich, *A source book in astronomy and astrophysics, 1900-1975*. Harvard University Press, Cambridge, MA, 1979. [Cited on page 43.]

[365] T. C. Weekes, M. F. Cawley, D. J. Fegan, K. G. Gibbs, A. M. Hillas, P. W. Kowk, R. C. Lamb, D. A. Lewis, D. Macomb, N. A. Porter, P. T. Reynolds, and G. Vacanti, *Observation of TeV gamma rays from the Crab nebula using the atmospheric Cerenkov imaging technique*, *The Astrophysical Journal* **342** (1989) 379–395. [Cited on page 43.]

[366] F. A. Aharonian, *Very high energy cosmic gamma radiation : a crucial window on the extreme Universe*. World Scientific Publishing, River Edge, NJ, 2004. [Cited on pages 44, 45, and 46.]

[367] B. Kozlovsky, R. J. Murphy, and R. Ramaty, *Nuclear Deexcitation Gamma-Ray Lines from Accelerated Particle Interactions*, *The Astrophysical Journal Supplement Series* **141** (2002) 523–541. [Cited on page 44.]

[368] R. Diehl, N. Prantzos, and P. von Ballmoos, *Astrophysical constraints from gamma-ray spectroscopy*, *Nuclear Physics A* **777** (2006) 70–97, [astro-ph/0502324]. [Cited on page 44.]

[369] A. Mücke, J. P. Rachen, R. Engel, R. J. Protheroe, and T. Stanev, *Photohadronic Processes in Astrophysical Environments*, *Publications of the Astronomical Society of Australia* **16** (1999) 160–166, [astro-ph/9808279]. [Cited on pages 45, 66, and 70.]

[370] C. Collaboration, *Measurement of the inelastic proton-proton cross section at $\sqrt{s} = 7$ TeV*, *Physics Letters B* **B722** (2013) 5–27, [arXiv:1210.6718]. [Cited on page 45.]

[371] TOTEM Collaboration, *Luminosity-independent measurements of total, elastic and inelastic cross-sections at \chem{\sqrt {s} = 7\,TeV}*, *Europhysics Letters* **101** (2013) 21004. [Cited on page 45.]

[372] A. I. Nikishov, *Absorption of high-energy photons in the universe*, *Journal of Experimental and Theoretical Physics* **42** (1962). [Cited on page 45.]

[373] F. A. Aharonian, A. M. Atoian, and A. M. Nagapetian, *Photoproduction of electron-positron pairs in compact X-ray sources*, *Astrofizika* **19** (1983) 323–334. [Cited on page 45.]

[374] F. A. Aharonian and A. M. Atoyan, *Cosmic ray positrons connected with galactic gamma radiation of high and very high energies*, *Journal of Physics G Nuclear Physics* **17** (1991) 1769–1778. [Cited on page 46.]

[375] P. S. Coppi and R. D. Blandford, *Reaction rates and energy distributions for elementary processes in relativistic pair plasmas*, *Monthly Notices of the Royal Astronomical Society* **245** (1990) 453–507. [Cited on page 46.]

[376] F. A. Aharonian and A. M. Atoyan, *Compton scattering of relativistic electrons in compact X-ray sources*, *Astrophysics and Space Science* **79** (1981) 321–336. [Cited on page 46.]

[377] J. A. Hinton and W. Hofmann, *Teraelectronvolt Astronomy*, *Annual Review of Astronomy & Astrophysics* **47** (2009) 523–565, [arXiv:1006.5210]. [Cited on pages 47 and 48.]

[378] J. Holder, *TeV gamma-ray astronomy: A summary*, *Astroparticle Physics* **39** (2012) 61–75, [arXiv:1204.1267]. [Cited on page 47.]

[379] F. M. Rieger, E. de Oña-Wilhelmi, and F. A. Aharonian, *TeV astronomy*, *Frontiers of Physics* **8** (2013) 714–747, [arXiv:1302.5603]. [Cited on pages 47 and 49.]

[380] F. Zwicky, *Production of Atomic Rays and of Cosmic Rays in Supernovae*, *Proceedings of the National Academy of Science* **25** (1939) 338–344. [Cited on page 47.]

[381] Fermi-LAT Collaboration, *Detection of the Characteristic Pion-Decay Signature in Supernova Remnants*, *Science* **339** (2013) 807–811, [arXiv:1302.3307]. [Cited on page 47.]

[382] W. Bednarek, *Propagation of very high energy γ-rays inside massive binaries LS 5039 and LSI +61 303*, *Monthly Notices of the Royal Astronomical Society* **368** (2006) 579–591, [astro-ph/0601657]. [Cited on page 48.]

[383] D. Khangulyan, F. Aharonian, and V. Bosch-Ramon, *On the formation of TeV radiation in LS 5039*, *Monthly Notices of the Royal Astronomical Society* **383** (2008) 467–478, [arXiv:0707.1689]. [Cited on page 48.]

[384] A. Sierpowska-Bartosik and D. F. Torres, *Pulsar wind zone processes in LS 5039*, *Astroparticle Physics* **30** (2008) 239–263, [arXiv:0801.3427]. [Cited on page 48.]

[385] D. V. Khangulyan, F. A. Aharonian, S. V. Bogovalov, A. V. Koldoba, and G. V. Ustyugova, *Hydrodynamics of Interaction of Pulsar and Stellar Winds and its Impact on the High Energy Radiation of Binary Pulsar Systems*, *International Journal of Modern Physics D* **17** (2008) 1909–1915, [arXiv:0809.5197]. [Cited on page 48.]

[386] K. *et al.*. Kosack, *TeV Gamma-Ray Observations of the Galactic Center*, *The Astrophysical Journal Letters* **608** (2004) L97–L100, [astro-ph/0403422]. [Cited on page 49.]

[387] MAGIC Collaboration, *Observation of Gamma Rays from the Galactic Center with the MAGIC Telescope*, *The Astrophysical Journal Letters* **638** (2006) L101–L104, [astro-ph/0512469]. [Cited on page 49.]

[388] HESS Collaboration, *HESS Observations of the Galactic Center Region and Their Possible Dark Matter Interpretation*, *Physical Review Letters* **97** (2006) 221102, [astro-ph/0610509]. [Cited on page 49.]

[389] M. Chernyakova, D. Malyshev, F. A. Aharonian, R. M. Crocker, and D. I. Jones, *The High-energy, Arcminute-scale Galactic Center Gamma-ray Source*, *The Astrophysical Journal* **726** (2011) 60, [arXiv:1009.2630]. [Cited on page 49.]

[390] T. Linden, E. Lovegrove, and S. Profumo, *The Morphology of Hadronic Emission Models for the Gamma-Ray Source at the Galactic Center*, *The Astrophysical Journal* **753** (2012) 41, [arXiv:1203.3539]. [Cited on page 49.]

[391] F. Aharonian, J. Buckley, T. Kifune, and G. Sinnis, *High energy astrophysics with ground-based gamma ray detectors*, *Reports on Progress in Physics* **71** (2008) 096901. [Cited on page 49.]

[392] M. Su, T. R. Slatyer, and D. P. Finkbeiner, *Giant Gamma-ray Bubbles from Fermi-LAT: Active Galactic Nucleus Activity or Bipolar Galactic Wind?*, *The Astrophysical Journal* **724** (2010) 1044–1082, [arXiv:1005.5480]. [Cited on page 49.]

[393] C. M. Urry and P. Padovani, *Unified Schemes for Radio-Loud Active Galactic Nuclei*, *Publications of the Astronomical Society of the Pacific* **107** (1995) 803, [astro-ph/9506063]. [Cited on page 49.]

[394] M. Punch, C. W. Akerlof, M. F. Cawley, M. Chantell, D. J. Fegan, S. Fennell, J. A. Gaidos, J. Hagan, A. M. Hillas, Y. Jiang, A. D. Kerrick, R. C. Lamb, M. A. Lawrence, D. A. Lewis, D. I. Meyer, G. Mohanty, K. S. O'Flaherty, P. T. Reynolds, A. C. Rovero, M. S. Schubnell, G. Sembroski, T. C. Weekes, and C. Wilson, *Detection of TeV photons from the active galaxy Markarian 421*, *Nature* **358** (1992) 477. [Cited on page 49.]

[395] F. Tavecchio, L. Maraschi, and G. Ghisellini, *Constraints on the Physical Parameters of TeV Blazars*, *The Astrophysical Journal* **509** (1998) 608–619, [astro-ph/9809051]. [Cited on page 49.]

[396] M. Boettcher, *Models for the Spectral Energy Distributions and Variability of Blazars*, *ArXiv e-prints* (2010) [arXiv:1006.5048]. [Cited on page 49.]

[397] MAGIC Collaboration, *MAGIC Upper Limits on the Very High Energy Emission from Gamma-Ray Bursts*, *The Astrophysical Journal* **667** (2007) 358–366, [astro-ph/0612548]. [Cited on page 50.]

[398] HESS Collaboration, *Very high energy gamma-ray observations of the galaxy clusters Abell 496 and Abell 85 with HESS*, *Astronomy & Astrophysics* **495** (2009) 27–35, [arXiv:0812.1638]. [Cited on page 50.]

[399] VERITAS Collaboration, *VERITAS Observations of Gamma-Ray Bursts Detected by Swift*, *The Astrophysical Journal* **743** (2011) 62, [arXiv:1109.0050]. [Cited on page 50.]

[400] F. M. Rieger, *Nonthermal Processes in Black Hole-Jet Magnetospheres*, *International Journal of Modern Physics D* **20** (2011) 1547–1596, [arXiv:1107.2119]. [Cited on page 50.]

[401] G. Zaharijas and D. Hooper, *Challenges in detecting gamma-rays from dark matter annihilations in the galactic center*, *Physical Review D* **73** (2006) 103501, [astro-ph/0603540]. [Cited on page 50.]

[402] A. Pinzke, C. Pfrommer, and L. Bergström, *Prospects of detecting gamma-ray emission from galaxy clusters: Cosmic rays and dark matter annihilations*, *Physical Review D* **84** (2011) 123509, [arXiv:1105.3240]. [Cited on page 50.]

[403] R. S. Miller and the Milagro Collaboration, *Milagro: The First TeV All-Sky Telescope*, in *AAS/High Energy Astrophysics Division #4*, vol. 31 of *Bulletin of the American Astronomical Society*, p. 719, (1999). [Cited on page 50.]

[404] Milagro Collaboration, *Milagrito, a TeV air-shower array*, *Nuclear Instruments and Methods in Physics Research A* **449** (2000) 478–499, [astro-ph/9912456]. [Cited on page 50.]

[405] ARGO-YBJ Collaboration, *The ARGO-YBJ experiment in Tibet*, *Nuovo Cimento C Geophysics Space Physics C* **24** (2001) 739. [Cited on page 50.]

[406] G. D'Alì Staiti and the ARGO-YBJ Collaboration, *The ARGO-YBJ experiment in Tibet*, *Nuclear Instruments and Methods in Physics Research A* **588** (2008) 7–13. [Cited on page 50.]

[407] Tibet ASγ Collaboration, *Tibet-AS γ Experiment*, *Proceedings of the 21st International Cosmic Ray Conference* **2** (1990) 427. [Cited on page 50.]

[408] M. A. Mostafá, *The High-Altitude Water Cherenkov Observatory*, *Brazilian Journal of Physics* **44** (2014) 571–580. [Cited on page 50.]

[409] J. A. Hinton and the HESS Collaboration, *The status of the HESS project*, *New Astronomy Reviews* **48** (2004) 331–337, [astro-ph/0403052]. [Cited on page 50.]

[410] J. Holder, *Ground-Based Gamma Ray Astronomy*, *Brazilian Journal of Physics* **44** (2014) 450–464, [arXiv:1407.1080]. [Cited on page 50.]

[411] C. Baixeras and the MAGIC Collaboration, *The MAGIC telescope*, *Nuclear Physics B Proceedings Supplements* **114** (2003) 247–252. [Cited on page 50.]

[412] P. Edwards, *The CANGAROO project*, in *High Energy Gamma Ray Astronomy* (J. Matthews, ed.), vol. 220 of *American Institute of Physics Conference Series*, pp. 265–269, (1991). [Cited on page 51.]

[413] T. Hara, T. Kifune, Y. Matsubara, Y. Mizumoto, Y. Muraki, S. Ogio, T. Suda, T. Tanimori, M. Teshima, T. Yoshikoshi, and P. G. Edwards, *A 3.8 m imaging Cherenkov telescope for the TeV gamma-ray astronomy collaboration between Japan and Australia*, *Nuclear Instruments and Methods in Physics Research A* **332** (1993) 300–309. [Cited on page 51.]

[414] R. Mirzoyan, R. Kankanian, F. Krennrich, N. Müller, H. Sander, P. Sawallisch, F. Aharonian, A. Akhperjanian, A. Beglarian, J. Fernandez, W. Fonseca, V.and Grewe, A. Heusler, A. K. Konopelko, E. Lorenz, M. Merck, A. V. Plyasheshnikov, D. Renker, M. Samorski, K. Sauerland, E. Smarsch, W. Stamm, M. Ulrich, C. A. Wiedner, and H. Wirth, *The first telescope of the HEGRA air Cherenkov imaging telescope array*, *Nuclear Instruments and Methods in Physics Research A* **351** (1994) 513–526. [Cited on page 51.]

[415] CTA Consortium, *Design concepts for the Cherenkov Telescope Array CTA: an advanced facility for ground-based high-energy gamma-ray astronomy*, *Experimental Astronomy* **32** (2011) 193–316, [arXiv:1008.3703]. [Cited on page 51.]

[416] A. M. Hillas, *Evolution of ground-based gamma-ray astronomy from the early days to the Cherenkov Telescope Arrays*, *Astroparticle Physics* **43** (2013) 19–43. [Cited on page 51.]

[417] R. Aloisio and V. Berezinsky, *Anti-GZK effect in ultra-high energy cosmic ray diffusive propagation*, *The Astrophysical Journal* **625** (2005), no. 1 249–255. [Cited on page 53.]

[418] V. Berezinsky and A. Z. Gazizov, *Diffusion of Cosmic Rays in the Expanding Universe. I.*, *The Astrophysical Journal* **643** (2006) 8–13, [astro-ph/0512090]. [Cited on pages 53, 54, 137, 138, and 139.]

[419] S. Mollerach and E. Roulet, *Magnetic diffusion effects on the ultra-high energy cosmic ray spectrum and composition*, *Journal of Cosmology and Astroparticle Physics* **10** (2013) 13, [arXiv:1305.6519]. [Cited on pages 54, 55, 58, 59, 60, 62, 63, and 92.]

[420] V. S. Berezinskii and S. I. Grigorieva, *A bump in the ultra-high energy cosmic ray spectrum*, *Astronomy & Astrophysics* **199** (1988) 1–12. [Cited on pages 54 and 140.]

[421] S. I. Syrovatskii, *The Distribution of Relativistic Electrons in the Galaxy and the Spectrum of Synchrotron Radio Emission*, *Soviet Astronomy* **3** (1959) 22. [Cited on pages 54 and 139.]

[422] R. Aloisio and V. Berezinsky, *Diffusive Propagation of Ultra-High-Energy Cosmic Rays and the Propagation Theorem*, *The Astrophysical Journal* **612** (2004) 900–913, [astro-ph/0403095]. [Cited on pages 54 and 55.]

[423] N. Globus, D. Allard, and E. Parizot, *Propagation of high-energy cosmic rays in extragalactic turbulent magnetic fields: resulting energy spectrum and composition*, *Astronomy & Astrophysics* **479** (2008) 97–110, [arXiv:0709.1541]. [Cited on page 54.]

[424] F. Miniati, *Intergalactic shock acceleration and the cosmic gamma-ray background*, *Monthly Notices of the Royal Astronomical Society* **337** (2002) 199–208, [astro-ph/0203014]. [Cited on pages 56, 81, 86, 97, and 112.]

[425] K. Dolag, D. Grasso, V. Springel, and I. Tkachev, *Constrained simulations of the magnetic field in the local Universe and the propagation of ultrahigh energy cosmic rays*, *Journal of Cosmology and Astroparticle Physics* **1** (2005) 9, [astro-ph/0410419]. [Cited on pages 56, 81, 82, 86, 95, and 97.]

[426] S. Das, H. Kang, D. Ryu, and J. Cho, *Propagation of Ultra-High-Energy Protons through the Magnetized Cosmic Web*, *The Astrophysical Journal* **682** (2008) 29–38, [arXiv:0801.0371]. [Cited on pages 56 and 97.]

[427] J. Donnert, K. Dolag, H. Lesch, and E. Müller, *Cluster magnetic fields from galactic outflows*, *Monthly Notices of the Royal Astronomical Society* **392** (2009) 1008–1021, [arXiv:0808.0919]. [Cited on page 56.]

[428] Pierre Auger Collaboration, *Constraints on the Origin of Cosmic Rays above 10^{18} eV from Large-scale Anisotropy Searches in Data of the Pierre Auger Observatory*, *The Astrophysical Journal. Letters* **762** (2013) L13, [arXiv:1212.3083]. [Cited on page 60.]

[429] D. Ryu, D. R. G. Schleicher, R. A. Treumann, C. G. Tsagas, and L. M. Widrow, *Magnetic Fields in the Large-Scale Structure of the Universe*, *Space Science Reviews* **166** (2012) 1–35, [arXiv:1109.4055]. [Cited on page 62.]

[430] A. Neronov, A. M. Taylor, C. Tchernin, and I. Vovk, *Measuring the correlation length of intergalactic magnetic fields from observations of gamma-ray induced cascades*, *Astronomy & Astrophysics* **554** (2013) A31, [arXiv:1307.2753]. [Cited on pages 62, 113, and 118.]

[431] G. Sigl, *Nonuniversal spectra of ultrahigh energy cosmic ray primaries and secondaries in a structured universe*, *Physical Review D* **75** (2007) 103001, [astro-ph/0703403]. [Cited on pages 62 and 93.]

[432] R. Aloisio, V. Berezinsky, and A. Gazizov, *The Problem of Superluminal Diffusion of Relativistic Particles and Its Phenomenological Solution*, *The Astrophysical Journal* **693** (2009) 1275–1282. [Cited on page 62.]

[433] D. Hooper and A. M. Taylor, *On the heavy chemical composition of the ultra-high energy cosmic rays*, *Astroparticle Physics* **33** (2010) 151–159, [arXiv:0910.1842]. [Cited on page 62.]

[434] D. Allard, *Extragalactic propagation of ultrahigh energy cosmic-rays*, *Astroparticle Physics* **39-40** (2012) 33–43, [1111.3290]. [Cited on page 62.]

[435] R. Aloisio, V. Berezinsky, and P. Blasi, *Ultra high energy cosmic rays: implications of Auger data for source spectra and chemical composition*, *ArXiv e-prints* (2013) [arXiv:1312.7459]. [Cited on page 62.]

[436] A. van Vliet, K.-H. Kampert, J. Kulbartz, L. Maccione, N. Nierstenhoefer, P. Schiffer, and G. Sigl, *CRPropa 2.0. Public Software to Model Extragalactic Propagation of Ultra-High Energy Nuclei*, in *European Physical Journal Web of Conferences*, vol. 52 of *European Physical Journal Web of Conferences*, p. 6006, (2013). [Cited on page 65.]

[437] J. R. Cash and A. H. Karp, *A variable order runge-kutta method for initial value problems with rapidly varying right-hand sides*, *ACM Transactions on Mathematical Software* **16** (1990) 201–222. [Cited on page 68.]

[438] B. Krusche, *Photoproduction of mesons off nuclei*, *European Physical Journal Special Topics* **198** (2011) 199–238, [arXiv:1110.0192]. [Cited on page 70.]

[439] A. Donnachie and P. V. Landshoff, *Total cross sections*, *Physics Letters B* **296** (1992) 227–232, [hep-ph/9209205]. [Cited on page 70.]

[440] M. Danos and E. G. Fuller, *Photonuclear Reactions*, *Annual Review of Nuclear and Particle Science* **15** (1965) 29–66. [Cited on page 71.]

[441] E. Hayward, *Photonuclear reactions*, NBS Monograph 118, U.S. Department of Commerce. National Bureau of Standards, 1970. [Cited on page 71.]

[442] J. L. Puget, F. W. Stecker, and J. H. Bredekamp, *Photonuclear interactions of ultrahigh energy cosmic rays and their astrophysical consequences*, *The Astrophysical Journal* **205** (1976) 638–654. [Cited on page 71.]

[443] E. Khan, S. Goriely, D. Allard, E. Parizot, T. Suomijärvi, A. J. Koning, S. Hilaire, and M. C. Duijvestijn, *Photodisintegration of ultra-high-energy cosmic rays revisited*, *Astroparticle Physics* **23** (2005) 191–201, [astro-ph/0412109]. [Cited on pages 71 and 72.]

[444] A. J. Koning, S. Hilaire, and M. C. Duijvestijn, *TALYS: Comprehensive Nuclear Reaction Modeling*, in *International Conference on Nuclear Data for Science and Technology* (R. C. Haight, M. B. Chadwick, T. Kawano, and P. Talou, eds.), vol. 769 of *American Institute of Physics Conference Series*, pp. 1154–1159, (2005). [Cited on page 71.]

[445] A. J. Koning and J. P. Delaroche, *Local and global nucleon optical models from 1 keV to 200 MeV*, *Nuclear Physics A* **713** (2003) 231–310. [Cited on page 71.]

[446] S. Goriely, S. Hilaire, and A. J. Koning, *Improved predictions of nuclear reaction rates with the TALYS reaction code for astrophysical application*, *Astronomy & Astrophysics* **487** (2008) 767–774, [arXiv:0806.2239]. [Cited on page 71.]

[447] N. Nierstenhoefer, *On the Origin and Propagation of Ultra-High Energy Cosmic Rays*. PhD thesis, University of Wuppertal, 2011. [Cited on page 71.]

[448] J. Rachen, *Interaction Processes and Statistical Properties of the Propagation of Cosmic Rays in Photon Backgrounds*. PhD thesis, University of Bonn, 1996. [Cited on page 71.]

[449] L. A. Kulchitskii, Y. M. Volkov, J. P. Ostriker, and V. I. Ogurtsov, *Energy levels of ^7Li observed in its photoemission*, *Izvestiya Rossiiskoi Akademii Nauk. Seriya Fizicheskaya* **27** (1963) 1412. [Cited on page 71.]

[450] V. V. Varlamov, *Photonuclear data. photodisintegration of lithium. evaluated cross sections of channels and reactions*, tech. rep., Moscow State University, Moscow, Russia, 1986. [Cited on page 71.]

[451] M. V. Kossov, *Approximation of photonuclear interaction cross-sections*, *European Physical Journal A* **14** (2002) 377–392. [Cited on page 71.]

[452] J. Ahrens, *The total absorption of photons by nuclei*, *Nuclear Physics A* **446** (1985) 229–239. [Cited on page 71.]

[453] A. J. Koning, S. Hilaire, and S. Goriely, *TALYS-1.6 User Manual*, 1st ed., (2013). [Cited on pages 72 and 73.]

[454] P. Axel, *Electric Dipole Ground-State Transition Width Strength Function and 7-Mev Photon Interactions*, *Physical Review* **126** (1962) 671–683. [Cited on page 72.]

[455] J. Kopecky and M. Uhl, *Test of gamma-ray strength functions in nuclear reaction model calculations*, *Physical Review C* **41** (1990) 1941–1955. [Cited on page 72.]

[456] M. B. Chadwick, P. Obloinský, P. E. Hodgson, and G. Reffo, *Pauli-blocking in the quasideuteron model of photoabsorption*, *Physical Review C* **44** (1991) 814–823. [Cited on page 72.]

[457] P. Obložinský and M. B. Chadwick, *Calculations of Photoproduction Reactions*, pp. 842–847. Research Reports in Physics. Springer, Berlin, Heidelberg, 1992. [Cited on page 72.]

[458] R. Capote, M. Herman, P. Obložinský, P. G. Young, S. Goriely, T. Belgya, A. V. Ignatyuk, A. J. Koning, S. Hilaire, V. A. Plujko, M. Avrigeanu, O. Bersillon, M. B. Chadwick, T. Fukahori, Z. Ge, Y. Han, S. Kailas, J. Kopecky, V. M. Maslov, G. Reffo, M. Sin, E. S. Soukhovitskii, and P. Talou, *RIPL - Reference Input Parameter Library for Calculation of Nuclear Reactions and Nuclear Data Evaluations*, *Nuclear Data Sheets* **110** (2009) 3107–3214. [Cited on page 73.]

[459] A. J. Koning, D. Rochman, and S. C. van der Marck, *Extension of TALYS to 1 GeV*, *Nuclear Data Sheets* **118** (2014) 187–190. [Cited on page 73.]

[460] K. Dolag and F. Stasyszyn, *An MHD GADGET for cosmological simulations*, *Monthly Notices of the Royal Astronomical Society* **398** (2009) 1678–1697, [arXiv:0807.3553]. [Cited on page 78.]

[461] H.-P. Bretz, M. Erdmann, P. Schiffer, D. Walz, and T. Winchen, *PARSEC: A parametrized simulation engine for ultra-high energy cosmic ray protons*, *Astroparticle Physics* **54** (2014) 110–117, [arXiv:1302.3761]. [Cited on pages 79 and 108.]

[462] K. M. Górski, E. Hivon, A. J. Banday, B. D. Wandelt, F. K. Hansen, M. Reinecke, and M. Bartelmann, *HEALPix: A Framework for High-Resolution Discretization and Fast Analysis of Data Distributed on the Sphere*, *The Astrophysical Journal* **622** (2005) 759–771, [astro-ph/0409513]. [Cited on page 79.]

[463] O. E. Kalashev and E. Kido, *Simulations of Ultra High Energy Cosmic Rays propagation*, *ArXiv e-prints* (2014) [arXiv:1406.0735]. [Cited on page 80.]

[464] M. Erdmann, D. Kuempel, G. Mueller, G. Sigl, D. Walz, and T. Winchen, *A Benchmark Scenario for UHECR Propagation*, Pierre Auger Collaboration internal note GAP 2012-138, 2012. [Cited on page 81.]

[465] K. Dolag, D. Grasso, V. Springel, and I. Tkachev, *Mapping Deflections of Ultrahigh Energy Cosmic Rays in Constrained Simulations of Extraglactic Magnetic Fields*, *Soviet Journal of Experimental and Theoretical Physics Letters* **79** (2004) 583–587, [astro-ph/0310902]. [Cited on pages 81, 95, 97, and 129.]

[466] W. Saunders, W. J. Sutherland, S. J. Maddox, O. Keeble, S. J. Oliver, M. Rowan-Robinson, R. G. McMahon, G. P. Efstathiou, H. Tadros, S. D. M. White, C. S. Frenk, A. Carramiñana, and M. R. S. Hawkins, *The PSCz catalogue*, *Monthly Notices of the Royal Astronomical Society* **317** (2000) 55–63, [astro-ph/0001117]. [Cited on page 81.]

[467] G. Sigl, F. Miniati, and T. A. Ensslin, *Ultrahigh energy cosmic rays in a structured and magnetized universe*, *Physical Review D* **68** (2003) 043002, [astro-ph/0302388]. [Cited on pages 81, 86, and 97.]

[468] E. Armengaud, G. Sigl, and F. Miniati, *Ultrahigh energy nuclei propagation in a structured, magnetized universe*, *Physical Review D* **72** (2005) 043009, [astro-ph/0412525]. [Cited on pages 81 and 97.]

[469] Pierre Auger Collaboration, *Interpretation of the depths of maximum of extensive air showers measured by the Pierre Auger Observatory*, *Journal of Cosmology and Astroparticle Physics* **2** (2013) 26, [arXiv:1301.6637]. [Cited on pages 82 and 105.]

[470] R. Teyssier, *Cosmological hydrodynamics with adaptive mesh refinement. A new high resolution code called RAMSES*, *Astronomy & Astrophysics* **385** (2002) 337–364, [astro-ph/0111367]. [Cited on page 85.]

[471] M.-S. Shin and J. Devriendt, "Oxford cosmological simulations." unpublished. [Cited on page 85.]

[472] D. G. Yamazaki, T. Kajino, G. J. Mathews, and K. Ichiki, *The search for a primordial magnetic field*, *Physics Reports* **517** (2012) 141–167, [arXiv:1204.3669]. [Cited on page 86.]

[473] A. Saveliev, C. Evoli, and G. Sigl, *The Role of Plasma Instabilities in the Propagation of Gamma-Rays from Distant Blazars*, *ArXiv e-prints* (2013) [arXiv:1311.6752]. [Cited on page 86.]

[474] C. Federrath, G. Chabrier, J. Schober, R. Banerjee, R. S. Klessen, and D. R. G. Schleicher, *Mach Number Dependence of Turbulent Magnetic Field Amplification: Solenoidal versus Compressive Flows*, *Physical Review Letters* **107** (2011) 114504, [arXiv:1109.1760]. [Cited on page 87.]

[475] M. A. Latif, D. R. G. Schleicher, W. Schmidt, and J. Niemeyer, *The small-scale dynamo and the amplification of magnetic fields in massive primordial haloes*, *Monthly Notices of the Royal Astronomical Society* **432** (2013) 668–678, [arXiv:1212.1619]. [Cited on page 87.]

[476] A. Guttman, *R-trees: A dynamic index structure for spatial searching*, in *Proceedings of the 1984 ACM SIGMOD International Conference on Management of Data*, SIGMOD '84, (New York, NY, USA), pp. 47–57, ACM, 1984. [Cited on page 88.]

[477] N. Roussopoulos, S. Kelley, and F. Vincent, *Nearest neighbor queries*, in *Proceedings of the 1995 ACM SIGMOD International Conference on Management of Data*, SIGMOD '95, (New York, NY, USA), pp. 71–79, ACM, 1995. [Cited on page 88.]

[478] D. Paoletti and F. Finelli, *CMB constraints on a stochastic background of primordial magnetic fields*, *Physical Review D* **83** (2011) 123533, [arXiv:1005.0148]. [Cited on page 91.]

[479] C. Foster and L. A. Nelson, *The Size, Shape, and Orientation of Cosmological Voids in the Sloan Digital Sky Survey*, *The Astrophysical Journal* **699** (2009) 1252–1260, [arXiv:0904.4721]. [Cited on page 91.]

[480] J. Jasche, F. S. Kitaura, C. Li, and T. A. Enßlin, *Bayesian non-linear large-scale structure inference of the Sloan Digital Sky Survey Data Release 7*, *Monthly Notices of the Royal Astronomical Society* **409** (2010) 355–370, [arXiv:0911.2498]. [Cited on page 91.]

[481] D. Ryu, H. Kang, and P. L. Biermann, *Cosmic magnetic fields in large scale filaments and sheets*, *Astronomy & Astrophysics* **335** (1998) 19–25, [astro-ph/9803275]. [Cited on page 91.]

[482] J. E. Forero-Romero, Y. Hoffman, S. Gottlöber, A. Klypin, and G. Yepes, *A dynamical classification of the cosmic web*, *Monthly Notices of the Royal Astornomical Society"* **396** (2009) 1815–1824, [arXiv:0809.4135]. [Cited on page 91.]

[483] E. Tempel, R. S. Stoica, V. J. Martínez, L. J. Liivamägi, G. Castellan, and E. Saar, *Detecting filamentary pattern in the cosmic web: a catalogue of filaments for the SDSS*, *Monthly Notices of the Royal Astronomical Society* **438** (2014) 3465–3482, [arXiv:1308.2533]. [Cited on page 91.]

[484] G. Sigl, F. Miniati, and T. A. Enßlin, *Ultrahigh energy cosmic ray probes of large scale structure and magnetic fields*, *Physical Review D* **70** (2004) 043007, [astro-ph/0401084]. [Cited on pages 97 and 104.]

[485] G. Sigl, F. Miniati, and T. A. Enßlin, *Cosmic Magnetic Fields and Their Influence on Ultra-High Energy Cosmic Ray Propagation*, *Nuclear Physics B Proceedings Supplements* **136** (2004) 224–233, [astro-ph/0409098]. [Cited on page 97.]

[486] M. A. Duvernois and M. R. Thayer, *The Elemental Composition of the Galactic Cosmic-Ray Source: ULYSSES High-Energy Telescope Results*, *The Astrophysical Journal* **465** (1996) 982. [Cited on page 109.]

[487] A. Neronov and D. V. Semikoz, *A method of measurement of extragalactic magnetic fields by TeV gamma ray telescopes*, *Journal of Experimental and Theoretical Physics Letters* **85** (2007) 473–477, [astro-ph/0604607]. [Cited on pages 113, 121, and 123.]

[488] A. Neronov and D. V. Semikoz, *Sensitivity of γ-ray telescopes for detection of magnetic fields in the intergalactic medium*, *Physical Review D* **80** (2009) 123012, [arXiv:0910.1920]. [Cited on pages 113, 121, 122, and 124.]

[489] A. Neronov, D. Semikoz, M. Kachelriess, S. Ostapchenko, and A. Elyiv, *Degree-scale GeV "Jets" from Active and Dead TeV Blazars*, *The Astrophysical Journal* **719** (2010) L130–L133, [arXiv:1002.4981]. [Cited on pages 113 and 121.]

[490] A. Eungwanichayapant and F. Aharonian, *Very High Energy Gamma Rays from e Pair Halos*, *International Journal of Modern Physics D* **18** (2009) 911–927, [arXiv:0907.2971]. [Cited on pages 113 and 121.]

[491] K. Dolag, M. Kachelrieß, S. Ostapchenko, and R. Tomàs, *Blazar Halos as Probe for Extragalactic Magnetic Fields and Maximal Acceleration Energy*, *The Astrophysical Journal* **703** (2009) 1078–1085, [arXiv:0903.2842]. [Cited on pages 113, 121, and 128.]

[492] P. Roustazadeh and M. Böttcher, *Very High Energy Gamma-ray-induced Pair Cascades in Blazars and Radio Galaxies: Application to NGC 1275*, *The Astrophysical Journal* **717** (2010) 468–473, [arXiv:1005.2379]. [Cited on page 113.]

[493] O. Klein and T. Nishina, *Über die Streuung von Strahlung durch freie Elektronen nach der neuen relativistischen Quantendynamik von Dirac*, *Zeitschrift fur Physik* **52** (1929) 853–868. [Cited on page 115.]

[494] S. Lee, *Propagation of extragalactic high energy cosmic and γ rays*, *Physical Review D* **58** (1998) 043004, [astro-ph/9604098]. [Cited on page 115.]

[495] V. N. Baier, V. M. Katkov, and V. M. Strakhovenko, *High-energy electromagnetic processes in oriented single crystals*, *Novosibirsk Izdatel Nauka* (1989). [Cited on page 116.]

[496] HESS Collaboration, *New constraints on the mid-IR EBL from the HESS discovery of VHE γ-rays from 1ES 0229+200*, *Astronomy & Astrophysics* **475** (2007) L9–L13, [arXiv:0709.4584]. [Cited on pages 118, 121, and 125.]

[497] F. A. Aharonian, P. S. Coppi, and H. J. Voelk, *Very high energy gamma rays from active galactic nuclei: Cascading on the cosmic background radiation fields and the formation of pair halos*, *The Astrophysical Journal Letters* **423** (1994) L5–L8, [astro-ph/9312045]. [Cited on page 121.]

[498] HESS Collaboration, *Detection of VHE gamma-ray emission from the distant blazar 1ES 1101-232 with HESS and broadband characterisation*, *Astronomy & Astrophysics* **470** (2007) 475–489, [arXiv:0705.2946]. [Cited on page 121.]

[499] HESS Collaboration, *Discovery of VHE γ-rays from the distant BL Lacertae 1ES 0347-121*, *Astronomy & Astrophysics* **473** (2007) L25–L28, [arXiv:0708.3021]. [Cited on page 121.]

[500] VERITAS Collaboration, *The Discovery of γ-Ray Emission from the Blazar RGB J0710+591*, *The Astrophysical Journal Letters* **715** (2010) L49–L55, [arXiv:1005.0041]. [Cited on page 121.]

[501] HEGRA Collaboration, *Observations of 54 Active Galactic Nuclei with the HEGRA system of Cherenkov telescopes*, *Astronomy & Astrophysics* **421** (2004) 529–537. [Cited on page 125.]

[502] M. Schroedter, H. M. Badran, J. H. Buckley, J. Bussons Gordo, D. A. Carter-Lewis, C. Duke, D. J. Fegan, S. F. Fegan, J. P. Finley, G. H. Gillanders, J. Grube, D. Horan, G. E. Kenny, M. Kertzman, K. Kosack, F. Krennrich, D. B. Kieda, J. Kildea, M. J. Lang, K. Lee, P. Moriarty, J. Quinn, M. Quinn, B. Power-Mooney, G. H. Sembroski, S. P. Wakely, V. V. Vassiliev, T. C. Weekes, and J. Zweerink, *A Very High Energy Gamma-Ray Spectrum of 1ES 2344+514*, *The Astrophysical Journal* **634** (2005) 947–954, [astro-ph/0508499]. [Cited on page 125.]

[503] MAGIC Collaboration, *The simultaneous low state spectral energy distribution of 1ES 2344+514 from radio to very high energies*, *Astronomy & Astrophysics* **556** (2013) A67, [arXiv:1211.2608]. [Cited on page 125.]

[504] G. Giacinti, M. Kachelrieß, and D. V. Semikoz, *Filamentary Diffusion of Cosmic Rays on Small Scales*, *Physical Review Letters* **108** (2012) 261101, [arXiv:1204.1271]. [Cited on page 126.]

[505] G. Giacinti, M. Kachelrieß, and D. V. Semikoz, *Anisotropic cosmic ray diffusion and its implications for gamma-ray astronomy*, *Physical Review D* **88** (2013) 023010, [arXiv:1306.3209]. [Cited on page 126.]

Eidesstattliche Versicherung
Declaration on oath

Hiermit erkläre ich an Eides statt, dass ich die vorliegende Dissertationsschrift selbst verfasst und keine anderen als die angegebenen Quellen und Hilfsmittel benutzt habe.

I hereby declare, on oath, that I have written the present dissertation by my own and have not used other than the acknowledged resources and aids.

Hamburg, den 15.04.2015

Unterschrift